Fluorescent Nanomaterials from Biomass:

Synthesis and Applications

A thesis presented for the degree of

Doctor of Philosophy

by

Aumber Abbas

School of Engineering,
Newcastle University, United Kingdom

June 2021

Abstract

Energy crisis, environmental deterioration and dwindling fossil resources are the rising global concerns. As a result, utilising biomass waste as a green and renewable resource into value-added materials is highly appealing for the sustainable world. Among various materials explored, carbon and its derivatives attract much more attention due to their intriguing properties and broad range of applications.

This work focused on the conversion of biomass into activated carbon (AC) and its further development into fluorescent carbon nanomaterials for the energy and sensing applications. ‘Spent tea’ was selected as a food waste feedstock. A systematic study was carried out to produce char by pyrolysis and activate it using chemical activation. Consequently, a series of ACs with varying levels of porosity and surface areas (10 to >2000 m^2g^{-1}) were produced. These ACs were employed as an alternate electrode material to study the effect of porosity on the charge transfer in vanadium redox flow battery.

A thorough investigation on the further transformation of char into fluorescent nanomaterials lead to the production of graphene quantum dots (GQDs). An upgraded approach was adopted for the purification of these GQDs. The results showed that GQDs possessed 3-5 layered graphene structure with a size range of 2-20 nm and band gap varying from 2.67 to 2.95 eV. Under the premise of acquiring high yield, the activation and synthesis steps were combined into a single-step microwave treatment and GQDs were synthesised with a high yield of ~84%. Finally, the intensified and green synthesis of GQDs was accomplished under the direct hydrothermal carbonisation of biomass waste. The as-prepared GQDs were applied to design a selective and sensitive sensor for Fe^{3+} ions with a detection limit of as low as 2.5×10^{-6} M. The present work highlights the significance of preparing high-value nanomaterials from little value biomass waste.

Dedication

I dedicate this thesis to my heaven on earth,

my beloved mother ‘**Ameeran Bibi**’,

who taught me how to speak.

Acknowledgement

All praise is due to Almighty Allah, Who guides us in darkness and helps in difficulties, and all respects for His Holy Prophet Muhammad (peace be upon him), who enabled us to recognise our creator.

I would like to avail this opportunity to convey my exclusive gratitude to my supervisor Dr Anh N Phan for her great supervision, kind guidance and extraordinary support throughout the PhD research. Without her continuous help, deep interest and vigilant guidance, the completion of this work would have not been possible. I also express my special gratitude to my co-supervisors: Prof. Steve Bull, Prof. K Mark Thomas and Dr Tuti Mariana Lim for their immense guidance and support in the accomplishment of my research and PhD thesis.

I would like to express special thanks to my beloved mother (Ameeran Bibi), my sweet wife (Taskeen Zahra) and other family members for their enormous moral support, prayers and encouragement throughout this period. Many thanks to all my friends, especially Dr Tanveer A Tabish, for their right directions and support.

I would also like to appreciate and acknowledge:

- Nanyang Technological University, Singapore for giving me an opportunity to conduct a part of my research in Nanyang Environment and Water Research Institute.
- EPSRC National Facility for XPS (HarwellXPS), operated by Cardiff University and UCL, under contract no. PR16195 for the XPS data collection.
- EPSRC National Facility for TEM at Leeds University for the TEM data collection.
- Dr Fabio Cucinotta, School of Chemistry, Newcastle University for his great support regarding the UV-Vis measurements and photoluminescence analysis.
- Dr Tracey Davey and Dr Kathryn White, School of Chemistry, Newcastle University for their kind support in the TEM analysis.
- Dr Emily, Dr Diana and Dr Leon at Durham University for their support in CHN, SEM and TEM analysis.

Finally, I would like to thank the Process Intensification Group, Newcastle University for providing access to prestigious labs and the equipment for experimentation.

Table of Contents

List of publications

1. **Abbas, A.**, Lim, T.M. and Phan, A.N. (2020) 'Effect of electrode porosity on the charge transfer in vanadium redox flow battery', Journal of Power Sources, 488, p. 229411.
2. **Abbas, A.**, Tabish, T., Bull, S.J., Lim, T.M. and Phan, A.N et al. (2020), High yield synthesis of graphene quantum dots from biomass waste as a highly selective probe for Fe^{3+} sensing, Scientific Reports, 10, p. 21262.
3. **Abbas, A.**, Lim, T.M. and Phan, A.N. (2018) 'Biomass-waste derived graphene quantum dots and their applications', Carbon, 140, pp. 77-99.
4. Abbas, S., **Abbas, A**., Liu, Z. and Tang, C. (2020) 'The two-dimensional boron nitride hierarchical nanostructures: Controllable synthesis and superhydrophobicity', Materials Chemistry and Physics, 240, p. 122145.
5. **Abbas, A.**, Abbas, S. and Wang, X. (2016) 'Nanoporous copper: fabrication techniques and advanced electrochemical applications', Corrosion Reviews, 34(5-6), pp. 249-276.
6. Abbas, S., **Abbas, A.**, Huang, Y., Lin, J., Liu, Z., Fang, Y. and Tang, C. (2018) 'Synthesis of boron nitride nanotubes using an oxygen and carbon dual-free precursor', RSC Advances, 8(8), pp. 3989-3995.
7. Abbas, S., Huang, Y., Lin, J., **Abbas, A**., Xu, X., Li, J., Wang, S., Jin, X. and Tang, C. (2016) 'High yield synthesis and optical properties of MgF_2 nanowires with high aspect ratios', RSC Advances, 6(35), pp. 29818-29822.
8. Tabraiz, S., Hassan, S., **Abbas, A.**, Nasreen, S., Zeeshan, M., Fida, S., Shamurad, B.A., Acharya, K. and Petropoulos, E. (2018) 'Effect of effluent and sludge recirculation ratios on integrated fixed films A_2O system nutrients removal efficiency treating sewage', Desalination and Water Treatment, 114, pp. 120-127.

List of Figures

List of Tables

List of abbreviations

AC	Activated carbon
AFM	Atomic force microscopy
BC	Biochar
BET	Brunauer-Emmett-Teller
CHN	Carbon-hydrogen-nitrogen
CNTs	Carbon nanotubes
DI	Deionised
DFT	Density functional theory
DSSC	Dye-sensitised solar cells
FFT	Fast Fourier transform
FTIR	Fourier transform infrared spectroscopy
GQDs	Graphene Quantum Dots
HTC	Hydrothermal carbonisation
HRTEM	High resolution transmission electron microscopy
ITO	Indium tin oxide
J_{sc}	Short circuit current density
PCE	Photo conversion efficiency
PEDOT	Poly(3, 4-ethylenedioxythiophene)
PEI	Poly(ethylene imine)
P3HT	Poly(3-hexylthiophene)
PL	Photoluminescence
PSS	Polystyrene sulfonate
PTFE	Polytetrafluoroethylene

RGO	Reduced graphene oxide
RH-GQDs	Rice husk-graphene quantum dots
SEM	Scanning electron spectroscopy
STL	Spent tea leaves
TEM	Transmission electron spectroscopy
UV-Vis	Ultraviolet visible
VRB	Vanadium redox flow battery
V_{oc}	Open circuit voltage
XPS	X-ray photoelectron spectroscopy
XRD	X-ray diffraction

Chapter 1 Introduction

1.1 Background

Global anxieties about energy crisis, environmental deterioration and dwindling fossil resources are intensifying. The depleting non-renewable global resources coupled with rapid deterioration of the natural environment means the economic feasibility and long-term supply of fossil-fuel derived valuable products are at substantial risk. In addition, the conversion of petroleum into value-added products is frequently driven by supplementary materials (e.g. platinum and rare-earth metals) having their own sustainability issues, therefore, the ability of material industry for stable supply of fossil-fuel derived products will soon come under ever-increasing threat. Moreover, the utilisation of fossil-fuels is inevitably combined with extreme CO_2 emissions. Consequently, the atmospheric CO_2 levels are dramatically increasing, causing acute climate changes. These challenges of global warming, environmental pollution and diminishing fossil-fuels have driven research into clean, sustainable, renewable, and environmentally friendly resources to produce valuable materials (Hu *et al.*, 2010). Among various functional materials investigated, substantial attention has been paid toward the carbon-based nanomaterials in numerous potential fields due to their intriguing properties, such as tunable structure, good conductivity, enlarged surface area, low toxicity, low cost, and long life (Shen *et al.*, 2012a; Ye *et al.*, 2013; Deng *et al.*, 2016). Production and utilisation of carbon-based materials has a very long history, e.g. carbon has been utilised in inks and dyes for over 3000 years (Suh *et al.*, 2009). With the innovation of fullerenes in the 1980s (Kroto *et al.*, 1985) and carbon nanotubes (CNTs) in the 1990s (Iijima, 1991), the material science and engineering associated with carbon materials has become an area of high interest. These carbon based materials find promising applications in the fields of carbon fixation, gas storage, adsorbents, catalyst support, carbon fuel cells, electrodes, cell biology and cosmetics (Yu *et al.*, 2004; Titirici *et al.*, 2007; Balcke *et al.*, 2017). Many preparation approaches, such as laser ablation, carbonisation, hydrothermal carbonisation (HTC), or pyrolysis have been reported for the synthesis of crystalline, amorphous, porous, or other carbonaceous materials with diverse shape, size, and chemistry (Iijima and Ichihashi, 1993; Su *et al.*, 2009; Hu *et al.*, 2010; Yao and Zhao, 2017).

Biomass waste (agricultural residues, food waste, municipal solid waste etc.) is an environmentally friendly renewable resource for preparation of carbon materials due to its high carbon content (40-55%wt) (Williams and Onwudili, 2006; Motghare *et al.*, 2016) and abundance. Carbon materials derived from biomass waste have revealed potential applications in hydrogen storage, biomedicine, sorption materials, and so on (Tilman *et al.*, 2006; Schmidt and Dauenhauer, 2007). However, less attention has been paid to their further conversion into advanced nanomaterials for engineering applications. In order to fulfil this gap, the aim of this project is to produce carbon materials from biomass waste and investigate their further development into luminescent nanomaterials for energy and sensing applications.

After water, tea is the second most consumed beverage globally and every year several billion tons of tea are produced for intake (Hayat *et al.*, 2015). Interestingly, 78% of the tea produced worldwide is black tea (Hayat *et al.*, 2015). Particularly, most of the tea brewed in the United Kingdom is prepared from tea bags (Nelson and Poulter, 2004). Usually, after consumption, these tea bags are discarded as useless materials and need disposal. These environmentally undesirable materials can be utilised as potential precursors for the sustainable production of carbon materials. Moreover, the tea is a hydrocarbon-rich substance containing over 100 compounds and its major components are polyphenols (Yashin *et al.*, 2015). Consequently, the optimised thermal carbonisation can lead to ~80 at% of carbon in its char. Therefore, ‘spent tea’ as a representative of the food waste, rich in carbon and renewable resource was selected as a promising precursor to produce carbon-based nanomaterials for engineering applications.

A number of techniques, such as pyrolysis, HTC, liquefaction and gasification, have been implemented for the thermochemical conversion of biomass into desirable products (Shafizadeh, 1982; Jain *et al.*, 2016). Pyrolysis (thermochemical decomposition of matter in absence of oxygen) is a well-known process and has considerably flexibility in terms of adjusting operating conditions (temperature, residence time, heating rate, etc.) to get desirable products i.e. gas, liquids and solids (known as charcoal (Shafizadeh, 1982). Slow pyrolysis (heating rate 1-30 °C/min (Ronsse *et al.*, 2013)) is used for charcoal production whereas fast pyrolysis (heating rate >100 °C/min) is primarily utilised for production of liquid or biofuels (Lin *et al.*, 2009). Hydrothermal processing is commonly performed in water at a temperature range of 180-300 °C (Tekin *et al.*, 2014; Jain *et al.*, 2016), to retain the important functional groups from the biomass. Thus, different techniques result in carbon materials with diverse properties.

During the last several years, continuous research has been conducted to further convert carbonaceous materials into graphene and its derivatives (Girit *et al.*, 2009; Ye *et al.*, 2013; Zheng *et al.*, 2015; Nirala *et al.*, 2017) and elaborate their fluorescence properties. Fluorescence has a wide range of applications ranging from minerology, sensing, medicine, bioimaging, fluorescent labelling, cosmic-ray detection and biological detectors to our daily life fluorescent lamps and light emitting diodes. However, graphene is zero-band gap material which makes the observation of its optical luminescence almost impossible. Thankfully, the bandgap has been manipulated in graphene nanoribbons (GNRs) and graphene quantum dots (GQDs) due to their quantum confinement and edge effects (Ritter and Lyding, 2009; Shen *et al.*, 2012a). Quantum confinement is the phenomenon observed when the diameter of a material decreases and reaches the magnitude of the de Broglie wavelength of the electron wave function (1.23 nm), the energy spectrum becomes discrete and the bandgap of the material becomes size dependent. Whereas, the small changes at the edges of GQDs result in pronounced effects on their properties and are known as edge effects. The fluorescence properties of GQDs can be regulated by adjusting the size.

When the particle size reaches an optimum value, the quantum confinement effect occurs leading to the collapse of continuous energy band of the bulk material into discrete energy levels like in an atom. Owing to the generation of discrete energy levels in a quantum dot, the gap between highest occupied electron levels and lowest unoccupied levels increases in comparison with the bulk material. As a result, the material's optical properties turn out to be size dependent, as shown in Figure 1.1.

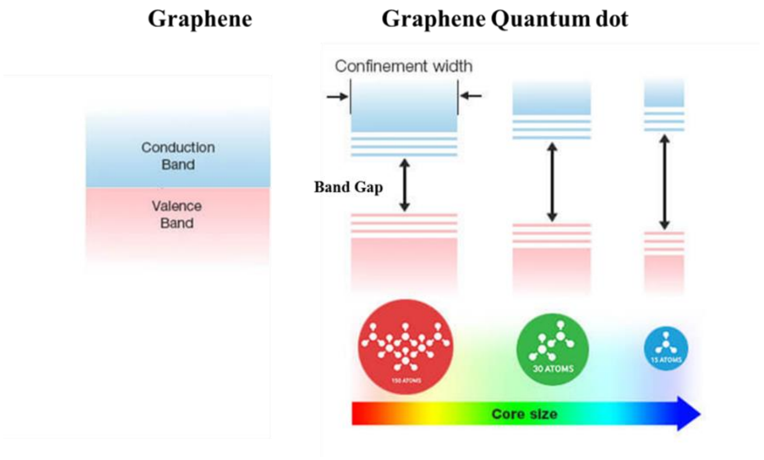

Figure 1.1. Transition from continuous to discrete energy levels with decrease of the size of particle from bulk to a quantum dot (Lappetito, 2015).

The minimum amount of energy necessitated to generate an exciton is decided by the bandgap of the material. When a quantum dot absorbs a photon of energy equal to or greater than the band gap, the electrons in the quantum dots are excited to the conduction band. This excited state is not stable, and the electron relaxes back to the valence band through the emission of a photon. This phenomenon is known as fluorescence.

1.2 Significance

GQDs, as a new type of zero-dimensional fluorescent nanomaterials, have gained substantial interest due to their exceptional size-dependent optical properties. The GQDs exhibit extraordinary properties such as strong fluorescence, good biocompatible, dispersibility in numerous solvents, and low toxicity, demonstrating substantial significance in medicine, bioimaging, photovoltaic devices, light-emitting diodes, solar cells, fuel cells, batteries, supercapacitors and sensors (Zhang *et al.*, 2012b; Zheng *et al.*, 2015; Abbas *et al.*, 2018; Liu *et al.*, 2020b). A number of synthesis approaches have been adopted to produce GQDs from various precursors. However, most of the synthesis techniques require expensive starting materials, toxic chemicals, harsh reaction conditions, complex processes, prolonged duration, and have low yields (Wang *et al.*, 2015a; Wang *et al.*, 2016a). Therefore, advanced synthesis approaches are highly desirable for getting a precise control over property-application relationship. Nonetheless, often this aim has to be well-adjusted by the demands for low cost and large-scale productions. Thus, searching for a cheap and green precursor from regular food along with simple and effective synthesis approach may overcome the above-mentioned limitations. Moreover, despite several efforts, a systematic study on the investigation of suitable biomass derived precursor for GQDs synthesis is still lacking. Thus, in this work, a systematic study is carried out to search the optimum biomass precursor for the synthesis of GQDs with high purity, high product yield and in considerable quantities for practical applications.

1.3 Aim and objectives

This project aims to convert biomass waste into superior carbon materials and discover their applications in energy and sensing. In a broader context, it seeks to solve the future materials demands and biowaste recycle problems as a part of sustainable future.

The following objectives are carried out to achieve the above aim:

I. The conversion of biomass waste feedstock into char and studying the char activation techniques to prepare AC materials with varying degree of porosity.

II. A systematic study of suitable biomass-derived precursors for the development of highly pure GQDs.

III. A single step preparation over a short timespan for achieving high yield of GQDs.

IV. The intensified and green preparation of GQDs for practical applications.

V. To evaluate the properties and performance of superior carbon-based materials on energy storage (i.e. battery) and sensing (e.g. photoluminescence sensor) applications.

1.4 Thesis layout

The thesis consists of eight chapters briefly described as follows.

Chapter 1 presents a brief background, research gap, research motivation, aim and objectives and structure of the thesis.

Chapter 2 describes the literature review related to the different approaches for the conversion of biomass into carbon-based materials and their further conversion into GQDs for various applications.

Chapter 3 provides materials and methods used in the experiments carried out in this study.

Chapter 4 illustrates the synthesis of AC from biomass waste, its characterisation and use a superior electrode material for vanadium redox flow battery application. Moreover, the effect of electrode porosity on the performance of battery is systematically investigated.

Chapter 5 demonstrates the further conversion of activated carbons into luminescent nanomaterials such as GQDs and their characterisation. In addition, an improved approach has been described for the purification of biomass derived GQDs.

Chapter 6 explains the strategy to combine activation and synthesis steps into a single step synthesis of GQDs. The single step microwave approach results in a record high yield (>80%) of GQDs. Moreover, the development of sensitive sensor for the detection of Fe^{3+} ion is presented.

Chapter 7 reveals the intensification of GQDs synthesis and introduces a green approach for the preparation of high quality GQDs on gram scale.

Chapter 8 summarizes the main findings of this work and presents some recommendations for the further process intensification and applications of GQDs.

Chapter 2 Literature review

Energy crisis, diminishing fossil resources, environmental deterioration and increasing customer needs have compelled scientists to search low cost, green and renewable resources for the sustainable production of advanced materials. Among various materials explored, carbon-based nanomaterials, especially graphene and graphene quantum dots (GQDs), have attracted extensive attention recently owing to their intriguing properties, such as high conductivity, extensive surface area, good biocompatibility, low toxicity, and long life. This chapter investigates the possibility of converting the biomass waste into superior carbonaceous materials. The possible routes for converting biowaste into activated carbon (AC) and its further conversion into luminescent nanomaterials such as GQDs, are discussed. Factors affecting the physical and chemical properties of GQDs for numerous promising applications have also been discussed. The recent engineering applications of GQDs have been reviewed here. Finally, the remaining challenges, future perspectives and possible research directions in the field are presented.

2.1 Background

Energy shortage, limited availability, and overconsumption of non-renewable resources coupled with rapid deterioration of the natural environment are the major problems of the modern world (Goldemberg *et al.*, 1988; Alam and Ramakrishna, 2013; Franco *et al.*, 2017). Although numerous efforts have been made to search the renewable resources, the fossil fuels still remain as main sources of energy, transportation fuel and precursor for many valuable products, and are anticipated to continue so for next 20-40 years. The global demand for these products is continuously increasing due to high population growth and industrialisation. Consequently, these fossil resources are depleting fast and are going to diminish at increasing rates. Moreover, the generation of CO_2 from burning fossil-fuels has been severely increased in recent years, imposing drastic challenges of global warming and environmental pollution. In this perspective, there is great need to search clean, sustainable, renewable, and environmentally friendly resources to produce value-added materials (Hu *et al.*, 2010). Among advanced functional materials investigated, carbon-based materials have attracted much attention in numerous potential fields due to their excellent properties, such as large surface area, tunable structure, high conductivity, low toxicity and long life (Shen *et al.*, 2012a; Ye *et al.*, 2013; Deng *et al.*, 2016).

Carbon-based materials are traditionally produced from non-renewable sources such as coal (Chingombe *et al.*, 2005; Ye *et al.*, 2013) and petroleum coke (Kawano *et al.*, 2008). However, increasing demand and sharp decline of non-renewable resources coupled with environmental deterioration require the synthesis of carbon-based materials from renewable raw materials for the sustainable world. On this account, biomass waste (agricultural residues, food waste, municipal solid waste etc.) stand out as an environmentally friendly renewable resource for the preparation of high valued carbon materials due to its high carbon content (40-55 wt.%) (Motghare *et al.*, 2016) and abundance (Xie and Goodell, 2014). Although biomass waste is high in carbon content (McKendry, 2002), only a small percentage (ca. 20-30%) from human daily activities and agriculture are recycled, composted or combusted at presented while other (ca. 70-80%) is disposed into landfill (Themelis and Arsova, 2015). It can be considered as a potential precursor to produce carbon-based materials with new functionalities and grow a more sustainable materials industry. Recently, carbon materials, such as activated carbon, derived from biowaste have revealed potential applications in hydrogen storage, biomedicine, sorption materials, and so on (Tilman *et al.*, 2006; Schmidt and Dauenhauer, 2007). However, more work is required for commercialisation of biomass derived carbon materials for sufficient performance, activity and effectiveness.

Several techniques have been implemented for the thermochemical conversion of biomass into desirable products (Shafizadeh, 1982; Jain *et al.*, 2016). Among other thermal chemical processes, pyrolysis and hydrothermal carbonisation (HTC) are the two common processes to produce biochar from biomass (Libra *et al.*, 2011). Pyrolysis is the thermochemical decomposition of organic matter at elevated temperature (450-650^{o}C) in inert environment into solid (char), liquid and gas with their proportion depending upon operating conditions (Shafizadeh, 1982). Slow pyrolysis (heating rate of 1–30 °C/min (Lua *et al.*, 2004; Ronsse *et al.*, 2013) and a holding time of 1-5 hours (Ringer *et al.*, 2006; Gani and Naruse, 2007; Montoya *et al.*, 2015) and a temperature range of 400 °C to 800 °C (Williams and Besler, 1996)) is applied for char production. The as produced char can be further treated with different chemical agents to produce activated carbon. On the other hand fast pyrolysis, usually carried out at a heating rate of ca. >100 °C/min (Kalgo, 2011; Montoya *et al.*, 2015), is primarily conducted for production of liquid product (Ratner *et al.*, 2004; Lin *et al.*, 2009; Bridgwater, 2012). Figure 2.1 shows the schematic representation of pyrolysis process and its product (char) applications.

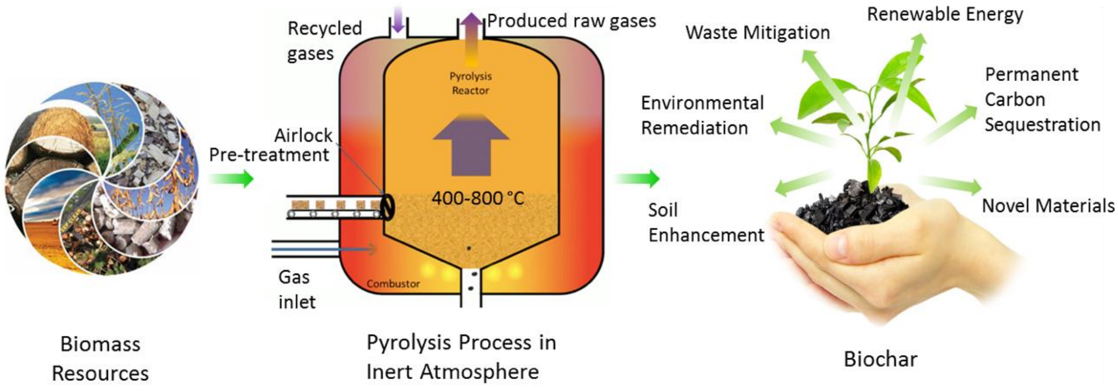

Figure 2.1. Schematic pyrolysis process and market benefits of the biochar derived from biomass waste.

HTC, which is the thermochemical degradation of biomass in the presence of water (water/biomass ratio may vary from 5:1 to 75:1) (Hoekman *et al.*, 2011; Guo *et al.*, 2016; Toufiq Reza *et al.*, 2016) at elevated temperature and pressure, is another promising technique to convert biomass into carbon materials (Funke and Ziegler, 2010; Hu *et al.*, 2010). Depending upon experimental conditions, HTC can be classified into two major categories (Hu *et al.*, 2010). A high temperature HTC process is performed at high temperature (400-800 °C) (Hirose *et al.*, 2002) to produce activated carbon materials, graphite, and carbon nanotubes (Jia *et al.*, 2007; Salvador *et al.*, 2007; Sevilla and Fuertes, 2009b; Titirici and Antonietti, 2010; Yang *et al.*, 2012). A low temperature HTC process is conducted at relatively low temperature (200-300 °C) to synthesise carbonaceous materials with varied morphology, size, shape, and surface functionalities (Sevilla and Fuertes, 2009a; Titirici and Antonietti, 2010; Tekin *et al.*, 2014; Jain *et al.*, 2016; Shen *et al.*, 2017). Based on the HTC route employed, the carbonaceous materials obtained with different size, shape, morphology and properties have been implemented in the field of energy, catalysis, sensors, biology or environment (Wei *et al.*, 2011).

2.2 Activated carbon

Activated carbon (AC) also known as activated porous carbon is a processed form of carbon having low volume small pores that enlarge the available surface area for chemical reactions. ACs with highly porous structure have been well-known for their utilisation in wide range of applications such as water purification, air filters, energy storage, industrial purification and removal of pollutants (Chingombe *et al.*, 2005; Jänes *et al.*, 2007; Kawano *et al.*, 2008; Jain *et al.*, 2016). The porous structure along with high surface area of AC deliver substantial benefits, especially as electrode material in energy storage applications. The large surface area offers abundant active sites to facilitate the electrochemical reaction while carbon skeleton provides high conductivity required for the charge carriers. However, most of ACs are traditionally produced from non-renewable fossil fuels which are expensive and depleting fast. Therefore, there is urgent need to search renewable precursors for the high-performance carbon electrodes. Herein, biomass stand out as a unique platform to prepare ACs with various desirable properties and structures. This approach is regarded as more favourable than the production of AC from conventional non-renewable fossil-fuels based precursors. This is due to the low cost, abundance, easy availability and green nature of biomass waste and overall environmentally friendly benign nature of pyrolysis process applied for the production of AC (Singh *et al.*, 2019a). The activation strategy of biomass waste is widely accepted as prevailing approach to improve the texture of otherwise nonporous carbon. Herein, different aspects of widely applied chemical and physical activation techniques for the synthesis of AC with varying degree of micro- and nano-porosity and large surface area are described.

2.2.1 Physical activation

The physical activation is a two-step process for the synthesis of AC: 1) The pyrolysis carbonisation of biomass waste to prepare char, 2) The activation of char at elevated temperature using CO_2 or steam. The steam or CO_2 based gasification of char generate porous network in carbon matrix and enlarge the specific surface area. The reactions taking place during the activation process can be summarised as follows (Singh *et al.*, 2019a):

$$C + CO_2 \rightarrow 2CO \tag{2.1}$$

$$CO + H_2O \rightarrow CO_2 + H_2 \tag{2.2}$$

$$C + H_2O \rightarrow CO + H_2 \tag{2.3}$$

The CO_2 based activation usually proceeds with the ($C + CO_2 \rightarrow 2CO$) reaction to produce relatively uniform microporosity with narrow pore size distribution. The surface area obtained under this strategy is usually in the range of 100 to 1000 $m^2\ g^{-1}$ (Zhang *et al.*, 2004). On the other hand, the physical activation using steam generates meso and microporosity. These differences are mainly attributed to the fast reaction of steam resulting in the widening of micropores into meso and macropores. In addition, more pores are created using steam as it can penetrate the interior structure of carbon. The combination of CO_2 and steam results in large surface area (over 2000 m^2g^{-1}) with superior levels of porosity (Yang *et al.*, 2010).

2.2.2 *Chemical activation*

The chemical activation process of biomass waste usually produces highly porous structure with large number of functional groups attached on the surface. Most importantly, the chemical activation produces extremely high surface area AC. However, the core mechanism of chemical activation is still under debate. It is suggested that the decomposition of biopolymers during pyrolysis accelerates in the presence of a chemical and the rearrangement of intermediate compounds followed by recombination results in the continuous network porous carbon structure. Frequently used chemical agents are KOH, K_2CO_3, H_3PO_4, and $ZnCl_2$, among which KOH is the most popular activating agent (Singh *et al.*, 2019a).

Activation of biomass with KOH is highly effective and widely used approach to produce AC with enhanced degree of porosity and improved electrochemical performance (Cui *et al.*, 2017). The products usually have dominant microporous structure and relatively large specific surface area. The underlying mechanism of KOH activation has been proposed in the literature (Lillo-Ródenas *et al.*, 2003; Raymundo-Pinero *et al.*, 2005; He *et al.*, 2010; Wang and Kaskel, 2012; Wang *et al.*, 2020), as follows:

The reaction of KOH with carbon starts at ~400 °C and almost all the KOH is converted into K_2CO_3 by 600 °C as follows:

$$6\ KOH + 2\ C \rightarrow 2\ K + 3\ H_2 + 3\ K_2CO_3 \tag{2.4}$$

When the temperature is increased over 700 °C, the following reactions take place:

$$K_2CO_3 + C \rightarrow K_2O + 2CO \tag{2.5}$$

$$K_2CO_3 \rightarrow K_2O + CO_2 \tag{2.6}$$

$$2\ K + CO_2 \rightarrow K_2O + CO \tag{2.7}$$

When the temperature is further increased, following reaction may take place at ≥ 800 °C:

$$K_2O + C \rightarrow 2\,K + CO \tag{2.8}$$

The gaseous species produced during the activation process seek to escape through the carbon structure, thereby generating pores. Significant weight loss occurs during the activation process and the yield of as-prepared AC is usually around 30-60 % of the original biochar. Owing to the considerable weight loss, the generation of abundant nanoscale pores can be expected.

Based on above discussions, there are three main widely accepted activation mechanisms of carbon by KOH (Otowa *et al.*, 1993; Raymundo-Piñero *et al.*, 2005), as follows.

1. Etching the carbon matrix by redox reaction between various potassium species as activating agents and carbon, as indicated in equation 2.5 and 2.6. This results in formation of porous network and is known as chemical activation.
2. Formation of steam (H_2O) and carbon dioxide (CO_2) in activation systems further participates in the development of pores through gasification of carbon, as shown in equation 2.1 to 2.3, which is called physical activation.
3. The metallic K and K_2O produced during the activation process efficiently intercalate into carbon lattice of carbon matrix, as indicated in equation 2.8 and 2.9. These intercalated K and K compounds are removed by washing and expanded carbon matrix cannot return to its original nonporous shape and thus a highly microporous network is generated.

2.2.3 Application in energy storage

Efficient energy storage is key to developing sustainable energy systems. Energy storage devices such as batteries, supercapacitors and fuel cells are well known electrochemical technologies for such systems. Among different energy storage technologies, redox flow batteries have shown great potential for medium to large scale energy storage systems due to their long life and high cycle efficiency (Ponce de León *et al.*, 2006; Yang *et al.*, 2011; Alotto *et al.*, 2014; Leung *et al.*, 2017; Singh *et al.*, 2019b). Among various redox flow batteries, vanadium redox flow battery (VRB) has attracted extensive attention due to its multiple key advantages, such as minimal safety concerns, no detrimental effect of cross-mixing, fast response and long cycle life (Skyllas-Kazacos *et al.*, 1991; Skyllas-Kazacos *et al.*, 2010; Ulaganathan *et al.*, 2016; Minke and Turek, 2018). However, the commercial VRB system is quite expensive because of high cost of electrolyte, graphite based electrode, ion-exchange membrane and others (Kear *et al.*, 2012; Leung *et al.*, 2012; Choi *et al.*, 2017). The electrode, which is key element of the battery, provides active sites for the redox reactions and facilitate the electrolyte transport. Therefore, the properties of electrode material, especially the microstructure, play a vital role in the performance of VRB. Unfortunately, the commercially available graphite electrodes are very expensive and suffer severe drawbacks including low degree of porosity, low surface area and poor hydrophilicity, resulting in low electrocatalytic activity and poor performance of VRB (Parasuraman *et al.*, 2013; Kim *et al.*, 2015b). Therefore, the search for high performance electrode materials and optimization of their microstructure to improve the reaction kinetics is critically important. Moreover, the development of low-cost electrode material is current need of the flow battery industry.

The electrochemical performance of the VRB can be monitored and tailored by understanding its reactions kinetics. The chemistry and operation of VRB are defined by the three vanadium redox reactions (V^{2+}/V^{3+}, V^{4+}/V^{3+}, V^{5+}/V^{4+}) taking place at the electrode electrolyte interface (Choi *et al.*, 2019). The thermodynamics of VRB under standard conditions consist of $V^{2+/}V^{3+}$ redox reactions at negative electrode and the VO_2^+/VO^{2+} (V^{5+}/V^{4+}) redox couple at the positive electrode, as shown in Figure 2.2. During charging of the battery V^{3+} reduces to V^{2+} at the negative half-cell, while V^{4+} oxidizes to V^{5+} at the positive half-cell through the exchange of protons (Ulaganathan *et al.*, 2016). Thus, when the battery is charged the difference between oxidation states of the vanadium ions at negative and positive sides changes from +1 to +3. This is easy to comprehend conceptually in that increased difference between the oxidation states of vanadium would help store the electricity (Kim, 2019). When battery is discharged, V^{2+} oxidizes to V^{3+} and V^{5+} is reduced to V^{4+} at the negative and positive sides, respectively. The redox reactions of VRB are described as follows (Ponce de León *et al.*, 2006; Ulaganathan *et al.*, 2016):

At the positive half-cell:

$$VO_2^+ + 2H^+ + e^- \underset{Charging}{\overset{Discharging}{\rightleftarrows}} VO^{2+} + H_2O \qquad E° = 1.0\ \text{V vs SHE} \tag{2.9}$$

At the negative half-cell:

$$V^{2+} \underset{Charging}{\overset{Discharging}{\rightleftharpoons}} V^{3+} + e^{-} \qquad E° = -0.26\ V\ vs\ SHE \qquad (2.10)$$

The overall reaction can be combined as:

$$VO_2^{+} + V^{2+} + 2H^{+} \rightleftharpoons V^{3+} + VO^{2+} + H_2O \qquad E° = 1.26\ V\ vs\ SHE \qquad (2.11)$$

Since the conventional VRB system utilizes a mixture of V^{4+} and V^{3+} electrolytes in 1:1 ratio, the operation of the battery includes an initial precharging step to convert the electrolyte mixture into anolyte and catholyte forms (Roznyatovskaya *et al.*, 2016), by the following reaction (Roznyatovskaya *et al.*, 2020):

$$VO^{2+} + 2H^{+} + e^{-} \underset{Charge\ (anolyte)}{\overset{Charge\ (catholyte)}{\rightleftharpoons}} V^{3+} + H_2O \qquad E° = 0.34\ V\ vs\ SHE \qquad (2.12)$$

The redox reactions of the V^{4+}/V^{3+} couple proceed by electrochemical catalytic mechanism and are known to have slow kinetics due to high activation energy (Roznyatovskaya *et al.*, 2016). The rate of V^{3+} oxidation is higher at electrode surface with high oxygen functionalisation (Roznyatovskaya *et al.*, 2016).

For VRB application, most of the carbon materials investigated to date are derived from non-renewable resources which are expensive and depleting fast. To this end, biomass waste, which has zero or sometimes even negative value, stand out as an abundant, renewable and environmentally friendly resource (Abbas *et al.*, 2018) for the production of carbon electrodes with tunable microstructure for VRB (Baldinelli *et al.*, 2018). A few studies have been reported on the application of biomass derived carbon electrodes in VRB. For example, coconut shells, orange peels, corn protein and shaddock peels have been studied to produce carbon electrodes and demonstrated improved VRB performance (Park *et al.*, 2014; Ulaganathan *et al.*, 2015; Maharjan *et al.*, 2017). However, none of these studies focused on the systematic investigation of effect of electrode microstructure on the performance of VRBs. Therefore, it is substantially important to develop biomass derived electrodes with tunable microstructure to improve the electrocatalytic activity and performance of VRB system.

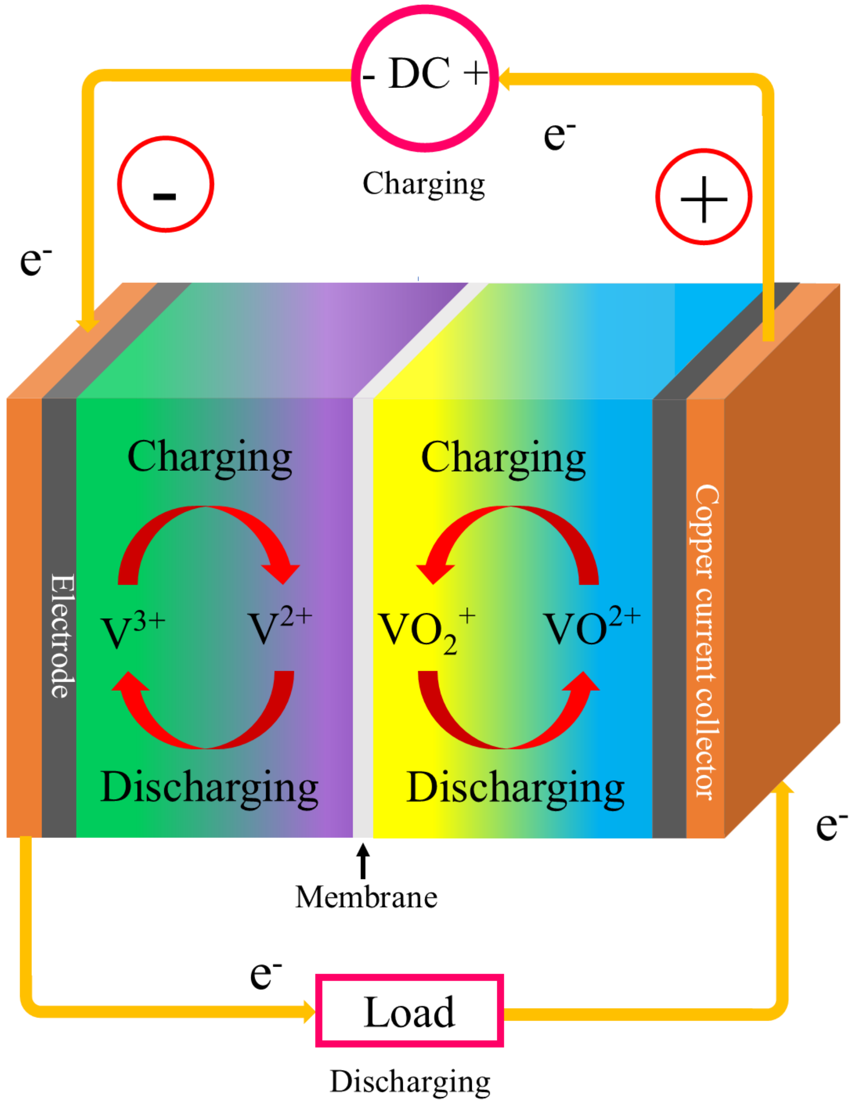

Figure 2.2. Schematic illustration of the VRB operation with carbon electrode facilitating the vanadium redox reactions.

2.3 Luminescent nanomaterials

During the last several years, there has been a continuous eagerness to further convert carbonaceous materials into luminescent nanomaterials, such as zero-dimensional GQDs (Girit *et al.*, 2009; Ye *et al.*, 2013; Zheng *et al.*, 2015; Nirala *et al.*, 2017) and study the phenomenon of quantum confinement and edge effects (Ritter and Lyding, 2009; Shen *et al.*, 2012a). Quantum confinement is the phenomenon observed when the diameter of a material decreases and reaches the magnitude of the de Broglie wavelength of the electron wave function, the energy spectrum becomes discrete and the bandgap of the material becomes size dependent.

Whereas, small changes in structure of the edges of GQDs result in pronounced effects on their properties and are known as edge effects.

2.3.1 Quantum confinement

The confinement of the electrons means limiting their movement in a space with dimensions of their de Broglie wavelength. The result of this confinement in space is the quantisation of their energy levels and momentum. When the spatial extent of the electronic wave function is comparable with the particle size, the electrons feel the presence of particle boundaries and respond to the changes in the particle size by adjusting their energy. This effect becomes most significant when the dimensions of the particle reaches near to or below the Bohr exciton radius of the bulk material and, as a result, the material properties become size dependent. In such a case, the materials properties are subjected to the principles of quantum mechanics rather than classical mechanics (Yoffe, 1993; Park *et al.*, 2001). In quantum mechanics, the energy, momentum and other quantities are restricted to discrete values and objects behave like both particles and waves.

When the particle size reaches the value of Bohr radius, the quantum confinement effect occurs leading to the collapse of the continuous energy band of the bulk material into discrete energy levels like an atom. The discrete assembly of energy states leads to the discrete absorption spectrum, as shown in Figure 2.3.

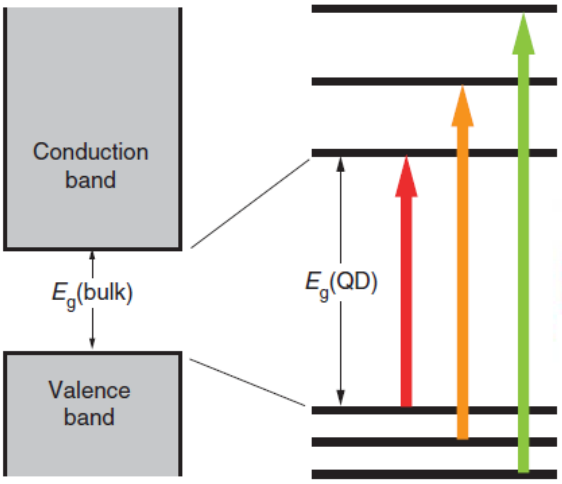

Figure 2.3. Transition from continuous to discrete energy levels with decrease of the size of particle from bulk to a quantum dot (Lappetito, 2015).

The conduction band starts from the upper edge of the bandgap and goes higher. The electrons in the valence band need energy equivalent to or more than the bandgap energy to cross the gap and reach the conduction band. After the electrons are excited to conduction band, they relax back to the valence band followed by emission of a photon. This property is called luminescence (Gullapalli and Barron, 2010).

2.3.2 Luminescence

Luminescence is the phenomenon of emission of light by certain substances after absorbing different types of energies, without the generation of heat. This is thus a type of cold body radiation. The term luminescence was first introduced by E. Wiedemann in 1888. When a substance is subjected to a certain type of energy, its electronic states are excited and upon returning to the ground state emit a photon. Luminescence is divided into different types based on the form of excitation energy. For example, photoluminescence caused by photons of light, chemi-luminescence is induced by chemical energy, and cathodo-luminescence is generated by electrons or cathode rays (Omary and Patterson, 1999).

Luminescence can also be divided into two groups based on the time frame during which the emission of light takes place, namely fluorescence and phosphorescence.

1) Fluorescence is the phenomenon of light emission which continues as long as the excitation persists.

2) Phosphorescence is the luminescence phenomenon which persists after the removal of excitation source.

The decay time is dependent on temperature. The mean lifetime of the excited states in phosphorescence is larger than in fluorescence.

The type of fluorescence in which the excitation is caused by the photons of light with shorter wavelength, usually ultraviolet, is called photoluminescence. In photoluminescence, when a molecule absorbs a photon of light with wavelength λ_1, it is excited to higher energy electronic state, however this state is not stable and it relaxes to lower energy excited state non-radioactively and then decays to ground state by emitting a photon of light with wavelength λ_2. Generally, the emission wavelength λ_2 is higher than the excitation wavelength λ_1. This is called Stokes shift. However, in resonance emission $\lambda 1 = \lambda 2$.

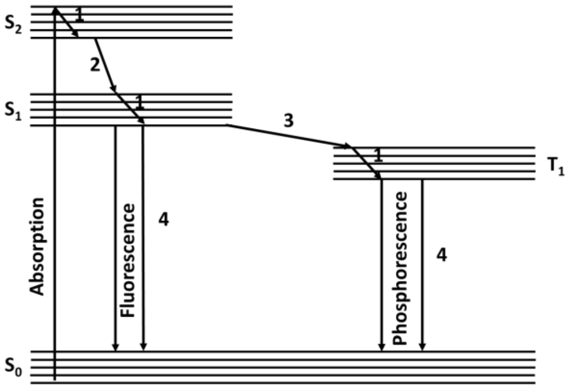

Figure 2.4. Energy level diagram of non-radiative and radiative transition during the luminescence (Omary and Patterson, 1999).

A singlet electronic state consists of paired electrons, while the triplet state comprises unpaired electrons. The spin multiplicities of any electronic state can either be a singlet or a triplet. Generally, the ground electronic state denoted as S_0 is a singlet state, while the excited states can either be singlet or triplet, designated as S_1, S_2 and T_1, respectively (Figure 2.4). Upon the absorption of photon an electron is shifted from lower energy ground state to higher energy excited state of same spin multiplicity. Since the selection rule for the electronic transition states that the spin state of the electron should be retained upon excitation. Thus, the excitation mechanism excludes shifting to triplet excited state because of its different spin multiplicity. The time spent in transition of electron from ground state to excited state is 10^{-14} –10^{-15} seconds. A series of radiative and non-radiative processes occur following the absorption of light (Omary and Patterson, 1999).

There are four types of non-radiative processes possibly taking place prior to luminescence.

1) Usually the molecules are excited to the higher vibrational level of the targeted-excited state and relax rapidly to the lowest vibrational level in a non-radiative manner in a very short time of 10^{-12} –10^{-14}. This phenomenon is called ***vibration relaxation*** and takes place prior to luminescence.

2) When the molecule is excited to a singlet state of energy higher than S_1, it relaxes rapidly to lowest energy singlet state such as S_2 in a non-radiative manner. This relaxation transition between the states of same spin multiplicity is called ***internal conversion***. The time scale of this process is 10^{-12} s.

3) If the relaxation takes place between the states of different spin multiplicity in a non-radiative way, such as S_1 to T_1 in Fig 1.4, the process is called ***intersystem crossing***.

4) After the occurrence of the above-mentioned processes, rest of the energy is released radiatively or non-radiatively. If the decay takes place non-radiatively by the release of energy in the form of heat, the process is called ***non-radiative de-excitation***. This minute amount of heat cannot be measured experimentally, however the quenching of luminescence is evidence of non-radiative excitation.

There are two types of possible radiative processes, fluorescence and phosphorescence. Fluorescence relates to the emission of light when the decay takes place from excited electronic state to the ground state while both states have same spin multiplicity. For example, the radiative transition from S_1 to S_0 is representing fluorescence. The transition of states in fluorescence is spin allowed, that is why it takes place very rapidly under the time scale less than 10^{-6} s. The phosphorescence is the emission of light as a result of the radiative electronic transition between the states of different spin multiplicity. For example, the transition from T_1 to S_0 in Figure 2.4**.** Since the phosphorescence transitions are spin forbidden, they take place slowly and the average lifetime of the excitation ranges from 10^{-6} to several seconds. It is also called “delayed fluorescence” (Ronda, 2007).

In order to excite the luminescence mechanism, the absorption of energy takes place by the host lattice or impurity ions/atoms added intentionally. Mostly the emission takes place on impurity ions that are called activator ions if they produce the required emission. When the activators show very weak absorption, then a second type of impurity can be added, known as a sensitizer. These sensitizers absorb the energy and then transfer it to the activator. The transport of energy in these processes takes place through the luminescent materials. Thus, the emission color can be adjusted by the selection of suitable impurity ions in the same host lattice. This is true for rare-earth metals which show emission at fixed spectral positions and their chemical environment has no influence on the emission. A phenomenon in which the photons of lower energy are absorbed by a material and re-emitted as a higher energy photos is called up-conversion and the opposite is known as down conversion (Ronda, 2007; Ronda *et al.*, 2010).

2.3.3 Quantum yield

The quantum yield of a photoluminescent material is defined as the ratio of number of photons emitted to the total number of photons absorbed. The absorption of a photoluminescent material is usually measured by passing a beam of light through its aqueous suspension and measuring the input and output intensities, considering there is no scattering. In order to minimise the effect of actual scattering, the concentration of the fluorescent material is kept as low as possible. Different strategies have been developed for the determination of quantum yield.

Generally, the quantum yield of a fluorescent material is measured as a relative value with respect to well-developed standards, such as quinine sulphate. The fluorescence of a standard with known quantum yield is measured and then the fluorescence of the substance in question is measured under same experimental conditions followed by comparison with standard to calculate the quantum yield. To date, advanced instrumental developments have been made to precisely determine the quantum yield. The following equation is used to calculate the quantum yield (Dai *et al.*, 2014):

$$\phi = \phi_r \frac{I(Ar)n^2}{I_r(A)n_r^2} \tag{2.13}$$

where, ϕ and ϕ_r are the quantum yields of the sample and standard reference, I and I_r are the integrated fluorescence intensities of the sample and reference, Ar and A are the absorbance values and n_r and n are the refractive indexes of the reference and required sample, respectively.

2.3.4 Graphene and carbon dots

Graphene is a single layer of carbon atoms arranged in a hexagonal pattern and is typically with the length of microns (Novoselov *et al.*, 2004) . If we keep cutting this micrometric sheet until it reaches less than 20 nm in size, the resulting product is called a quantum dot (Pan *et al.*, 2010). Thus, GQDs are disks of graphene in the size range of 1-20 nm. The main difference between graphene and GQDs is the band gap. Graphene is a zero bandgap material while the GQDs show band gap due to their quantum confinement and edge effects (Ponomarenko *et al.*, 2008; Peng *et al.*, 2012b). GQDs are composed mainly of sp^2 hybridised carbon and they are crystalline (Ponomarenko *et al.*, 2008; Jang *et al.*, 2017). GQDs are fluorescent due to their quantum confinement, surface defects and zigzag/armchair edges (Ponomarenko *et al.*, 2008). The tunable bandgap gives GQDs tunable fluorescence properties. The theoretical predictions and experimental works have indicated that the quantum confinement and edge effects are more pronounced in GQDs than other semiconductor quantum dots (SQDs).

On the other hand, carbon quantum dots –also called carbon dots (C-dots)– are quasi-spherical carbon nanoparticles consisting of graphite and a turbostratic carbon mixture in different ratios and are in the size range of 2-10 nm (Georgakilas *et al.*, 2015; Shamsipur *et al.*, 2017). They are composed mainly of sp^3 hybridised carbon and are usually amorphous. Their XRD patterns show double peak character (18.2° and 23.8°) attributed to amorphous and graphitic constituents. C-dots contain larger amount of oxygen with lower content of carbon as compared to GQDs (Baker and Baker, 2010; Lim *et al.*, 2015). Due to their high oxygen content these materials are sometimes referred to as carbogenic nanodots (Peng and Travas-Sejdic, 2009). The fluorescence in C-dots is due to their surface defects and functionalisation, which explains why they can be quenched in some media (Georgakilas *et al.*, 2015).

To date the difference between GQDs and C-dots is not very clear and sometimes GQDs are considered as a type of C-dots similarly as graphene is a type of carbon. Therefore, these are considered as a family of quantum dots made of carbon.

GQDs are strongly luminescent, biocompatible, dispersible in a number of solvents, and usually nontoxic, demonstrating a great potential for integration onto devices of bio-imaging, batteries, supercapacitors, photovoltaics and light emitting diodes (Shen *et al.*, 2012a; Zhang *et al.*, 2012b; Ananthanarayanan *et al.*, 2015; Feng *et al.*, 2017; Li *et al.*, 2017), as summarised in Figure 2.5.

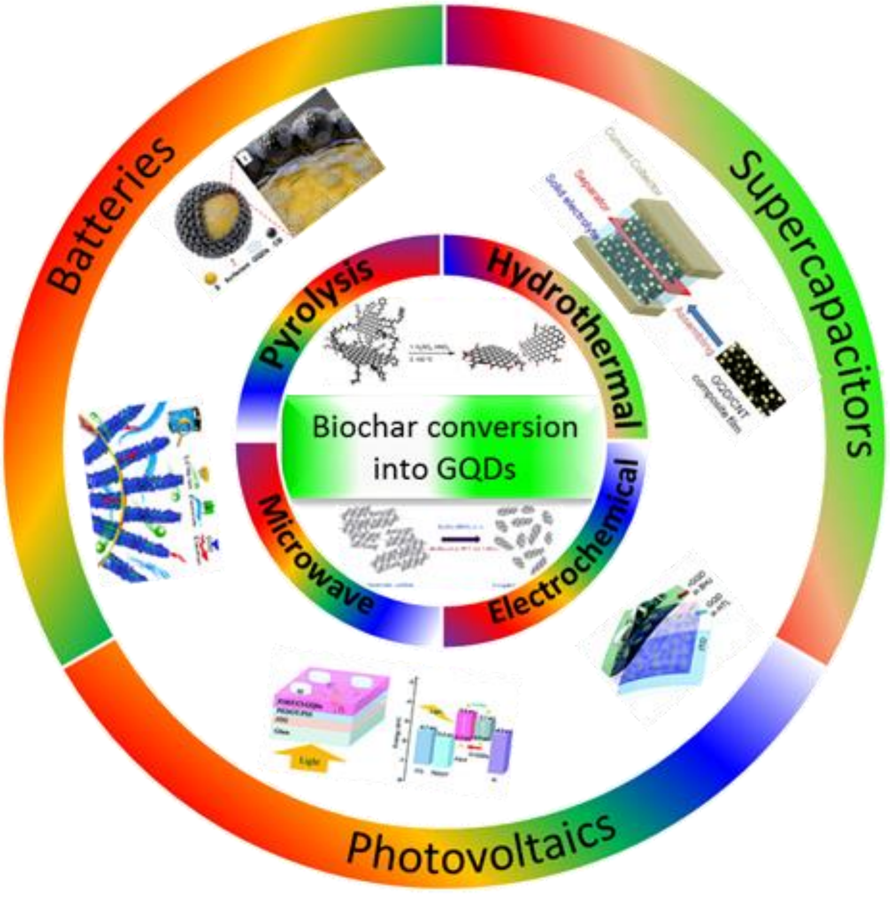

Figure 2.5. Schematic illustration of the conversion of biowaste into GQDs through various approaches and their energy applications.

A number of techniques have been developed for the synthesis of GQDs, such as hydrothermal, electrochemical, microwave, electron beam lithography or thermal treatment (Wang *et al.*, 2016c). However, most of these methods comprise expensive non-renewable raw materials, such as CNTs, graphene, graphene oxide and its derivatives. These graphene-based precursors are very expensive and if prepared from bulk graphite, require a series of processes that could take several days and involve a lot of toxic chemicals. In addition, the strong and well-ordered structure of graphene requires special high pressure–high temperature equipment and strong acidic treatment for disintegration into small sized GQDs (Zheng *et al.*, 2015), leading to very low yields and limiting their scalable production. Some other carbon sources such as C60 molecules, glucose, and starch, etc. have also been used along with relatively green approaches such as electrochemical treatment, however, the yield is so low that real world application is far from realisation (Zheng *et al.*, 2015).

As a result, biomass stand out as a green, natural, inexpensive, sustainable and renewable carbon source for the scalable production of GQDs. Although there is no published literature with respect to total cost of GQDs materials, it is expected that the cost of a biomass waste derived precursor should be much lower than any other precursor (graphite, carbon fibre, CNTs, citric acid, glucose, etc.) since biomass is abundant and cheap. Despite the multiple advantages of biomass based raw materials, reports on the production of GQDs from biomass are scarce. Only a few types of biomass wastes, such as various plant leaves, rice husks, coffee grounds, and wood charcoal have been used to produce GQDs with properties comparable to graphene based expensive precursors (Roy *et al.*, 2014; Suryawanshi *et al.*, 2014; Wang *et al.*, 2016a; Wang *et al.*, 2016d; Nirala *et al.*, 2017). In addition, it has been demonstrated that the pyrolysis treatment of biomass can produce a very interesting and highly porous form of carbon consisting of tiny nanometre scale graphene-like entities juxtaposed with each other in a disordered fashion. This form of carbon is known as turbostratic carbon (Biswal *et al.*, 2013). The thermal treatment of this disordered carbon can lead to the production of GQDs (Suryawanshi *et al.*, 2014). In spite of multiple efforts, the research on the biomass derived GQDs is still at its infancy and several challenges need to be tackled, such as introduction of inherent impurities, low yield, reduced control over particle size and shape, wide size distribution and multiple synthesis and purification steps involved. More importantly, biomass derived GQDs face the challenge of precise control over particle size and usually give a large particle size of 5-7 nm. Since bandgap is dependent on the size of GQDs due to the quantum confinement effect, controlling the size is critically important. Thus, more work is required in terms of controllable production of GQDs from biomass.

The synthesis techniques and promising applications of GQDs are reviewed in the following section. The possible routes for converting biowaste into activated carbon (AC) to synthesise GQDs are also discussed.

2.4 GQDs synthesis

The techniques available for the synthesis of GQDs can be categorised into two major groups based on the reaction mechanism: bottom-up and top-down (Figure 2.6).

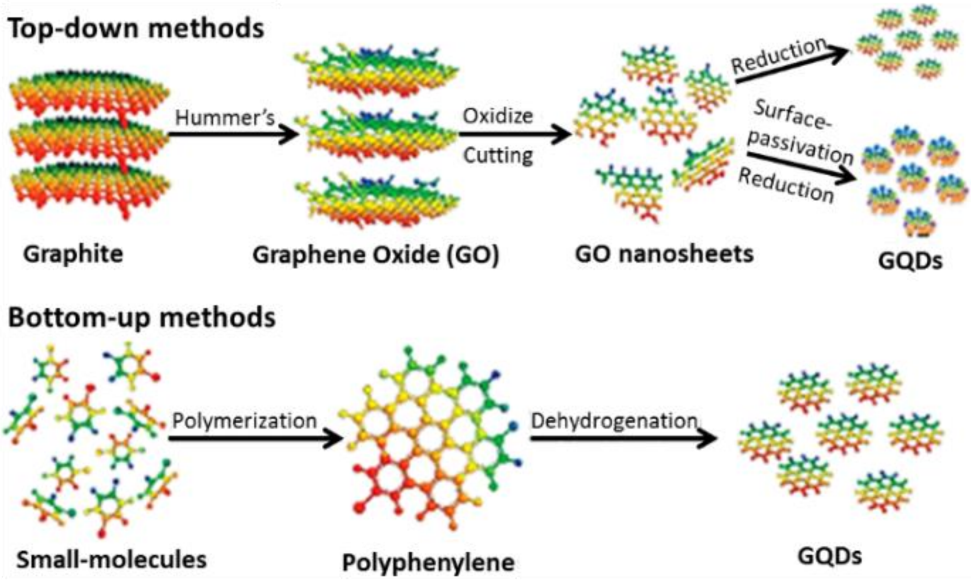

Figure 2.6. Schematic demonstration of the top-down and bottom up approaches for synthesis of GQDs. Adapted with permission from (Shen *et al.*, 2012a). Copyright (2012) Royal Society of Chemistry.

The bottom-up technique is associated with the synthesis of sp^2 carbon domains (the 2-dimensional arrangement of carbon atoms in a pattern where the angle between two consecutive bonds is 120°) from organic molecules through intermolecular coupling and carbonation process, resulting in a controllable size and morphology of the products. However, these approaches are time consuming and rather complicated. The main reaction mechanism involved in the top-down methods is the oxidation process (etching or cutting) or mechanical shearing converting large sp^2 carbon domains into smaller ones (Pan *et al.*, 2010). These methods are simple, easy to operate and time saving, but the final yields are very low and precursors are limited to those with large area of sp^2 carbon domains, such as graphene, carbon fibre, carbon black, etc. (Pan *et al.*, 2010; Peng *et al.*, 2012b; Ye *et al.*, 2013).

2.5 Top-down methods

The 3-dimensional (3D) bulk materials or 2-dimensional (2D) sheets consisting of large sp^2 carbon domains can be cracked down in to 0D quantum dots (QDs) via oxidation processes or mechanical shearing. In order to achieve these goals different preparation methods have been developed. For the oxidation of large sp^2 carbon domains, electrochemical scissoring, chemical etching, hydrothermal or solvothermal cutting processes have been developed. The key mechanism of the oxidation processes can be classified into molecular oxidation (mainly in the case of H_2SO_4, HNO_3, $KClO_3$ and $KMnO_4$ as oxidants) (Ritter and Lyding, 2009; Yang *et al.*, 2014b) and free radical oxidation approaches (particularly in H_2O_2 oxidation and electrochemical scissoring) (Zhou *et al.*, 2012; Zhu *et al.*, 2015b; Yang *et al.*, 2017b). Through systematic studies, it has been noticed that the precursor material, filling factor, heating rate, reaction time, and temperature significantly affect the shape, size distribution, morphology and surface chemistry of GQDs (Wang *et al.*, 2016c). The synthesis of GQDs from biomass-waste via different reaction mechanisms is discussed in the following section.

2.5.1 Molecular oxidation

Molecular oxidation is a versatile approach implemented for the synthesis of GQDs with relatively high yields. GQDs have been successfully synthesised by the molecular oxidation of turbostratic carbon derived from biomass using strong acids (Suryawanshi *et al.*, 2014). An interesting carbon material is acquired by the controlled pyrolysis of the biomass at a temperature below 1000 °C. At this temperature, graphitisation process is incomplete which results in small graphene-like entities combined in an irregular manner. This type of carbon is recognised as turbostartic carbon (Biswal *et al.*, 2013). GQDs were synthesised by refluxing the turbostratic carbon mixed with as-received strong acids (H_2SO_4 & HNO_3, 3:1) at 90 °C for 5 hours (Figure 2.7a) (Suryawanshi *et al.*, 2014). This method results in the formation of oxygenated groups (OH, COOH, etc.) on basal plans, activating them and making them defective. These activated sp^2 carbon domains eventually break down into smaller pieces after long time exposure at elevated temperature (5h, 90 °C), forming GQDs.

Hydrothermal treatment is another molecular oxidation technique widely implemented for the synthesis of GQDs from various precursors, especially biomass (Wang *et al.*, 2016a; Wang *et al.*, 2016d). Pan et al. first introduced the hydrothermal route for the synthesis of GQDs with blue-luminescence (Pan *et al.*, 2010). Biomass derived carbonaceous material consisting of large sp^2 domains are reacted with oxidizing reagents (e.g. HNO_3) for introducing epoxide groups on basal planes. Finally, the GQDs are obtained by hydrothermal cutting followed by deoxidisation in alkaline media (Figure 2.7b). A milligram scale synthesis of GQDs from rice husk was reported by Wang et al (Wang *et al.*, 2016d). Rice husks were pyrolysed at 700 °C for 2 h and reacted with NaOH at 900 °C to produce rice husk carbon. The obtained carbon was then activated with strong acids and subjected to hydrothermal treatment at 200 °C for 10 h to produce GQDs with a yield of 15% (Figure 2.7c). The as-prepared GQDs exhibit intense photoluminescence and high biocompatibility showing a bright promise for the biomedical field (Wang *et al.*, 2016d). The GQDs have also been prepared from graphene oxide sheets derived from plant leaf extract (Roy *et al.*, 2014). The acquired graphene oxide sheets were hydrothermally treated at 300 °C for 8 h to break down into GQDs (Figure 2.7d). As obtained GQDs were used for preparing white light emitting diodes (Roy *et al.*, 2014). Another report was presented by Wang et al. for the synthesis of GQDs from coffee grounds (Wang *et al.*, 2016a). Hydrazine hydrate was used as an activating agent. The coffee grounds were mixed with hydrazine hydrate and water under mild ultrasonication. The hydrothermal treatment of the as-prepared mixture at 150-200 °C for 6-10 h resulted in blue luminescent GQDs. They also prepared poly (ethylene imine) (PEI) functionalised GQDs with high band-edge luminescence for bio-imaging and sensing applications (Wang *et al.*, 2016a).

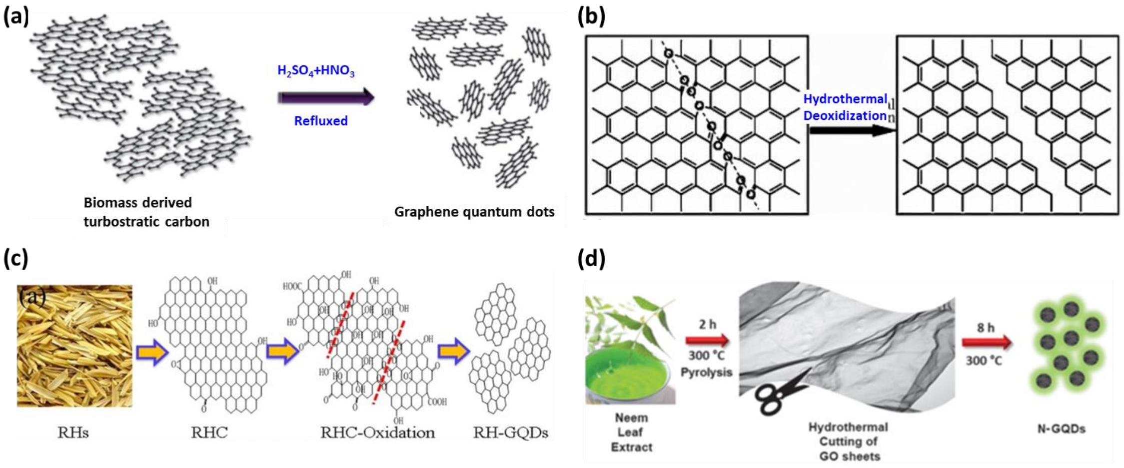

Figure 2.7. Top down approaches for the synthesis of GQDs. (a) Schematic for the fabrication of GQDs by acidic oxidation of turbostratic carbon obtained from biomass. Reprinted with permission from ref. (Suryawanshi *et al.*, 2014). Copyright (2014) Royal Society of Chemistry. (b) Mechanism for the synthesis of GQDs by cutting the mixed epoxy chains of graphene sheets under hydrothermal treatment. Reprinted with permission from ref. (Pan *et al.*, 2010). Copyright (2010) Wiley Publishing Group. (c) Top-down approach for the synthesis of GQDs from rice husk. Reprinted with permission from ref. (Wang *et al.*, 2016d). Copyright (2016) American Chemical Society. (d) Schematic representation of the synthesis procedure for GQDs from Neem leaf via hydrothermal route. Reprinted with permission from ref. (Roy *et al.*, 2014). Copyright (2014) Centre National de la Recherche Scientifique and Royal Society of Chemistry.

Although, GQDs have been successfully prepared from above techniques, the use of toxic strong oxidizing media was required imposing additional health and safety issues. Moreover, lengthy purification processes were required to remove the excess chemicals and impurities.

2.5.2 Free radical based electrochemical oxidation

The electrochemical approach based on free radical oxidation is a relatively clean approach for the synthesis of GQDs (Zhou *et al.*, 2012; Zhu *et al.*, 2015b). This approach is different from traditional molecular oxidation approach in reaction mechanism. Molecular oxidizing and acidic intercalation destroy the perfect sp^2 structure of the natural graphite resulting in the introduction of sp^3 carbon and large amount of oxygen containing groups. These sp^3 carbon domains are preferentially oxidised, playing a key role in the morphological trimming of graphene into GQDs. On the other hand, free radical oxidation involves high reaction activities of OH* causing the rapid oxidation and cutting of sp^2 carbon domains into smaller fragments without any microstructural damage (Zhu *et al.*, 2015b; Yang *et al.*, 2017b). For example, in the electro-oxidation process free radicals (OH*, O*) produced by the anodic oxidation of water cut the large sp^2 carbon domains of graphene into GQDs without changing the original sp^2 structure (Nirala *et al.*, 2017). GQDs have been synthesised by the electrochemical scissoring of different carbon materials such as wood charcoal (Nirala *et al.*, 2017), carbon nanotubes (Li *et al.*, 2012b), reduced graphene oxide films (Li *et al.*, 2011a), graphite rods (Li *et al.*, 2010), and 3D graphene (Li *et al.*, 2010; Li *et al.*, 2011a; Li *et al.*, 2012b; Ananthanarayanan *et al.*, 2014).

When electrical energy more than the binding energy of H and O atoms is applied, water decomposes into free radicals. Thus, the anodic oxidation of water results in the formation of hydroxyl and oxygen free-radicals (OH*, O*) which work as electrochemical scissors to generate GQDs (Figure 2.7d) (Lu *et al.*, 2009). This process starts at the edge sites and is hastened by the defect sites. Due to high operating costs this cleavage process needs to be accelerated by combing with other techniques, for example, introduction of defects into the lattice by surface functionalisation. The functional groups can be introduced by utilizing strong base or acid based electrolytes (Li *et al.*, 2011b; Ananthanarayanan *et al.*, 2014; Sun *et al.*, 2015). This electrochemical approach is quite simple and relatively clean (Sun *et al.*, 2015). Recently, Nirala et al. reported the one step electrochemical route for the synthesis of GQDs from wood charcoal, a kind of biomass (Nirala *et al.*, 2017). Electrochemical oxidation of charcoal was performed by using it as a working electrode in ammonium persulfate electrolyte at 5 V potential. Anodic oxidation of water generated *O and *OH free radicals. These free radicals act as “scissors” to cut the graphene sheets of charcoal into very small particles, called E-GQDs (Nirala *et al.*, 2017).

This technique was proposed as relatively clean approach for the synthesis of GQDs, however, the use of persulfate-based toxic oxidants was unavoidable. Moreover, the process was quite lengthy, and the yield was low due to the reaction taking place only at the electrode surface. In addition, expensive commercial precursors were used as the working electrode adding cost and imposing additional sustainability issues. Due to above challenges, this approach needs to develop further before it can be used significantly in the field.

2.6 Bottom-up methods

The bottom-up processes consist of synthesising GQDs through chemical assembly of small organic building blocks. The main reaction mechanism involved in these methods is the intermolecular coupling or carbonation process.

2.6.1 Intermolecular coupling

These methods are beneficial for the synthesis of GQDs with relatively good control over size and shape. GQDs have been synthesised with high precision through step-by-step organic synthesis, although low-output and strong π-π interaction causing aggregation was difficult to prevent (Yan *et al.*, 2010a; Li *et al.*, 2012b). GQDs can be prepared through a hydrothermal carbonisation reaction of the small organic frameworks (Wang *et al.*, 2014b). Heating the small organic molecules above their melting point leads to condensation, nucleation, and subsequently the formation of larger C-Dots or GQDs. Numerous precursors have been utilised in this technique, such as organic salts (Bourlinos *et al.*, 2008; Deng *et al.*, 2013), citric acid (Dong *et al.*, 2012b; Wang *et al.*, 2015b), ascorbic acid (Jia *et al.*, 2012), glycerol (Lai *et al.*, 2012), etc.

The bottom-up approach is highly valuable for preparing GQDs with tuneable size. The growth is controlled by the heat treatment time as the intermolecular coupling depends on time, leading to the tunable size distribution of GQDs. For example, honey is used as a carbohydrate precursor to synthesise GQDs with tuneable size via an emulsion-templated method (Figure 2.8a) (Mahesh *et al.*, 2016). Aqueous solutions of honey were emulsified in 1-butanol and heated at 80 °C under vigorous stirring for 1 h. As a result, GQDs with an average size of 2.4 nm were produced and found promising application in white light emission applications (Mahesh *et al.*, 2016). Recently. Kalita et al. reported on the controlled growth of GQDs from rice grains (Kalita *et al.*, 2016). When rice powder is heated, the thermal degradation of starch leads to the formation of glucose oligomers. These oligomers start to nucleate at high temperature (200 °C), and subsequently grow during pyrolysis to form a GQD (Figure 2.8b).

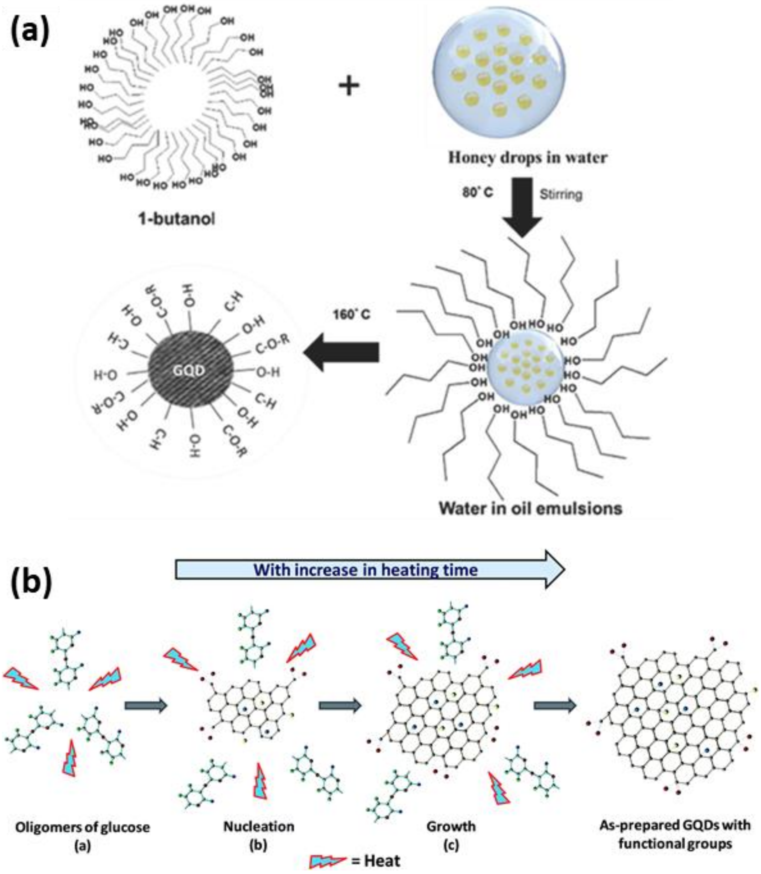

Figure 2.8. (a) bottom-up emulsion-templated carbonisation of honey for the synthesis of GQDs. Reprinted with permission from Ref. (Mahesh *et al.*, 2016). Copyright (2015) Wiley Publishing Group. (b) Bottom-up method for the synthesis of GQDs from rice grains. Reprinted with permission from ref. (Kalita *et al.*, 2016). Copyright (2016) Royal Society of Chemistry.

Interestingly, in these bottom-up processes, the doping effects of heteroatoms can be conveniently achieved from the precursor materials. Nitrogen doped GQDs, for example, have been produced by hydrothermal techniques using citric acid as a source of carbon and ethyl amine, diethylene amine, ethylene diamine or urea as a source of nitrogen (Qu *et al.*, 2014b). The concentration of nitrogen doping and luminescence yield principally depends on nitrogen precursor selected (Qu *et al.*, 2014b; Sun *et al.*, 2015). Similarly, sulphur doped monodispersed GQDs have been synthesised through hydrothermal treatment of fructose using sulfuric acid as the sulphur source (Li *et al.*, 2014). Table 2.1 summarises the various biomass resources for GQDs synthesis via different techniques.

Table 2.1. A brief overview of the GQDs synthesis from various types of biomass through different approaches.

Precursor	**Preparation approach**	**Product**	**Yield (wt.%)**	**Size (nm)**	**Height (nm)**	**Ref.**
Neem leaves	Pyrolysis and hydrothermal treatments	GQDs, Am-GQDs	-	5-6	0.4-1.7	(Suryawanshi *et al.*, 2014)
Rice Husks	Pyrolysis, hydrothermal treatment	GQDs	15	3-6	0.8-1.6	(Wang *et al.*, 2016d)
Wood charcoal	Electrochemical oxidation	GQDs	-	3-6	~6	(Nirala *et al.*, 2017)
Coffee grounds	Hydrothermal treatment	GQDs, PEI-GQDs	33	1.88-2.67	2.23-3.18	(Wang *et al.*, 2016a)
Neem leaf extract	Pyrolysis, hydrothermal treatment	GQDs	25.2	2-8	-	(Roy *et al.*, 2014)
Fenugreek leaf extract	Pyrolysis, hydrothermal treatment	GQDs	-	3-10	-	(Roy *et al.*, 2014)
Honey	Emulsion templated carbonisation	GQDs	-	1.8-2.8	-	(Mahesh *et al.*, 2016)
Rice grains	Pyrolysis	GQDs	-	2-6.5	1-2	(Kalita *et al.*, 2016)

2.6.2 Reaction mechanism

Most studies on biomass derived GQDs focused on controlling their properties via different techniques. However, the detailed reaction mechanism is not well understood. In order to develop a strong structure-property-application relationship, an in-depth understanding of the reaction mechanism is necessary. It was reported initially that heating the small organic molecules above their melting point leads to condensation, nucleation, and subsequently the formation of larger C-Dots or GQDs. Subsequently, many researchers suggested that the bottom-up approach involves two major reactions, dehydrogenation and carbonisation. The dehydrogenation and carbonisation of small molecules under hydrothermal or solvothermal conditions produce GQDs. However, there are still some challenges associated with this reaction mechanism. The complex dehydrogenation and carbonisation processes result in the introduction of heteroatoms on the surface or edges rather than lattice doping.

Recently, Yang’s group reported on the mechanism for the synthesis of sulphur (S) doped GQDs from biomass (durian) (Wang *et al.*, 2018a). They proposed that the platinum catalyst played the main role to fuse the sp^2 heterocyclic compounds and sulphur together to produce the sulphur doped GQDs. They demonstrated the source of C and S, its doping in the lattice structure and controlling the doping concentrations by simply controlling the processing time and temperature. Low molecular weight saccharides and the mercaptan constituents of durian are suggested to be the main source of the sp^2 carbon network and S doping, respectively, in the preparation of S-GQDs. Elsewhere (Yang *et al.*, 2017a), they demonstrated that, in general, the mechanism proceeds by the abstraction of H from C-H, N-H, S-H, etc. bonds, resulting in generation of respective H, C, N, and S atoms with dangling bonds. Subsequently, the formation of C-C, C-N/C-S bonds take place between the growing monomers, followed by release of hydrogen. These monomers then combine to form the sp^2 network of carbon with N or S doping in the lattice structure (Yang *et al.*, 2017a). High resolution XPS analysis of the S 2p spectrum showed two peaks (~163.9 eV, ~165.1 eV) corresponding to the thiophene structure (Figure 2.9a), suggesting the S doping to be mainly in the form of thiophene inside the lattice. The mechanism of S doping was proposed to be substitutional as shown schematically in Figure 2.9b.

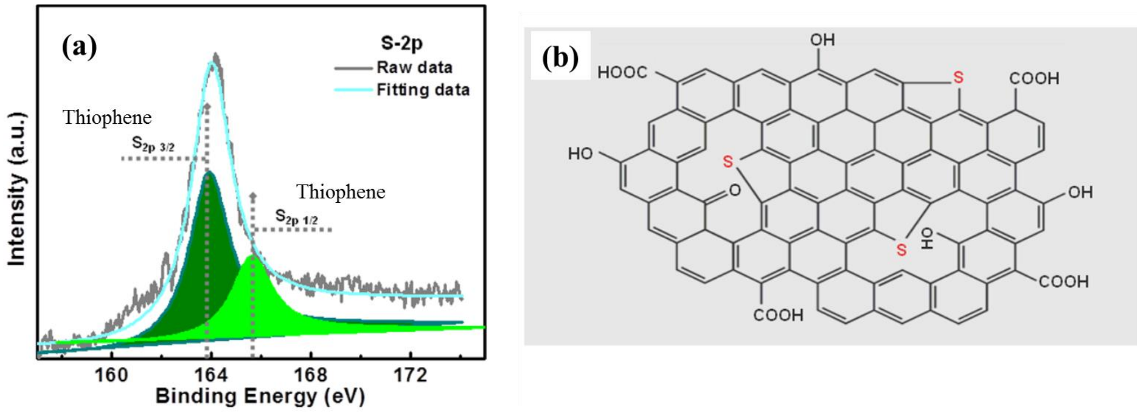

Figure 2.9. (a) High-resolution XPS S 2p spectrum showing the thiophene presence in the skeleton of S-GQDs. and (b) schematic diagram representing the S doping in lattice substitutional manner in the structure of S-GQDs. Reprinted with permission from ref. (Wang *et al.*, 2018a). Copyright (2018) American Chemical Society.

The doping concentration was controlled systematically by heating time and temperature. The doping concentration decreases linearly with increasing reaction time or temperature due to the effect of removal of the heteroatom in the sp^2 carbon structure under high temperature or long reaction times (Wang *et al.*, 2018a). Further demonstrations indicated that the PL behaviour and quantum yield changes significantly with doping concentration. PL emission of S-GQDs was suggested to continuously shift from blue to red with increasing the doping concentration.

The PL shift is attributed to the change in the total amount of oxygen containing functional groups due to lattice replacement of S atoms in the sp^2 C network (Yang *et al.*, 2017a). Variation in quantum yield is induced by n-π^* transition between the lattice doped nitrogen and GQD conjugate structure, which is the key factor for high quantum yield (Sun *et al.*, 2015).

2.7 Modification approaches

In order to expand the appliance of GQDs, their properties need to be controlled for specific applications. Numerous synthetic and post-synthetic methodologies have been investigated for acquiring the defined and desired properties of GQDs. These strategies can be broadly divided into three major categories: (1) size and shape control, (2) surface modification, and (3) heteroatom doping.

2.7.1 Size and shape control

It is well understood (Mohanty *et al.*, 2012; Sk *et al.*, 2014) that the photoluminescence of GQDs is largely dependent on their size due to quantum confinement and somehow on their shape due to edge effects. The minimum amount of energy necessary to generate an exciton is defined by the bandgap of the material. In case of a quantum dot the bandgap varies inversely with the size of particle. It means the energy required for excitation of an electron will vary with the size of quantum dots, resulting in tunable photoluminescence emission (Park *et al.*, 2001).

Sk et al. reported on the variation in PL emission with a change in the size of the pristine zig-zag edged GQDs (Sk *et al.*, 2014), as presented in Figure 2.10a. The fluorescence of as-prepared GQDs changes from the UV (bandgap 6.81 eV) to the infrared (bandgap 1.64 eV) by tuning the size from 0.46 to 2.31 nm due to bandgap shrinkage induced by π-electron delocalisation. The PL emission is dictated by the isolated small sp^2 domains of heterogeneously hybridised and large sized GQDs (Sk *et al.*, 2014; Zheng *et al.*, 2015).

A good control over the shape and size of GQDs might be achieved through step-wise organic synthesis (Yan *et al.*, 2010b). For example, well defined GQDs have been synthesised by ruthenium-catalysed cage-opening of C_{60} molecules (Lu *et al.*, 2011). The morphology of the GQDs can be varied from hexagonal, parallelogram, triangular, and trapezoid to mushroom shaped by alteration in the annealing temperature and the carbon clusters’ density (Zheng *et al.*, 2015).

2.7.2 *Surface modification*

Besides the prominent shape- and size-dependence, the PL properties of GQDs can also be modified by surface engineering, including surface oxidation (Zheng *et al.*, 2013a), polymer passivation, and chemical moiety attachment (Sekiya *et al.*, 2016). Introduction of the oxygenated functional groups on GQDs make them hydrophilic leading to the ease of further chemical functionalisation. On the other hand, PL efficiency is affected due to the surface emissive traps induced by these groups. Therefore, a precise control over the degree of oxidation is necessary for the defined and desired properties. It was suggested that the PL emission is red shifted with an increase in the amount of GQD oxidation (Figure 2.10b) (Zhu *et al.*, 2012; Hu *et al.*, 2013b; Sun *et al.*, 2013; Sk *et al.*, 2014).

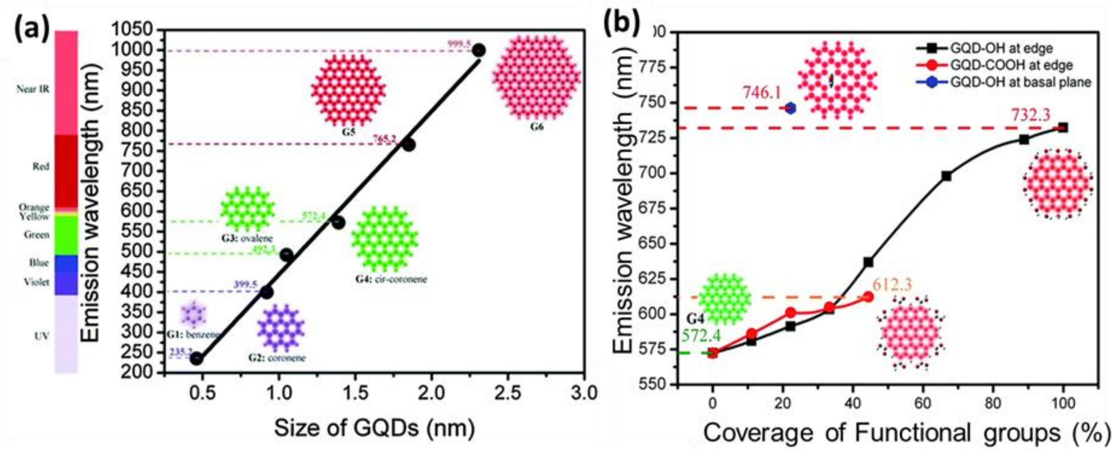

Figure 2.10. (a) Calculated emission wavelength of zig-zag edged GQDs as a function of size. (b) Emission wavelength of oxidised GQDs as function of coverage of –OH and –COOH groups. Adapted and modified with permission from ref. (Sk *et al.*, 2014). Copyright (2014) Royal Society of Chemistry.

Alternatively, these oxygen functional groups (-OH, -COOH) usually cause an overall increase in the surface emissive traps because these groups have high tendency to accept an electron resulting in non-radiative recombination of excitons. Consequently, the quantum yield is decreased. To overcome this challenge, several approaches have been developed such as reduction and surface passivation. For example, reduction of GQDs with $NaBH_4$ blue-shifted the PL emission and increased the quantum yield by two times (Li *et al.*, 2012a). An attractive strategy to enhance the quantum yield of GQDs is the polymer passivation of surface emissive traps. Various polymers have been reported for surface passivation, the most common of which is polyethylene glycol (PEG) (Shen *et al.*, 2011; Shen *et al.*, 2012b; Wang *et al.*, 2013). With a thin layer of PEG, the quantum yield of GQDs was doubled (Shen *et al.*, 2012b). Furthermore, a number of chemical groups, such as thiol (Montoya *et al.*, 2015), diamine (Sun *et al.*, 2015), alkylamine (Zhu *et al.*, 2012), hydrazide (Zhang *et al.*, 2012a), etc., have been attached onto the GQDs. These electron donating groups prevent the non-radiative recombination and usually cause wavelength shift thereby enhancing the quantum yield (Zhu *et al.*, 2012). For example, green oxygenated GQDs turned blue when carboxyl groups were replaced with alkylamine (Zhu *et al.*, 2012). Tetsuka et al. demonstrated that precise control over the degree of amine functionalisation could widely tune the emission wavelength of GQDs (blue to yellow) (Tetsuka *et al.*, 2012).

Similarly, the properties of biomass-waste derived GQDs have also been modified by the addition of various functional groups and passivating agents. Similar to the Zhu et al. modification approach, Suryawanshi et al. modified the Neem leaf-derived GQDs by amine (-NH_2) functionalisation to enhance the PL properties (Suryawanshi *et al.*, 2014). They added ammonia solution to the as-prepared GQDs and hydrothermally treated them at 200 °C for 12 h. The green luminescence of unmodified GQDs changed to blue after amine functionalisation. This PL shift is attributed to the decrease in agglomeration and change of the oxygenated functional groups into $–CONH_2$ and $–C–NH_2$ surface groups, which suppress the non-radiative recombination path, resulting in the improvement of PL intensity and quantum yield by a factor of two. Similarly, Wang et al. functionalised the coffee ground derived GQDs with poly(ethylene imine) (PEI) by hydrothermal treatment at 120 °C for 10 h and enhanced the quantum yield from 8 to 24% (Wang *et al.*, 2016a).

However, surface passivation imposes limitations on the applications due to the complicated process and increased particle size of passivated GQDs. Moreover, in the aforementioned cases, the blue emission changed to either cyan or green after surface passivation, totally changing the properties of GQDs and limiting their use in the desired applications.

2.7.3 Heteroatom doping

Recently, heteroatom doping (most often nitrogen or sulphur doping) has emerged as a promising technique to fine tune the physicochemical properties (PL, quantum yield, etc.) of GQDs (Wang *et al.*, 2014c). Heteroatoms can be added through the precursor materials during synthesis or via post-synthesis techniques. Nitrogen-doping improves the quantum yield and blue shifts the PL emission (the higher the N-doping, the shorter the emission wavelength) of GQDs due to the high electronegativity and electron withdrawing properties of nitrogen atoms (Li *et al.*, 2011b; Hu *et al.*, 2013a; Ju and Chen, 2014; Sk *et al.*, 2014). Some researchers propose that N-doping can also offer up-conversion PL properties to GQD (Shen *et al.*, 2011).

The catalytic properties and PL characteristics of GQDs have also been changed by doping with various other elements such as S (Li *et al.*, 2014), P (Prasad *et al.*, 2013), Si (Qian *et al.*, 2014), and B (Zhang *et al.*, 2014). For example, a quantum yield of GQDs as high as 71% has been achieved by S and N co-doping (Qu *et al.*, 2013).

Heteroatom doping via the precursor material has become a popular technique in the synthesis of biomass derived GQDs (Wang *et al.*, 2014c; Wang *et al.*, 2018a). Sulphur doping red shifts the PL emission and enhances the quantum yield. Very recently, Wang et al. prepared a series of GQDs with controllable sulphur (S) doping using durian (biomass) as the precursor material, as well as the source of sulphur (Wang *et al.*, 2018a). The doping concentration was controlled via reaction time. With increase in the reaction time, the doping decreases linearly due to the removal effect of heteroatom in sp^2 carbon structure under long reaction times. A wide broadband PL emission (420-620 nm) from S-doped GQDs can be acquired by variation in the doping concentration (Wang *et al.*, 2018a).

The introduction of surface functional groups and defects causes a red shift in the PL emission of GQDs while pyrrolic N-doping and armchair edges cause a blue-shift (Li *et al.*, 2011b; Sk *et al.*, 2014; Wang *et al.*, 2016c). The PL properties of GQDs are governed by a combination of defect and intrinsic state emission. The former is a result of energy trap states owing to the dopants, chemical groups, or vacancy defects while quantum confinement, edge effects and the radiative recombination of electron-hole pairs are the major driving factors for the latter. On the positive side, these bestow GQDs a broad range of fascinating properties. Nevertheless, synthesising GQDs with homogeneous properties is challenging because of their high tunability (Wang *et al.*, 2016c).

2.8 Applications of biomass derived GQDs

Graphene as a noble material, has triggered a gold rush to exploit its potential for energy storage/conversion applications (Guo and Dong, 2011; Sun *et al.*, 2011; Xu *et al.*, 2013; Georgakilas *et al.*, 2016; Yao and Zhao, 2017). The main factor behind the attraction and significance of graphene in energy devices is its large specific surface area and high electrical conductivity (Mao *et al.*, 2015). Nevertheless, graphene as an electrode material faces a considerably reduced surface area owing to the irreversible agglomeration or restacking of graphene sheets by the strong π–π bonding and van der Waals interactions between them, consequently limiting its practical applications (Hu *et al.*, 2015; Mao *et al.*, 2015). In addition to graphene, RGO has also been utilised in energy devices but its reduced electrical conductivity due to its defective nature limits its commercial applications (Rui *et al.*, 2011; Georgakilas *et* *al.*, 2016). To this end, GQDs stand out as a new material combining the exceptional properties of both graphene and quantum dots (Zhang *et al.*, 2012b). As a result of the intriguing properties, such as good electrical conductivity, enlarged surface area, high solubility in many solvents, strong luminescence, high mobility, decreased chemical impedance, and tunable bandgap (Ritter and Lyding, 2009; Li *et al.*, 2011a; Zhang *et al.*, 2012b; Qu *et al.*, 2013; Wang *et al.*, 2014b), GQDs exhibit an edge over other graphene based materials and have great promise for use as fluorescence sensors (Dong *et al.*, 2012a; Wang *et al.*, 2012a; Bai *et al.*, 2013; Suryawanshi *et al.*, 2014), photovoltaic devices (Li *et al.*, 2011a; Kim *et al.*, 2015a), light-emitting diodes (Tang *et al.*, 2012; Song *et al.*, 2014), solar cells (Diao *et al.*, 2017; Marinovic *et al.*, 2017), fuel cells (Li *et al.*, 2011b; Van Tam *et al.*, 2017), batteries (Chao *et al.*, 2015; Park *et al.*, 2016), and supercapacitors (Liu *et al.*, 2013b; Islam *et al.*, 2017). Herein, the numerous applications of biomass derived GQDs are summarised.

2.8.1 PL sensors

In the context of strong luminescence properties, GQDs have been used to detect different analytes (Dong *et al.*, 2012a; Bai *et al.*, 2013; Suryawanshi *et al.*, 2014). Wang et al. (Wang *et al.*, 2012a) reported on the GQD based PL sensor for the first time and demonstrated that the luminescence of GQDs can be quenched selectively by Fe^{3+} ion through a charge transfer mechanism. Chi et al. developed a selective, sensitive and relatively green PL sensor for detection of chlorine in water (Dong *et al.*, 2012a). This advancement indicates that not only the cations, but anions can also be detected selectively by GQD-based sensors. Inspired by these studies, biomass derived GQDs have also been investigated for detection of heavy metal ions in water based on their strong fluorescence properties (Suryawanshi *et al.*, 2014; Wang *et al.*, 2016a).

Wu et al. reported on the coffee grounds-derived PEI-functionalised GQDs as a PL sensor for the detection of Fe^{3+} and Cu^{2+} ions for environment analysis (Figure 2.11a) (Wang *et al.*, 2016a). The PL quenching mechanism was attributed to the strong binding affinity and chelating effect of Fe^{3+} and Cu^{2+} ions with the N functional groups of the PEI functionalised GQDs. Recently, Ding et al. reported on the preparation of GQDs from Durian and modified by sulfhydryl to prepare a PL sensor for the detection of a range of metal ions (Ag^{+}, Hg^{+}, Cd^{+}, and Zn^{+}) (Figure 2.11b) (Wang *et al.*, 2018a).

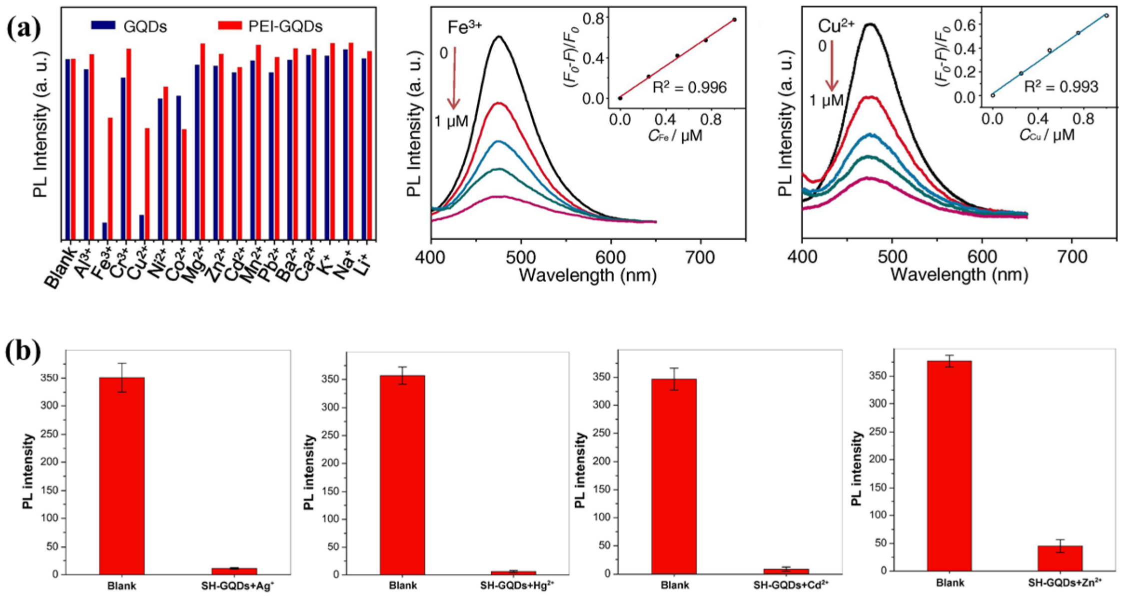

Figure 2.11. (a) Difference among the PL intensity of PEI functionalised GQDs without (blank) and with the addition of different metal ions, and variation in the PL intensity with change in the concentration of Fe^{3+} and Cu^{2+} ions. Reprinted with permission from ref. (Wang *et al.*, 2016a). Copyright 2016 Elsevier. (b) Difference in the PL intensity of GQDs between blank and heavy metal ions (Ag^{+}, Hg^{2+}, Cd^{2+}, Zn^{2+}) added solution. Reprinted with permission from ref. (Wang *et al.*, 2018a). Copyright (2018) American Chemical Society.

Apart from switch-OFF PL sensors, switch ON-OFF-ON sensors have been developed from biomass derived GQDs (Suryawanshi *et al.*, 2014; Wang *et al.*, 2016a). Suryawanshi et al. reported on the synthesis of amine-terminated GQDs from biomass as an efficient and selective ON-OFF-ON sensor for detection of Ag^{+} ion in water owing to their strong luminescence and specific functionalisation (Suryawanshi *et al.*, 2014). Fluorescence intensity of amine ($-NH_2$) functionalised GQDs (Am-GQDs) was quenched by the addition of different metal ions such as Co(II), Cu(II), Ni(II), Fe(II), Fe(III), Hg(II) and Pb(II).

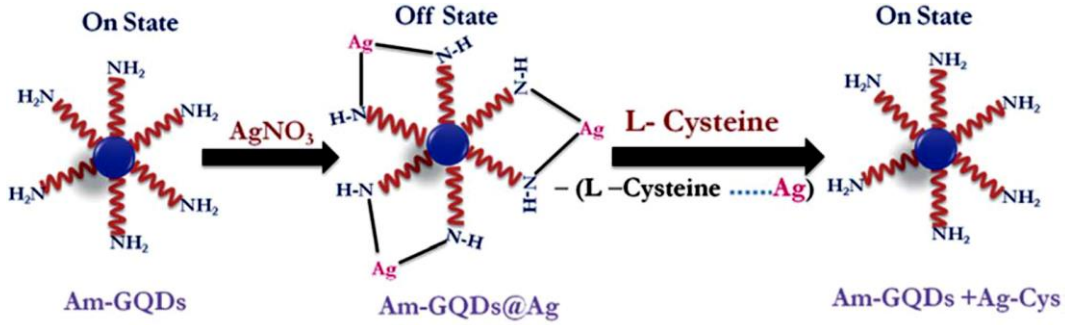

Figure 2.12. Schematic of the suggested mechanism for detection of Ag+ ions by Am-GQDs' PL ON-OFF-ON states induced through the addition of $AgNO_3$ and L-cysteine. Reprinted with permission from ref. (Suryawanshi *et al.*, 2014). Copyright (2014) Royal Society of Chemistry.

Although the fluorescence of Am-GQDs was quenched by the different metal ions but this system was modified for the selective detection of Ag+ ions. This was accomplished by the use of an amino acid “L-cysteine” which has strong affinity towards Ag+ ions. By the addition of L-cysteine into the Am-GQDs–Ag^+ system, the quenched fluorescence was regenerated due to removal of Ag^+ ion from Am-GQDs and attachment with –SH group of L-cysteine (Figure 2.12). The mechanism for such a selective detection was attributed to the Pearson’s hard-soft acid base (HSAB) theory.

2.8.2 Light-emitting diodes

In contrast to the significant studies on GQD-based LEDs (Choi, 2017; Shamsipur *et al.*, 2017), there has been relatively few reports demonstrating the use of biomass derived GQDs in LEDs. It was first reported that LEDs employing GQDs as dopant exhibit white electroluminescence having an external quantum efficiency of 0.1% (Kwon *et al.,* 2014). Later on, Roy et al. reported on the development of white light emitting diode based on the Neem leaf-derived GQDs (Roy *et al.*, 2014). The as-prepared GQDs emit green light with a high quantum yield of 41.2%. The white light emitting material was developed by mixing the green light emitting GQDs with blue light emitting quinine sulphate and red-light emitting chlorophyll solutions in PMMA at an optimised ratio. The resultant mixed solution was coated onto a laboratory-made PET cap which was fitted onto a near UV LED and excited to emit white light (Figure 2.13a, b).

Similarly, Mahesh et al. prepared GQDs from Honey for white light emission (Mahesh *et al.*, 2016). When these purely green light emitting GQDs were mixed with Rhodamine B having an orange red fluorescence, the resulting solution showed white light emission upon excitation at 340 nm (Figure 2.13c,). The CIE 1931 chromaticity coordinates for GQDs after mixing suggested the emission of highly pure white light (Figure 2.13d). Thus, these GQDs can be used for producing white light emitting diodes and other devices.

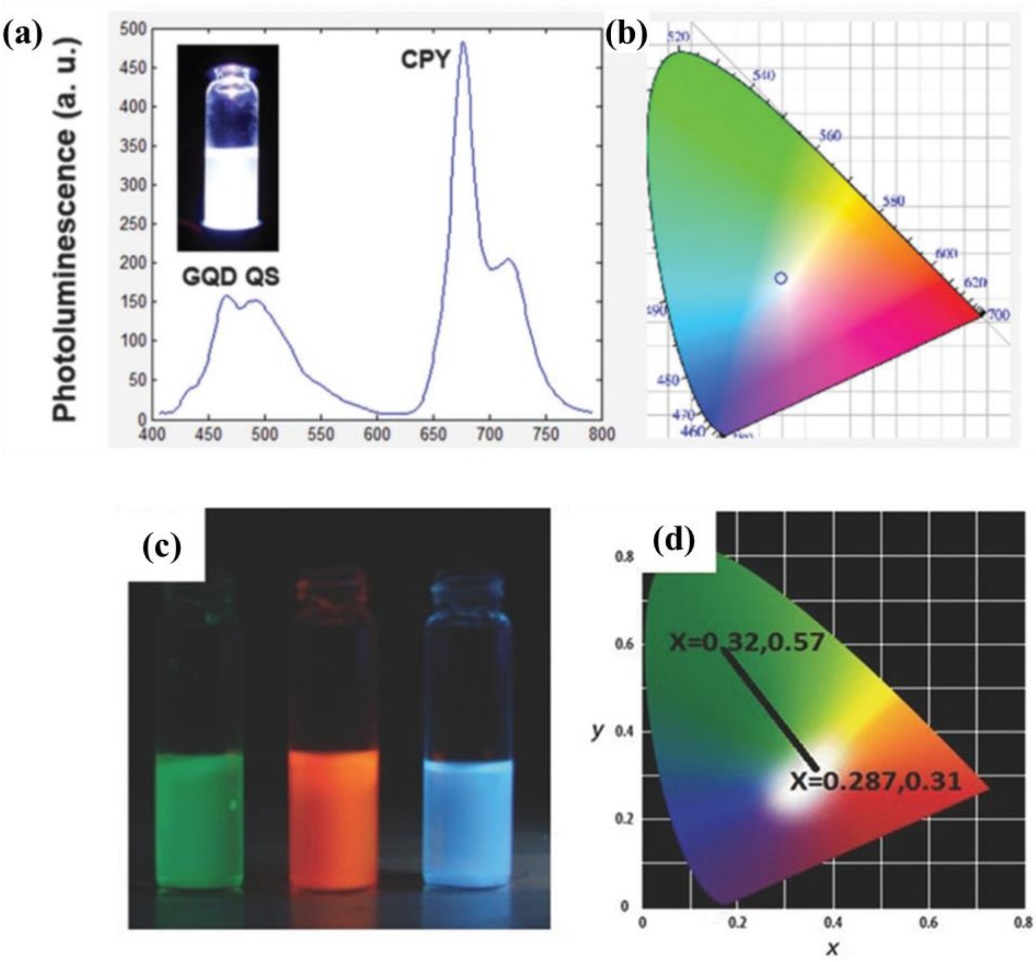

Figure 2.13. PL spectra of GQDs, QS and CPY solution coated on PET cap (inset is the photograph of the solution illuminated by near UV LED, showing white light emission), (b) corresponding color coordinate, CIE spectrum after excitation with near-UV LED light. Reprinted with permission from ref. (Roy *et al.*, 2014). Copyright (2014) Centre National de la Recherche Scientifique and Royal Society of Chemistry. (c) GQDs, RhB, and the mixture showing white light emission, (d) color coordinate for the mixture of GQDs-RhB solution showing white light emission. Reprinted with permission from ref. (Mahesh *et al.*, 2016). Copyright (2016) Wiley Publishing Group.

2.8.3 Biomedical applications

Biomass derived GQDs have been widely investigated for biomedical applications, especially bioimaging. Among a number of different types, GQDs derived from natural food precursors such as rice grains (Kalita *et al.*, 2016), rice husks (Wang *et al.*, 2016d), coffee beans (Wang *et al.*, 2016a) and so on, are suggested to be the most promising candidates for biomedical applications. Wang et al. reported on the biomedical applications of GQDs derived from rice husk biomass (Wang *et al.*, 2016d). Rice husks (RH) were reported to be an abundant source for the controllable preparation of high-quality RH-GQDs suitable for bioimaging of Hela cells. The biocompatibility of the RH-GQDs was investigated by analysing the toxicity and cell viability of Hela cells after treatment with various concentrations of RH-GQDs. At low concentrations of RH-GQDs (20-50 µg/ml) almost no toxicity was observed even after 48 h and over 90% cell viability was observed up to 100 µg/ml concentration (Figure 2.14a). No obvious damage to the cell morphology was observed which indicates the high biocompatibility of RH-GQDs for bioimaging applications. Furthermore, in vitro bioimaging of Hela cells with RH-GQDs (50 µg/ml) was investigated and the cells combined with the RH-GQDs showed blue fluorescence with cell morphology and cytoplasm clearly presented (Figure 2.14b). The luminescence of Hela cells in the presence of RH-GQDs is quite stable showing the feasibility of this biomedical system.

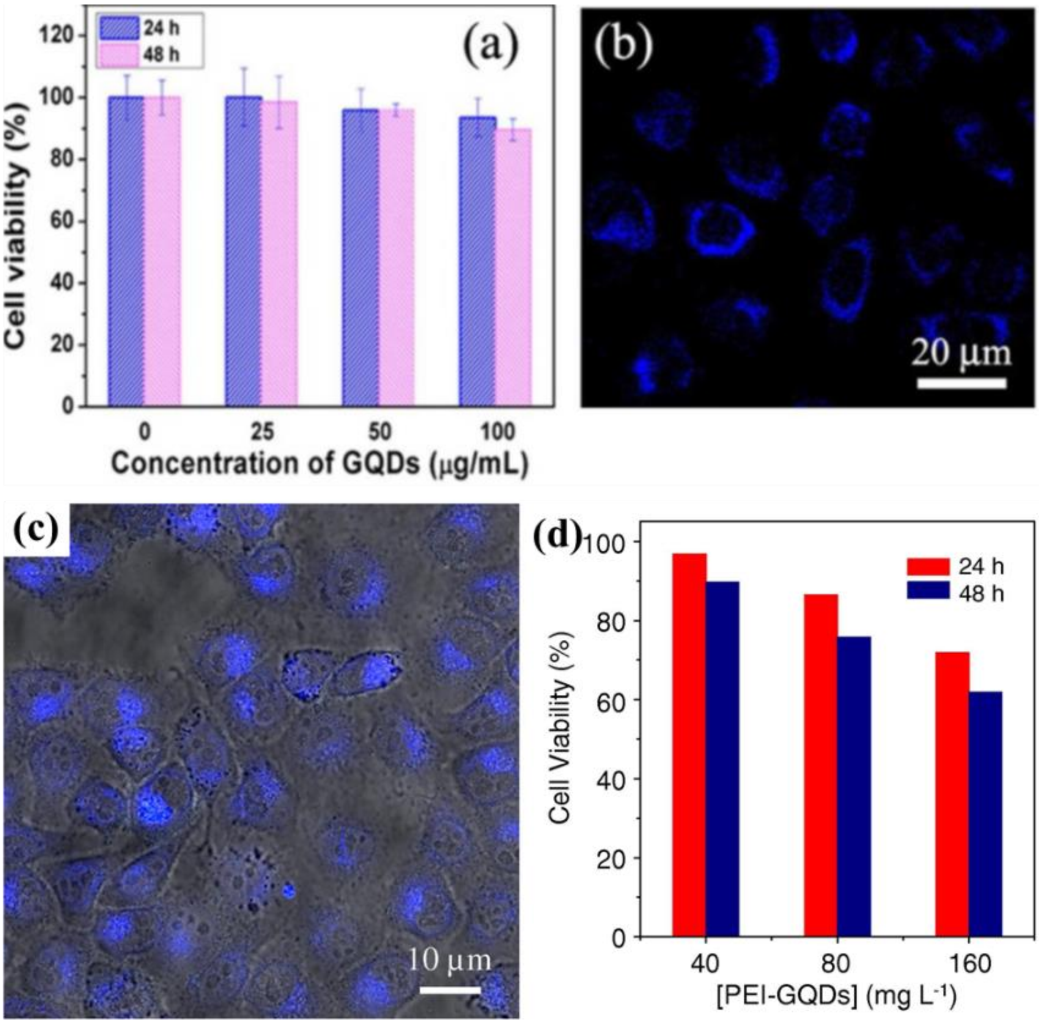

Figure 2.14. (a)Viability of Hela cells incubated with different concentrations of RH-GQDs after a period of 24 and 48 h, (b) imaging of the Hela cells combined with 50 µg/mL of RH-GQDs at 335 nm with a confocal microscope. Reprinted with permission from ref. (Wang *et al.*, 2016d). Copyright (2016) American Chemical Society. (c) Confocal microscope image at 405 nm excitation of Hela cells using PEI-GQDs, (d) cytotoxicity assessment of PEI-GQDs at different doses for incubation period of 24 and 48 h using Hela cells. Reprinted with permission from ref. (Wang *et al.*, 2016a). Copyright 2016 Elsevier.

Wu et al. developed a fluorescent probe for bioimaging of the Hela cells based on the GQDs derived from coffee grounds (Wang *et al.*, 2016a). Hela cells were cultured in 40 mg/L dose of GQDs and images were taken at 405 nm using a confocal microscope (Figure 2.14c). Enhanced fluorescence of cytoplasm around their nucleus indicates the penetration of GQDs into the cells and their emissive stability. The PEI-functionalised GQDs show brighter imaging owing to their high quantum yield. The cytotoxicity and cell viability results indicate the high biocompatibility of these GQDs even after 24 h of incubation period at low dosage of 40 mg/L (Figure 2.14d).

Similarly, Kalita et al. prepared GQDs from rice grains and evaluated their bioimaging compatibility and biocompatibility with Hela cells (Kalita *et al.*, 2016). GQDs treated Hela cells were imaged using 375, 488 and 561 nm laser light and strong green and blue fluorescence was observed. Strong green and blue fluorescence indicate that the GQDs are present as agglomerates in the nucleus and cytoplasm of the cells. After treatment cells do not show any obvious morphological damage, indicating the good biocompatibility of GQDs for bioimaging applications. A cell viability of over 90% was observed after 24 h incubation period at different concentrations of GQDs up to 1mg/ml. Very low cytotoxicity and high cell viability confirmed the biocompatibility of these GQDs for biomedical applications.

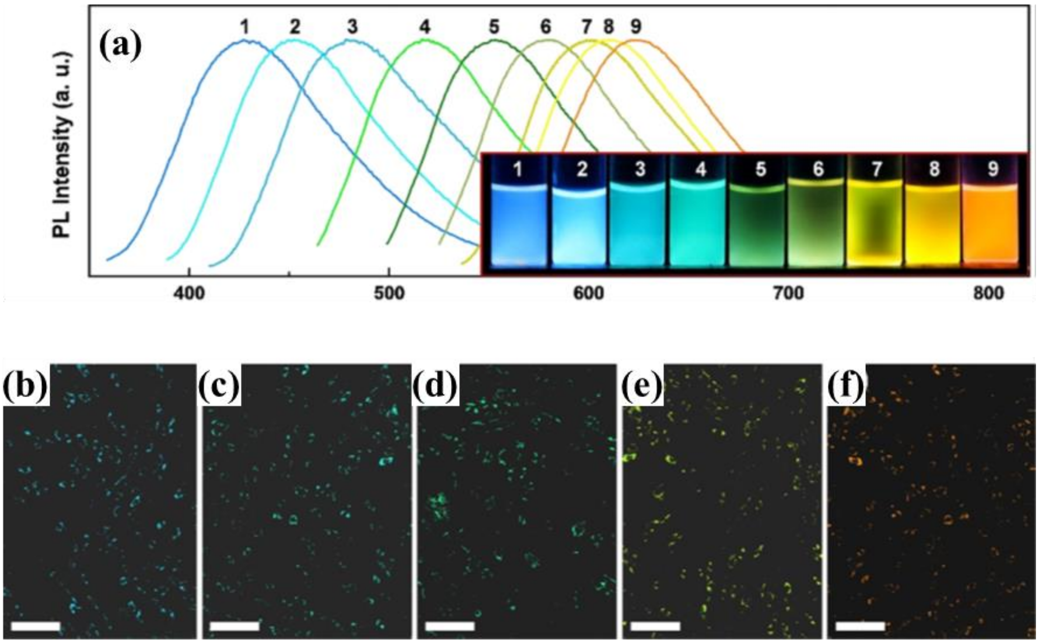

Figure 2.15. (a) PL spectra of S-GQDs with varying concentration of heteroatom doping, and (b) respective imaging of fibroblast cells incubated with S-GQD series 1, 3, 5, 7, and 9 (scale bar: 20 µm). Reprinted with permission from ref. (Wang *et al.*, 2018a). Copyright (2018) American Chemical Society.

Very recently, Ding et al. reported on the bioimaging of fibroblast cells with sulphur-doped GQDs synthesised by the hydrothermal treatment of durian (Wang *et al.*, 2018a). Different GQDs with varying amount of S doping indicate different color in bioimaging of the fibroblast cells, showing their high bioimaging capability (Figure 2.15).

The hydroxyl and carboxyl functional groups attached onto the surface and basal planes of GQDs make them highly soluble in water. High water solubility and nanoscale size of GQDs make them suitable for permeation into the cell through cell membrane. When these GQDs are internalised into the HeLa cells, their confocal images show the flourishing cell morphology (Chung *et al.*, 2019). Moreover, specific functional groups, such as nitrogen and chlorine, help GQDs bind to histones in the cell nuclei, which facilitate the targeted drug delivery. For example, GQDs demonstrated targeting of cell nucleus when HeLa cells were stained with 4, 6-diamidino-2-phenylindole and GQDs (Wang *et al.*, 2018b).

GQDs have attracted extensive research interests for selective drug delivery not only due to their surface functional groups and minimal toxicity but also due to their high drug loading capacity and continuous tracking owing to their strong fluorescence properties (Chung *et al.*, 2019). GQDs have been used as chemotherapeutic delivery system for anticancer therapeutics such as methotrexate (MTX) and doxorubicin (DOX). The GQDs with appropriate size assist in the drug delivery by reducing the translocation free energy permeating into biomembrane. The molecular structures of anticancer therapeutics enable them to be attached onto the basal planes of GQDs via π-stacking followed by delivery as a hydrophilic carrier. The large surface area to volume ratio of these GQDs enable high drug loading. Biotin-conjugated or N-doped GQDs have been used as promising drug delivery systems. For example, N-doped GQDs were simply mixed with dilute solution of MTX and MTX-N-GQDs complex was formed. The complex was observed to release 60% of drug in first 9 hours and a full release over 48 hours by a slow liberation (Khodadadei *et al.*, 2017). The anticancer therapeutics are potent but cannot be delivered to their targets in the body in free form due to their low solubility. GQDs have shown to increase the therapeutic effects of these drugs, showing possibilities of GQDs based drug delivery systems.

2.9 Energy applications of GQDs in general

In addition to biomass, numerous different types of precursors (such as graphene, carbon fibre, CNTs, etc.) have been used to prepare GQDs aiming at different applications. GQDs derived from biomass have properties similar to the ones derived from graphene-based precursors, as verified in the synthesis section. Thus, regardless of the precursor being used, GQDs with various tunable properties have been implemented in energy applications. Owing to their extraordinary properties, such as large surface area, good electrical conductivity, tunable luminescence, decreased chemical impedance, and tunable bandgap (Ritter and Lyding, 2009; Li *et al.*, 2011a; Zhang *et al.*, 2012b; Qu *et al.*, 2013; Wang *et al.*, 2014b), GQDs have shown great promise in energy applications, such as photovoltaic devices (Li *et al.*, 2011a; Kim *et al.*, 2015a), batteries (Chao *et al.*, 2015; Park *et al.*, 2016), and supercapacitors (Liu *et al.*, 2013b; Islam *et al.*, 2017), as discussed below.

2.9.1 Supercapacitors

A number of two dimensional (2D) materials, such as graphene, graphitic carbon nitride, phosphorene, hexagonal boron nitride (h-BN), and transition metal dichalcogenides, have been extensively utilised in supercapacitors (Zhu *et al.*, 2011c; Butler *et al.*, 2013; Wang *et al.*, 2014c; Zhang, 2015; Walsh *et al.*, 2016; Castañeda *et al.*, 2017; Zhang *et al.*, 2017). In many cases, the quantum dot derivatives of these 2D materials exhibit superior performance due to their large specific surface area, abundant electrochemically active sites, ability to be easily integrated with various nanomaterials and low toxicity (Wang *et al.*, 2016c).

Liu et al. (Liu *et al.*, 2013b) synthesised a GQD-based symmetric micro-supercapacitor by electrophoretic deposition of GQDs on an interdigital Au finger microelectrode and acquired fast power response, high rate performance, and long cycling life (97.8% stability after 5000 cycles) (Figure 2.16). They obtained a high specific capacitance of 534.7 µF cm^{-2} at a current density of 15 µA cm^{-2} with a power density of 7.5 µW cm^{-2} and an energy density of 0.074 µW h cm^{-2}. These outstanding properties of the micro-supercapacitor are attributed to the role of GQDs. Particularly, the exceptionally small corresponding relaxation time constant (τ_0=103.6 µs) of the GQD//GQD symmetric micro-supercapacitor indicates its extraordinary power response. With changing the aqueous electrolyte (Na_2SO_4) to an ionic liquid electrolyte ($EMIMBF_4$/AN), the corresponding relaxation time constant was further declined to τ_0=53.8 µs and, as a result, a seven times higher power and energy density was obtained. The potential window was further increased two times by fabricating one electrode (negative) coated with GQDs and the other (positive) modified with highly pseudo-capacitive nanomaterials, such as MnO_2 or polyaniline (PANI) (Liu *et al.*, 2013b).

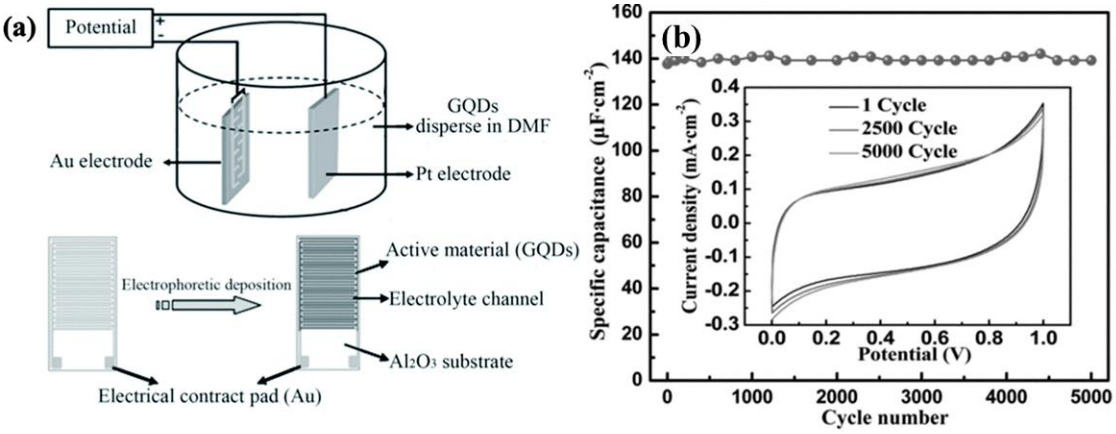

Figure 2.16. (a) The preparation of a symmetric micro-supercapacitor by depositing GQDs on an interdigital Au finger microelectrode, (b) specific capacitance retention after 5000 cycles. Reprinted with permission from ref. (Liu *et al.*, 2013b). Copyright (2013) Wiley Publishing Group.

The unique structure of these pseudo-capacitive materials helps accelerate the transport of electrolyte ions and provides abundant surface for the reactions involving charge transfer. The enhancement of specific capacitance and energy density in this asymmetric supercapacitor is based on the synergistic effects between negative and positive electrodes. Hu et al. (Hu *et al.*, 2013c) fabricated GQD/CNT hybrid film demonstrating a capacitance (44 mF cm^{-2}) two times higher than the bare CNT film.

Chen et al. (Chen *et al.*, 2014) reported on additive free monolithic electrode based on a 3D graphene/GQD composite. Astonishingly, the conductivity of the 3D graphene structure was increased 10 times by the introduction of GQDs with a specific capacitance of 268 F g^{-1}, demonstrating a progress of 490% over undecorated 3D graphene. Mondal et al. reported on a high performance supercapacitor based on GQD modified PANI nanofibers via chemically oxidizing aniline in the environment of GQDs (Mondal *et al.*, 2015). Figure 2.17a represents the preparation scheme of GQD/PANI composite. They achieved a large specific surface area, high aspect ratio, and a specific capacitance of 1044 F g^{-1} at a current density of 1A g^{-1} (Figure 2.17b). They observed a great retention rate of 80.1% after 3000 cycles (Figure 2.17c). Further enhancement in the specific surface area of GQDs can be achieved via KOH activation. Ultrafine pores and zig zag edges are introduced on GQDs by activation, resulting in a dramatic improvement (200%) in specific capacitance (236 F g^{-1}), a value much higher than that of graphene (172 F g^{-1}) activated under similar conditions (Hassan *et al.*, 2014).

Table 2.2. Comparison of the performance of the supercapacitors based on GQDs and other graphene derivatives.

Materials	**Preparation approaches**	**Performance**	**Ref.**
GQDs-deposited on interdigital Au finger	Hydrothermal cutting and electrophoretic deposition	Capacitance: 534.7 µF cm^{-1} at 15 µA cm^{-1}, power density: 0.074 µW cm^{-2}, rate performance: 97.8% after 5000 cycles	(Liu *et al.*, 2013b)
GQDs/ carbon fibre	In-situ direct grafting	Rate performance: 97 % after 5000 cycles at 2A g^{-1}	(Islam *et al.*, 2017)
GQDs/PANI	Electrodeposition	667.5 µF cm^{-1} at 15 µA cm^{-1}, power density: 7.5 µW cm^{-2}	(Liu *et al.*, 2013a)
GQDs/CNT	Electrochemical, CVD, electrodeposition	Capacitance: 44 mF cm^{-2},	(Hu *et al.*, 2013c)
GQDs/3D graphene	Electrochemical synthesis, electrodeposition	Capacitance: 268 F g^{-1}	(Chen *et al.*, 2014)
GQDs/PANI nanotubes	Electrodeposition	Capacitance: 1044 F g^{-1} at 1A g^{-1}, rate performance: 80.1% after 3000 cycles	(Mondal *et al.*, 2015)
Graphene/PANI composite sheets	Anodic electro-polymerisation	Capacitance: 233 F g^{-1}	(Wang *et al.*, 2009)
MnO_2/graphene/GF	Hydrothermal process, electrodeposition	Capacitance: 9.6 mF cm^{-2}	(Yu *et al.*, 2014)
CNT/graphene hybrid	Hydrothermal, CVD	Capacitance: 0.74 mF cm^{-2} at 10 mA cm^{-2}	(Kou *et al.*, 2014)
GF@3D G core-sheath fibre	Hydrothermal, electrodeposition	Capacitance: 1.2–1.7 mF cm^{-2}	(Cheng *et al.*, 2014)

Recently, Mohammad et al. prepared GQD-grafted carbon fibre for high performance supercapacitors and observed a 5.5% enhanced capacitance compared to that of bare carbon fibre. They demonstrated a high specific capacitance with a retention rate of 97% after 5000 cycles (Islam *et al.*, 2017). Table 2.2 shows the comparison of the performance of supercapacitors based on GQDs and other graphene-based materials. It is clearly observed that GQDs exhibit the best performance (capacitance: 1044 F g^{-1} at 1A g^{-1} (Mondal *et al.*, 2015) and 97.8% stability after 5000 cycles (Liu *et al.*, 2013b; Islam *et al.*, 2017)) among all graphene based materials. The plentiful and accessible ion-interacting edges, large specific surface area, defects, functional groups and chemical moiety sites associated with GQDs are responsible for their better capacitive performance.

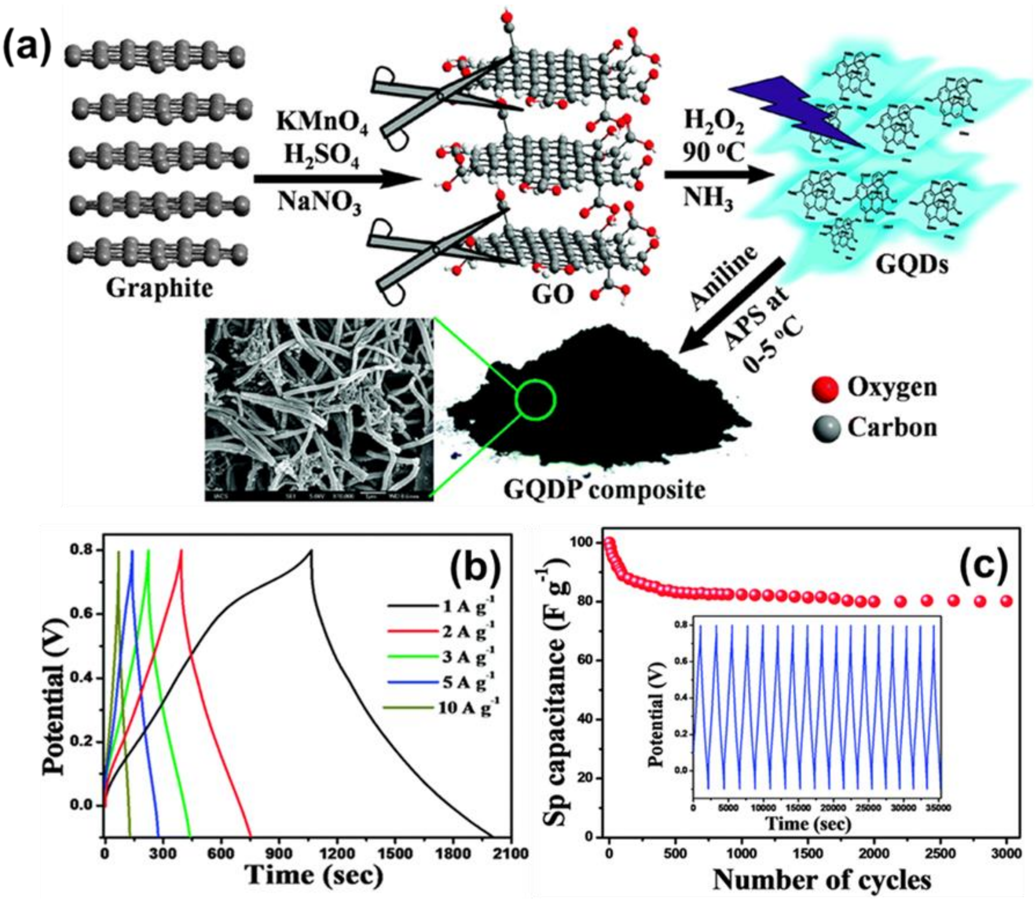

Figure 2.17. (a) Schematic representation of the GQD/PANI composite preparation. (b) Galvanostatic charge discharge curves at various current densities, (c) life stability of GQD/PANI composite after 3000 cycles, inset is curve for 10 consecutive charge discharge cycles. Reprinted with permission from ref. (Mondal *et al.*, 2015). Copyright (2015) Royal Society of Chemistry.

2.9.2 Batteries

GQDs were first utilised in Li-ion batteries (LiBs) by Fan and co-workers (Chao *et al.*, 2015). Fan et al. reported on improving the cathode material for LiBs by synthesising a GQD-coated VO_2-nanobelt arrays on 3-D graphene foam (Figure 2.18a-c) (Chao *et al.*, 2015). A high specific capacitance of 421 mA h g^{-1}, 99% Coulombic efficiency, and high rate performance were obtained at a current density of 1/3 C (1 C = 300 mA g^{-1}), outperforming VO_2-nanobelt arrays without GQDs coating (Figure 2.18d). Contrary to the poor stability of other VO_2 based electrodes, the GQDs-anchored VO_2 electrode show tremendous enhancement in its stability (a retention of 94% capacity after 1500 cycles) (Chao *et al.*, 2015). This electrode also shows good performance in the case of sodium ion batteries as a cathode material (a retention of 88% capacitance after 1500 cycles, and capacitance of 306 mA h g^{-1} at 1/3 C). At a high charge-discharge rate of 120 C, the electrode has a power density of 42 kW kg^{-1} with a good energy density of 4100 Wh kg^{-1} (Figure 2.18e).

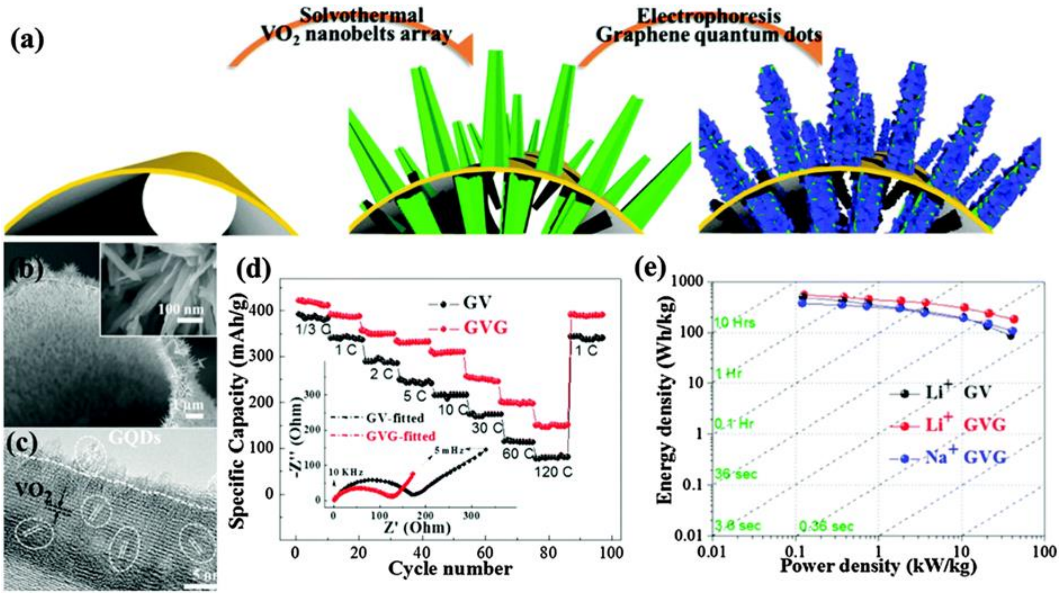

Figure 2.18. Preparation of GQD-coated VO_2 nanobelt array supported on 3D graphene (GVG). (b, c) SEM and HRTEM images of the hybrid structure. (d) Rate performance of the as fabricated electrode with (GVG) and without (GV) GQD coating, inset in (d) is AC impedance plots. (e) Ragone plot of GVG electrode for Na and Li ion batteries. Reprinted with permission from ref. (Chao *et al.*, 2015). Copyright (2015) American Chemical Society.

In another study, the same group synthesised an anode material for LiBs by assembling CuO + Cu + GQDs on triaxial nanowire arrays (Zhu *et al.*, 2015a). The schematic illustration of electrode fabrication is presented in Figure 2.19a. Coating of the GQDs outer layer results in a mossy surface of CCG nanowires (Figure 2.19b) which indicates their enlarged surface area and enhanced connection sites for electrochemical reactions. Meanwhile, annealing of a CuO nanowire in Ar + H_2 converts some of it into Cu metal and a smooth surfaced CuO + Cu coaxial nanowire is obtained (Figure 2.19c). Adding GQDs in a CuO nanowire array in this manner offers enhanced surface conductivity, improved stability and a high columbic efficiency (87%) (Figure 2.19d). The as-fabricated electrode demonstrates a high specific capacity of 780 mA h g^{-1} at 1/3 C and 330 mA h g^{-1} at 4 C, outperforming the CuO + Cu electrode without GQDs (Figure 2.19d) (Zhu *et al.*, 2015a). In both studies, improved performance of GQDs was based on several factors. Firstly, the GQDs layer prevents the formation of a solid electrolyte interface film, which results in an enlarged Coulombic efficiency. Secondly, the conductivity and charge collection efficiency of the electrode is enhanced by an ordered covering of GQDs over the surface of active material, leading to high rate performance. Thirdly, a rough electrode surface conferred by the GQDs results in a large surface area leading to an improved metal ion storage. Lastly, GQDs act as a stabilizer to protect the electrode active materials from dissolution and/or agglomeration, leading to an improved cycling life of the electrode.

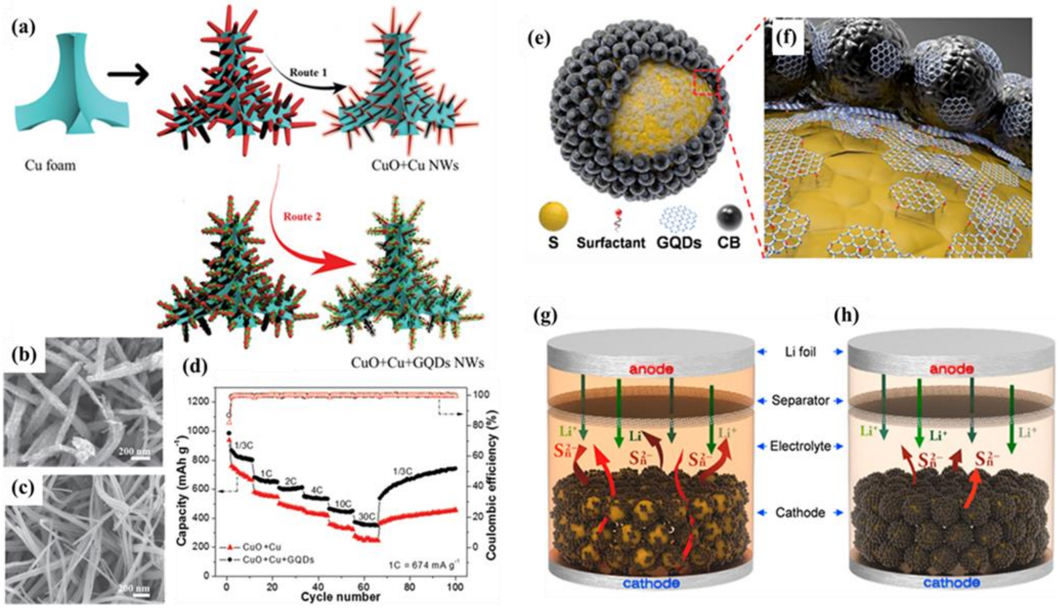

Figure 2.19. (a) Schematic illustration of the synthesis process for CuO-based nanowire electrode. Route 1 is for the fabrication of CuO-Cu (CC) core-shell nanowire and route 2 is for the preparation of CuO+Cu+GQD (CCG) triaxial nanowire. (b) SEM image of CCG triaxial nanowires, (c) CC core shell nanowires, (d) rate performance with Columbic efficiency of CCG and CC nanowire electrodes. Adapted and modified with permission from ref. (Zhu *et al.*, 2015a). Copyright (2015) Wiley Publishing Group. (e) Schematic diagram showing the structure and (f) magnified structure of GQDs-sulphur /carbon black (GQDs-S/CB) composite. The sulphur (yellow ball) was wrapped with carbon-black (S/CB) and compactly covered with GQDs and CB (GQD-S/CB). (g) Schematic arrangement of sulphur/carbon-black (S/CB) and (h) GQDs-S/CB utilised as a cathode in Li-S batteries. Adapted with permission from ref. (Park *et al.*, 2016). Copyright (2016) Nature Publishing Group.

GQDs have also been employed in lithium-sulphur (Park *et al.*, 2016), Lithium-silicon (Lijuan *et al.*, 2016), lithium-titanate (Ruiyi *et al.*, 2015), and metal-air batteries (Wang *et al.*, 2016b). Park et al. reported on the introduction of GQDs into the sulphur cathode of lithium-sulphur (Li-S) batteries and demonstrated an enhanced sulphur-sulphide utilisation, yielding high performance (Park *et al.*, 2016). High structural integrity of the sulphur-carbon composite electrode is induced by the oxygen rich functional groups of GQDs. Figure 2.19e, f shows a schematic structure of GQDs-sulphur/carbon-black (GQDs-S/CB) composite. Fast charge transfer was acquired owing to the hierarchical structure of sulphur-carbon composite and the physiochemical properties of GQDs. The schematic diagram in Figure 2.19g, h shows the conventional Li-S battery, in which lithium foil serves as an anode material and the cathode is made up of sulphur/carbon-black (S/CB) or GQDs-S/CB composites. The cathode structure greatly influences the irreversible loss of high order polysulfides during the cyclic charging-discharging process. The surface of sulphur particles is partially exposed in the S/CB composite, as a result the polysulfides are dissolved in the solvent and change the colour to orange (Figure 2.19g). The introduction of GQDs into the S/CB composite induces a densely packed structure and greatly enhances the performance of the Li-S battery by preserving the high-order polysulfides (HOPSs) in the structure of the GQD-S/CB composite. At 0.5 C, a Coulombic efficiency of 100% and cyclic performance of ~ 1000 mA h g^{-1} was maintained up to 100 cycles for a GQD-S/CB based battery. The GQD-S/CB electrode showed outstanding rate capability at 10 C (540.17 mA h g^{-1}) as compared to the S/CB composite (120.35 mA h g^{-1}). The GQD-S/CB system showed extraordinary cyclic performance of 950 mA h g^{-1} even when an electrode with high sulphur loading was prepared. These cyclic performance values are much higher than reported values for other sulphur/carbon composites (Park *et al.*, 2016). GQDs have been utilised in lithium-silicon batteries for the passivation of silicon, which is very promising anode material for LIBs but faces a challenge of large volume variation and rapid capacity loss during the charging-discharging process. Lijuan et al. coated a layer of phenylalanine-functionalised GQDs on silicon nanoparticles to improve the electrical conductivity and prevent direct contact of the electrolyte with silicon (Lijuan *et al.*, 2016). As a result, they produced a stable material with high capacitance of 3796 mA h g^{-1} at 100 mA g^{-1} and 76% retention (3068 mA h g^{-1}) after 100 cycles (Lijuan *et al.*, 2016). The incorporation of N and S co-doped GQDs onto the titanate anode of lithium-titanate batteries can enhance the power density and rate performance due to enhanced electron transfer and lithium storage capacity (Ruiyi *et al.*, 2015). LIBs based on GQDs show superior capacitive performance (4066 mA h g^{-1}) (Lijuan *et al.*, 2016) over other graphene based materials (up to 770 mA h g^{-1}) (Ye *et al.*, 2014) (Table 2.3).

Table 2.3. Comparison of the performance of Li-ion batteries based on GQDs and other graphene derivatives.

Materials	**Preparation approaches**	**Performance**	**Ref.**
GQDs-VO_2-3D graphene	Hydrothermal, solvothermal processes and electrophoresis deposition	Capacitance: 421 mA h g^{-1} at 1/3 C, Stability: 94 % after 1500 cycles at 60 C	(Chao *et al.*, 2015)
CuO + Cu+ GQD triaxial	Hydrothermal, electrochemical and electrophoresis	Capacitance: 780 mA h g^{-1} at 1/3 C	(Zhu *et al.*, 2015a)
GQDs-S/CB	Refluxing, chemical reduction, high temperature stirring	Capacitance: 1000 mA h g^{-1} at 0.5 C	(Park *et al.*, 2016)
PF-GQD@SiNP	Hydrothermal treatment, thermal annealing, stirring	Capacitance: 4066 mA h g^{-1} at 50 mA g^{-1}	(Lijuan *et al.*, 2016)
LTO/GO and LMO/MWNT	Hydrothermal, rolled approach	Energy density: 27 W kg^{-1} power density: 880W kg^{-1}	(Ren *et al.*, 2014)
Graphene on graphene hybrid film	CVD, GO reduction	Capacitance: 770 mA h g^{-1} at 372 mA g^{-1}	(Ye *et al.*, 2014)
SnO_2-graphene composite	Self-assembly	Capacitance: 625 mA h g^{-1} at 10 mA g^{-1}, 760 mA h g^{-1} at 8 mA g^{-1}	(Wang *et al.*, 2010)

2.9.3 Photovoltaics

Owing to their extraordinary electronic/optical properties, GQDs may be used in various components of photovoltaics, such as sensitizers, activators, active layers, and catalysts for the counter electrode. Gao et al. used GQDs as active layer to fabricate a Si/GQD heterojunction solar cell (Gao *et al.*, 2014). The GQD active layer suppresses charge recombination and promotes electron-hole separation (Figure 2.20a). A photo conversion efficiency (PCE) of 6.6% was displayed by the cell, much higher than that of an undecorated Si based cell (2.26%) or one with GO sheets acting as active layers (3.99%). Dutta et al. synthesised GQD/ZnO nanowire heterojunction solar cells which showed a current density (J_{sc}) 75 times higher than that of a bare ZnO nanowire-based cell (Dutta *et al.*, 2012). However, a low PCE was obtained due to the limited GQD connections with the hole-transport layer causing a low hole-collection efficiency. Using a hot injection approach, Tavakoli and co-workers synthesised PbS QD/GQD core/shell hybrids (Figure 2.20b) (Tavakoli *et al.*, 2015). In contrast with commonly utilised capping molecules, the ultrathin layer of GQDs makes surface passivation of PbS QDs incomplete, reduces the number of trap states and promotes faster extraction of charge carriers. An improved current density (13.4 mA cm^{-2}), PCE (3.6%) and open cell voltage (0.58 V) was obtained for a solar cell with PbS QD/GQD active layers compared to that of organic molecule-capped PbS QD-based devices (Figure 2.20b) (Tavakoli *et al.*, 2015). Cd doping of PbS QDs can further improve the PCE of a PbS QD/GQD cell by 4.1%. Qu et al. prepared a polymer based bulk-heterojunction (BHJ) solar cell with a structure of ITO/PEDOT:PSS/P3HT:GQD/Al (Li *et al.*, 2011a). Plentiful p–n junctions formed inside the P3HT:GQD active layer promote the reduction of photogenerated excitations and electron transfer. Ideally, the open circuit voltage can be improved from 0.5 V to 0.8 V by introduction of GQDs. A PCE of 1.28% was obtained from an actual device with J_{sc} of 6.33 mA cm^{-2} and open circuit voltage (V_{oc}) of 0.67 V. The charge carrier concentration of the polymer device can be improved by 30% by the addition of Cl-doped GQDs to the P3HT active layer (Figure 2.20c) (Zhao *et al.*, 2015a).

Gupta and co-workers developed a solar cell using aniline functionalised GQDs as a filler for P3HT and the cell configuration consist of ITO/PEDOT:PSS/P3HT:Ani–GQDs/LiF/Al (Gupta *et al.*, 2011). The device demonstrated a superior PCE (1.14%) compared to the control device with an active layer of P3HT:Ani–graphene sheet (PCE: 0.65%). The rough structure of the P3HT:Ani–graphene film due to large sized graphene sheets induces extra phase separation surpassing the diffusion length of excitons, resulting in a poorer performance (Zheng *et al.*, 2013b).

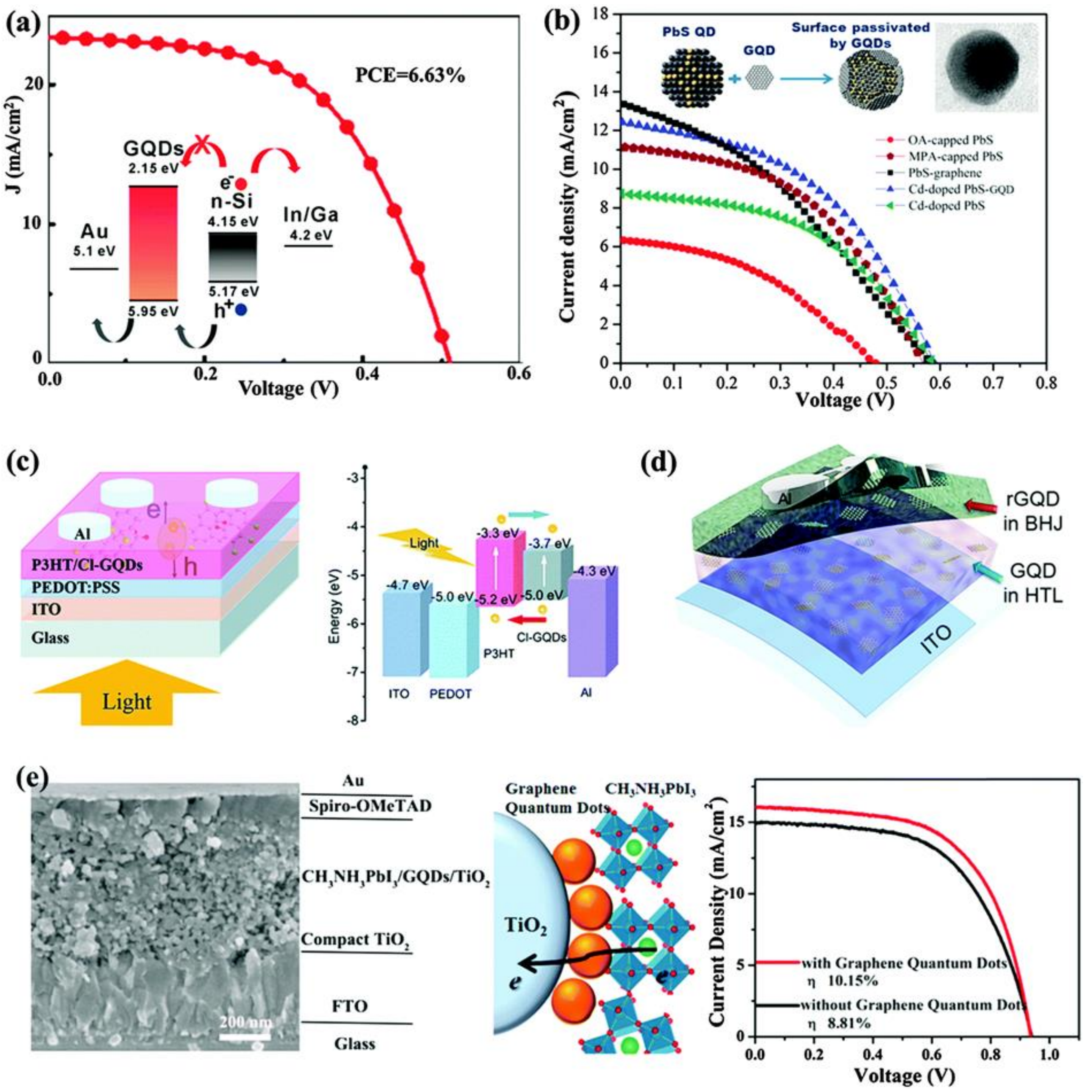

Figure 2.20. (a) CH3-SI/GQD heterojunction solar cell showing J-V curve at Am1.5G (the inset shows its energy band diagram). Adapted and modified with permission from ref. (Gao *et al.*, 2014). Copyright (2014) American Chemical Society. (b) A schematic diagram of PbS QDs surface passivated by GQDs and PbS based solar cells' J-V curves under Am1.5G. Reprinted with permission from ref. (Tavakoli *et al.*, 2015). Copyright (2014) American Chemical Society. (c) Schematic of a photovoltaic device based on GQD-Cl hybrid and its working mechanism. Reprinted with permission from ref. (Zhao *et al.*, 2015a). Copyright (2015) Royal Society of Chemistry. (d) Illustration of a photovoltaic device based on GQDs in hole-transport layer and hydrothermally reduced GQDs in the BHJ layer. Reprinted with permission from ref. (Kim *et al.*, 2015a). Copyright (2015) Nature Publishing group. (e) SEM image (cross sectional view) of perovskite solar cell on left side, illustration of its working mechanism in middle, and J-V curves of the cell without or with GQD on right. Adapted with permission from ref. (Zhu *et al.*, 2014). Copyright (2014) American Chemical Society.

Kim et al. developed a BHJ solar device based on polymer active layer containing GQDs with different numbers of oxygenated groups (Zheng *et al.*, 2013b). The oxygen functional groups on the surface of GQDs were found to improve the optical absorptivity of the device leading to a significantly enhanced J_{sc}, while the superior conductivity of less-oxidised GQDs resulted in better charge carrier extraction that can improve the fill factors (FFs). The balance between these two features gives a highest PCE of 7.6%. Elsewhere, they reported that, with the addition of hydrophilic GQDs onto the PEDOT:PSS hole transporting layer, the J_{sc} of the BHJ solar cell can be enhanced from 15.6 mA cm^{-2} to 17.3 mA cm^{-2}. This improvement can be assigned to the enhanced conductance of charge carriers in the ITO/PEDOT:PSS layer due to the strong interaction between GQDs (having a negative charge) and PEDOT (with a positive charge) (Kim *et al.*, 2015a). In order to understand the synergistic effects, hydrophilic GQDs were introduced into the EDOT:PSS hole transport layer and hydrothermally reduced hydrophobic GQDs were incorporated into polymer layer (Figure 2.20d), and a greatly enhanced PCE of 8.67% was achieved. Using chemical-group-free GQDs, Yan and co-workers tried to sensitise a TiO_2 photoanode for a solar cell (Yan *et al.*, 2010a). However, the Jsc of the cell was decreased by two orders of magnitude compared to that of dye-sensitised solar cells (DSSC) due to the poor binding affinity of GQDs with TiO_2. If GQDs with oxygen groups are used, the performance could be considerably improved because these GQDs can interact significantly with TiO_2 (Long, 2013; Williams *et al.*, 2013). When N719 dye and GQDs are used together as sensitizer and co-sensitizer in TiO_2 photoanodes, an uplift of PCE from 4.9 to 6.1% and rise of Jsc from 9.72 to 14.07 mA cm^{-2} is observed (Fang *et al.*, 2014).

Mihalache et al. reported similar findings, an increase in Jsc and PCE for DSSC through N-doped GQDs as co-sensitizer along with N_3Ru–Dye (Mihalache *et al.*, 2015). The improved performance of the DSSC device can be attributed to the improved charge separation, overlapped of the PL spectrum of GQDs with the absorption spectrum of N_3Ru–dye, and suppressed electron recombination in the redox couple in the electrolyte. Lee et al. increased the amount of light used by DSSCs by depositing GQDs onto TiO_2 promoting upconversion PL and observed an increase of PCE from 7.28 to 9.2% (Lee *et al.*, 2013a). Chen et al. introduced GQDs to the polypyrrole counter electrode to make it highly porous and generated an enhanced PCE of the DSSC (Chen *et al.*, 2013). In a recent study, an ultrathin layer of GQDs was introduced to a perovskite solar device with a structure of $CH_3NH_3PbI_3$/GQDs/TiO_2, and an improvement in PCE from 8.81 to 10.15% and J_{sc} from 17.07 to 15.34 mA cm^{-2} was obtained (Figure 2.20e) (Zhu *et al.*, 2014). This enhanced performance is attributed to the faster electron extraction, which guarantees improved photon-to-current conversion in the visible region, and 75% PL quenching of the perovskite-TiO_2 film.

Table 2.4. A comparison of the preparation approaches, performance and characteristics of the photovoltaic devices based on GQDs and other graphene derivatives.

Materials	**Preparation approaches**	**Performance**	**Ref.**
Ani-GQDs and P3HT	Spin casting	PCE: 1.14%, J_{SC}: 6.33 mA cm^{-2}, V_{oc}: 0.67 V, fill factor: 0.53	(Gupta *et al.*, 2011)
GQDs	Electrochemical corrosion	PCE: 1.28%, J_{SC}: 6.33 mA cm^{-2}, V_{oc}: 0.67 V	(Li *et al.*, 2011a)
Colloidal GQDs	Solution synthesis	Faster component: 18 ± 3 ps, slower component: 100 ps	(Mueller *et al.*, 2010a)
GQDs/TiO$_2$ composite	Chemically anchored method	The electron injection: <15 fs, exciton recombination: 0.5-2 ps, charge recombination: 80–130 fs	(Williams *et al.*, 2013)
Monodispersed GQDs	Solution synthesis method	Emitting both fluorescence and phosphorescence, relaxing into triplet states	(Mueller *et al.*, 2010b)
Graphene and Pt composite fibres	Spinning and electrodeposition	J_{SC}: 12.67–17.11 mA cm^{-2}, V_{oc}: 0.73 V, fill factor: 0.42–0.67	(Yang *et al.*, 2013)
Graphene/ CdS quantum dot composite	Layer by layer assembly	Photoresponse: 1.08 mA cm^{-2} under 100 mW cm^{-2}, quantum efficiency: 16% at 400 nm	(Guo *et al.*, 2010)
Graphene/CNT/Pt composite fibres	Biscrolling approach, electrodeposition	Capacitance: 31.50 F g^{-1}, conversion efficiency: 8.36 %	(Sun *et al.*, 2014b)

PCE: power conversion efficiency, J_{SC}: short circuit current density, V_{oc}: open circuit voltage

Phosphorene is desirable for photovoltaic applications because of its bipolar characteristics, high hole mobility and narrow bandgap (0.3 to 1.5 eV based on the number of layers) (Dai and Zeng, 2014). Deng et al. prepared a heterojunction between n-type monolayer MoS_2 and p-type few layer phosphorene, fabricating a p-n diode for photovoltaic energy conversion with PCE of 0.3% (Deng *et al.*, 2014). The theoretical predictions indicate that PCE of a p-n diode can be increased to 18% by reducing the thickness of phosphorene to only two layers (Dai and Zeng, 2014). Based on the bipolar characteristic of few layer phosphorene, Buscema et al. utilised a single phosphorene sheet to fabricate a p-n heterojunction with 2 regions differently biased by 2 h-BN dielectric gates (Buscema *et al.*, 2014). As a result, the photovoltaic effect can be extended to the near-IR region. The electrical band gap between graphene and transition metal dichalcogenide is filled by phosphorene. Thus, the application gap between GQDs and TMD-QDs could be filled by phosphorene QDs. A large number of photovoltaic devices based on GQDs have been synthesised which outperform other graphene-based materials (Table 2.4).

2.10 Challenges and perspectives

Biomass is a sustainable and rich source of carbon. For the efficient utilisation of carbon resources, it is necessary to understand carbon chemistry and factors influencing its properties. GQDs derived from biomass waste are emerging zero-dimensional materials which show an extensive range of intriguing properties (e.g. chemical, electrochemical, optical, catalytic, electronic, etc.). Owing to the lower dimensionality of GQDs, they often achieve extra advantages over their 2D counterparts. Firstly, the properties of GQDs are tunable with more sensitivity by size, thickness, chemical functionalities, edge configuration, thickness, defects, or heteroatom dopants. This could help improve promising properties for unique applications. Secondly, minute perturbations or interactions can have a significant effect on their properties. This is needed for the development of high sensitivity sensors. In addition, these GQDs are often easier to functionalise than other nanomaterials to acquire composite properties. Moreover, due to better solubility they have better responsiveness for solution-based processes. Finally, the tiny size is the key benefit for bio-imaging purpose of GQDs because these are used as fluorescent tags on molecular targets and the function and dynamics of targets may be changed if large tags are used.

Due to their range of excellent properties, GQDs show high promise for an extensive series of potential applications. Although only a few applications of biomass derived GQDs have been studied so far, GQDs are also highly promising for catalysis, drug delivery, bioimaging, photodynamic therapy, optical sensing, electrochemical sensors, optoelectronics, displays, etc. (Hu *et al.*, 2012; Konstantatos *et al.*, 2012; Li *et al.*, 2012b; Shen *et al.*, 2012a; He *et al.*, 2013; Ananthanarayanan *et al.*, 2014; Biju, 2014; Ge *et al.*, 2014; Hola *et al.*, 2014; Sun *et al.*, 2014a; Wang *et al.*, 2014d; Hong *et al.*, 2015; Lin *et al.*, 2016; Kumawat *et al.*, 2017; Su *et al.*, 2017; Yao *et al.*, 2017). It has been revealed that, owing to their numerous key features (e.g. biocompatibility, photostability, non-toxicity, etc.), GQDs are superior to widely used conventional semiconductor QDs and organic fluorophores for various biological applications, such as bioimaging (Zheng *et al.*, 2015; Feng *et al.*, 2017; Li *et al.*, 2017). Using insulin-functionalised GQDs, for example, Zheng et al. visualised the distribution and dynamics of insulin receptors in live adipocytes (Zheng *et al.*, 2013b).

Despite the recent progress, research on biomass derived GQDs is still in its early phase and many challenges need to be tackled. Some of the key issues that require urgent attention include:

1. Introduction of inherent impurities in GQDs from biomass feedstock due to intense presence (~40-50%) of elements other than carbon. Moreover, the synthesis of GQDs

from biomass usually involves large quantity of strong oxidants and their removal is a very tedious process which takes several days if not weeks, still may leave impurity traces in the product.

2. The low product yield of GQDs due to low efficiency of conversion of all biomass carbon into aromatic quantum dots.
3. For the practical applications, the intensified production of GQDs is required. On this path, several researchers have tried to develop large scale production of GQDs from biomass, however, still the actual amount was in milligrams (Suryawanshi *et al.*, 2014; Wang *et al.*, 2016d).
4. Overall, the conversion of biomass into GQDs is a very lengthy process involving multiple steps such as synthesis of biochar, activation of biochar with strong acids/oxidants, removal of excess acids, synthesis of GQDs, and purification processes.
5. The precursor employed has a significant effect on the final properties and engineering control of GQDs. Thus, controlling the properties of biomass derived GQDs is relatively difficult due to the inherent nature of the feedstock.
6. Due to high sensitivity of GQDs towards size, thickness, edge engineering, heteroatom doping and chemical functionalisation, developing advanced preparation methods are highly desired for the precise control over these parameters.

In this perspective, there is urgent need to search for novel feedstocks for efficient conversion into GQDs, advanced preparation methods to achieve high product yield, simple and effective purification techniques to acquire high quality product, and elimination of multiple steps to realise rapid synthesis. Last but not least, the intensified synthesis of GQDs is highly demanding for practical applications. Since biomass is a renewable and abundantly available source, a scalable and cheap synthesis approach using a biomass precursor has great promise for commercialisation.

Chapter 3 Materials and methods

The materials, chemicals, experimental setup, experimental methods and characterisation techniques employed in this study are described in this chapter. The main analysis of the product was carried out using scanning and transmission electron microscopies, nitrogen adsorption-desorption surface area measurements, X-ray diffraction, Fourier transform infrared, Raman and X-ray photoelectron spectroscopies. Optical properties were studied using UV-visible and photoluminescence analysis, while electrochemical properties were examined via cyclic voltammetry, impedance and galvanostatic charge-discharge studies.

3.1 Materials

Spent tea was derived from PG tips tea bags manufactured by Unilever UK. Spent tea bags were collected from a local tea shop in Newcastle Upon Tyne, United Kingdom. In order to avoid variation in the feedstock, a sufficient quantity of spent tea bags was collected at once to prepare adequate samples.

All the chemicals were of analytical grade and used without further modifications unless otherwise specified. Sulfuric acid (H_2SO_4, ≥ 97%), nitric acid (HNO_3, ≥ 67%), hydrochloric acid (HCl, ≥ 37%), sodium hydroxide (NaOH), potassium hydroxide (KOH), potassium carbonate (K_2CO_3), N-Methyl-2-pyrrolidone (NMP, ≥ 99%), polyvinylidene fluoride (PVDF), quinine sulfate (99%) and absolute ethanol (C_2H_5OH, ≥99%) were purchased from Fisher Scientific, UK. The salts such as silver nitrate ($AgNO_3$), aluminium chloride ($AlCl_3$), calcium chloride ($CaCl_2$), cobalt chloride ($CoCl_2$), chromium chloride ($CrCl_3$), cooper chloride ($CuCl_2$), magnesium chloride ($MgCl_2$), manganese chloride ($MnCl_2$), molybdenum dichloride ($MoCl_2$), iron (III) chloride ($FeCl_3$), strontium chloride ($SrCl_2$), zinc chloride ($ZnCl_2$), sodium chloride (NaCl), and lithium chloride (LiCl) were supplied by Sigma Aldrich. Gases (nitrogen, helium, and argon with 99.998% purity) and liquid nitrogen were provided by BOC, UK. Graphite bipolar plate with 0.6 mm thickness (TF6, SGL Carbon, Germany), 4.6 mm thick PAN based carbon felt (SIGRACELL® GFD 4.6 EA, SGL Carbon, Germany), fluorinated anion-exchange membrane (Fumasep® FAP-450, 50 µm, FuMa-Tech GmbH, Germany), Vanadium electrolyte solution (1.6 M $V^{+3.5}$, AMG Titanium Alloys and Coatings, GFE, Germany) and carbon black (Super P, 99%, Alfa Aesar) were also used. Other materials include dialysis bags of 1kD MWCO (Spectrum Labs), polyvinylidene difluoride (PVDF) filtration membranes (0.1 µm, Merck Millipore), Whatman filter paper (3, 5 and 8 µm, Whatman), Mica discs (Agar scientific, AGF7013) and TEM grids (Electron Microscopy Sciences, CF-400-Cu-UL). De-ionised (DI) water was used for all the experiments.

3.2 Feedstock preparation

The collected spent tea bags were washed thoroughly with tap water followed by DI water to remove the dissolvable organic components (e.g. color) and dust particles, if any. The washed tea bags were dried for 24 hours at atmospheric conditions. The samples were then oven dried at 80 °C for further 12 h to remove absorbed moisture. After removing from the tea bags, the dried black tea obtained was ground by a commercial blender and sieved to get a fine powder ($\leq 90\ \mu m$) for efficient conversion into activated carbon and easy breakdown into nanoscale quantum dots. The prepared samples were stored in clean glass bottles for further studies.

3.2.1 Characterisation

The carbon content in the biomass is the main constituent for the preparation of carbon-based advanced materials. Therefore, to determine the carbon content and other elements present in the biomass, ultimate analysis was performed. The ultimate analysis was performed on an elemental analyser (EA1108, CARLO ERBA, UK). Briefly, it quantifies the elements by combusting the substance at elevated temperature and analysing the emission gases. The oxygen content was calculated by difference as follows:

$$O\% = [100 - (C + H + N)]\ \% \tag{3.1}$$

The proximate analysis (ASTM standard D3172) of the biomass was carried out to determine the moisture content, volatile matter, fixed carbon and ash content. Fixed carbon was obtained by difference as follows:

$$\text{Fixed carbon}\ \% = 100 - (\text{Volatile matter}\ \% + \text{Ash}\ \%] \tag{3.2}$$

The elemental composition and proximate analysis of the feedstock utilised in this work is given in Table 3.1.

Table 3.1 Proximate and ultimate analysis of the spent tea used in this study.

Proximate analysis	**wt.%**	**Ultimate analysis (dry ash free)**	**wt.%**
Moisture	8.42	Carbon	50.5
Ash	2.87	Hydrogen	6.4
Volatile matter	76.3	Nitrogen	4.48
Fixed carbon	20.83	Oxygen*	38.6

*Determined by difference

3.3 Experimental setup

3.3.1 Biochar production via Pyrolysis

Pyrolysis treatment of samples was carried out in a VCTF4 furnace (Vecstar Ltd.) to produce biochar. A schematic illustration of the pyrolysis setup is presented in Figure 3.1.

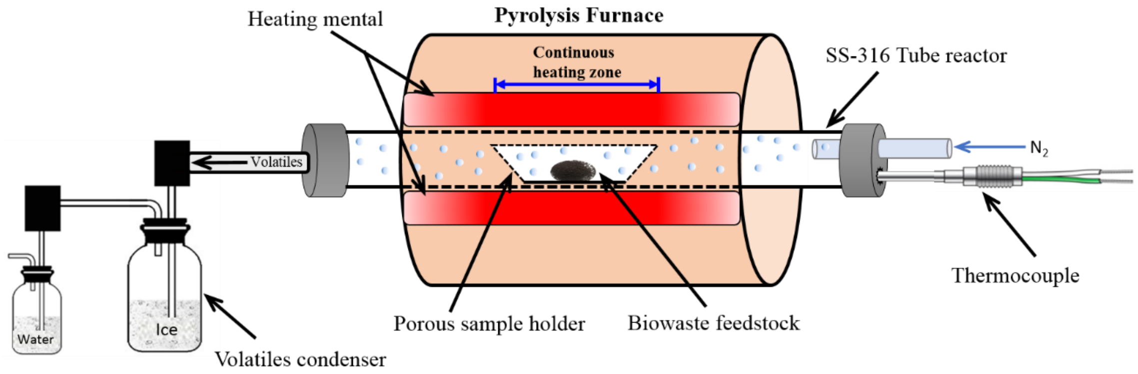

Figure 3.1. Schematic illustration of the pyrolysis setup for the production of biochar from biomass feedstock.

The experimental setup consists of a pyrolysis furnace, stainless-steel tube reactor (4 cm x 70 cm), sample holder (3cm x 20 cm), thermocouple, and volatiles condenser. The furnace could operate up to 1000 °C with variable heating rates of 1–20 °C/min. The temperature was controlled by the furnace automatically and monitored by an external thermocouple. Approximately 10 g sample was placed in a 316-stainless steel sample holder located in centre of the furnace (uniform temperature zone) under a continuous flow of nitrogen (N_2). The N_2 flow rate was set at 50 ± 5 mL/min to create the inert atmosphere and recover the volatiles and emission gases. The flow of the nitrogen gas was controlled by the gas regulator connected to the outlet of the nitrogen cylinder. The outlet of the reactor was connected to condensers chilled with ice and water for collecting volatiles. The black tea sample was heated at a heating rate of

10 °C min^{-1} to the desired temperature (200-800 °C), followed by a holding time of 3 h. Furnace was then allowed to cool down to room temperature and the product was collected. Figure 3.2 shows a schematic illustration of the biochar preparation from spent tea.

Figure 3.2. Schematic illustration of the biochar preparation from spent tea.

The yield of the product obtained at different pyrolysis temperatures was recorded (Figure 3.3). The biochar samples prepared at different pyrolysis temperatures were designated as BC-X, where BC stands for biochar and X indicates the heat treatment temperature (HTT), e.g. BC-500 corresponds to the biochar with HTT of 500 °C.

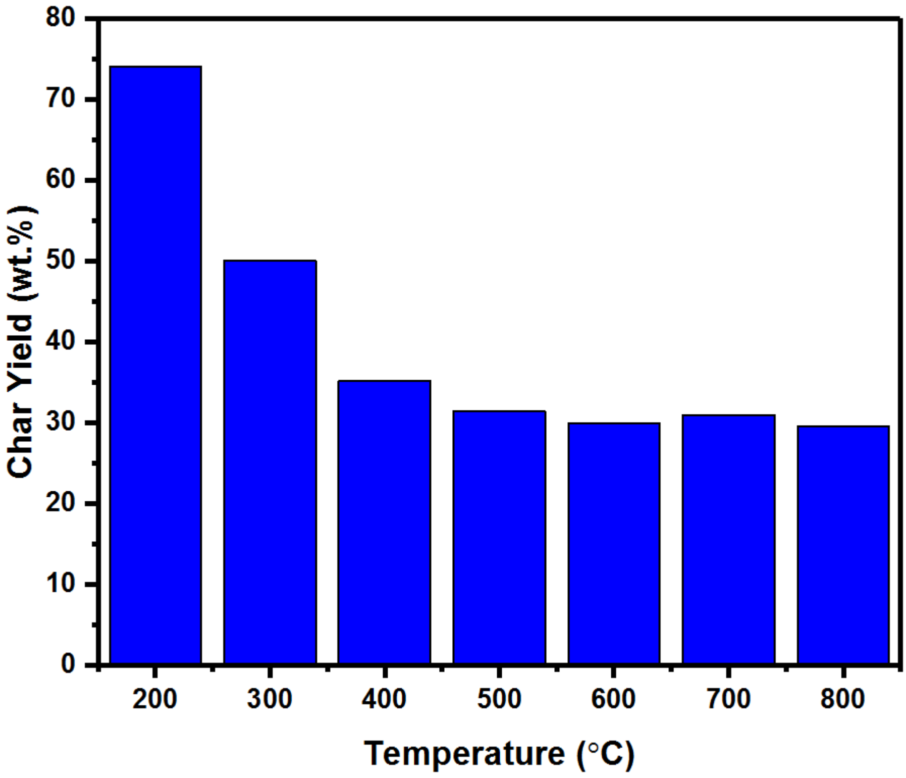

Figure 3.3. Effect of pyrolysis temperature on the yield of char acquired from spent tea at a fixed heating rate of 10 °C min^{-1} and holding time of 3 h.

3.3.2 *Hydrothermal carbonisation*

Hydrothermal carbonisation was performed to convert biochar into nanoscale fragments to produce fluorescent materials. The hydrothermal treatment of activated biochar was carried out in Teflon-lined autoclave (PARR: 4760). The reactor had a capacity of 300 ml and could operate at maximum of 350 °C and up to 200 bar pressure. A gas supply inlet was fitted to the reactor for generating an inert atmosphere inside the reactor. The reactor was equipped with band heater for heating to a specified value controlled by temperature control system (Elmatic desktop dual controller). The actual temperature inside the reactor was monitored by K-type thermocouple supplied with the reactor. The pressure inside the reactor was measured by pressure gauge installed at the top of the high-pressure reactor. A safety valve was also fitted to the reactor to release the extra pressure in case of overpressure. Homogeneous mixing of the reaction mixture was provided by an external magnetic stirrer. The setup used in this study is presented in Figure 3.4.

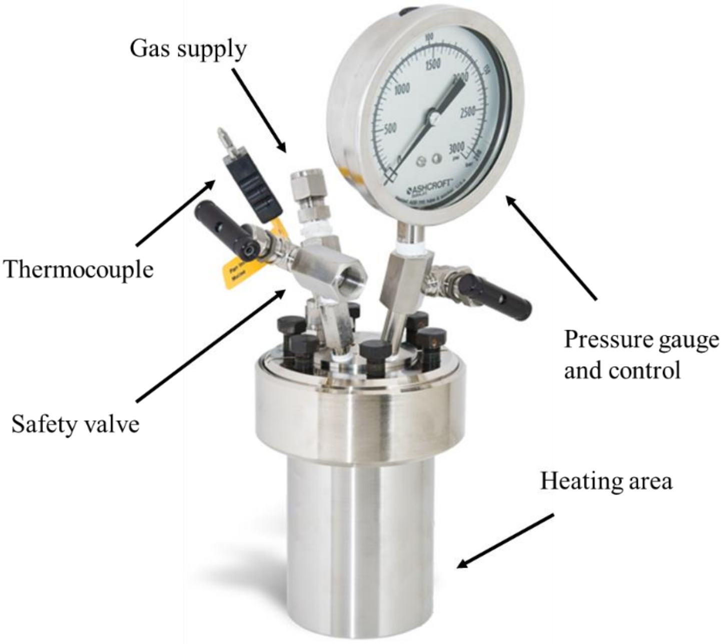

Figure 3.4. High pressure reactor for the hydrothermal carbonisation process.

3.3.3 *Microwave digestion*

Microwave treatment is a simple and efficient heating method since it provides uniform heating, usually at high rates. Owing to the rapid reaction rates, microwave digestion was used for the high yield synthesis of carbon-based materials from biochar. The experimental setup consists of a microwave digestion tank with an ability to operate up to 900 W power. The digestion tank was equipped with an experiment-design control system to setup a unique combination of power and time. The centre of the digestion tank consists of a reactor holder and magnetic stirrer. A two-neck round bottom flask was used for treating the reaction mixture under uniform heating. The top neck of the flask was connected to a water condenser for condensing the volatiles and creating reflux. The side neck of the flask was equipped with a thermocouple for controlling the temperature. The system consisted of a semi-transparent safety glass to visualise the reaction process. The experimental setup for the microwave digestion used in this study is presented in Figure 3.5.

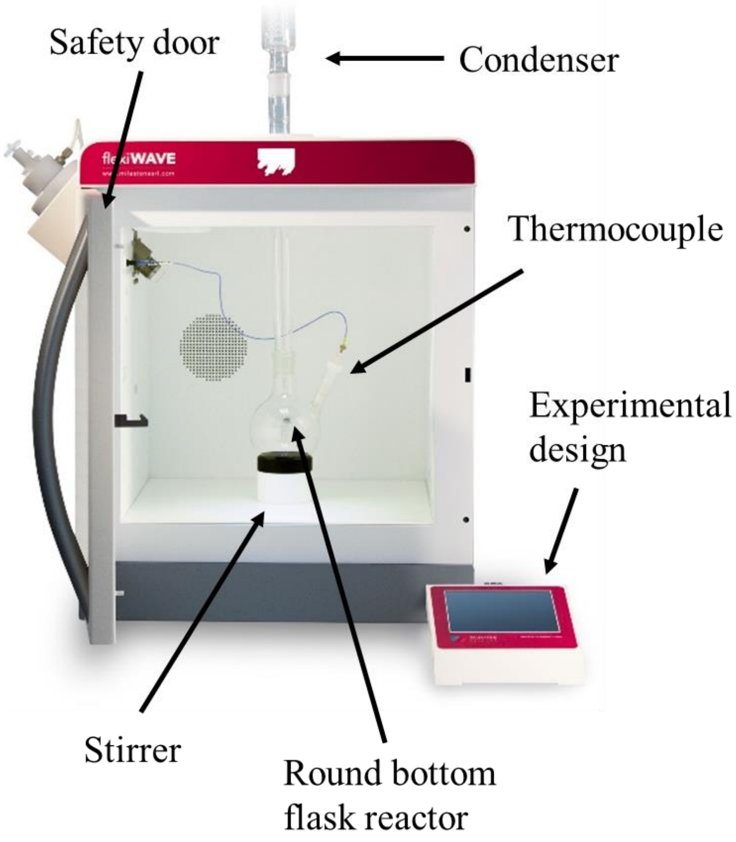

Figure 3.5. Microwave digestion reactor for the rapid microwave treatment of samples.

3.4 Experimental procedures

3.4.1 Synthesis of activated carbon

The activated carbon samples were prepared by impregnation of BC-600 (biochar prepared at 600 °C) with potassium hydroxide followed by activation at high temperature, according to the well-developed approach (Peng *et al.*, 2013). In a typical procedure, about 10 g of BC-600 sample was impregnated overnight (12 h) with a range of KOH ratios (mass ratios of KOH/biochar = 1–5) in 50 ml water. A range of activation ratios was selected to identify the best ratio for activating agent to give a high degree of porosity. The acquired solutions were dried at 110 °C overnight. The dried impregnated samples were loaded into the pyrolysis furnace (VCTF4) and heated to 800 °C at a rate of 5 °C min^{-1} under N_2 flow of 100 ± 5 mL min^{-1}. All the samples were held at 800 °C for 1 h for activation and then cooled down to room temperature naturally. A slow heating rate (5 °C min^{-1}) was chosen to attain well-developed porosity, while a short holding time (1 h) was selected to prevent the growth of micropores. The resultant products were washed with hot DI water (~90 °C) and then boiled in 1 M HCl to remove the impurities and reduce the ash content (Bouleghlimat *et al.*, 2013). The samples were again washed with hot DI water followed by cold DI water until neutral pH was obtained in the filtrate. Finally, the washed samples were dried in an oven at 60 °C overnight and AC products were obtained. The acquired AC samples were denoted at AC-X, where X indicates the activation ratio (1, 2, 3, 4 or 5). For example, AC-2 shows the AC samples acquired at KOH/biochar ratio of 2.

3.4.2 Synthesis of highly pure GQDs by hydrothermal treatment

High quality GQDs were prepared from biomass in a 3-step approach: synthesis of biochar, activation and hydrothermal carbonisation. An effective and simple technique was implemented for the purification of GQDs.

This 3-step approach combines the merits of both ‘bottom up’ and ‘top down’ techniques. The biomass was initially pyrolysed to produce carbonaceous char materials in a “bottom-up” method. These materials were then activated by chemical treatment and hydrothermally treated to reduce the particle size in a “top-down” approach (Figure 3.6). The whole process is easy and potentially scalable. GQDs with controllable properties for promising potential applications can be obtained using this synthetic approach. Moreover, this technique can be applied to a wide range of biomass precursor materials.

Biochar derived from pyrolysis processing was ground and subsequently subjected to activation with strong acids (H_2SO_4 and/or HNO_3) using an ultrasonic system to promote mixing/mass transfer. The strong acids react with basal planes and edges under ultrasonic conditions to incorporate functional groups on the carbon skeleton (Pan *et al.*, 2010). 100 mg of biochar was mixed with an 80 mL mixture of HNO_3 and H_2SO_4 at a volumetric ratio of 3:1 and sonicated (50-60Hz, 750W) for 15 h to ensure significant mixing and activation (Pan *et al.*, 2010). At the end of the process, the biochar was almost completely mixed with the acids to form a dark brown colored suspension. This solution was diluted 3 times with DI water, filtered using a 0.1 µm Polyvinylidene fluoride (PVDF) filtration membrane and washed with DI water to remove the acids. The samples were further washed with hot DI water to remove any excess acids. The complete removal of excess acids was verified by monitoring the pH of the filtrate. The activated biochar collected from the filter was then stored in glass vials for further usage. Activated biochar samples were designated as BC-X-A, where A stands for activated.

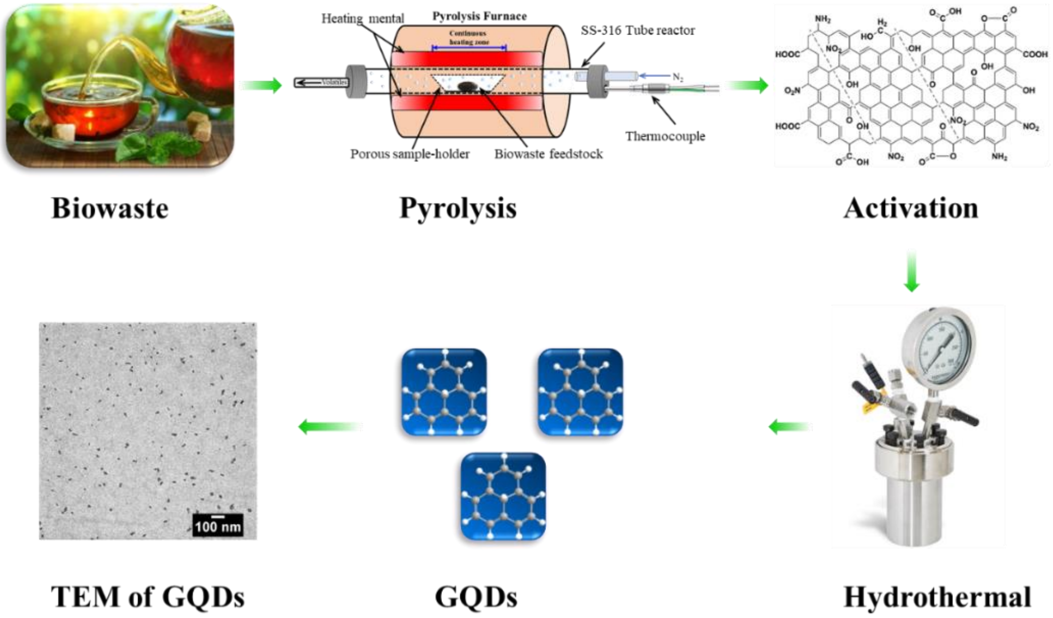

Figure 3.6. The schematic illustration of the synthesis procedure for GQDs via hydrothermal treatment.

Highly pure GQDs were synthesised by hydrothermal treatment of activated biochar in the Teflon-lined autoclave (PARR: 4760). Hot water washed DI activated biochar was used for the preparation of highly pure GQDs. 100 mg of the activated biochar was dispersed in 100 mL of water and the dispersion was then transferred into the 300 mL Teflon-lined Parr reactor. The reactor was heated and maintained at 200 °C for 12 h to ensure the significant reduction in size of carbon domains into nanosized fragments. The reactor was then allowed to cool to room temperature. The resulting brown suspension was filtered through a 100 nm PVDF filtration membrane and GQDs remained in the filtrate showing a pale-yellow color. Previous studies (Zhu *et al.*, 2011a; Li *et al.*, 2012a) reported that the pale yellow color of the solution in visible light is an indication of GQDs formation. The product obtained was further dialysed in a dialysis bag for 1 day to remove any residual impurities. The elimination of a neutralisation process resulted in the generation of no salt. Thus, no external impurities were introduced, and a pure product was obtained. The GQDs samples were designated as BC-X-GQDs, where the X is the pyrolysis temperature of the biochar precursor.

The main mechanism involved in the formation of GQDs under this approach involves a combination of carbonisation, oxidation and nitration with controlled hydrothermal fragmentation that removes the nitro groups in the formation of GQDs. A range of carbonaceous materials with varying microstructures are produced from biomass in a *bottom-up* method and then activated by chemical treatment and hydrothermally cut into GQDs in a *top-down* approach. The aromatic carbon domains are developed from biomass at a higher temperature (500-800 °C) by the rearrangement of carbon lattice in a hexagonal pattern. These aromatic carbon domains are chemically activated and various functional groups are attached on the surface, defect sites and basal planes of carbon matrix. The in-plane epoxy functional groups (C-O-C) attached at the defect sites facilitate the disintegration of carbon domains into nanoscale quantum dots under high temperature and high pressure hydrothermal treatment (Rajender and Giri, 2016). Owing to their zero dimensionality, quantum confinement and surface functionalisation, these quantum dots exhibit bright fluorescence.

3.4.3 Microwave-based high yield synthesis of GQDs as a PL sensor

High yield preparation of GQDs was performed by microwave assisted thermochemical cutting of a carbon rich biochar sample. No activation treatment was involved, and as-prepared biochar was used as the precursor material to produce GQDs. 20 mg of the as-prepared carbon rich sample (BC-500) was added into the reactor containing 10 ml of DI water. About 2 ml of as received HNO_3 was added to the reactor to create an acidic environment for the oxidative cutting of carbon domains. Then the reactor was treated at a microwave power of 100–900 W for 15–180 mins under reflux. Upon the completion of the pre-set duration, the obtained brown dispersion was diluted with 100 ml of DI water and filtered through 0.1 μm PVDF filtration membranes to separate the larger unreacted particles. The obtained pale-yellow filtrate contained the GQDs and hence shows bright luminescence. Figure 3.7 shows a schematic illustration of the synthesis procedure for GQDs.

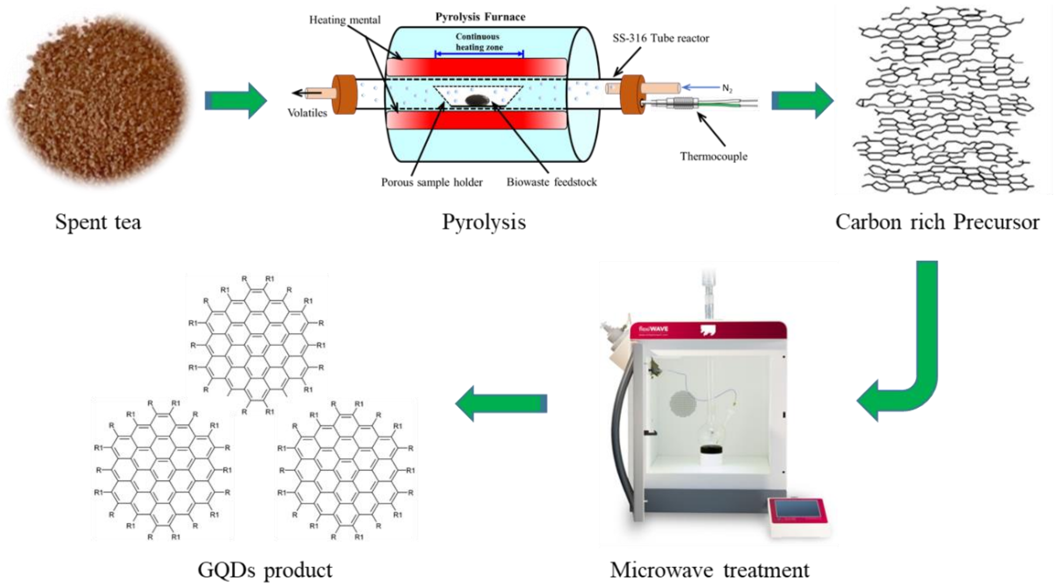

Figure 3.7. The schematic illustration of the synthesis procedure for GQDs via microwave treatment.

The modification of as-prepared GQDs was performed by hydrothermal treatment in water. 20 mg of the as-synthesised GQDs were dispersed in 50 ml DI water and added to the Teflon lined autoclave for hydrothermal treatment. After hydrothermal treatment at 200 °C for 8 h, the dispersion was filtered through a 0.1 µm PVDF filtration membrane and excess water was removed using a rotary evaporator. The obtained concentrated solutions were freeze dried and named as GQDs-X-M, where X indicates the microwave power and M stands for modified form.

The mechanism of microwave treatment combines the chemical activation and hydrothermal disintegration into a single step fast treatment. When a carbonaceous material is subjected to microwave treatment under acidic conditions, the activation of carbon domains takes place with strong acids along with simultaneous disintegration at high temperature. As a result, GQDs are produced in a very short duration and at high yields (Abbas *et al.*, 2020). Among various approaches, microwave treatment is indeed beneficial due to its uniform and rapid heating, thereby leading to extremely short reaction time.

3.4.4 Intensified and sustainable synthesis of GQDs directly from biomass waste

Large scale and sustainable synthesis of GQDs from biomass waste was performed in a single step using two approaches. In first approach, the GQDs were prepared on a gram scale via hydrothermal carbonisation of biochar under mild acidic conditions. In a typical procedure, about 500 mg of as-prepared biochar was dispersed in 50 mL DI water and nearly 2 ml of as-received HNO_3 was added to the reaction mixture to create mild acidic conditions. The reaction mixture was transferred into a 100 mL acid digestion Parr reactor. The reactor was heated to 200 °C and maintained for 12 h. The reactor was then naturally cooled to room temperature. The obtained suspension was filtered through a 0.1 µm PVDF filtration membrane and GQDs were obtained in the filtrate. The obtained solution was freeze dried to acquire GQDs powder.

The second approach was a sustainable synthesis of GQDs directly from biomass via hydrothermal carbonisation. Neither oxidising nor reducing agent was employed and only water was used as hydroxyl scissors to cut the carbon domains into nano-sized fragments at high pressure. 1 g of biomass was dispersed in 100 mL of DI water and transferred into a 300 mL Parr reactor. The reactor was heated at 200-300 °C for 12-24 h, followed by cooling to room temperature. The products obtained at various temperatures and intervals were collected, filtered and freeze dried. The final products were denoted as GQDs-x-y, where x indicates the hydrothermal temperature and y indicates the treatment time. For example, GQDs-200-8 denotes the GQDs prepared at 200 °C for 8 h.

The major mechanism involved in both techniques is the development of aromatic carbon domains from biomass and their cutting into nanoscale entities under high pressure and temperature. The aromatic carbon domains are developed by removal of volatiles and organic components of biomass and rearrangement of carbon matrix into a specific order. The arrangement of carbon matrix into a hexagonal pattern results in the formation of aromatic carbon domains. These carbon domains are not very stable due to inherent presence of functional groups and cut into small pieces due to high temperature and pressure. These nanoparticles demonstrate a few layers graphene structure and exhibit excellent optical properties. The prominent optical properties make them suitable building blocks for a wide range of applications.

3.5 Characterisation techniques

The structure, morphology and properties of the feedstock, biochar, activated carbons and GQDs were studied by wide range of characterisation techniques. The technique used in this study are discussed here.

3.5.1 Morphology characterisation

The surface morphology of the samples was studied by scanning electron microscopy (SEM), while the nanoscale structure was explored by transmission electron microscopy (TEM).

SEM is one of the most versatile techniques to examine the morphological features of the carbon-based samples. SEM provides the knowledge about the morphology, orientation and composition of the samples. The most common working signal of the SEM is based on image generation from secondary electrons. When a sample is bombarded with a beam of focused high energy electrons (5-15 keV), secondary electrons are generated by inelastic interactions with much lower energy (~25 eV). These secondary electrons are then detected by a scintillator/ photomultiplier detector to create an image current. The scanning of the focused electron beam across the sample surface and detection of secondary electrons emitted are correlated, and the variation of image current with position modulates the brightness of the image resulting in a topographical view. In this study, the morphology of the samples was characterised by a high efficiency environmental scanning electron microscope (Philips XL30 FEG-ESEM) fitted with a high brightness filed effect electron gun (FEG) which is suitable for imaging samples with appreciable water content and a high-resolution imaging machine (FESEM, JEOL-7600F) both operating at 5-15 kV. The ESEM was equipped with Energy Dispersive X-ray spectroscopy (EDX, Oxford Xmax80, LN_2 Free). The SEM samples were prepared by dropping char powder on the sample holder containing a sticky carbon tape. The sample holder was placed on sample stage located inside the SEM setup. The samples were monitored with an internal camera to select suitable places to analyse in detail. SEM images were taken at different magnifications for better understanding of the morphology of the material.

TEM is used to study the nanoscale structure of the samples. As indicated by its name, the working of the TEM is based on the formation of an image from transmitted electrons. When a thin sample is subjected to a focused electron beam, many of these electrons are transmitted through the sample but are scattered by its internal structure. An electron source at the top of the microscope emits electrons that travel through a vacuum in the column of the microscope. Electromagnetic lenses are used to focus the electrons into a very thin beam, and this is then directed through the specimen of interest. The electrons passing through the specimen then impact on a detector. Traditional bright field imaging relies on incident electrons being scattered and disappearing from the main beam depending upon the compositional density and crystal orientation of the sample. The intensity of un-scattered electrons gives rise to a "shadow image" of the specimen, with different parts of a specimen displayed in varied darkness according to density. The magnification depends on the extent to which the beam can be focussed at the plane of the sample. The beam can be scanned over the sample to get high resolution analytical information in a scanning transmission electron microscope (STEM). In this work, the microstructure of samples was studied by a TEM fitted with several detectors; FEI Titan3™

Themis 300: X-FEG operating at 300 kV. TEM samples were prepared by drop casting the aqueous suspension of sample on a TEM grid. After letting it settle for ~5 minutes, the excess sample was removed by triangular filter paper followed by mild washing with DI water to remove the impurities, if any. The prepared TEM samples were dried at 60 °C to remove the moisture before use.

Selected area electron diffraction (SAED) patterns are often used to determine the crystal structure and interplanar distances in TEM. However, High Resolution TEM (HRTEM) was used here as the carbon nanoparticles produced are very small (generally <10nm) and poorly crystalline. In this case, the SAED contain just diffuse rings and little structural information. Taking a Fast Fourier Transform (FFT) of a small area of a HRTEM images can generate similar information. This is because the FFT gives the frequency distribution of the pixel intensities in the HRTEM image. Any periodicity observed in the HRTEM image will give spots in the FFT. So, the FFT may be interpreted as a "diffraction pattern" provided the crystalline particles are in the right orientation. Thus, the crystallographic information was obtained from FFT of the HRTEM images.

3.5.2 Atomic force microscopy

Atomic force microscopy (AFM) is a promising technique to study the thickness of graphene and number of graphene layers in graphene derivatives. AFM is a unique approach to distinguish between GQDs and carbon quantum dots. The thickness of GQDs is measured by operating AFM in tapping mode and number of graphene layers are calculated by dividing total thickness by thickness of one graphene layer (3.34 Å).

The working principle of AFM is based on movement of nanoscale sharp tip attached to a cantilever that scans over the sample. This cantilever/tip assembly is also known as a probe. This AFM probe interacts with substrate in raster scanning motion. When the tip is brought in close proximity of the sample, forces between the sample and tip cause the deflection of the cantilever according to Hook’s Law. The cantilever bends as soon as the tip comes near the sample surface, and this bending is detected by a laser diode and a position sensitive photodetector denoted as PSPD. The bending is indicative of tip-sample interaction force. When operating in tapping mode, the cantilever is caused to vibrate near its resonance frequency and as a result the tip moves up and down in a sinusoidal motion. This motion is reduced by attractive or repulsive interactions as the tip comes near the sample and in this way thickness of the sample is measured (Cappella and Dietler, 1999).

3.5.3 *Nitrogen adsorption-desorption analysis*

Nitrogen (N_2) adsorption-desorption analysis was performed to study the total surface area, mesoporous/microporous specific surface area, pore size, pore size distribution, pore volume and specific pore volume of the samples using the Brunauer-Emmett-Teller (BET) method (Brunauer *et al.*, 1938). In this study, BET analysis was performed using a Thermo Scientific Surfer Gas Adsorption Porosimeter. The analysis procedure started with the cleaning, drying and degassing of the empty burette at 120 °C for 30 min. The degassed burette is weighed to get the actual weight under vacuum. The char sample is placed in the burette and degassed at 150–200 °C for 15–24 h. Different degassing time periods were studied to analyse the effect of degassing time on the surface area of the sample. The burette containing the degassed sample was weighed. The actual weight of the degassed sample was calculated by subtracting the weight of empty burette from the weight of burette with sample. The measurement of actual weight was very important for the precise calculation of BET surface area. Finally, the burette was installed into the surfer and the sample was exposed to N_2 gas molecules at variable relative pressure (P/P_o = 0.1–1, where P is the equilibrium pressure and Po is the saturation pressure of the nitrogen adsorbate at 77 K, the boiling point of N_2. As the pressure is increased, N_2 molecules adsorb on the surface of sample. BET theory assumes multilayer adsorption of gas molecules on the surface of a material without interacting chemically with the sample. BET theory (Brunauer *et al.*, 1938) is based on following hypotheses:

1. The N_2 gas molecules adsorb physically over the surface of a material in layers infinitely
2. The N_2 molecules can only interact with the neighboring layers
3. Langmuir theory can be applied to each layer.

The resultant BET equation is:

$$\frac{1}{v[\left(\frac{P_0}{P}\right)-1]} = \frac{c-1}{v_m c}\left(\frac{P}{P_0}\right) + \frac{1}{v_m c} \tag{3.3}$$

where, P is equilibrium pressure and P_0 is the saturation pressure of nitrogen, υ is the quantity of adsorbed gas, υ_m is the quantity of gas adsorbed with monolayer coverage, and c is BET constant.

After the completion of BET analysis, specific surface area, porosity and pore size distribution were calculated using surfer software. The specific surface area (S_{BET}) and total surface area (S_{total}) were determined by BET method using the following equations:

$$S_{total} = \frac{v_m(Ns)}{V} \tag{3.4}$$

$$S_{BET} = \frac{S_{total}}{a} \tag{3.5}$$

Where, v_m is the monolayer adsorbed gas quantity in the units of volume, N is the Avogadro number, s is the adsorption cross section of adsorbing species, V is the volume of adsorbate gas and a is the mass of sample or adsorbent.

The total pore volume was estimated from amount of gas adsorbed at P/Po = 0.99, where all the pores are expected to be filled. This amount of adsorbed gas is converted into liquid volume using the gas/liquid volume ratio which is 647 for N_2 at 77 K. So total pore volume is calculated using the following equation:

$$V_p = \frac{X_a}{V_{g/l}} \tag{3.6}$$

Where, X_a is amount of gas adsorbed, V_p is total pore volume and $V_{g/l}$ is the gas to liquid volume ratio of N_2 at 77 K.

The microporous/mesoporous surface area and volume were acquired using the t-plot method. This method involves estimating the thickness of an adsorbate (N_2) layer as a function of relative pressure. This is generally known as statistical thickness, denoted by symbol t. The t values are calculated using one of these equations: Halsey equation (3.7) (Halsey, 1948) and de Boer equation (3.8) (De Boer *et al.*, 1965).

$$t\ (\text{Å}) = 3.54\left[\frac{5}{2.303\log\left(\frac{P_O}{P}\right)}\right]^{\frac{1}{3}} \tag{3.7}$$

$$t\ (\text{Å}) = \left[\frac{13.99}{0.034 - \log\left(\frac{P}{P_O}\right)}\right]^{\frac{1}{2}} \tag{3.8}$$

The numeral values mentioned in these equations are specifically for N_2 as an adsorbate. The procedure for determination of micropore volume and surface area using t-plot method is the same as BET method. Generally, for carbon black and related materials, relative pressure range is selected as $0.2 < P/P_o < 0.5$. Then, the adsorption capacity ([STP]/g) is plotted as ordinate against thickness t (nm) as abscissa and a straight line is generated. The intercept and slop of the straight line are interpreted as micropore volume and external surface area using following equations:

$$V_{MP} = i \times 0.001547\ (\text{cm}^3) \tag{3.9}$$

$$S_t\ (\text{m}^2/\text{g}) = 15.47 \times s \tag{3.10}$$

Where, i is the intercept (cm^3[STP]/g), s is the slope of straight line fitted to t-plot and 15.47 is the conversion factor of gas to liquid volume.

In this study, QuadraWin software was used for the t-plot method calculations.

Pore size distribution was determined from desorption data using density functional theory (DFT) (Bardestani *et al.*, 2019).

3.5.4 XRD analysis

X-ray diffraction (XRD) is a non-destructive analytical technique used to determine the crystal structure of a sample. The XRD principle can be better understood from Bragg's Law. When an X-ray beam impinges on the sample it interacts with the crystal planes of the material that are suitably oriented with the beam. The incident X-rays can be reflected with a wavelength that depends on the interplanar distance (d) of the crystal and at an angle equal to the incidence angle. The diffracted X-rays cause the constructive interference when the path difference of the reflected beam is equal to an integer multiple of its wavelength ($2d\sin\theta = n\lambda$), that is when Bragg's Law is satisfied. A detector scanning the diffracted beams will pick up a "Bragg reflection" at this angle. The position of these reflections gives us the interlayer spacing of atoms in the crystal structure. The peak intensities of these reflections tell us how much of a specific phase is present in the sample. Variations on the x-ray diffraction technique can give the position of atoms in a crystal, their order-disorder, chemical bonding and much other information. The properties of the analysed substance can be related back with the arrangement of atoms in its crystal structure.

In this study, the crystallographic examination of the samples was performed on a powder X-Ray diffractometer (XRD, Bruker D8 Advance) using Cu K_α radiation (λ = 1.5418 Å). The XRD pattern of the samples was recorded by scanning the sample at an angle to the incident beam (which is twice the diffraction angle, θ) of 10–90°.

3.5.5 Raman spectroscopy

Raman spectroscopy is one of the most versatile techniques to study the structure of carbonaceous samples. Raman spectroscopy is based on the inelastic scattering of the incident photons. When a monochromatic light is incident on a sample, the resultant energy of the photons in shifted up or down. This shift in the energy gives information about the vibrational modes of the molecules in the sample and hence the chemical bonds within it. In this study, Raman spectra were obtained through a Renishaw Plus Raman spectrometer using 514 nm laser excitation. Raman samples were prepared in situ and placed on a glass substrate (20 mm x 60 mm). The glass substrate was installed on the sample stage for detection of photon emission. The data collection settings were optimised as follows: 532 nm laser, 455mW (95% power at source, 5% at filter). The optimised acquisitions were for 10 sec with 10 accumulations, the objective was at 10x and aperture was set at 200 µm. The spectra were measured with a resolution of 2 cm^{-1}.

3.5.6 Fourier transform infrared spectroscopy

Fourier transform infrared (FTIR) spectroscopy is a complimentary technique to Raman spectroscopy and was used to study the surface functional groups of the sample. The FTIR spectrum is generated based on the vibrational or rotational motions of molecules. When a sample is subjected to infrared radiations of continuous frequency, certain frequencies are absorbed by the molecules based on their vibrational or rotational modes. Consequently, the spectra are recorded for transmitted frequencies against the wave number. The surface functional moieties are identified by the absorbed frequencies at a specific wavenumber since each molecule absorb frequencies at a certain wavenumber. Whereas Raman spectroscopy is sensitive to the vibrations of centrosymmetric molecules, FTIR is most useful in the absence of such symmetry.

In this study, the FTIR spectra were recorded with the help of Bio-Rad FTIR spectrometer (Cary 630 FTIR, Agilent Technologies) using a Diamond ATR.KBr tip. Spectra of the samples were collected over the range of 650-4000 cm^{-1}. The system was initiated with the collection of 265-scans of background for air and water vapours followed by recording the spectra of desired samples. After cleaning the sample stage and collecting the background spectra, solid/liquid samples were placed on sample stage and characterised. The spectra were obtained with a resolution of 4 cm^{-1}.

3.5.7 XPS analysis

X-ray photoelectron spectroscopy (XPS) provides quantitative information about the electronic structure, composition, and oxidation state of the top surface (~10 nm) of a material. In the XPS process, when a sample is irradiated by X-rays, inner shell electrons are emitted. The binding energy of the emitted electrons to their atoms is determined by the difference in the energy of incident X-rays and the emitted electrons. The spectrum is obtained by determining the quantity of electrons emitted over a rage of binding energies. The elements involved are then determined by the electrons emitted at a specific energy.

In this study, the Surface elemental composition was analysed by X-ray photoelectron spectroscopy (XPS) on a Thermo Fisher Scientific NEXSA spectrometer. Samples were analysed using a micro focused monochromatic Al x-ray source (72 W) over an area of approximately 400 µm. Data were recorded at pass energies of 200 eV for survey scans and 50 eV for high resolution scans with 1 eV and 0.1 eV step sizes, respectively. Charge neutralisation of the sample was achieved using a combination of both low energy electrons and argon ions. High resolution XPS spectra were also obtained for each element and all the peaks were fitted to their possible structure using Gaussian-Lorentzian model with the help of CASA XPS software.

3.5.8 Optical properties analysis

Optical properties of the samples were evaluated by studying their ultraviolet and visible (UV-vis) absorbance and photoluminescence characteristics. The UV-vis spectroscopy is the quantitative measurement of the absorption of light by a material. In the analysis process, a sample is scanned by an incident light of a continual changing wavelength (in the UV or visible range) and the sample absorbs light of a specific wavelength. The amount of light that passes through the sample is measured with respect to the intensity of light through a reference sample. Incident light may generate fluorescent light emitted in a different direction and a detector may be positioned to capture thus in a fluorimeter. In this study, the absorption spectra were recorded on a Shimadzu UV-1800 spectrophotometer, while the fluorescence measurements were performed on Shimadzu RF-6000 Spectro fluorophotometer. The spectra were measured with a resolution of 1 nm^{-1}.

3.5.9 Photoluminescence sensing

A photoluminescence sensor was developed with high selectivity and sensitivity. GQDs were employed as a fluorescence probe for the detection of ferric ions (Fe^{3+}) in aqueous media. The sensing of Fe^{3+} was performed at 340 nm excitation using normal quartz cuvette. The fluorescence spectra were measured using the mixture of GQDs and metal ions. In order to evaluate the selectivity of GQDs towards Fe^{3+} sensing, following fourteen different metal ions were selected: Ag^{1+}, Al^{3+}, Ca^{2+}, Co^{2+}, Cr^{3+}, Cu^{2+}, Mg^{2+}, Mn^{2+}, Mo^{2+}, Fe^{3+}, Sr^{2+}, Zn^{2+}, Na^{1+}, Li^{1+}. The concentration of GQDs was kept constant and 50 μM of each metal ion was added. After mixing for 2 min, the fluorescence spectra were measured. The quantitative measurement of Fe^{3+} was carried out by preparing a series of $FeCl_3$ and GQDs solutions, in which the concentration of GQDs was kept constant but the concentration of Fe^{3+} varied from 0 to 50 μM. The fluorescence intensities of these solutions were recorded using fluorescence spectrophotometer. A linear plot was obtained for fluorescence intensity verses Fe^{3+} concentration.

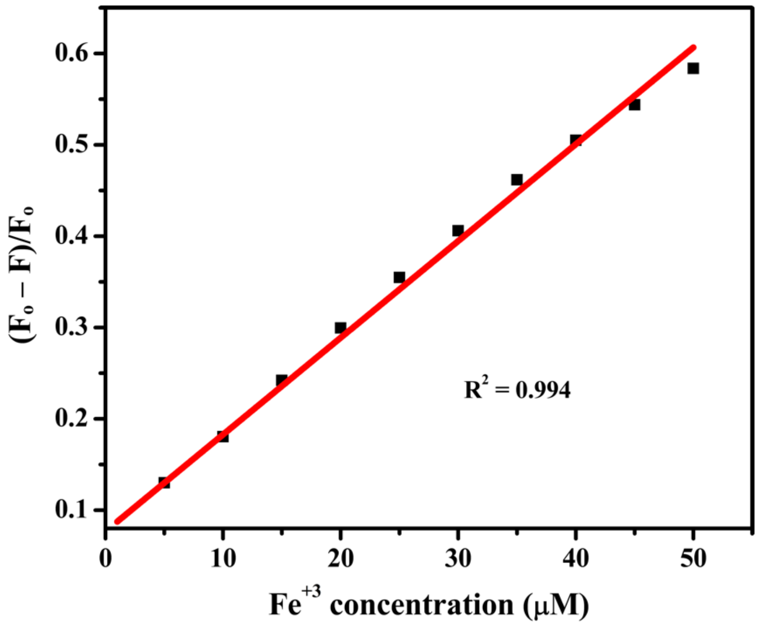

Figure 3.8. Linear plot of fluorescence intensity verses Fe^{3+} concentration at a range of 0-50 μM.

3.6 Electrochemical measurements

3.6.1 Electrode preparation

The electrodes for electrochemical measurements were prepared by mixing AC (90 wt%) and PVDF (10 wt%) in NMP solution by stirring overnight in a small glass vial. The homogeneous slurry was coated onto the surface of graphite plates and a working electrode was prepared with an area of 1 cm^2. The amount of slurry loaded onto the surface of graphite plate was 30 µL cm^{-2}. The working electrodes for the static cell were also prepared in a similar manner but with an area of 4 cm^2 (2 cm x 2 cm). A coating on the exact working area was obtained using a masking technique. The coated electrodes were dried in oven overnight at 60 °C. The coating thickness was measured to be ~0.3 mm.

3.6.2 Cell assembly

The performance of as-prepared AC was evaluated in a static cell. The arrangement of static cell components was made as reported previously (Maharjan *et al.*, 2017) and similar to commercially available VRB batteries. The PAN based graphite felt was cut in pieces with size similar to the working electrode (4 cm^2) and immersed in 1.6 M $V^{+3.5}$ (50/50 mixture of V^{3+} and V^{4+}) solution to fill with the electrolyte.

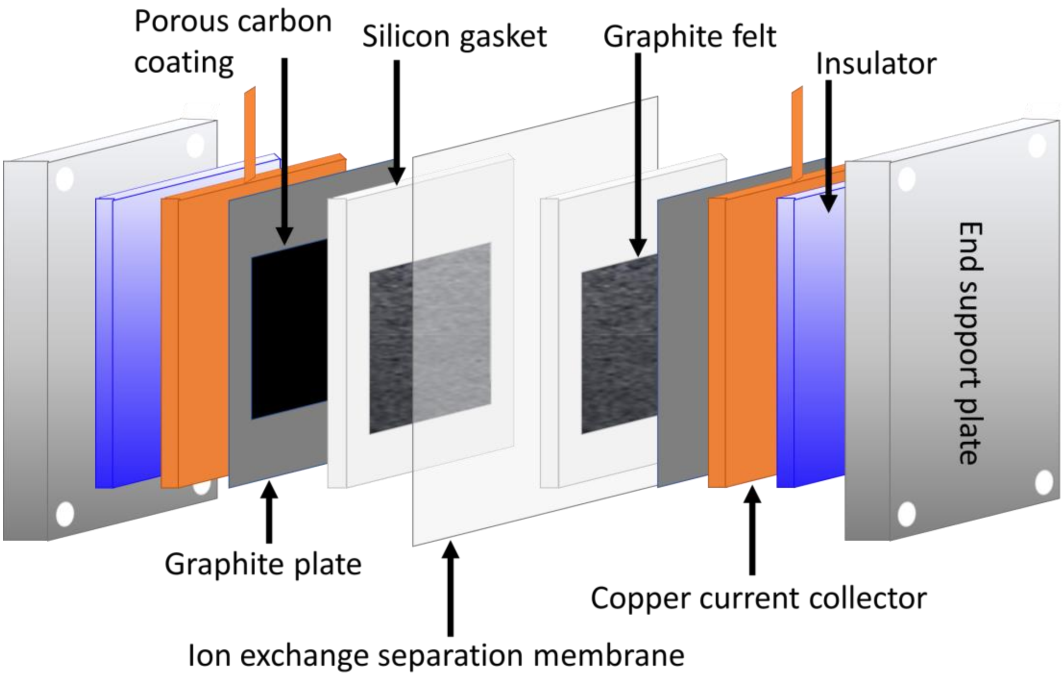

Figure 3.9. Schematic representation of the static cell assembly used in this study.

Each half cell consisted of a coated graphite plate placed in between the porous graphite felt and copper plate current collector. The copper plate was followed by an insulator and an end steel plate as a support. The two half cells were separated by an ion exchange membrane. The end support plates were bolted and tightened to avoid any leakage of electrolyte. A schematic illustration of cell assembly is presented in Figure 3.9.

In this study, the cells were prepared with high care and equal amount of electrolyte was loaded onto each of the half-cells. The cells were assembled by maintaining an equal amount of compression on all sides and all cells. After compression, the thickness of graphite felt was reduced to ~3.00 mm and the thickness of the coating on graphite plate was ~0.3 mm, accounting for 10% of the total thickness. In all the tests, the same graphite felts, plates, membranes and electrolytes were employed.

3.6.3 Electrochemical performance study

The electrochemical performance of the samples was evaluated by cyclic voltammetry (CV) and electrochemical impedance spectroscopy (EIS). A three-electrode cell design (Figure 3.10) was employed for CV and EIS measurements where a platinum sheet and a saturated calomel electrode (SCE) served as counter and reference electrodes, respectively. The pristine and coated graphite plates were used as working electrodes.

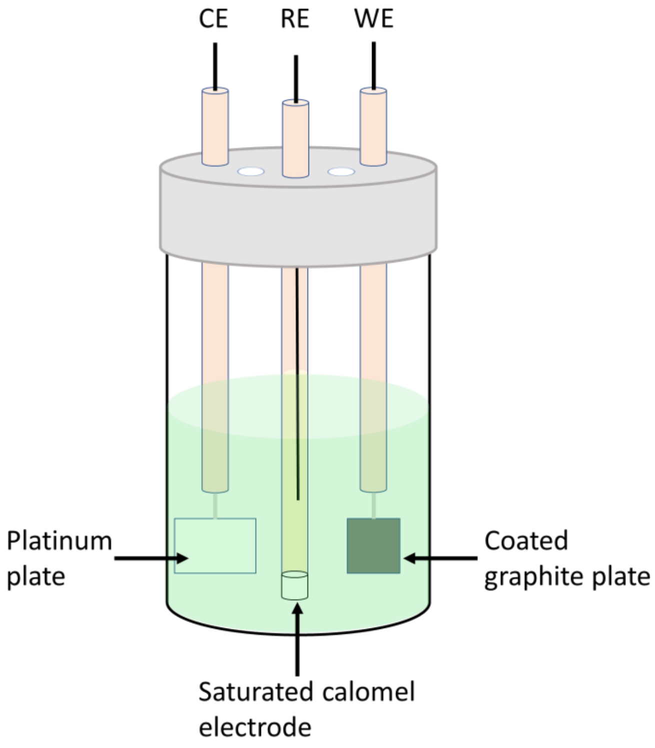

Figure 3.10. Schematic depiction of the three-electrode setup for CV and EIS measurements.

All the electrochemical measurements were carried out in 1.6 M $V^{3.5+}$ in 4.5 M total sulphate solution. The CV measurements were performed over a scan window of –0.8 V to 1.6 V at different scan rates. The EIS measurements were carried out at open circuit potential at 50% state of charge in $V^{2.5+}$ (negative) and $V^{4.5+}$ (positive) electrolytes at a frequency range of 100 kHz to 100 mHz with an amplitude of 10 mV.

The performance of the static cell was evaluated by charge-discharge cycles in a battery testing system (NEWARE, China). The charge-discharge cycles were performed at current densities of 5, 10 and 20 mA cm^{-2} in the potential window of 1.1 to 1.6 V. The energy efficiency, columbic efficiency and voltage efficiency were calculated from charge-discharge results of the static cells, as follows.

$$EE = \frac{Discharge\ energy}{Charge\ energy} \times 100 = \frac{\int V_d I_d\, dt}{\int V_c I_c\, dt} \times 100 \tag{3.11}$$

$$CE = \frac{Discharge\ capacity}{Charge\ capacity} \times 100 = \frac{\int I_d\, dt}{\int I_c\, dt} \times 100 \tag{3.12}$$

$$VE = \frac{Average\ discharge\ voltage}{Average\ charge\ voltage} \times 100 = \frac{EE}{CE} \times 100 \tag{3.13}$$

where, V_d and V_c are discharging and charging voltages and I_d and I_c are discharging and charging currents, respectively.

Chapter 4 Effect of electrode porosity on the performance of vanadium redox flow battery

4.1 Introduction

The vanadium redox flow battery (VRB) has attracted enormous attention as a large-scale energy storage system owing to its long life, stable capacity and high safety. The electrode porosity plays a crucial role in the performance of VRBs. This chapter discusses the effect of electrode porosity on the electrocatalytic activity and charge transfer in VRB using biomass derived porous carbon as electrode material. The electrode porous microstructure is systematically modified, and specific surface area is enhanced from ~10 to ~2085 $m^2 g^{-1}$, with microporosity up to ~1930 $m^2 g^{-1}$. The electrochemical performance of modified electrodes is comprehensively investigated by cyclic voltammetry, impedance spectroscopy and galvanostatic charge/discharge studies. The modified electrode with high a degree of porosity improves the charge transfer process and exhibits lower charge transfer resistance with higher electrocatalytic activity for vanadium redox reactions. Moreover, the VRB static cell performance demonstrates superior energy, voltage and Coulombic efficiencies for modified electrodes than the pristine graphite electrode at all tested current densities. The results suggest that the tailored porosity substantially influences the charge migration and significantly improves the VRB performance.

This is the first study that investigates the effect of electrode porous microstructure on the catalytic activity, charge transfer and performance of VRB system using biomass derived carbon. The lab-synthesised porous electrodes demonstrate superior performance to the commercially available graphite electrodes, which suggests their promise as a cost effective, sustainable and high-performance alternate electrode material for future VRB applications.

4.2 Morphology and structure analysis

Activation of biomass with KOH is highly effective and widely used approach to produce ACs with enhanced degree of porosity and improved electrochemical performance (Cui *et al.*, 2017). The underlying mechanism of KOH activation has been proposed in the literature (Lillo-Ródenas *et al.*, 2003; Raymundo-Pinero *et al.*, 2005; He *et al.*, 2010; Wang and Kaskel, 2012; Wang *et al.*, 2020), and described in section 2.2.2.

Significant weight loss occurred during the activation process and the yields of as-prepared ACs were around 60 % of the original biochar. Owing to the considerable weight loss, the generation of abundant nanoscale pores can be expected.

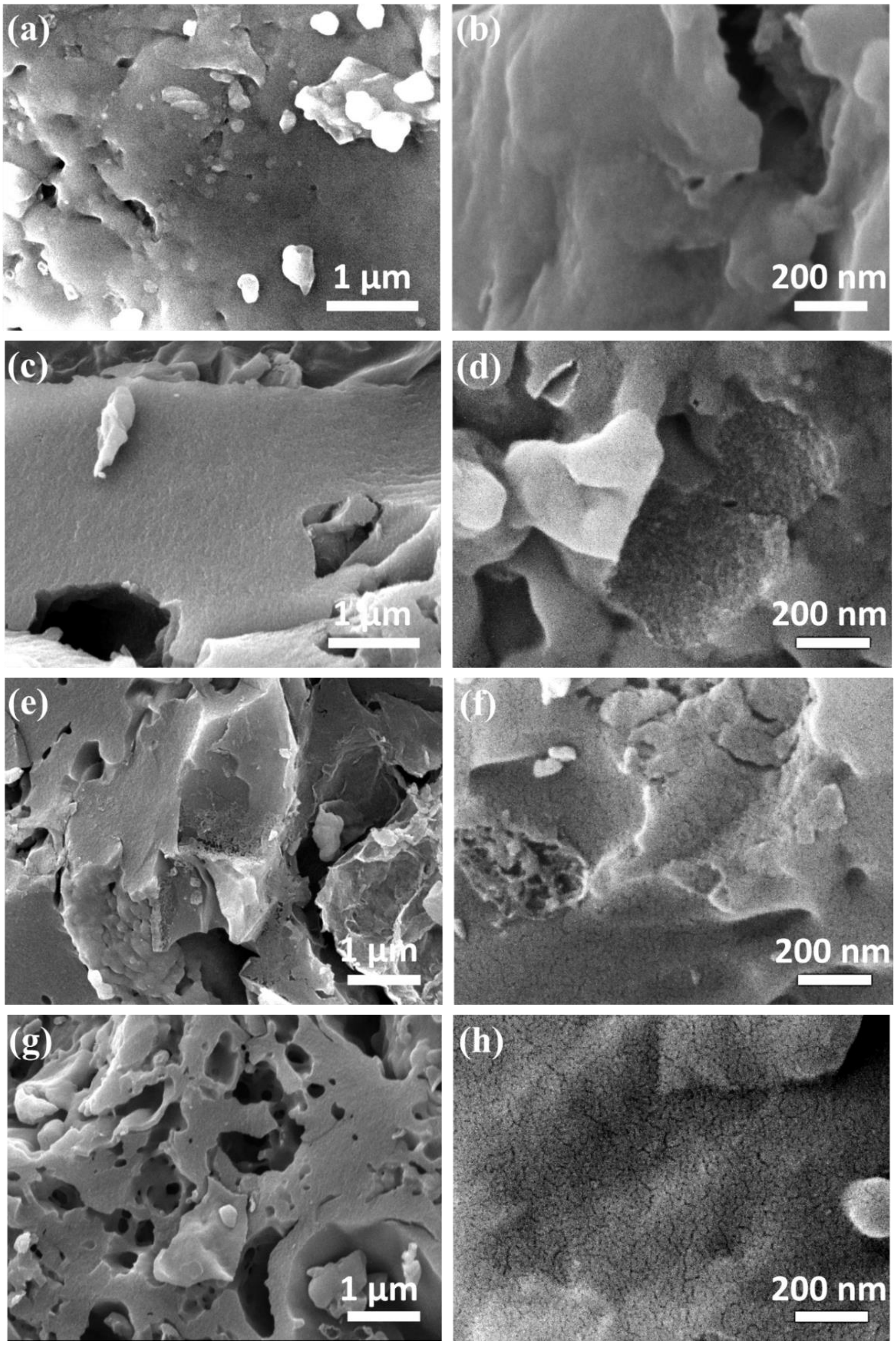

Figure 4.1. SEM images of (a, b) biochar showing flat nonporous morphology, (c, d) AC-2, (e, f) AC-3, and (g, h) AC-4 demonstrating well established microporous structure.

The morphological characteristics of the spent tea derived ACs were studied by SEM analysis. Figure 4.1shows the SEM images of biochar and three type of AC samples prepared at different activation ratios. The SEM images of biochar (Figure 4.1a, b) show a flat morphology without any noticeable porous structure. In contrast, the samples obtained after the activation show significant porous morphology with enhanced degree of microporosity (Figure 4.1c-h). The low magnification images (Figure 4.1c, e, g) indicate the presence of a small number of macropores. Interestingly, as the activation ratio increased, more macropores were formed in AC-4 (Figure 4.1g). These macroporous channels facilitate the electrolyte ions' transport into the interior mesopores and micropores (Wu *et al.*, 2019).

The microporous structure of the as-prepared carbon materials was further studied by high magnification SEM analysis. The high magnification SEM images (Figure 4.1d, f, h) indicate the generation of substantial micropores in the carbon matrix. Moreover, this microporosity increased with increase in activation ratio. Therefore, AC-2 has the lowest level of porosity and AC-4 has the highest level of porosity. In addition, a smooth surface morphology with uniform porosity is observed for AC-4. The increasing porosity leads to higher specific surface area. The substantial porous network helps in electrolyte transport (Wang *et al.*, 2012b) and high surface area offers excessive sites across the electrode/electrolyte interface (Maharjan *et al.*, 2017).

To ascertain the highly porous structure and increasing level of porosity in ACs, surface area measurements were performed. Nitrogen (N_2) adsorption-desorption studies were performed to study the specific surface area and pore structure of biochar and AC samples. The isotherm of biochar is shown in Figure 4.2, which indicates almost no adsorption at low relative pressure ($P/Po < 0.3$), suggesting the absence of micropores. Meanwhile, a minute rise in the isotherm curve at high relative pressure shows the presence of some macropores (Wu *et al.*, 2019). The specific surface area of biochar was calculated to be ~10 $m^2\ g^{-1}$. Such a low surface area of biochar is attributed to its non-porous nature (Lee *et al.*, 2013b), consistent with the SEM analysis.

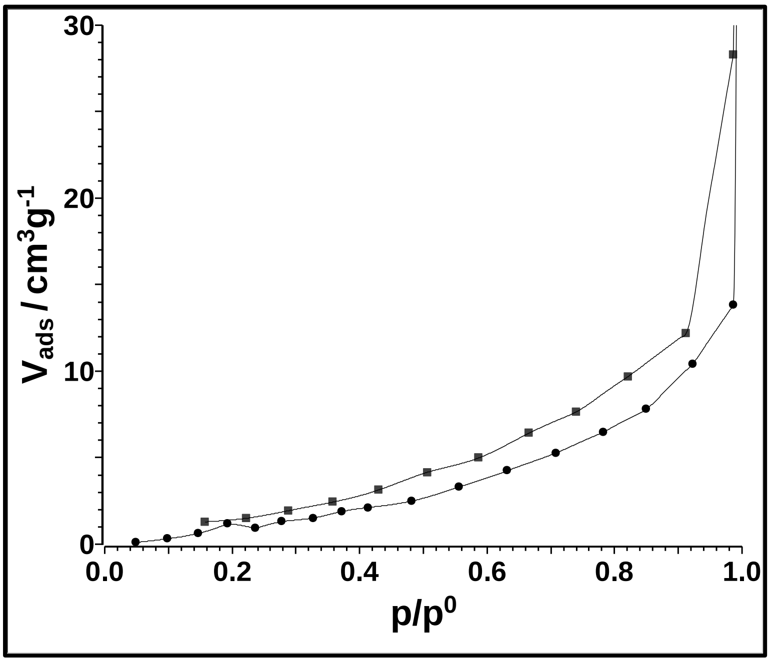

Figure 4.2. Nitrogen adsorption-desorption isotherms of biochar prepared by pyrolysis treatment at 600 °C.

The N_2 adsorption-desorption isotherm of the AC-2, AC-3 and AC-4 are presented in Figure 4.3(a-c). According to IUPAC classification (Sing, 1985), all three types of ACs exhibit type IV isotherms and H4 hysteresis loop. According to IUPAC, the H4 hysteresis is associated with narrow slit-like pores (Sing, 1985). The isotherm curves indicate that major N_2 adsorption takes place at relative pressure (P/Po) less than 0.3. A substantial sharp rise in the N_2 adsorption-desorption isotherm at low relative pressure (P/Po < 0.05) suggests the presence of abundant micropores in all ACs. An obvious hysteresis loop at medium relative pressure (P/Po = 0.5 – 0.8) in AC-2 indicate the existence of abundant mesopores. On the other hand, a horizontal adsorption plateau observed in AC-3 and AC-4 at medium relative pressure (P/Po = 0.4 – 0.8) suggest the dominance of micropores. There still may exist some mesopores because of the small hysteresis and little deviation of curves from almost horizontal plateau.

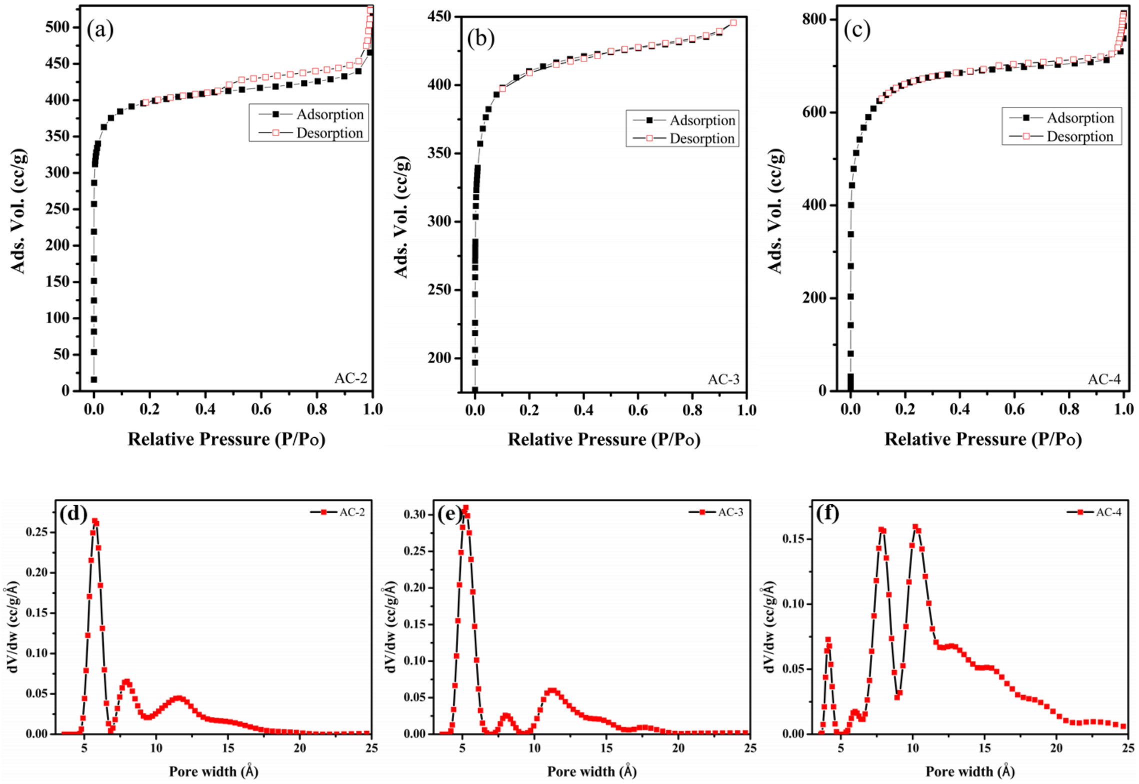

Figure 4.3. (a-c) Nitrogen adsorption-desorption isotherms and (d-f) pore size distributions of AC-2, (a, d) AC-3 (b, e) and AC-4 (c, f).

The high relative pressure area (P/Po = 0.97 – 1.0) consists of a quite pronounced hysteresis loop which implies the formation of extensive pores and widening of existing pores during activation process (Peng *et al.*, 2013; Maharjan *et al.*, 2017; Wu *et al.*, 2019). The specific surface areas of ACs were calculated using the standard BET method. The pores size distribution of these carbon materials calculated by density functional theory (DFT) model are presented in Figure 4.3(d-f). The distribution curves clearly demonstrate the dominance of micropores (d < 20 Å) in all the samples. It is apparent that KOH activation can generate abundant nanoscale pores. The specific surface area, total pore volume and pore structure parameters are summarised in Table 4.1. With increase in the activation ratio, the specific surface area and pore volume increased significantly due to increase of activation. The specific surface areas of AC-2, AC-3 and AC-4 were determined to be 1260, 1610 and 2085 m^2 g^{-1}, and total pore volumes were calculated to be ~0.8, 0.69 and 1.17 cm^3 g^{-1}. These results indicate that the activation ratio is the major factor affecting the surface area and pore volume of ACs. Among all samples, AC-4 exhibit largest specific surface area, abundant micropores and highest total pore volume, which is attributed to the highest activation ratio. These results are consistent with the SEM studies, where AC-4 shows the extensive porous structure consisting of micropores.

Table 4.1. The BET surface area and pore structure parameters of AC-2, AC-3 and AC-4.

Sample	**BET surface area (m^2 g^{-1})**	**Micropore surface area (m^2 g^{-1})**	**Mesopore surface area (m^2 g^{-1})**	**Total pore volume (cm^3 g^{-1})**	**Micropore volume (cm^3 g^{-1})**	**Mesopore volume (cm^3 g^{-1})**
AC-2	1260	1136	124	0.805	0.563	0.242
AC-3	1610	1484	126	0.69	0.58	0.11
AC-4	2085	1930	155	1.174	0.97	0.204

The total surface area was determined by BET method. The total pore volume was estimated from the amount adsorbed at P/Po = 0.99, where all the pores are expected to be filled. The microporous/mesoporous surface area and volume were acquired from the t-plot method.

The structural features of the as-prepared ACs were further studied by XRD and Raman analysis. The XRD patterns of as-synthesised ACs are presented in Figure 4.4a. All the samples exhibit a broad diffraction peak at 2θ value of ~43° corresponding to the (100) plane of carbon (Vázquez-Santos *et al.*, 2012). The broad nature of the bands observed suggest the formation of an amorphous or nanocrystalline carbon structure (Chu and Li, 2006). Considerable intensity of the low-angle scattering in all the samples indicates a high density of pores (Zhu *et al.*, 2011b).

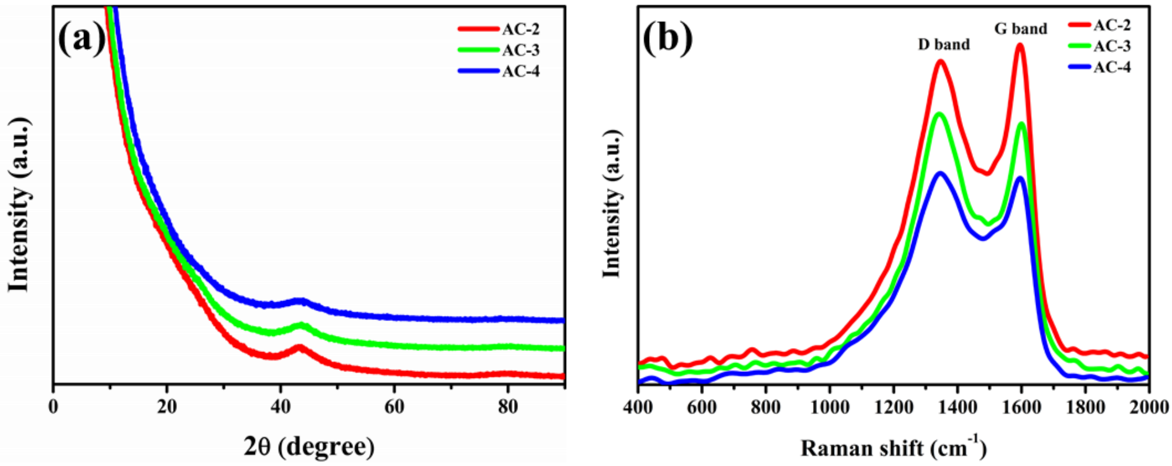

Figure 4.4. (a) XRD and (b) smoothed Raman spectra of AC-2, AC-3 and AC-4.

Figure 4.4b shows the Raman spectra of the as-prepared ACs, displaying two broad bands at ~1346 and ~1597 cm^{-1} designated as the D (disorder) and G (graphite/crystalline) bands, respectively. The D band is related to the disorder and defects in the carbonaceous structures, while the G band is due to E_{2g} vibrations of graphitic material (Tuinstra and Koenig, 1970;

Ferrari and Basko, 2013). The intensity ratio of D and G bands (I_D/I_G) indicates the degree of graphitic ordering in the carbon structure. The I_D/I_G ratio of AC-2, AC-3 and AC-4 were calculated to be 0.97,1.03, 1.01, respectively. All these values indicate a high density of defects/disorder related to the amorphous or semi graphitic carbon (Schwan *et al.*, 1996; Ferrari and Robertson, 2000). According to XRD and Raman analysis, it is suggested that as-prepared ACs exhibit relatively low degree of order.

The qualitative identification of the surface functional groups of the as-prepared ACs was performed by FTIR analysis. The Figure 4.5 shows that the spectra of all the AC samples are very similar and indicate the presence of oxygenated functional groups. The functionalised surface of ACs implies that the chemical activation treatment and acidic washing introduced active species on the surface (Bouleghlimat *et al.*, 2013). The oxygen containing functional groups on the surface of porous carbon materials are beneficial for the electrochemical activity (Park *et al.*, 2014).

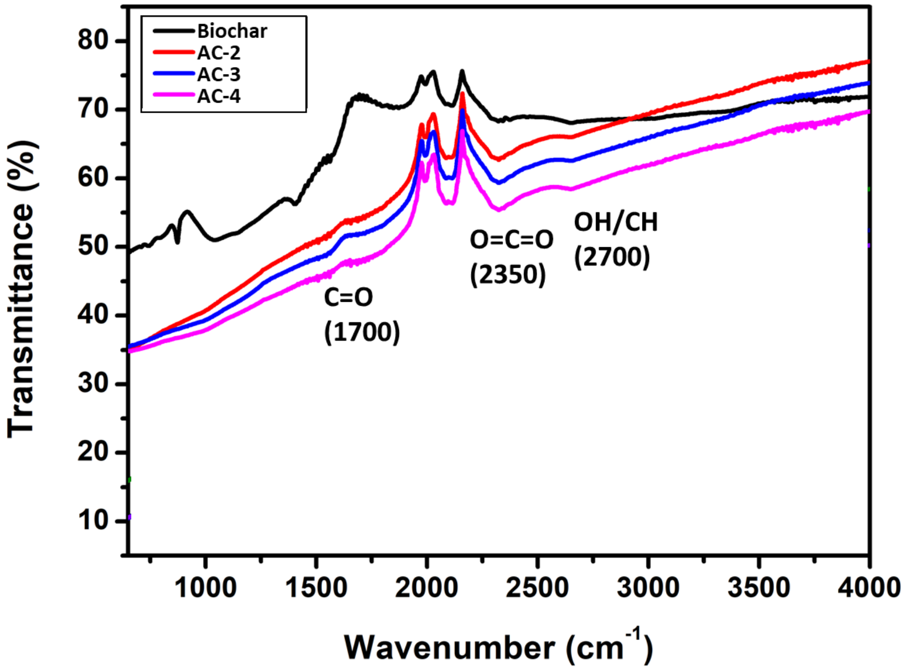

Figure 4.5. FTIR spectra of biomass derived biochar, AC-2, AC-3, and AC-4 samples.

The surface elemental composition of the ACs were further studied by XPS analysis. Figure 4.6 shows the XPS spectra of ACs and their corresponding high resolution C1s and O1s spectra. The survey XPS spectra (Figure 4.6 a, d, g) of ACs exhibit two main peaks at ~285.4 eV and ~533.4eV, which are assigned to C1s and O1s, respectively. Another small peak at ~399.4eV is attributed to the traces of nitrogen. This confirms that all the samples are composed of C, N and O elements. The contents of C, O and N elements derived from XPS analysis are compared with their bulk elemental analysis (Table 4.2).

Table 4.2. The comparison of the elemental composition determined by XPS analysis and ultimate analysis of AC-2, AC-3 and AC-4.

	AC-2	**AC-3**	**AC-4**
XPS elemental analysis (at. %)			
C	92.66	83.78	87.33
N	0.02	0.34	0.35
O	7.32	15.89	12.32
Ultimate analysis (dry basis, wt.%)			
C	88.11	76.56	79.54
H	0.84	1.61	1.15
N	1.25	0.95	1.33
O*	9.8	20.88	17.98

*Calculated by difference

The outcomes of both analyses are quite similar and demonstrate a rise in oxygen and nitrogen contents with increase in the activation ratio. These oxygen and nitrogen species are known to introduce defects in graphitic structure, resulting in improvement of electrocatalytic activity (Jin *et al.*, 2013; Park *et al.*, 2014). The high resolution C1s spectrum (Figure 4.6b, e, h) consist of three major peaks associated with the bonding of carbon atoms with carbon and oxygen atoms. The peaks at 284.75, 286.9, and 289.5 eV are related to C-C/C=C, C-O-C and C=O, respectively (Nakayama *et al.*, 1990; Park *et al.*, 2014). The peak at 291.8eV is attributed to π-π* bonding (Maharjan *et al.*, 2017). The sp^3 alignment of bonds generates σ–σ* bands while sp^2 sites form π-π* bands, indicating the sp^2 dominant structure of the samples (Maharjan *et al.*, 2017).

The high resolution O1s spectrum (Figure 4.6c, f, i) can be deconvoluted into three components, suggesting that oxygen atom exist in three distinct bonding types in the carbon structure. The peaks at 531.5, 533, and 536 eV can be attributed to C=O carbonyl groups, C-O-C ether groups (or C-OH phenol groups) and chemisorbed oxygen groups (COOH carboxylic groups or water), respectively (Oh *et al.*, 2014). These results indicate the incorporation of abundant oxygenated functional groups on the surface of ACs, which act as active sites for vanadium redox couples and improve electrochemical performance (Park *et al.*, 2014). Moreover, these oxygen functional groups have been known to facilitate the charge transfer by increasing the hydrophilicity (Sun and Skyllas-Kazacos, 1992; Rui *et al.*, 2013).

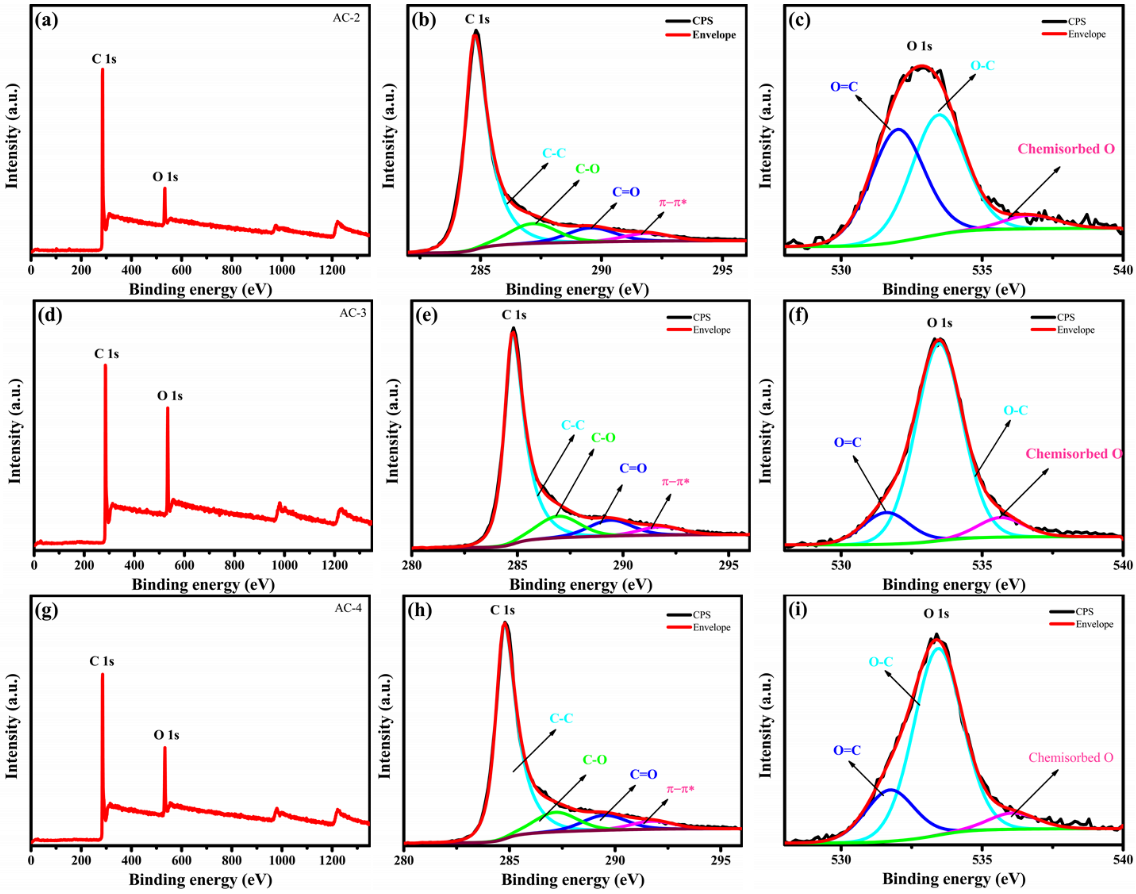

Figure 4.6. Survey XPS spectra showing the C and O elements, high resolution C1s spectra indicating the presence of C-C, C-O and C=O groups, and high resolution O1s spectra displaying C=O, C-O and COOH groups in (a-c) AC-2, (d-f) AC-3 and (g-i) AC-4, respectively. (CPS represent the original data and envelop is the fitted data).

4.3 Electrochemical performance

4.3.1 Battery operation

The electrochemical performance of the VRB can be monitored and tailored by understanding their reactions kinetics. The chemistry and operation of VRBs has been discussed in section 2.2.3. As discussed earlier, an ideal electrode with optimised degree of meso- and microporosity, good hydrophilicity and high electrocatalytic activity should facilitate the VRB redox reactions with good reversibility. To this end, a series of advanced carbon electrodes with well-defined structures are designed (Figure 4.7).

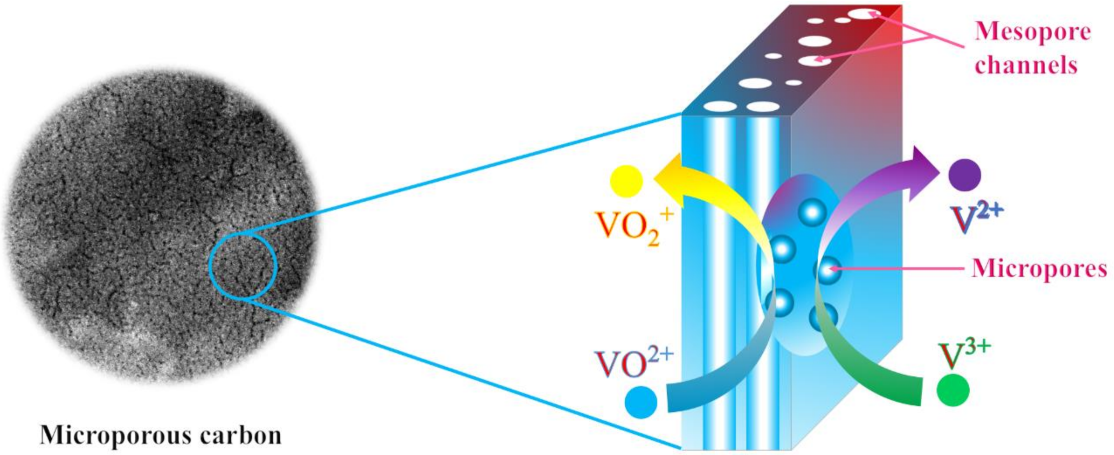

Figure 4.7. Schematic illustration of the meso- and micro-porous structure of carbon electrode facilitating the vanadium redox reactions.

4.3.2 Electrochemical analysis

In order to study the effect of porosity on charge transfer in VRB, the electrochemical performance of as-prepared carbon samples was evaluated by CV, EIS and charge-discharge studies. Figure 4.8a represents the CV curves for AC-2, AC-3, and AC-4 coated graphite plate electrodes at a scan rate of 5 mV s^{-1} in 1.6 M $V^{3.5+}$ electrolyte solution. All three type of electrodes demonstrate two obvious redox couples: V^{5+}/V^{4+} and V^{2+}/V^{3+} at positive and negative potentials, respectively. An outstanding electrochemical reversibility of both redox couples is clearly noticeable for all the electrodes, which indicates the prominent potential of all ACs for VRB and is consistent with the previous reports (Li *et al.*, 2013a; Ulaganathan *et al.*, 2015). It is important to note that anodic and cathodic current response for AC-2 modified electrode is quite low as compared to its counter parts, which can be ascribed to the low porosity and relatively low specific surface area of the electrode. On the other hand, significantly higher current response is observed towards both redox reactions for AC-4, indicating the improved charge transfer and electrocatalytic activity of AC-4.

Interestingly, another redox couple V^{3+}/V^{4+} is also found for AC-4 coated graphite plate at ~0.42 V having a peak separation of ~0.65 V. In case of AC-3 modified electrode the peaks for V^{3+}/V^{4+} redox couple are suppressed and totally disappear for AC-2 electrode. The V^{3+}/V^{4+} redox couple is associated with an initial precharging step for converting the electrolyte mixture into catholyte and anolyte forms. Since the redox reactions of V^{3+}/V^{4+} couple requires high electrocatalytic activity due to its slow kinetics (Roznyatovskaya *et al.*, 2016), it is observed only for the AC-4 coated graphite plate. These results indicate the good electrocatalytic activity of the AC-4 modified electrode. This can be attributed to the improved charge transfer process due to the increased amount of electrochemically active sites created by the high degree of porosity, the large surface area and abundant oxygen functional groups.

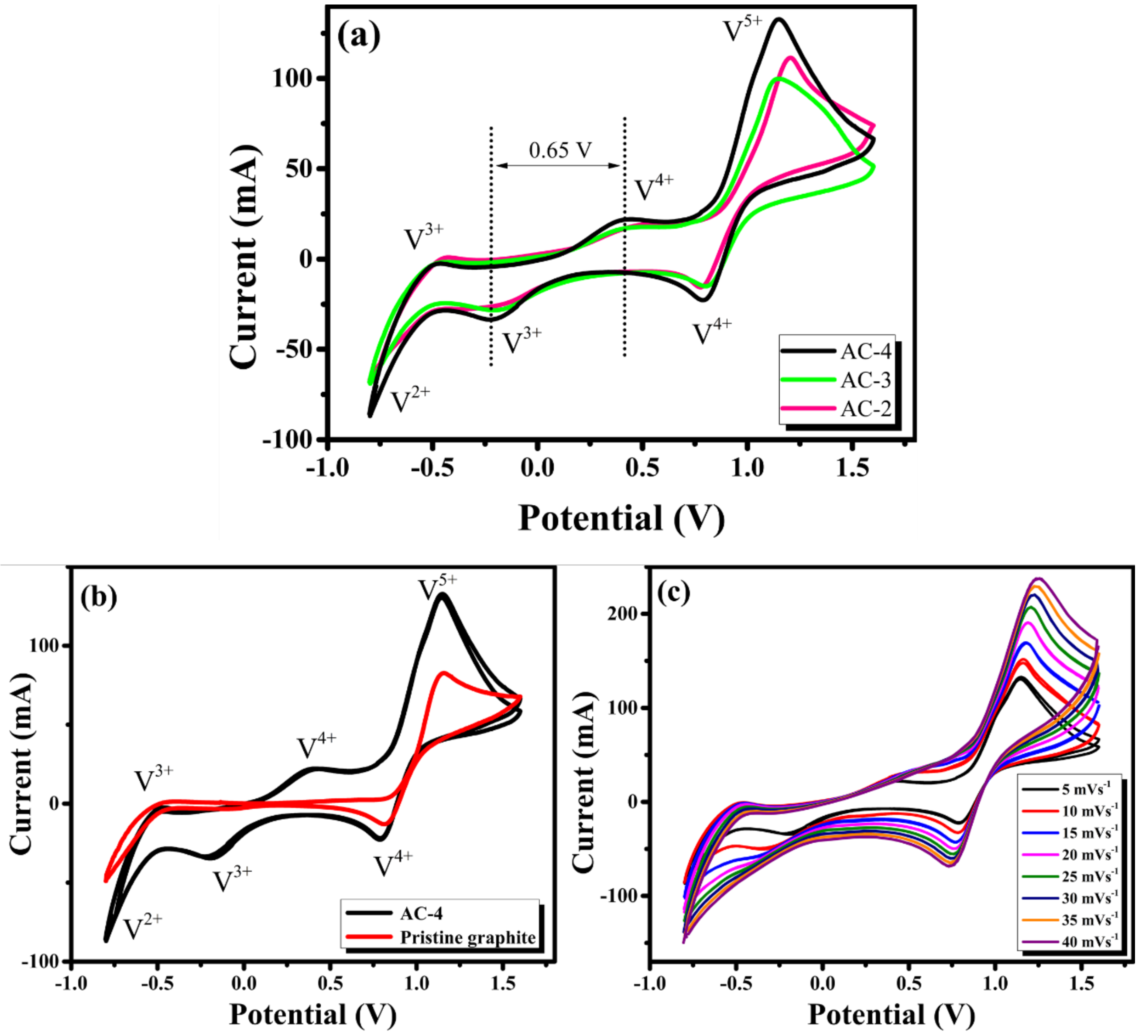

Figure 4.8. (a) Cyclic voltammetry (CV) curves for AC-2, AC-3 and AC-4 modified graphite electrodes in 1.6 M $V^{3.5+}$ electrolyte solution at a scan rate of 5 mV s^{-1}, indicating the enhanced electrochemical performance of AC-4. (b) Comparison of CV curves for AC-4 modified and pristine bipolar graphite electrodes. (b) CV curves for AC-4 modified electrode at different scan rates.

In order to gain further insight into the performance of AC-4 modified electrode, it was compared with the pristine bipolar graphite electrode. Figure 4.8b shows the CV curves for the pristine and AC-4 coated graphite plate electrodes at a scan rate of 5 mV s^{-1}. As expected, V^{5+}/V^{4+} and V^{2+}/V^{3+} redox couples are observed for both pristine and AC-4 modified bipolar graphite electrodes. It is important to note that good electrochemical reversibility with significantly higher anodic and cathodic current response is observed for the AC-4 modified electrode as compared with the pristine bipolar plate, which verifies the enhanced charge transfer activity of the AC-4 for both redox couples. Moreover, the obvious peaks of V^{3+}/V^{4+}

redox reactions for the AC-4 modified electrode are totally missing for pristine bipolar electrode. These results further signify the exceptional electrochemical performance of the AC-4 modified electrode as compared to the conventional bipolar plate.

To investigate performance stability of the modified electrode, CV was carried out at higher scan rates (Figure 4.8c). As the scan rate is increased, the V^{3+}/V^{4+} redox couple gets suppressed due to its inherent slow kinetics (Roznyatovskaya *et al.*, 2016), however, the other two redox couples V^{2+}/V^{3+} and V^{5+}/V^{4+} still exist with prominent peaks. As usual, with an increase in the scan rate the peak potential changes toward lower potential during the reduction and higher potential in oxidation. However, the potential difference still exists between reduction and oxidation peaks which is a positive sign of the outstanding reversibility and redox reaction kinetics (Maharjan *et al.*, 2017). Moreover, the electrode coating was still intact after CV cycling at high scan rates, which indicates the good stability of the modified electrode for long cycle life.

To further explore the origin of the improved electrocatalytic activity of AC-4, EIS measurements were performed. Figure 4.9 shows the EIS results for AC-4 modified and pristine graphite electrodes at 50% SOC in anolyte and catholyte. The Nyquist plots consist of a semicircle which originates from charge transfer reactions and ohmic resistance, and a linear fragment that is due to the diffusion and transfer of the vanadium ions from pores of the electrode (Yao *et al.*, 2012). Charge transfer resistance is the main concern in this study since it correlates with the electrode kinetic. The high frequency intercept to real part of the impedance for both samples was moved to the same point to compare the charge transfer resistance of modified and pristine electrodes. The EIS results derived from Nyquist plots in Figure 4.9a demonstrate that the charge transfer resistance of pristine bipolar plate (5.32 Ω) is almost tenfold higher compared with the AC-4 modified electrode (0.5 Ω) in the negative (V^{2+}/V^{3+}) electrolyte. Likewise, the AC-4 modified graphite electrode displayed lower charge transfer resistance (0.365 Ω) than the pristine bipolar electrode (0.673 Ω) in the positive (V^{5+}/V^{4+}) electrolyte (Figure 4.9b). Thus, in both electrolytes the AC-4 modified electrode manifested reduced charge transfer resistance that improves the electrochemical reactions (Maharjan *et al.*, 2019). The CV and EIS combined analyses suggest that the improved electrochemical reactions are governed by decreased charge transfer resistance which can be attributed to the abundant oxygenated functional groups in the highly porous network of AC-4, as reported previously (Maharjan *et al.*, 2017).

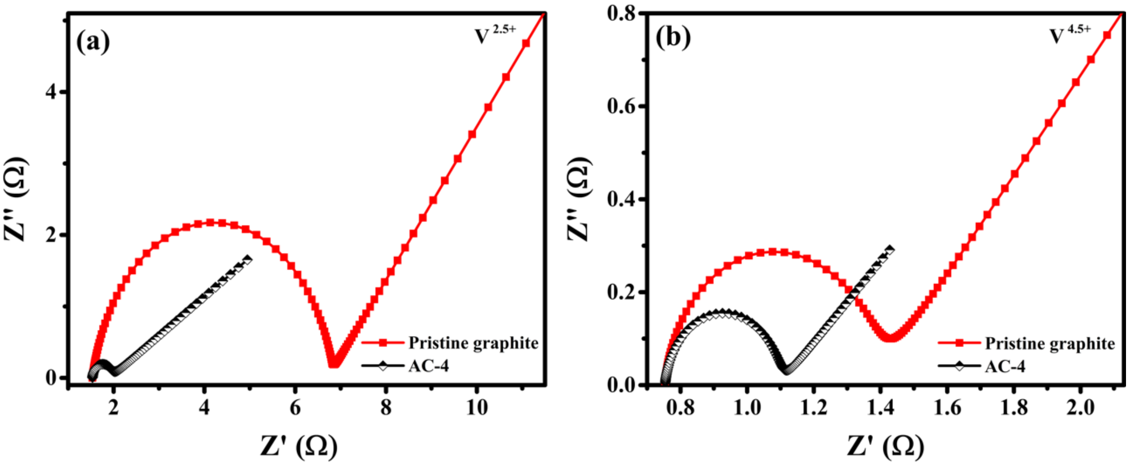

Figure 4.9. Nyquist curves for AC-4 modified and pristine bipolar graphite electrodes in (a) catholyte $V^{2.5+}$ and (b) anolyte $V^{4.5+}$ at 50% state of charge.

The superior electrochemical performance of AC-4 can be better understood by the VRB electrocatalytic mechanism proposed by Skyllas Kazacos and co-workers (Sun and Skyllas-Kazacos, 1992; Corcuera and Skyllas-Kazacos, 2012; Kim *et al.*, 2015b). They reported that the C-OH phenolic group act as an active site for the vanadium redox reactions. The whole process at the positive half-cell can be divided into three main steps as follows:

1. The diffusion of the VO^{2+} ion from the electrolyte to the electrode surface and an ion exchange between VO^{2+} and the H^+ of the phenolic group.
2. The transfer of an O atom from C-O groups on the electrode surface to the VO^{2+} ion to form VO_2^+ and subsequent transfer of an electron to the electrode along the C-O-V bond.
3. The ion exchange between VO_2^+ and H^+ in the electrolyte completing the oxidation reaction.

In negative half- cell, the reduction reaction takes place in similar way (Sun and Skyllas-Kazacos, 1992): the exchange of V^{3+} and H^+ ions, the transfer of an electron from the electrode to V^{3+} to form V^{2+} and final ion exchange between V^{2+} and H^+ ions of electrolyte.

The AC-4 with high O/C ratio verified by XPS and bulk elemental analysis, possesses extensive oxygenated moieties embedded in its highly porous network. These nanoscale pores with rich oxygen functionalities act as active sites for the vanadium redox reactions and improve the charge transfer process thereby enhancing electrocatalytic activity of the electrode.

4.3.3 Static cell performance

To recognise the above-mentioned benefits of the AC-4 modified electrode in three electrode system, its performance in VRB static cell configuration was evaluated. The charge-discharge cyclic study was carried out at potential cut-off window of 1.1 to 1.6 V at various current densities. The charge-discharge profiles of the initial five cycles at a current density of 5 mA cm^{-2} for cells with pristine and modified electrodes are presented in Figure 4.10a. It can be seen that the AC-4 modified electrode exhibits stable charge-discharge performance and reveals improved capacity compared to the pristine graphite plate. The pristine bipolar electrode finishes its 5 cycles in 1/3 time of the AC-4 modified electrode's same number of cycles. A longer charge discharge time of the AC-4 modified electrode indicates its enhanced capacity due to increase in electrochemically active area.

Figure 4.10b-c show the comparison of energy and voltage efficiencies of cells with modified and pristine bipolar electrodes at various current densities (5-20 mA cm^{-2}). It is interesting to note that almost all the AC modified electrodes display higher values for both voltage and energy efficiencies at all tested current densities. A good and stable Coulombic efficiency is observed for both pristine and modified electrodes (Figure 4.10d). The energy and voltage efficiencies decline with the current density, which can be ascribed to high ohmic polarisation (Aziz *et al.*, 2020) or high dynamic voltage (IR) drop at higher current densities (Maharjan *et al.*, 2017). A small increase in the energy efficiency of AC-4 modified electrode at 10 mAcm^{-2} might be due to increased Coulombic efficiency at higher current density (Aziz *et al.*, 2017). The superior performance of AC modified electrodes can be attributed to the improved electrochemical activity, plenty of oxygenated functional groups available and good contact between bipolar plate and the porous graphite felt. Consistent with CV and EIS studies, the AC-4 modified electrode demonstrates superior energy and voltage efficiencies than its counterparts AC-2 and AC-3 at almost all tested current densities. Such an exceptional behavior of AC-4 is ascribed to its ultrahigh microporosity and excess reaction sites available for electrochemical reaction to occur.

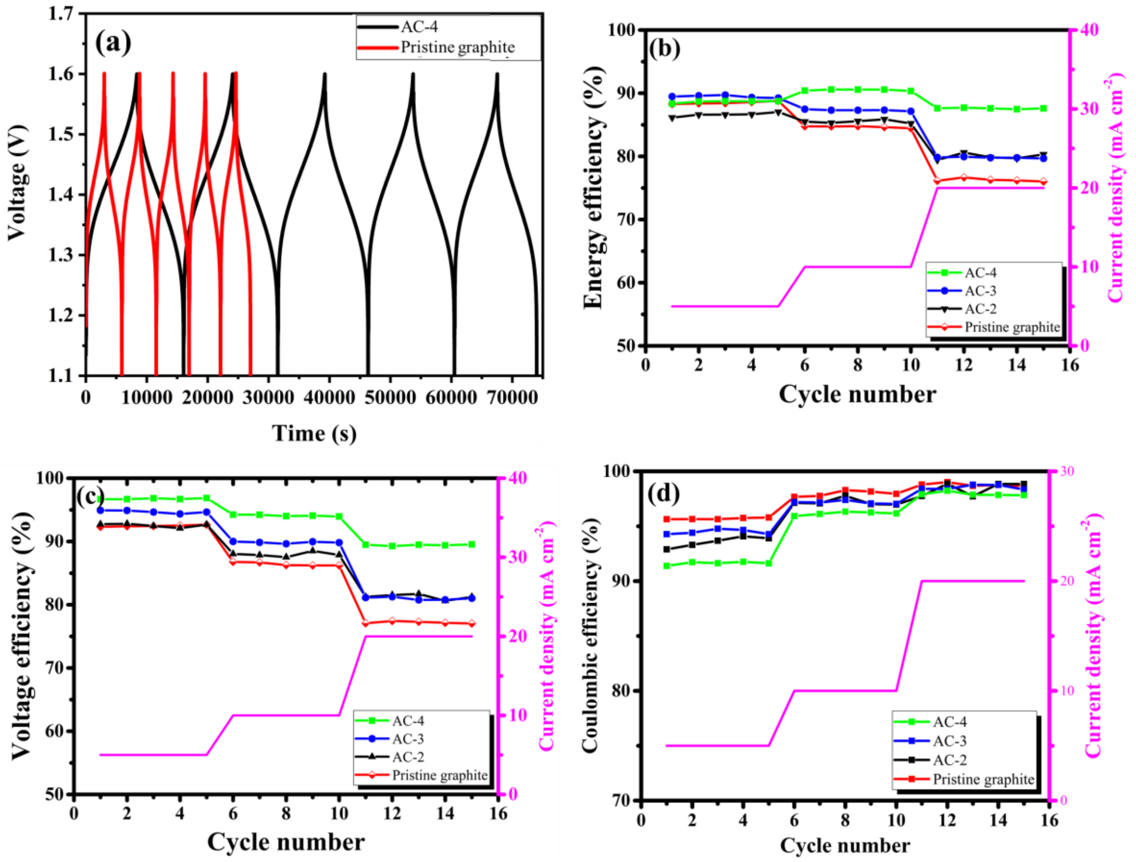

Figure 4.10. Charge-discharge profiles of AC-4 modified and pristine bipolar graphite electrodes at constant current density of 5 mA cm^{-2}. (b) Comparison of energy efficiency and (c) voltage efficiency of bipolar plate reference and ACs coated electrodes at different constant current densities of 5, 10 and 20 mA cm^{-2}.

In order to confirm the performance stability of the modified electrodes in practical applications, the charge-discharge studies were performed for 50 cycles at a constant current density of 10 mA cm^{-2} in a VRB static cell configuration. Figure 4.11a-b shows the energy efficiency and voltage efficiency of cells with pristine and modified electrodes over 50 cycles. The cell with AC-4 modified electrode demonstrate a stable and superior cyclic performance compared to the pristine graphite plate throughout the 50 cycles. Energy and voltage efficiencies of over 90% were observed for the AC-4 modified electrode in the VRB cell configuration. Moreover, a stable Coulombic efficiency of ~98% was noted for the AC-4 modified electrode (Figure 4.12). A slight decrease in energy efficiency over the long cycling performance could be due to electrolyte crossover through the membrane (Bhattarai *et al.*, 2018; Bhattarai *et al.*, 2019). Nonetheless, the AC-4 modified electrode exhibit more stable performance than the pristine electrode. The energy efficiency of present system is comparable with a commercial VRB system.

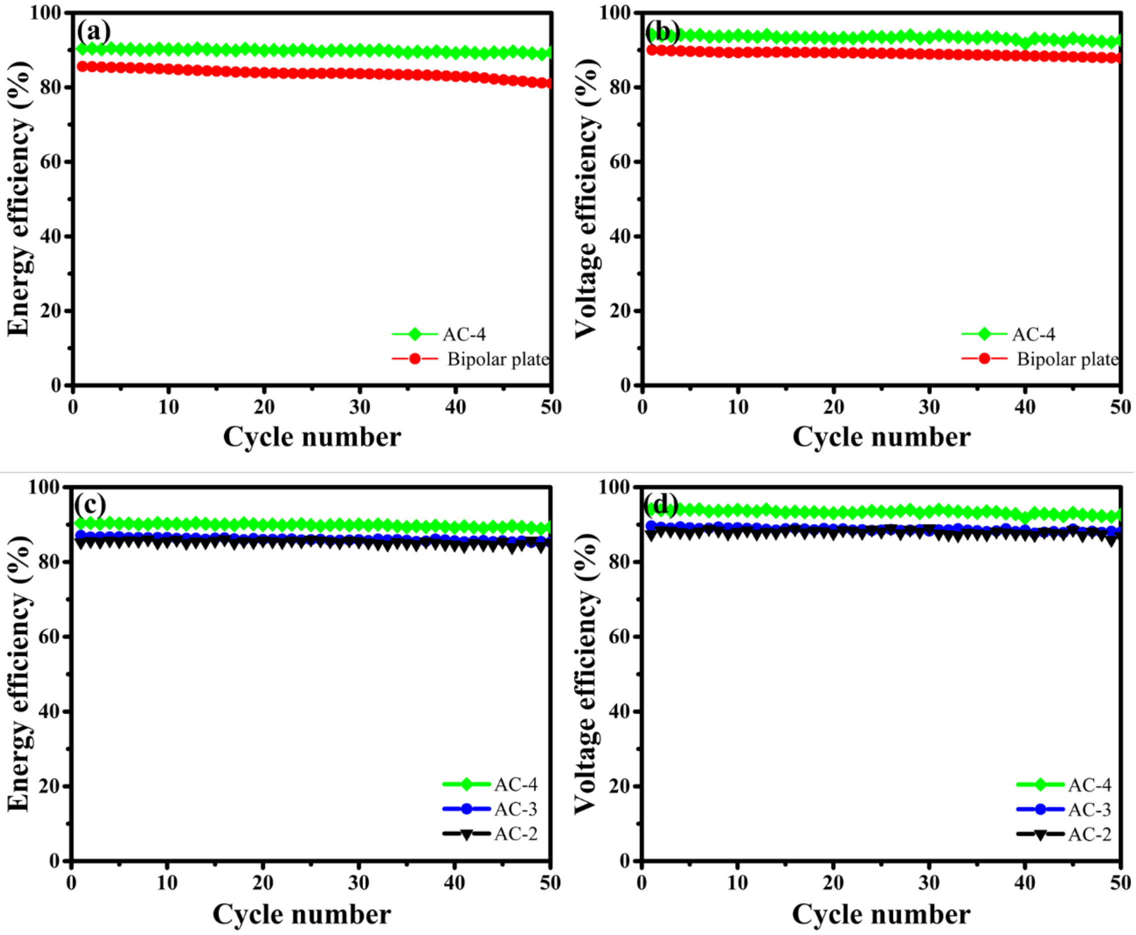

Figure 4.11. (a) The energy efficiency and (b) voltage efficiency of bipolar graphite plate reference and AC-4 coated graphite electrode at constant current density of 10 mA cm^{-2}. (c) Comparison of the energy and (b) voltage efficiencies of AC-2, AC-3 and AC-4 coated graphite electrodes at constant current density of 10 mA cm^{-2}.

The long-term cyclic performance of the 3 AC samples was also evaluated. As evidenced from Figure 4.11c-d, the efficiency of the cell increased with an increase in active area. Moreover, this trend was stable throughout 50 cycles. A similar trend was observed for Coulombic efficiency of all the electrodes and ~98% of stable the Coulombic efficiency was observed (Figure 4.12). The highest energy and voltage efficiencies were obtained for the most porous sample AC-4. Such an improved long cyclic life of the electrode is attributed to stable structure, enlarged microporosity, high electrocatalytic activity, excessive reaction sites and uninterrupted charge transfer process.

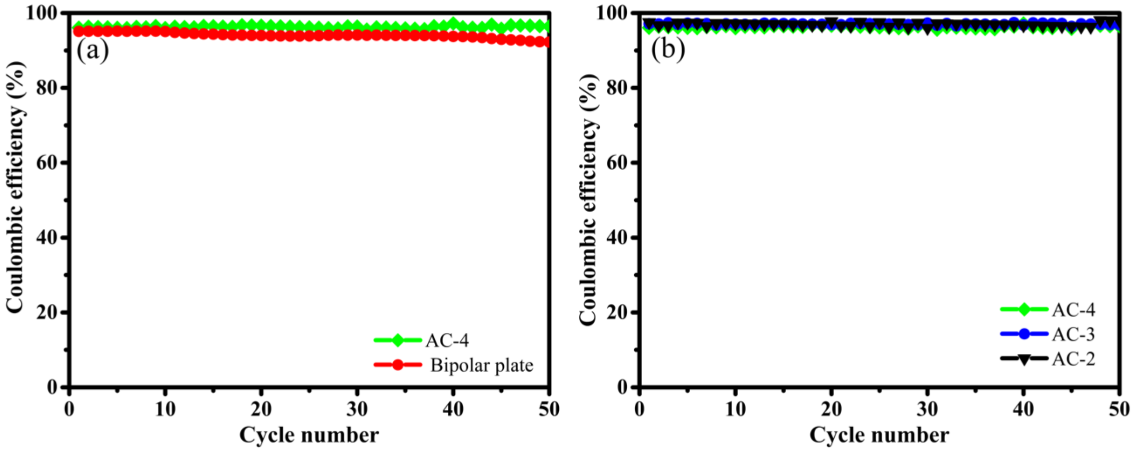

Figure 4.12. (a) Coulombic efficiency of bipolar graphite plate reference and AC-4 coated graphite electrode, and (c) comparison of the Coulombic efficiencies of AC-2, AC-3 and AC-4 coated graphite electrodes at constant current density of 10 mA cm^{-2}

Generally, the current graphite-based electrodes are produced from non-renewable resources and are costly. Thus, the present study clearly demonstrates that highly porous AC derived from a renewable source such as tea leaves can be a potential candidate as electrode material for VRB applications. The AC modified electrode would benefit from low cost and enhanced electro-catalytic activity. Furthermore, the present ACs could be used as filler materials in next generation bipolar graphite plates which would benefit from lower cost. Finally, it is believed that this study will pave the way to investigate the usage of wide variety of biomass wastes as a renewable precursor for the production of high-performance electrodes for redox flow batteries. This will simultaneously solve the future energy storage demands and biomass waste recycling problems.

4.4 Summary

In summary, a range of highly porous carbon materials have been prepared from tea waste and the effect of electrode porosity on the performance of VRB is evaluated. The specific surface area is enhanced from 10 m^{2}g^{-1} to over 2000 m^{2}g^{-1} and a high degree of microporosity is achieved. The modified electrodes manifest superior electrochemical performance than the pristine graphite electrode. The highly microporous electrode reveals dual benefits: firstly, it offers excess active sites to facilitate the reversible redox reactions; secondly, it improves the electrochemical performance due to improved charge transfer and high electrocatalytic activity. The synergetic effect of high surface area, microporosity and oxygenated functional groups lead to the enhanced electro-catalytic activity which enabled the improved charge transfer process.

Such a unique finding certainly opens the way to utilise cost effective biomass derived porous carbon-based high-performance electrodes in VRBs.

Chapter 5 Sustainable synthesis of graphene quantum dots with high purity

5.1 Introduction

Graphene quantum dots (GQDs) have attracted extensive attention in a wide variety of applications owing to their fascinating optical properties. Despite several efforts, a systematic study on the investigation of suitable biomass precursor for the synthesis of GQDs is still lacking. Moreover, the fundamental issues of high cost and introduction of impurities in product remain open challenges. In this chapter, a green, cheap, and renewable biomass source was used for the cost-effective sustainable synthesis of GQDs with high purity and controllable optical properties. The elimination of commonly employed acid-base neutralisation process was the key to obtain ultra-pure GQDs. The GQDs possess 3-9 layer graphene structure with a size range of 2-20 nm and exhibit excitation dependent photoluminescence emission. The tunable size of GQDs paved the way to controllable photoluminescence properties with the band gap varying from 2.67 to 2.95 eV. The specific surface area of GQDs (104 m^2 g^{-1}) was measured for the first time, which additionally verified the synthesis of bulk samples. The simple, cost-effective, and sustainable development of highly pure GQDs with tunable optical properties presents bright promise for their future applications in sensing, photocatalytic and biomedical fields.

5.2 Biochar Synthesis and characterisation

5.2.1 Morphological study of biochar

The morphologies of the black tea feedstock and biochar samples were obtained by SEM (Figure 5.1a_1-c_1). Pores are observed in the structure of the tea surface. The higher magnification images (1000x-5000x from Figure 5.1b-c) further verify the structure and show micrometer sized pores at the center of flower-like morphology. The morphology of the tea changes significantly with pyrolysis treatment. The SEM images of biochar synthesised at 200 °C show very heterogeneous morphology and irregular structure due to the dehydration and beginning of decarboxylation reactions (Figure 5.1a_2-c_2) (Yu *et al.*, 2017).

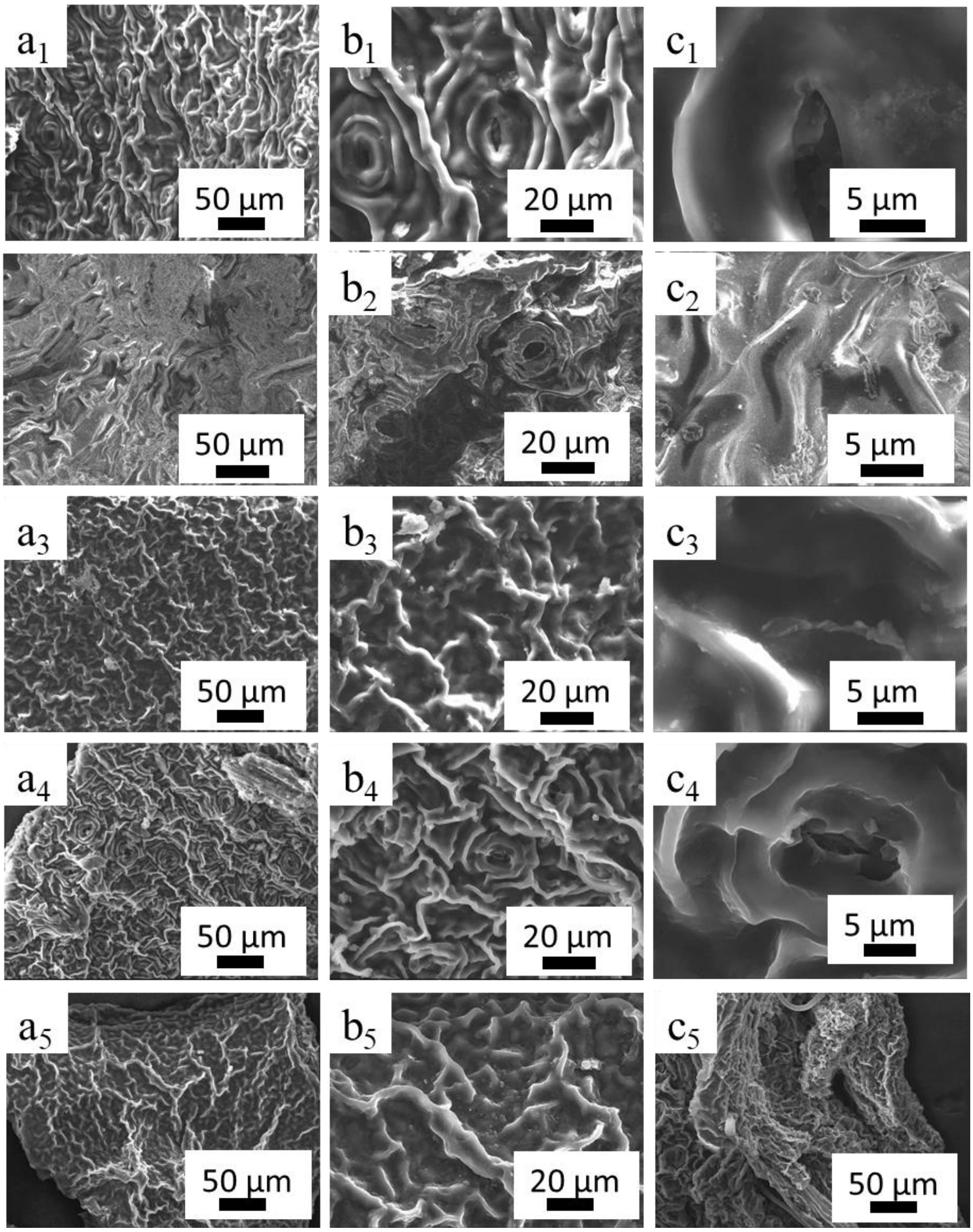

Figure 5.1. SEM images of raw black tea (a_1, b_1, c_1) and their char derivatives obtained at 200 °C (a_2,b_2,c_2), 300 °C(a_3, b_3, c_3), 400 °C (a_4, b_4, c_4) and 500 °C(a_5, b_5, c_5) at different magnifications.

It was reported (Bilbao *et al.*, 1989) that the decomposition of hemicellulose is dominant at a temperature range of ≥200^{o}C-230 °C, cellulose decomposition dominates at 260-290 °C and the lignin decomposition takes place along with cellulose above 290 °C and continues up to 600 °C. As a result, the morphology of tea develops, and the porosity increases with pyrolysis temperature. At 400 °C more porosity is seen at higher magnification along with well-ordered surface morphology. At 500 °C the morphology of spent black tea changes to somehow like a layered structure (Figure 5.1a_5-c_5). Meanwhile, the porosity increases, as evidenced by the cross-sectional view image (Figure 5.1c_5).

It was observed that increasing pyrolysis temperature up to 500 °C increases the porosity and provides well-defined pore structure of biochar. These pores form when volatile substances are released from hot surface. The natural porosity of biomass is increased by the pyrolysis of cellulose, leaving channels which provide an easy escape route for the volatile products (Yu *et al.*, 2017).

5.2.2 Structural analysis of biochar

The structural properties of biochar were investigated using Raman and FTIR spectroscopies. The FTIR spectra of the black tea feedstock shown in Figure 5.2a displays a broad peak at ~3100-3700 cm^{-1} corresponding to the stretching vibrations of O-H groups, whereas the peaks at around 2900 and 2850 cm^{-1} are attributed to the aliphatic C-H (alkanes) groups. The peaks at about 1735 and 1636 cm^{-1} are assigned to C=O bonds of carbonyl and C=C in aromatic groups, respectively. The bands at 1450-1460 cm^{-1} are related to the (C-C) and alkane groups. The peak at 1321 cm^{-1} is related to the strong content of oxygenated species: esters, ethers, carboxylic acids and alcohols. The band at about 1232 cm^{-1} is attributed to aliphatic amines, whereas the sharp band at around 1000 cm^{-1} is attributed to the C-O stretching of the ether group. The bands at 875-750 cm^{-1} correspond to the aromatic C-H out of plane bending vibrations (Lazim *et al.*, 2015).

A continuous reduction in the intensity of these infrared bands is observed with increase in the pyrolysis temperature. These changes indicate that the major chemical and/or structural changes that take place are attributed to the degradation of cellulose and hemicellulose constituents of tea. This process initiates at around 250-300 °C with a maximum decomposition rate at about 370 °C (Yu *et al.*, 2017) and takes place by the breakage of C-O, C-H and C-C bonds by dehydration, decarboxylation and decarbonisation (Lin *et al.*, 2009). On the other hand, the decomposition of lignin takes place over a wide range (280-600 °C) with a highest degradation rate at about 450 °C (Nassar and MacKay, 2007; Brebu and Vasile, 2010) to produce phenolic groups (Gani and Naruse, 2007). The FTIR peaks due to aliphatic groups at around 2900 cm^{-1} only disappear when the pyrolysis temperature was ~500 °C.

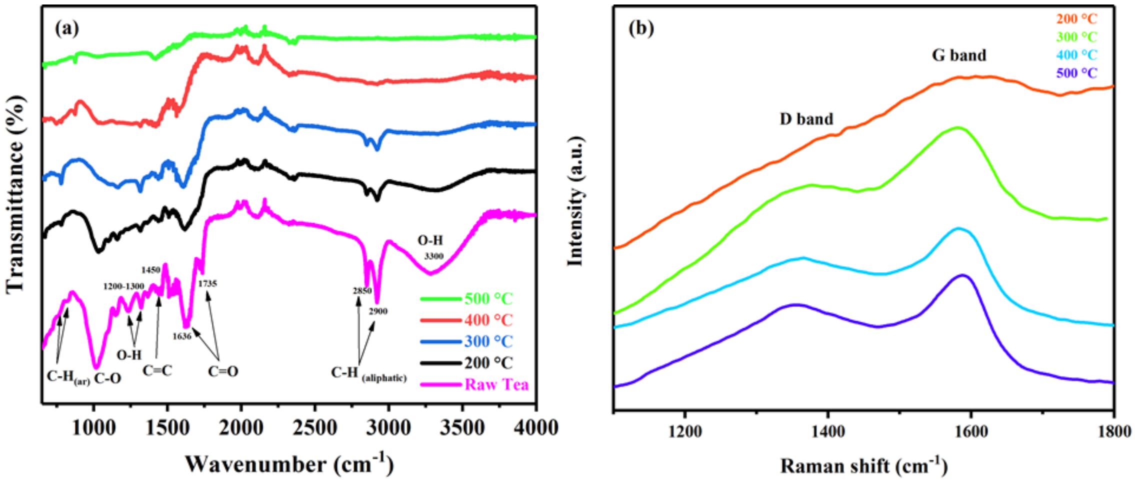

Figure 5.2. (a) FTIR spectra of raw black tea, and biochar samples obtained by pyrolysis of black tea at different temperatures from 200 to 500 °C. (b) Raman spectra of biochar samples with HTT range of 200-500 °C.

Raman spectra of char samples acquired from the pyrolysis of black tea at 200-500 °C are presented in Figure 5.2b. The Raman spectra for biochar samples derived from 300-500°C contain two broad bands at ~1360 and ~1587 cm^{-1} designated as the D (disorder) and G (graphite) bands respectively, which are indicative of a carbonaceous structure. The G bands have similar shapes and only small differences in the energies of the bands (Figure 5.2b). There appear to be shifts in the D and G bands with pyrolysis temperature, but the spectra are similar to the well-known spectra for disordered carbons. The G band is related to the E_{2g} stretching mode of graphite (Tuinstra and Koenig, 1970; Sheng, 2007; Tabish *et al.*, 2017). The D band corresponds to the breathing mode of A_{1g} symmetry involving phonons near Brillouin zone boundary (Ferrari and Robertson, 2000). Since the D band shows disorder and there is no disorder in pure crystalline graphite, this D band has negligible intensity in pure crystalline graphite (Gupta *et al.*, 2006). The intensity ratio I_D/I_G provides a useful characterisation of the crystallinity of the char produced and this decreases with increasing temperature (Tuinstra and Koenig, 1970). Our results show I_D/I_G ratio of about 0.84 for biochar samples at 400 and 500 °C which clearly demonstrates their sp^2 dominant carbon structure (Tuinstra and Koenig, 1970; Ferrari *et al.*, 2006).

The surface elemental composition of the biochar was further confirmed by X-ray photoelectron spectroscopy (XPS). The XPS analysis of the BC-500 is presented in Figure 5.3. The survey spectrum shows three main peaks at 284.4, 400.4 and 532.4 eV, which are assigned to C1s, N1s and O1s, respectively (Figure 5.3a). Another peak at 347.4 eV associated with Ca 2p is also observed. The XPS elemental analysis indicates that the biochar is mainly composed of C(78.27 at%) , O(15.59 at%) and N(3.39 at%), with a limited amount of Ca from the feedstock. The high resolution C1s spectrum (Figure 5.3b) can be deconvoluted into three peaks at 284.75, 285.64, and 288.16 eV, which are attributed to C-C/C=C, C-O-C and C=O, respectively (Ding *et al.*, 2015). The other small peak at 290.08 is attributed to carbonate and two peaks at 293.27 and 296.11 eV are assigned to plasmon loss features. The N1s spectrum (Figure 5.3c) consists of two broad bands at 398.64 and 400.46 eV, corresponding to the pyridinic N (C-N-C) and pyrrolic N (N-H), respectively (Pels *et al.*, 1995b). The O1s spectrum (Figure 5.3d) consists of two major peaks at 531.98 and 533.58 eV, which can be attributed to C=O and C-OH/C-O-C groups, respectively (Sevilla and Fuertes, 2009a; Ding *et al.*, 2015). These results are in good agreement with the results of FTIR which shows the presence of C=O and O-H groups in biochar.

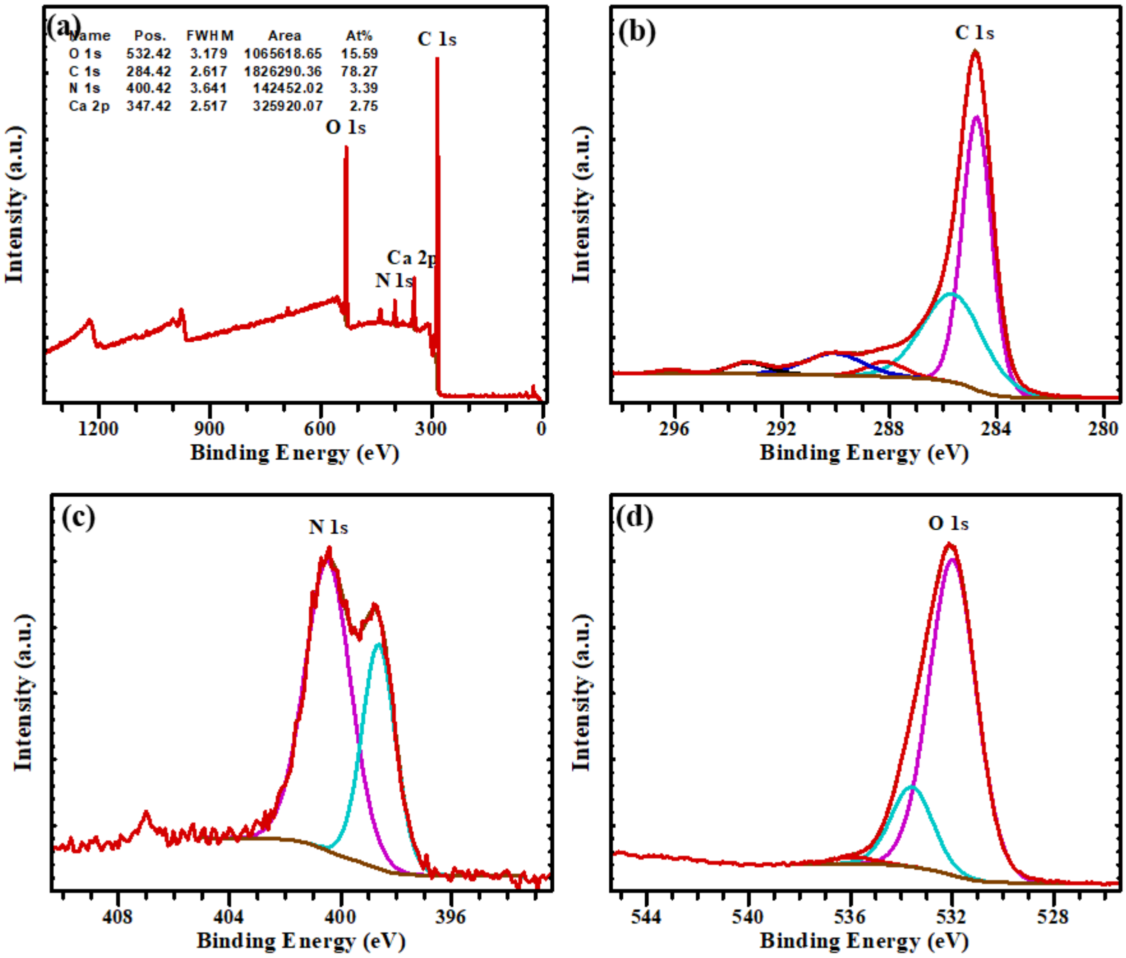

Figure 5.3. The (a) XPS survey spectrum of BC-500 and its corresponding high resolution (b) C 1s, (c) N 1s, (d) O 1s spectra.

The CHN analytical data for biochar obtained at different pyrolysis temperatures is given in Table 5.1. Elemental analysis (dry and ash free basis) of biochar prepared at different HTTs. The carbon content increases and hydrogen content decreases with increase in pyrolysis temperature, which is consistent with a carbonisation process. The analytical data gave a C/N ratio of ~16 for the bulk sample while XPS data gave C/N of ~23 at the surface.

Table 5.1. Elemental analysis (dry and ash free basis) of biochar prepared at different HTTs.

Sample	**HTT**	**Carbon**	**Hydrogen**	**Nitrogen**	**Oxygen***
Black Tea	Dried at 80 °C	44.82	5.69	3.98	45.51
BC-200	200 °C	52.38	4.89	4.63	38.1
BC-300	300 °C	64.97	4.54	5.21	25.28
BC-400	400 °C	68.26	3.46	5.19	23.09
BC-500	500 °C	71.09	2.24	5.18	21.49

*Calculated by difference

5.3 Characterisation of activated char

Activation is the state of increased tendency of a substance to undergo a chemical reaction. Among the numerous approaches developed, activation of biochar with strong acids is widely accepted approach for its conversion into graphene-based materials. The biochar activation was carried out with individual acids and acid mixture for investigating their effect on the properties of the product. In order to investigate the effect of activating agents on optical properties, different acids were used. The mixture of sulfuric acid and nitric acid as well as only nitric acid were utilised as activating agents. The activated char from both techniques was subjected to hydrothermal carbonisation and GQDs with varying properties were obtained. As shown in Figure 5.4, the photoluminescence spectra of GQDs prepared from two activation techniques are quite different. The normalised PL spectra showed an obvious shift of ~35 nm in emission maximum between the two. A broad emission band was obtained for activation with HNO_3 only. The PL spectra of GQDs synthesised from biochar activated using only HNO_3 was shifted to the higher wavelength region showing the larger size of the quantum dots produced as compared to the ones formed by using mixture of acids as activating agents. Thus, using a mixture of strong acids was found to be a key factor in activating the biochar for the synthesis of small sized GQDs. The mixture of acids was also found to lead to improve the optical properties.

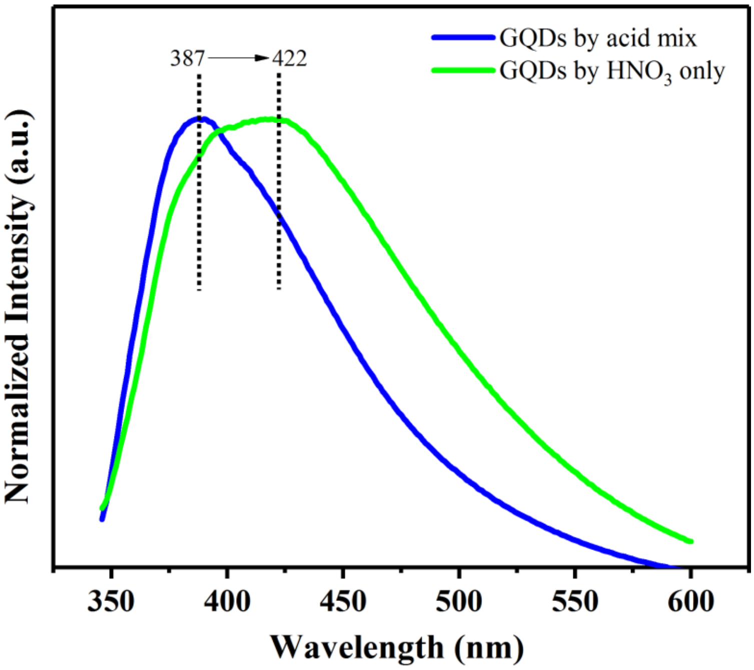

Figure 5.4. Comparison of the photoluminescence spectra of GQDs obtained by hydrothermal treatment of biochar activated by mixture of H_2SO_4 and HNO_3 (blue), and only HNO_3 (green).

During the activation process hydroxyl, oxygenated and nitro groups (-OH, -COOH, -COO, NO- etc.) are added on the surface of basal planes of sp^2 carbon domains (Duan *et al.*, 2016). This phenomenon makes the carbon domains weak, reactive, and hydrophilic in nature. Consequently, these carbon domains become suitable for disintegration into small fragments.

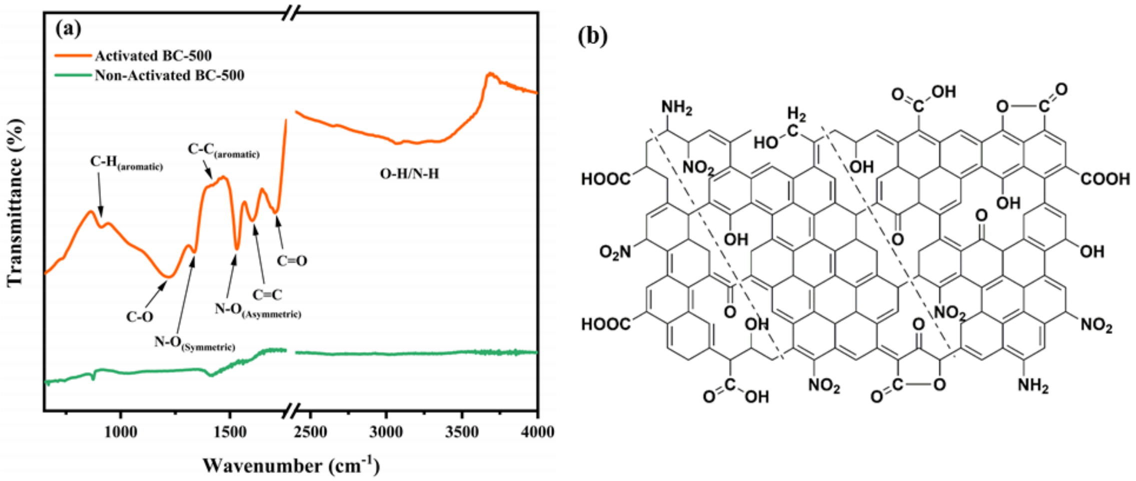

Figure 5.5. (a) FTIR analysis of BC-500 before (green) and after (orange) activation with a mixture of HNO_3 and H_2SO_4 (3:1 vol.%). (b) Schematic illustration of oxygenated, hydroxyl and nitro groups on the surface and basal planes of sp^2 carbon domains.

The activation of biochar was characterised by FTIR spectroscopy. The FTIR spectrum of activated char in Figure 5.5a shows that activation led to the incorporation of organic functional groups into the carbon structure compared to non-activated sample. There is a broad peak at ~3000-3500 cm^{-1} assigned to the stretching vibrations of hydroxyl (O-H) and amine (N-H) groups. The strong band at ~1700 cm^{-1} is assigned to the stretching vibration of carbonyl (C=O) groups. The band at 1600 cm^{-1} is assigned to aromatic C=C stretching in lignin. The bands at ~1530 cm^{-1} and ~1340 cm^{-1} are assigned to asymmetric and symmetric stretching vibrations of nitro (NO) groups, respectively (Bekyarova *et al.*, 2009). The band at ~1430 cm^{-1} is attributed to C-C stretching vibrations in aromatics. The bands at 1000-1250 cm^{-1} are allocated to the C-O stretching vibrations in xylan and lignin. The peak at ~905 cm^{-1} is related to the out of plane bending vibrations of C-H bond in aromatic rings.

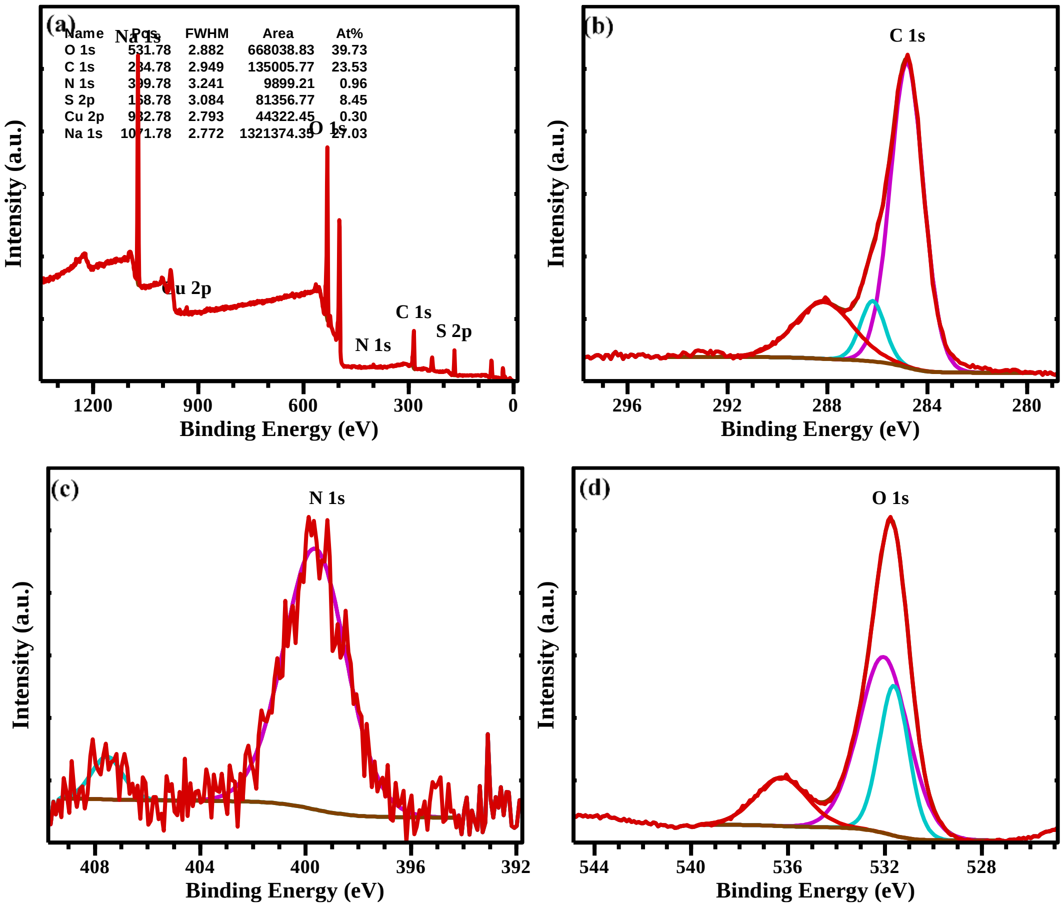

Name	Pos.	FWHM	Area	At%
O 1s	531.78	2.882	668038.83	39.73
C 1s	284.78	2.949	135005.77	23.53
N 1s	399.78	3.241	9899.21	0.96
S 2p	168.78	3.084	81356.77	8.45
Cu 2p	932.78	2.793	44322.45	0.30
Na 1s	1071.78	2.772	1321374.35	27.03

Figure 5.6. The (a) XPS survey, (b) C 1s, (c) N 1s, (d) O 1s high-resolution XPS spectra of BC-500-GQDs obtained after neutralisation with NaOH. Spectra shows numerous contaminations introduced in the product.

Interestingly, washing the activated char with hot DI water was the key to remove excess acids from the surface and acquire neutral pH. On the other hand, when the same sample was washed with room-temperature DI water, neutral pH was not attained due to incomplete removal of excess acids, thus requiring the neutralisation with a base (e.g. NaOH). This neutralisation process introduced sodium (Na) impurities in the sample. To analyze the effect of these impurities on the final product, XPS analysis of the product was performed. The XPS analysis indicates that the introduction of leftover sulphur (from the acid) and Na (from the base) contaminations in the final product was inevitable and these were present as impurities as shown in Figure 5.6.

Thus, extensive washing with hot water and elimination of the neutralisation step played a vital role in the preparation of a highly pure product. A schematic illustration of the activated biochar is shown in Figure 5.5b. It shows that during the activation process, the hydroxyl, oxygenated and nitro groups (-OH, -COOH, -COO, -NO, etc.) are added on the surface and basal planes of carbon which make it suitable for disintegration into quantum sized fragments.

The XPS spectra of activated and hot water washed sample (BC-500-A) are shown in Figure 5.7. The survey XPS spectrum of the activated/oxidised biochar BC-500-A exhibits three major peaks at 285.25, 400.25 and 532.25 eV, corresponding to C1s (68.15 At%) , N1s (6.44 At%) and O1s(24.28 At%), respectively (Figure 5.7a). The activation process has increased both the oxygen and nitrogen contents substantially. Interestingly, the Ca impurities from the biochar have been removed by the strong acids. The high resolution C1s spectrum (Figure 5.7b) shows three peaks at 284.66, 286.1, 288.52 eV, which can be attributed to C-C/C=C, C-N and C-O/C=O, respectively (Ding *et al.*, 2015). Comparison with non-activated samples in Figure 5.3 shows a marked increase in the C=O peak due to activation. The N1s spectrum (Figure 5.7c) consist of two bands at 399.8 and 405.5 eV. The former has a shape consistent with being composed of two bands corresponding to pyridinic/pyrrolic components in a carbonaceous structure. Pyridinic nitrogen has a peak at 398.6 eV and pyrrolic at 400.5 eV (Pels *et al.*, 1995b).

The latter band at higher energy, which appeared due to activation, is attributed to N-oxide (NO_2^-) (Pels *et al.*, 1995a; Bekyarova *et al.*, 2009). The interesting observation is the presence of a high concentration of N-oxides in activated biochar. These N-oxides play a vital role in the strong activation of carbon and its fragmentation into GQDs. The results are consistent with the stability of N-functionalities in carbon in relation to HTT. Previously, high concentrations of N-oxides have been observed in carbons with low O contents (Xiao *et al.*, 2005).

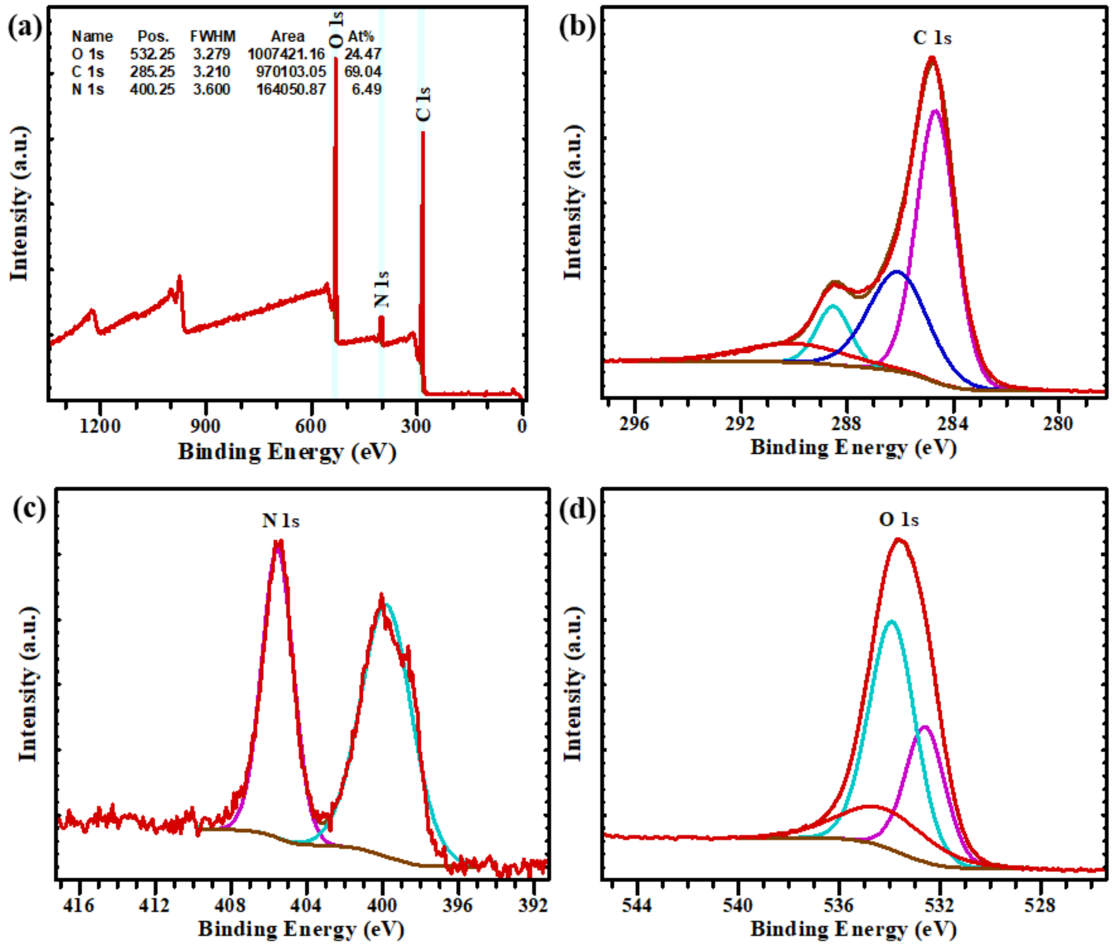

Figure 5.7. The (a) XPS survey spectrum, (b) C1s, (c) N1s, (d) O1s high-resolution spectra of activated biochar BC-500-A after washing with hot DI water.

The O1s spectrum (Figure 5.7d) can be resolved into three peaks at 532.6, 533.9 and 534.2 eV, which can be attributed to C-O, C=O and C-OH groups, respectively (Sevilla and Fuertes, 2009a; Ding *et al.*, 2015). The XPS results reveal the presence of oxygenated groups on the surface of biochar, confirming the results of FTIR. A relatively high oxygen to carbon ratio (O/C = 35%) was found as compared to non-activated biochar (O/C = 20%), verifying the extensive oxidation of the biochar.

The addition of these functional groups on the surface of activated char facilitates the formation of GQDs at high temperature. The results of XPS and FTIR analysis indicate that during the activation process, the hydroxyl, oxygenated and nitro groups (-OH, -COOH, -COO, $-NO_2$ etc.) are added on the surface, as reported previously (Duan *et al.*, 2016). This increases carbon reactivity and the hydrophilic character of the material. Consequently, this highly reactive carbon is efficiently disintegrated at high temperature and pressure into quantum dots.

5.4 Characterisation of GQDs

5.4.1 Morphological study of GQDs

The surface morphology of the samples was studied by TEM and AFM. Figure 5.8 shows the TEM image of the products formed upon the hydrothermal treatment of BC-200 and BC-300 precursors. The development of sp^2 carbon domains in the precursor material is critical to synthesise GQDs. Therefore, only large sized particles with high degree of agglomeration (Figure 5.8a) or sheet formation (Figure 5.8b) are observed when a precursor (BC-200 and BC-300) with little or no sp^2 carbon domains is utilised. This is verified by the characterisation profile of the samples in Figure 5.2, where a precursor with good sp^2 content is obtained at temperatures above 400 °C. Heat treatment of biomass at temperatures below 400°C does result in some carbonisation as shown by the FTIR spectra (Figure 5.2a). However, the thermal degradation products for HTT below 400 °C do not fragment to sp^2 carbon domains and are, therefore, not suitable precursors for the synthesis of GQDs.

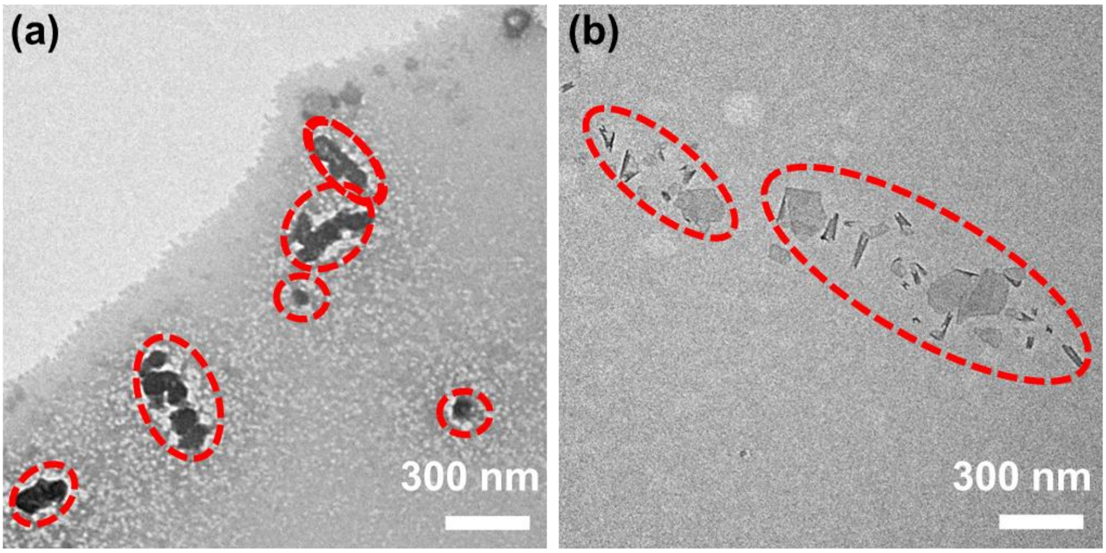

Figure 5.8. The product obtained from hydrothermal treatment process of (a) BC-200 sample and (b) BC-300 sample.

Moreover, the hydrothermal temperature plays a key role in the disintegration of sp^2 carbon domains, as the low temperature would not be enough to breakdown the carbon domains into small fragments. On the other hand, the higher temperature would destroy their surface and structure, leading to diminished photoluminescence properties. Therefore, a series of experiments were carried out to investigate the most suitable hydrothermal temperature for the synthesis of GQDs. After a systematic study, 200 °C was found to be the optimum temperature for the synthesis of GQDs with uniform distribution and prominent photoluminescence properties.

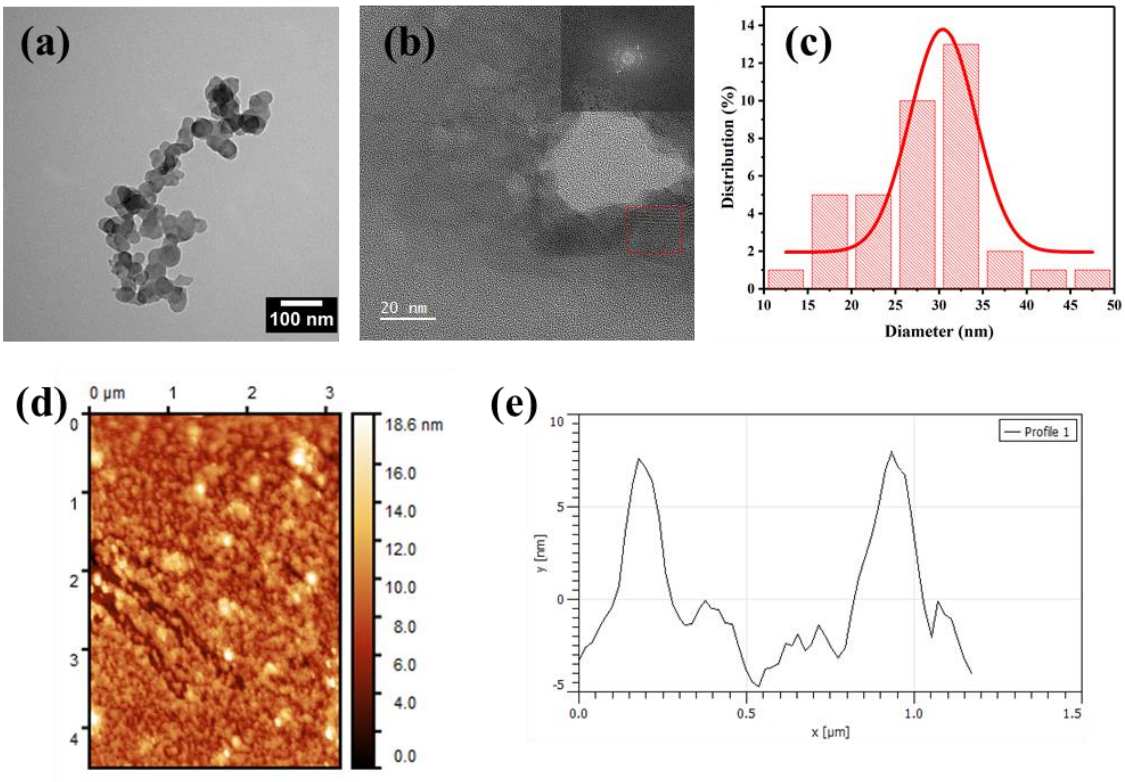

Figure 5.9. (a) TEM image, (b) HRTEM image (inset is the corresponding FFT of the red marked square), (c) histogram showing the size distribution, (d) AFM image and (e) height profile of the BC-400-GQDs obtained by hydrothermal treatment of BC-400 precursor.

Figure 5.9a shows the TEM image of as-synthesised product obtained by hydrothermal carbonisation of BC-400 precursor. The formation of quantum dots (BC-400-GQDs) with fairly uniform shape and size distribution can be observed. The corresponding histogram in Figure 5.9c reveals that as-prepared GQDs have a lateral diameter of 30.4 ± 4.4 nm. The high-resolution TEM (HRTEM) image in Figure 5.9b demonstrates the high crystallinity of as-prepared GQDs with a lattice spacing of 0.237 nm, corresponding to the $(11\bar{2}0)$ planes of graphene (0.24 nm) (Wang *et al.*, 2016d). Inset in Figure 5.9b is the corresponding FFT image of the GQD in the region marked by the square. The as-prepared GQDs were further characterised by AFM to gain insight into their thickness. AFM observations (Figure 5.9d, e) reveal the typical topographic morphology of GQDs dispersed on mica substrate and corresponding height profile, respectively suggesting that as-prepared GQDs have a thickness of 5–8 nm, corresponding to 15-20 graphene layers. These GQDs also show a small degree of agglomeration.

These results indicate that partially carbonised biochar precursors containing little or no content of sp^2 structure are not suitable for the synthesis of GQDs with uniform size and shape distribution. BC-500 was used for the synthesis of evenly dispersed GQDs and hydrothermal treatment gave GQDs with narrow size distribution.

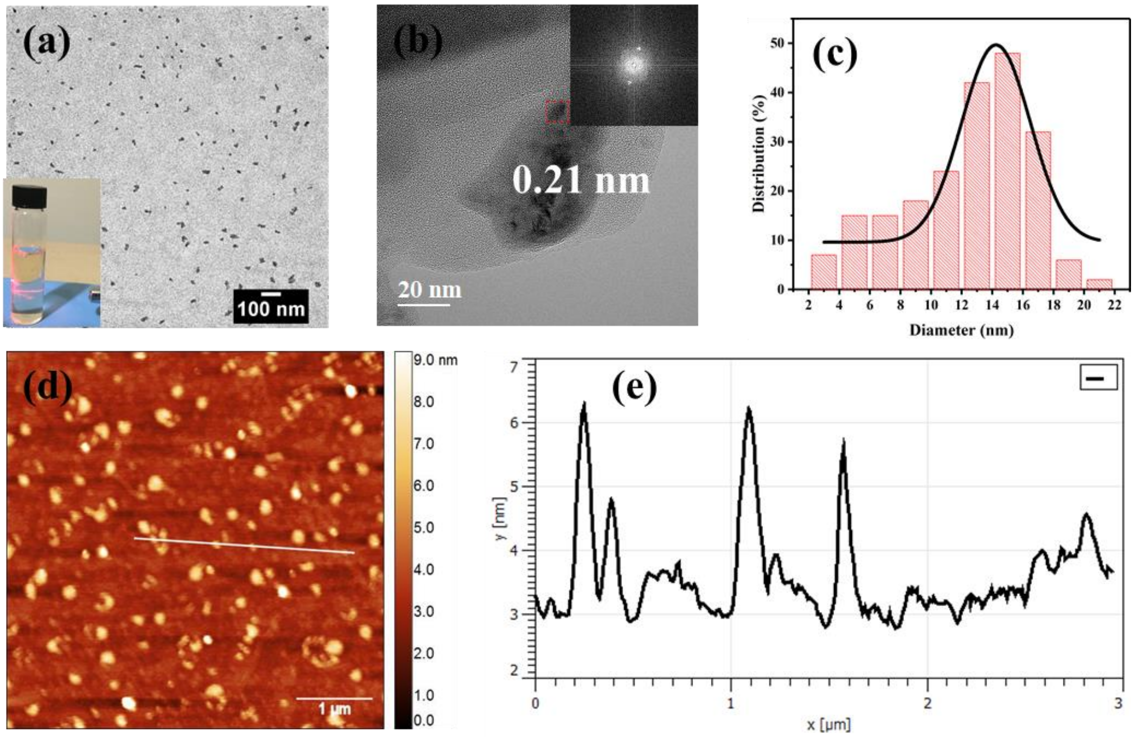

Figure 5.10. (a) TEM image, inset is the Tyndall light scattering effect, (b) HRTEM image (inset is the corresponding FFT of the marked square), (c) histogram showing the size distribution, (d) AFM image and (e) height profile of the BC-500-GQDs obtained by hydrothermal treatment of BC-500 precursor.

The products obtained from the hydrothermal carbonisation of BC-500 precursor are presented in Figure 5.10. The TEM image demonstrates the evenly dispersed quantum dots (BC-500-GQDs) with uniform shape and size distribution. Fine size and even distribution of the quantum dots with no agglomeration can be clearly observed. The careful size measurement of as-synthesised BC-500-GQDs is presented in Figure 5.10c and exhibit a size distribution of 14 ± 2.6 nm. The nanometer particle size and dispersion of the GQDs were verified by light scattering. The Tyndall effect (Figure 5.10a inset) was clearly observed in the colloidal suspension of GQDs in water. The HRTEM image (Figure 5.10b) further reveal that as-prepared BC-500-GQDs show a lattice parameter of 0.21 nm corresponding to (1100) hexagonal lattice plane spacing of graphene (Huang *et al.*, 2020). Inset is the FFT pattern from the marked square in HRTEM. The AFM image (Figure 5.10d) shows the typical topographic morphology of BC-500-GQDs and corresponding height profiles (Figure 5.10e, f) indicate a thickness of 1 to 3 nm, related to 3-9 layers of graphene.

The bulk properties of the GQDs were confirmed by measuring the surface area using gas adsorption. Surface areas was measured using the nitrogen adsorption/desorption method. The BET surface areas of BC-400-GQDs and BC-500-GQDs were 23 and 104 m^2 g^{-1}. The large surface area of BC-500-GQDs further verifies their size is smaller than BC-400-GQDs, which is consistent with the TEM measurements.

5.4.2 Structural studies of GQDs

The structural and electronic properties of as-synthesised GQDs were characterised by spectroscopic methods. The FTIR of both types of GQDs (Figure 5.11a) show a strong absorption due to oxygenated functional groups, consistent with the previous reports (Hu *et al.*, 2013a). The spectra show the presence of hydroxyl (O-H) groups at ~3200 cm^{-1}. A week band at ~2800 cm^{-1} is related to the presence of alkanes (C-H). The carbonyl (C=O) groups were found at ~1685 cm^{-1}. The peak at ~1600 cm^{-1} is attributed to the C=C stretching in alkenes. The band at ~1552 cm^{-1} is attributed to the influence of carboxylate groups. The peak at 1367 cm^{-1} is associated with the presence of C-OH groups. The peaks at ~1230 cm^{-1} and 1097 cm^{-1} are due to C-O stretching in carboxy and alkoxy groups, respectively. The bands at 920 cm^{-1} and 750 cm^{-1} are attributed to the out of plane bending vibration of C-H groups (Si and Samulski, 2008; Acik *et al.*, 2010; Hu *et al.*, 2013a). The number of carboxyl and hydroxyl groups present on the surface of GQDs impart hydrophilic properties and enhance the luminescence. These functional groups make GQDs easily dispersible in water to make a stable suspension. Interestingly, the absence of NO- groups indicates that large amount of nitro groups present in the activated carbon were removed completely from the final product. In addition, the oxygenated functional groups on the surface of GQDs may act as a passivation layer and hinder their agglomeration (Tang *et al.*, 2012).

Raman spectra (Figure 5.11b) of GQDs consist of two distinctive bands: disorder (D) band (1385 cm^{-1}) and crystalline (G) band (1600 cm^{-1}), which are similar to the spectra of BC-500. The D band is related to the defect mediated zone-edge (near K-point) phonons that shows the defects, edges and disorder in the carbon lattice. The G band is associated with the in-plane vibration of sp^2 carbon atoms and usually indicates the crystallinity of the carbon. In graphene, the G band is related to E_{2g} phonons at Brillouin zone center and its frequency decreases with increasing the number of graphene layers (Gupta *et al.*, 2006). Figure 5.11b shows that the intensity of the D band is lower than that of the G band which is in good agreement with graphene where the D band is usually weaker than the G band (Gupta *et al.*, 2006; Kim *et al.*, 2013). An obvious blue shift was also observed for the both bands, as reported previously (Pan *et al.*, 2012). A blue shift of about 17 cm^{-1} was seen for BC-400-GQDs as compared to BC-500-GQDs. The intensity ratios (I_D/I_G) of BC-400-GQDs and BC-500-GQDs are about 0.88 and 0.89, respectively, which show their degree of crystallinity and are in good agreement with the previous reports (Kim *et al.*, 2012; Kim *et al.*, 2013).

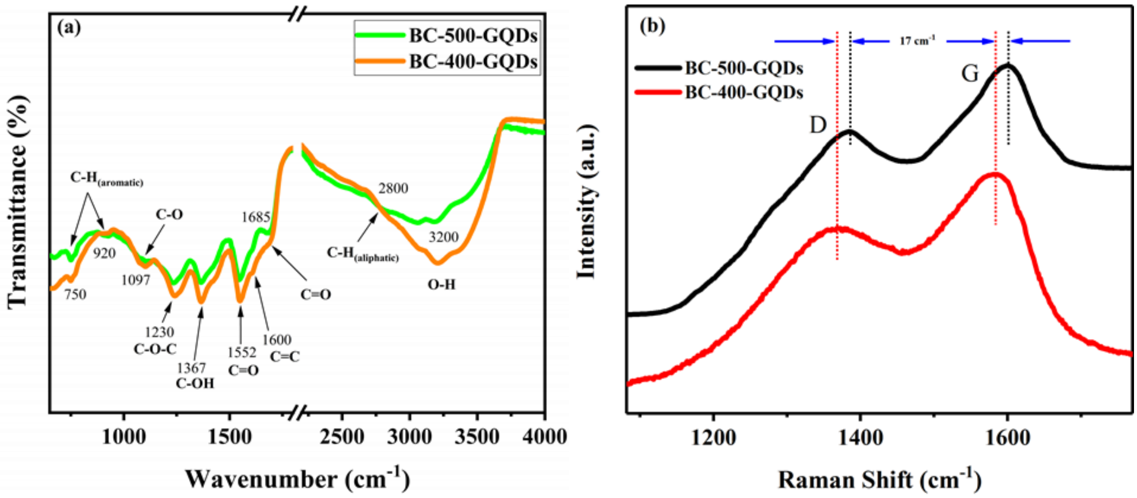

Figure 5.11. (a) FTIR spectra of the BC-400-GQDs and BC-500-GQDs showing different types of functional groups attached on the surface of GQDs. (b) Raman spectra of BC-400-GQDs and BC-500-GQDs with the bands in the range of 1200-1800 cm^{-1} which is typically of carbonised materials.

In order to confirm the products in this study are indeed GQDs and not their carbon dot counterpart, further analysis was performed by various techniques such as XRD, XPS, AFM, etc. Figure 5.12 shows the XRD pattern of the BC-500-GQDs. The XRD pattern of the purified product exhibit one prominent peak at 2θ value of 24-25° corresponding to (002) plane of graphite. This specifies the presence of layered structure, which can be confirmed to be a few layered graphene structure of GQDs. The broad nature of this peak is due to small crystallite size of the GQDs. This is in agreement with the previous reports (Zhang *et al.*, 2012a; Li *et al.*, 2013b; Suryawanshi *et al.*, 2014).

The surface elemental composition of the GQDs was verified by XPS. The survey XPS spectrum of the BC-500-GQDs shows three peaks at about 284.4, 399.4 and 532.4 eV, which are assigned to C1s, N1s and O1s, respectively (Figure 5.13a). The absence of any impurity atoms (Ca, S, etc.) confirms the high purity of the product obtained.

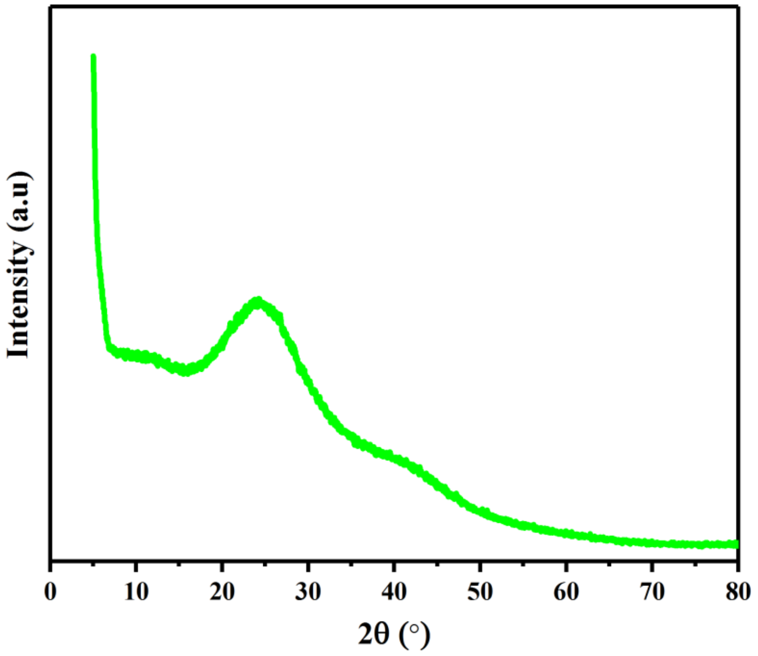

Figure 5.12. The XRD pattern of the purified BC-500-GQDs.

The high resolution C1s spectrum (Figure 5.13b) show three peaks at ~284.8, ~286.5, and ~288.8 eV, which can be attributed to C-C/C=C, C-O-C and O-C=O, respectively (Ding *et al.*, 2015). The N1s spectrum (Figure 5.13c) consist of a single broad bands at ~399.8 eV, corresponding to the traces of pyridinic/pyrrolic nitrogen present in the product (Pels *et al.*, 1995b). The XPS analysis of GQDs shows the absence of N-oxide functionality observed in the activated biochar (see Figure 5.7c). The O1s spectrum (Figure 5.13d) consist of two major peaks at 532.1 and 533.5 eV, which can be attributed to O=C and O-C, respectively (Sevilla and Fuertes, 2009a; Ding *et al.*, 2015).

The XPS elemental analysis indicate that GQDs are mainly composed of C, O and N, which show the high purity of the product. These results are in good agreement with the results of FTIR which shows the presence of oxygenated groups on the surface of biochar. The O/C ratio was found to be ~16%, indicating the oxygenated nature of the GQDs which make them hydrophilic in nature. This is an indication of the formation of GQDs because the carbon dots usually possess high oxygen ratio of over 50% (Baker and Baker, 2010; Li *et al.*, 2012a). On the other hand, the O/C ratio of activated biochar was ~35%. The controlled introduction of oxygen functionalities in GQDs makes their properties controllable. In addition to XRD and XPS results, AFM analysis has shown the thickness of GQDs to be 1-3 nm consisting of 3-9 graphene layers. These results suggest that the product obtained is indeed GQD and not the carbon dot counterpart.

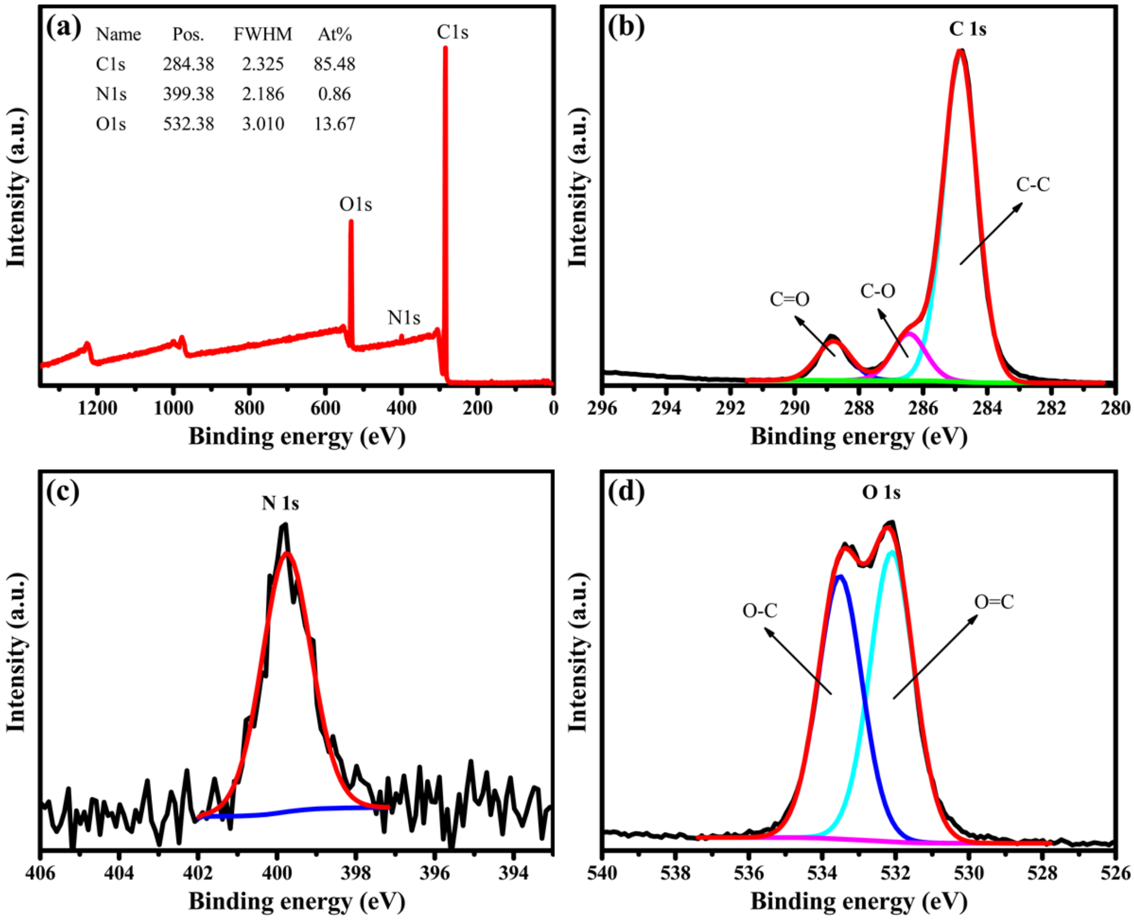

Figure 5.13. The (a) XPS survey, (b) C 1s, (c) N 1s, (d) O 1s high-resolution XPS spectra of BC-500-GQDs.

5.4.3 Photoluminescence and UV Visible absorption studies

The optical properties of GQDs were studied through the analysis of their UV-Visible and photoluminescence spectra. The UV-Vis absorption spectrum of BC-400-GQDs prepared at 200 °C is shown in Figure 5.14a. It can be observed clearly that as-prepared GQDs exhibit a strong absorption in the UV region. A broad absorption band was observed at around 284 to 334 nm with a mean value of about 300 nm which is attributed to the n–π* transition, typically observed in graphene like systems (Suryawanshi *et al.*, 2014).

The photoluminescence properties of GQDs were studied at a range of excitation wavelengths from 350 nm to 410 nm (Figure 5.14b). The as-prepared GQDs exhibit excitation dependent photoluminescence emission as a result of the quantum confinement effect or different functional groups introducing various emissive states (Li *et al.*, 2012a; Ananthanarayanan *et al.*, 2014; Suryawanshi *et al.*, 2014). When excited at 350 nm, the BC-400-GQDs show as excitation peak at 430 nm. BC-400-GQDs exhibit an increase in photoluminescence intensity with a rise in excitation wavelength and the strongest peak is observed at 465 nm when excited at 390 nm (Figure 5.14b). The emission wavelength shows a red shift of 50 nm when the excitation wavelength is varied from 350 to 400 nm (Figure 5.15a). The obvious red-shift of about 50 nm is attributed to the decreased degree of the quantum confinement effect because low energy photons only excite large sized quantum dots with a smaller bandgap (Wang *et al.*, 2016d). The bandgap of BC-400-GQDs based on the strongest emission peak was calculated to be 2.67 eV.

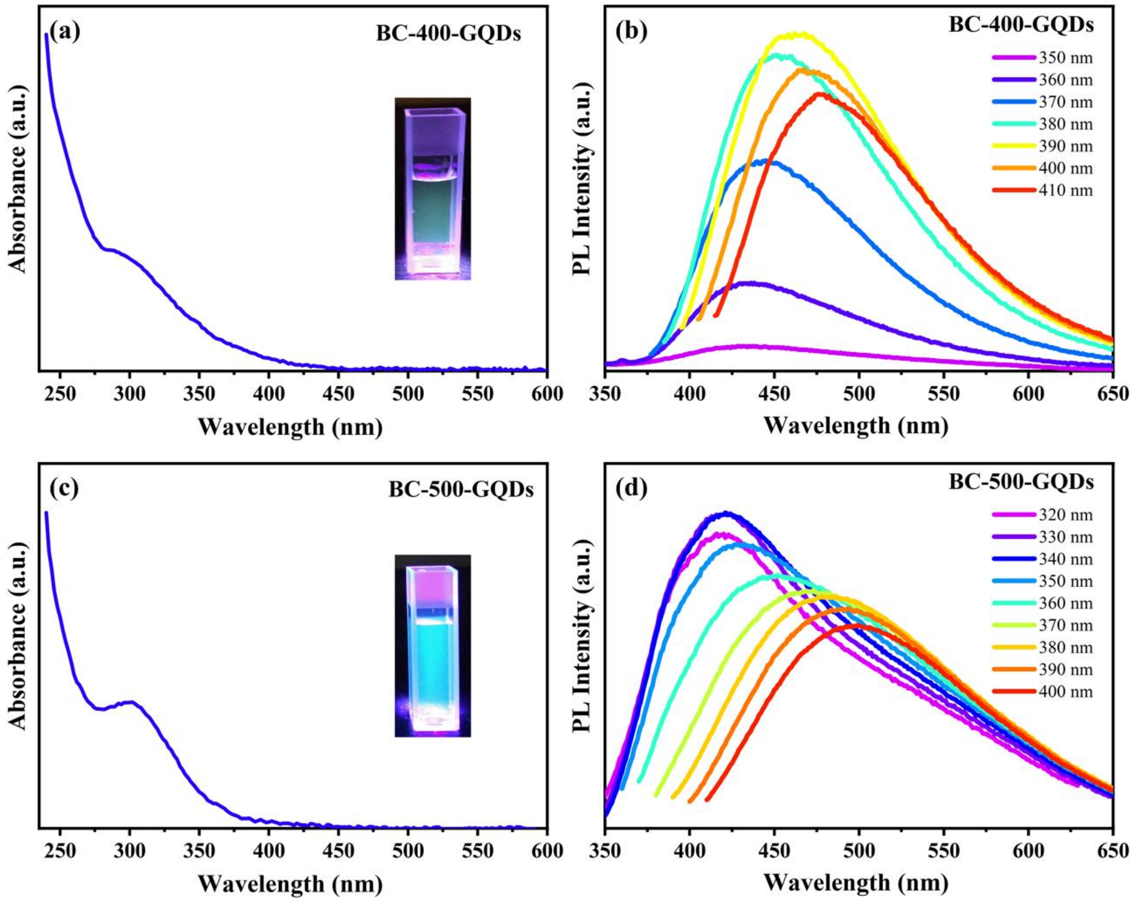

Figure 5.14. (a) UV-Vis absorbance and (b) photoluminescence (PL) spectra of BC-400-GQDs at a range of excitation wavelengths; inset in (a) is the GQDs solution under 365 nm UV light. (c) UV-Vis absorbance and (b) PL spectra of BC-500-GQDs at different excitation wavelengths, inset in (c) is the photograph of BC-500-GQDs solution under 365 nm UV lamp.

The UV-Vis absorption spectrum of BC-500-GQDs showed a strong absorption in the UV range (Figure 5.14c). A deep absorption band was observed at about 295 nm which is attributed to the n–π* transition, usually observed in nanostructured graphene (Suryawanshi *et al.*, 2014). The photoluminescence spectra of BC-500-GQDs are presented in Figure 5.14d. When excited by a 320 nm laser, these GQDs show emission band at around 415 nm. The most intense emission peak was found at 420 nm when excited by 340 nm wavelength, which is consistent with previously reported GQDs (Li *et al.*, 2012c; Kwon *et al.*, 2016). With a change in the excitation wavelength to 400 nm, the photoluminescence emission peak shifts to ~500 nm. With an increase in the excitation wavelength, the emission maxima shift toward the red wavelength regime. The emission wavelength shows a red shift of 80 nm when excitation wavelength is varied from 320 to 400 nm, which is due to a decreased quantum confinement effect in the quantum dots with larger size (Figure 5.15b). Interestingly, it was noted that degree of red shift was gradually decreased with increase in excitation wavelength. This is because the photoluminescence excited by high-energy photons only comes from the small sized GQDs, while the low energy photons mainly excite the GQDs with large size whose quantity and size distribution decreases after the mean value (Figure 5.10c). These excitation dependent emission properties make them suitable building blocks for integration onto devices exhibiting different colors. The band gap of BC-500-GQDs was calculated to be 2.95 eV.

The photoluminescence properties of GQDs indicate a strong relationship with their particle size, which controls their band gap. The band gap of BC-400-GQDs and BC-500-GQDs were calculated to be 2.67 and 2.95 eV based on their strongest emission, respectively. GQDs with smaller size has higher bandgap and therefore require high energy photons for their excitation (Ye *et al.*, 2015). On the other hand, larger size GQDs exhibit a smaller bandgap and can be excited with lower energy photons. Thus, higher energy is required for exciting BC-500-GQDs as compared to BC-400-GQDs.

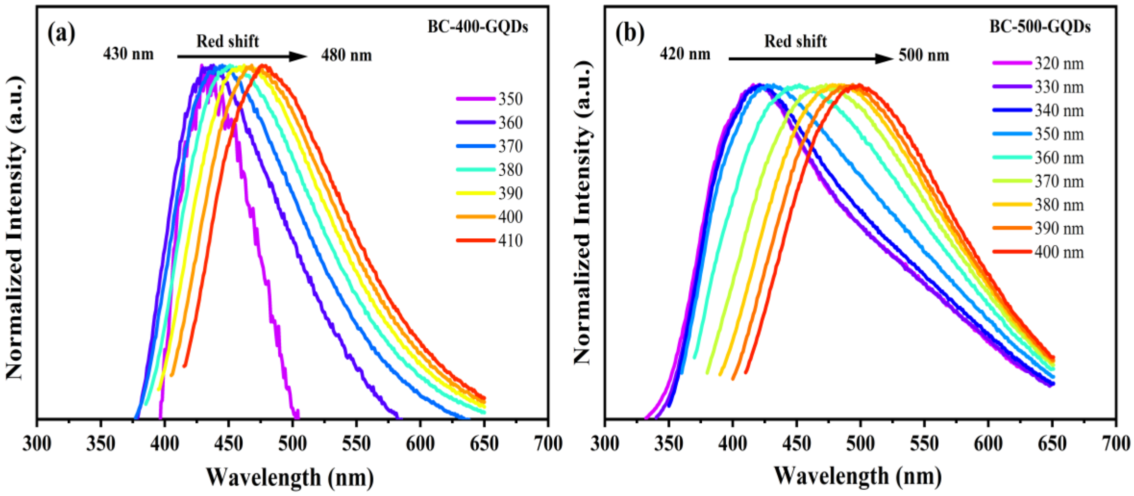

Figure 5.15. (a) The normalised PL spectra of BC-400-GQDs showing a red shift from 430 nm to 480 nm with change in excitation wavelength and (b) normalised PL spectra of BC-500-GQDs showing a red shift of about 80 nm in emission maxima.

Both type of GQDs exhibit variable photoluminescence properties due to different bandgap based on their size, which is in agreement with previous reports (Yan *et al.*, 2010b; Li *et al.*, 2012b; Lee *et al.*, 2013a). A decrease in GQDs size leads to a shift in photoluminescence emission at higher energy (Li *et al.*, 2012a; Tetsuka *et al.*, 2012; Kumar *et al.*, 2014; Sk *et al.*, 2014). Thus, based on our TEM results, small sized BC-500-GQDs exhibit a blue shift in emission maximum (415 nm) compared to large sized BC-400-GQDs (465 nm). This is further confirmed in the inset in Figure 5.14a and c, where the solution of GQDs under 365 nm excitation changes color from light green to sky blue. These results indicate that the bandgap of our GQDs can be tuned by varying their size and thus the photoluminescence properties can be controlled. The tunable photoluminescence properties of our GQDs make them suitable building blocks for a range of applications.

The photoluminescence excitation (PLE) spectra of as-prepared GQDs is presented in Figure 5.16a. The PLE of BC-400-GQDs was recorded at the strongest luminescence emission 465 nm and a broad excitation band at ~330 nm was observed. This PLE band corresponds to the absorption band (290-350nm) of BC-400-GQDs. The PLE spectra of BC-500-GQDs was determined at 415 nm corresponding to the strongest emission maxima. A sharp PLE band was observed at around 310 nm, which is related to the strong absorption band (300 nm) of BC-500-GQDs. Thus, the UV, PL and PLE results of our GQDs are consistent.

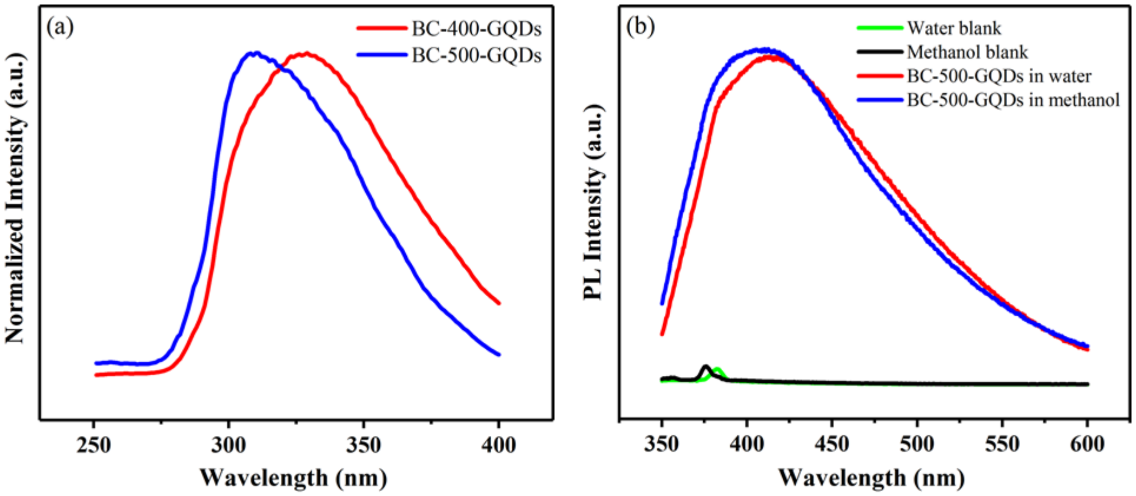

Figure 5.16. (a) The normalised photoluminescence excitation (PLE) spectra of BC-400-GQDs at 465 nm and BC-500-GQDs at 415 nm emission wavelength. (b) Photoluminescence analysis of water (green) and methanol (black) blanks showing no emission, and photoluminescence emission (at 330 nm excitation) of freeze-dried BC-500-GQDs dispersed in water (red) and methanol (blue) exhibiting retention of inherent photoluminescence properties with no significant effect of dispersant.

In order to confirm that the photoluminescence properties were not coming from the dispersant or impurities, the photoluminescence properties of the dispersant (water and methanol) were measured as a control sample. As shown in Figure 5.16b, the blank samples did not show any luminescence with water or methanol only. However, the strong luminesce emission observed upon the addition of BC-500-GQDs in the dispersant and the luminescence properties were independent of the dispersant. The GQDs did not lose their luminescence properties after freeze-drying and the strong emission recovered upon dispersion in solvent.

It has been proposed (Pan *et al.*, 2010; Shen *et al.*, 2011) that the luminescence of GQDs may originate from emissive free zigzag sites having a carbene like triplet ground state, known as $\sigma^1\pi^1$. The carbine ground state multiplicity is associated with the energy difference between π and σ orbitals that should be < 1.5 eV as calculated by Hoffmann (Hoffmann, 1968). The electronic transition of ~310 nm and ~330 nm in the photoluminescence excitation spectra can be attributed to the transitions from σ and π orbitals, namely highest occupied molecular orbitals (HOMO) to lowest unoccupied molecular orbital (LUMO) (Pan *et al.*, 2010). Thus, the photoluminescence spectra of GQDs are related to the decay of activated electrons from LUMO to HOMO. A decrease in the particle size of GQDs result in the blue shift. Moreover, the emission intensity of these GQDs depends upon the degree of reduction, namely the reaction time and temperature, higher degree of reduction could result in photoluminescence quenching. These results are consistent with the previous reports, where the PL intensity is ascribed to the concentration change of small sp^2 carbon clusters with higher band gap embedded in sp^3 matrix during reduction (Eda *et al.*, 2010).

5.5 Summary

An easy approach for the sustainable production of ultra-pure GQDs from a renewable source has been developed. A novel process combines carbonisation, oxidation and nitration with controlled hydrothermal fragmentation that removes the N-oxide groups in the formation of GQDs. The removal of the neutralisation process by the introduction of hot water washing played a key role in the production of highly pure GQDs. The typical topographic morphology of GQDs indicated a thickness of 1 to 3 nm, corresponding to 3-5 layers of graphene. The average sizes of GQDs prepared by hydrothermal treatment of two biochars with HTTs of 400 and 500 °C were 14 ± 2.6 nm and 30.4 ± 4.4 nm. The surface area measurements further verified the TEM results confirming the presence of GQDs in bulk amount (100 mg). The band gaps of the GQDs were 2.95 and 2.67 eV, resulting in the controllable photoluminescence properties. The GQDs exhibited excitation dependent photoluminescence emission with a blue shift in emission with decrease in size of GQDs. This simple synthetic method shows advantages for low cost, sustainability, and the possibility of scale-up to make larger quantities of highly pure GQDs with controllable optical properties. Moreover, the present study highlights the significance of employing low-value biomass resources to produce high-value nanomaterials.

Chapter 6 High yield synthesis of graphene quantum dots as an efficient photoluminescence sensor

Despite many efforts, the product yield of graphene quantum dots (GQDs) is still exceptionally low. In this chapter, the renewable biomass source was utilised for the high yield synthesis of GQDs via microwave treatment. The synthesis approach involved the oxidative cutting of short range ordered carbon derived from the pyrolysis of biomass waste. GQDs were successfully synthesised with a high yield (> 80%), the highest value reported to date for biomass derived GQDs. The synthesised GQDs were highly hydrophilic and exhibited unique excitation independent photoluminescence emission attributed to intrinsic state emission. The prepared GQDs were further modified by simple hydrothermal treatment and employed for the selective and sensitive detection of Fe^{3+} ions with a detection limit of as low as 2.5×10^{-6} M.

This technique has not been reported previously for the synthesis of GQDs from biomass. Moreover, such a high product yield has not been obtained from any other technique for GQDs derived from biomass. Thus, the utilisation of a renewable resource along with simple microwave treatment highlights that green, high yield and cost-effective synthesis of GQDs is possible.

6.1 Preparation and characterisation of GQDs

GQDs were successfully synthesised by oxidative cutting of short range ordered carbon using HNO_3 as an oxidising agent via microwave heating in a short duration. In order to evaluate the effect of microwave power and processing time on the optical properties of GQDs, a thorough study was carried out at a range of microwave powers (100-900 W) and processing times (15-180 min). The optical properties of products were studied by recording their photoluminescence (PL) emission. The PL emission intensities of the products prepared at 100, 300, 500 and 900 W power, and after 15, 30, 60, 120 and 180 min of heating are compared in Figure 6.1. It can be seen clearly that the PL emission intensity of GQDs increases with power up to 500 W and shows a decline with further increase in power to 900 W. This indicates that optical properties of GQDs enhance with microwave power, while a substantial rise in microwave power impose an adverse effect. Similarly, the PL intensity increases with an increase in the processing time up to 120 min and decreases thereafter (Figure 6.1b). These results suggest that the optical properties of GQDs are dependent on their processing time and power. Therefore, the PL intensity increases with power and time up to a certain value and starts declining afterwards.

This is perhaps due to an increase in the cleavage of carbon domains into nanosized quantum dots with increase in power and processing times, while increasing the power and time over a certain limit may result in destruction of the surface and structure of GQDs leading to diminished PL emission. These findings suggest that the intermediate values of 500 W power and 120 min process duration are suggested to be the best conditions for the synthesis of high quality GQDs with excellent optical properties.

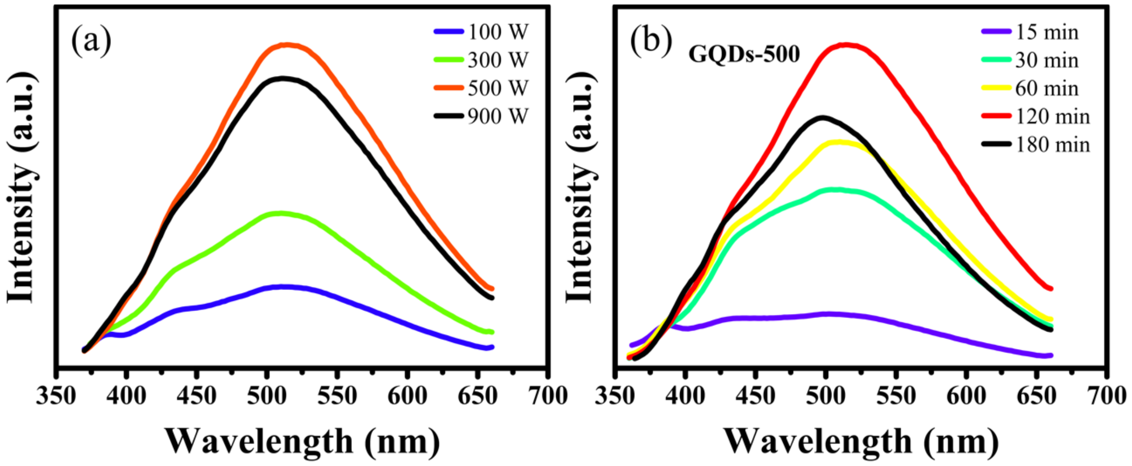

Figure 6.1. Comparison of the effect of (a) microwave power and (b) processing time on the PL emission of GQDs at an excitation wavelength of 340 nm.

For further understanding, the optical properties of GQDs prepared at 500 and 900 W (named as GQDs-500 and GQDs-900) were studied in detail by ultraviolet-visible (UV-Vis) absorption and PL emission spectroscopies. The UV-Vis spectra of GQDs-500 and GQDs-900 are presented in Figure 6.2. Both type of GQDs exhibit strong absorption in the UV range. Nature of both GQDs is similar and show absorption at ~300 nm. However, it can be noticed that the absorption band of GQDs-500 is relatively stronger as compared to that of GQDs-900. This might be due to destruction of the surface structure of GQDs-900 at high microwave power. The peaks observed at about 300 nm are due to n-π* transition of C=O, generally observed in graphene systems (Luo *et al.*, 2009). The non-bonding or ‘n’ electrons are the unpaired electrons on oxygen of the carbonyl group (C=O). Therefore, n to π* transition takes place when one of the unpaired oxygen electrons is excited to the antibonding π* orbital (Aidas *et al.*, 2005).

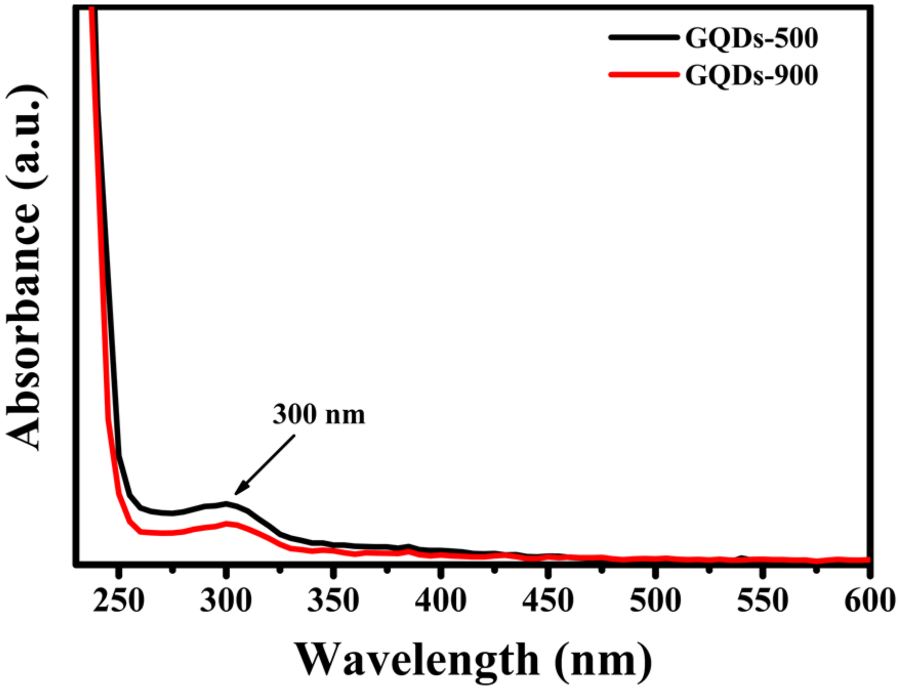

Figure 6.2. UV-Vis spectra of (a) GQDs-500 and (b) GQDs-900 showing a strong absorption in UV range.

The optical emission of GQDs was explored by carrying out a detailed study of luminescence emission at various excitation wavelengths. Figure 6.3 shows the PL spectra of GQDs-500 and GQDs-900 at various excitation wavelengths. Both type of GQDs exhibit excitation independent PL emission at a range of excitation wavelengths from 300 to 400 nm. When excited by 300 nm excitation wavelength, the GQDs-500 display a weak PL emission with a peak at ~514 nm. The PL intensity of GQDs-500 increases gradually with increase in the excitation wavelength and exhibit a strongest emission at 340 nm excitation. The PL intensity decreases thereafter but this decline reduces gradually and stabilises at about 390 nm. Therefore, the PL intensities at 390 and 400 nm excitation are almost the same. Similarly, GQDs-900 also show PL emission having a peak at ~514 nm. The PL intensity of GQDs-900 also variates with change in the excitation wavelength and shows a strongest emission at ~514 nm when excited by 340 nm incident light. These results suggest that both types of these quantum dots are similar in nature, although the PL intensity of GQDs-500 is stronger as compared to GQDs-900.

The optical bandgap of these GQDs was calculated based on the UV-Vis absorbance spectra using Tauc plot (Tauc *et al.*, 1966) as follows:

$$(\alpha h\upsilon)^{1/\gamma} = A(h\upsilon - E_g) \tag{6.1}$$

where, α is optical absorption coefficient, h is Planck’s constant, υ is frequency of light, A is a constant and E_g is optical bandgap. The γ factor depends on the nature of material and is equal to 1/2 for direct bandgap materials and 2 for indirect bandgap materials. The optical bandgap was determined from the curve of $(\alpha h\upsilon)^{1/\gamma}$ versus photon energy $h\upsilon$ converted from the UV-vis spectra. The linear segment of the curve was extrapolated to x-axis and interception point gave an estimate of the bandgap. The direct bandgap values of both type of GQDs were calculated to be ~5.12 eV.

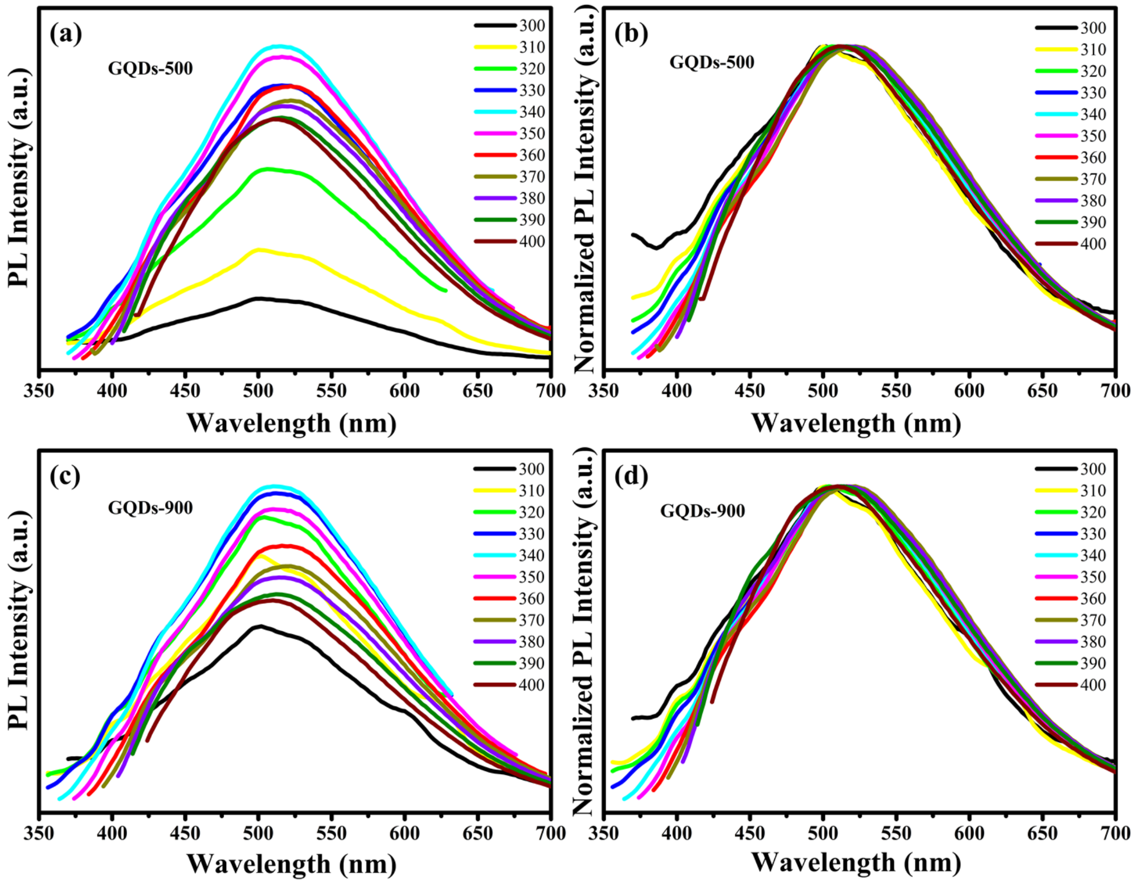

Figure 6.3. (a) Photoluminescence (PL) spectra of GQDs-500 at different excitation wavelengths and (b) their normalised PL spectra exhibiting excitation independent emission with no shift in the PL peak position. (c) PL spectra of GQDs-900 (d) their normalised PL spectra showing no shift in PL peak position.

Most of the carbon based quantum dots exhibit excitation dependent photoluminescence emission (Pan *et al.*, 2010; Li *et al.*, 2011a; Tetsuka *et al.*, 2012; Abbas *et al.*, 2018; Wu *et al.*, 2018; Yan *et al.*, 2018; Yuan *et al.*, 2018; Atchudan *et al.*, 2020; Das *et al.*, 2020). Their PL emission peak position changes with a change in excitation wavelength. However, it is interesting to note that GQDs prepared through the present approach demonstrate an excitation independent emission. The PL intensity changes with change in excitation wavelength for both type of GQDs, however, they exhibit excitation independent photoluminescence emission. When the excitation wavelength is changed from 300 to 400 nm, the intensity of photoluminescence emission increased to a maximum at 340 nm excitation and then further decreased, however the peak position did not shift and remained fix at ~514 nm. In order to analyse the peak shifting, the PL spectra was normalised to the maximum of strongest emission (340 nm excitation). The normalised PL spectra in Figure 6.3b and d show no shifting in peak positions with change in excitation wavelength and further confirm the independency of PL emission from the excitation wavelength. This characteristic of the present GQDs is different from other carbon based quantum dots (Pan *et al.*, 2010; Li *et al.*, 2011a; Zhu *et al.*, 2011a; Tetsuka *et al.*, 2012). Therefore, it requires more in-depth understanding of their formation mechanism.

Several mechanisms have been presented which explain the origin of photoluminescence emission of carbon quantum dots. The most common ones involve oxygenated functional groups, quantum size, zigzag edge sites, defect effects and recombination of electron-hole pairs (Wunsch *et al.*, 2008; Zhu *et al.*, 2012; Yang *et al.*, 2014a; Ding *et al.*, 2015; Sun *et al.*, 2015). Most of the GQDs produced so far exhibit excitation dependent emission which is generally attributed to emissive traps and defect states (Zhang *et al.*, 2016). However, the zigzag edge sites, quantum size and recombination of electron-hole pairs are regarded as intrinsic state emission and generate excitation independent emission (Maiti *et al.*, 2017). It was reported (Ye *et al.*, 2013; Zhang *et al.*, 2016) that the photoluminescence emission from GQDs at 500-530 nm is mainly attributed to the conjugated carbon skeleton containing zigzag edge sites. Thus, the excitation independent emission of the present GQDs at 514 nm can be attributed to the zigzag sites and recombination of electron-hole pairs. Thus, it may be suggested that the present GQDs prepared via microwave irradiation do not have considerable emissive traps or defects and exhibit PL due to intrinsic state emissions (Buzaglo *et al.*, 2015; Maiti *et al.*, 2017).

The effect of microwave power and treatment time on the product yield was systematically studied. The product yield was recorded for each treatment and the results are summarised in Table 6.1.

Table 6.1. Values of the product yield obtained at different microwave powers and time periods.

Microwave Power (W)	Microwave duration (min)	Product Yield (%)
500	15	5
	30	20
	60	25
	120	73
	180	84.5
900	15	10
	30	33
	60	80
	120	84

The product yield of both types of GQDs increased with increasing the reaction time. The highest product yield of around 84% was achieved for a reaction time of 180 min at microwave power of 500 W or 60 min at 900 W power. These results suggest that higher microwave power could induce the rapid cutting of carbon domains into GQDs, resulting in high yield in short duration. To the best of the author’s knowledge, these are the highest values of product yield reported to date for the synthesis of GQDs from biomass waste. The product yields of GQDs derived from various biomass precursors are summarised in Table 6.2.

Table 6.2. Comparison of the product yield of quantum dots derived from various biomass-based precursors.

Precursor	Product	Synthesis approach	Product yield (wt %)	Ref.
Spent tea derived carbon	GQDs	Microwave treatment	5 – 84.5	Present work
Plant leaf extract	N-GQDs	Hydrothermal treatment	25.2	(Roy *et al.*, 2014)
Paper lignin	GQDs	Pyrolysis	8.74 – 18.02	(Wang *et al.*, 2019)
Neem leaves	GQDs	Pyrolysis	-	(Suryawanshi *et al.*, 2014)
Rice-husk carbon	GQDs	Pyrolysis + Hydrothermal treatment	15	(Wang *et al.*, 2016d)
Coffee grounds	GQDs	Hydrothermal treatment	33	(Wang *et al.*, 2016a)
Durian	S-GQDs	Hydrothermal treatment	6.8%	(Wang *et al.*, 2018a)
Alkali lignin	GQDs	Hydrothermal treatment	21	(Ding *et al.*, 2018)
Garlic	CQDs	Hydrothermal treatment	-	(Zhao *et al.*, 2015b)

Fresh tomato	Carbon dots	Microwave pyrolysis	-	(Liu *et al.*, 2017)
Coconut shells	CQDs	Hydrothermal treatment	-	(Adinarayana *et al.*, 2017)
Chitosan	CQDs	Hydrothermal treatment	10	(Liang *et al.*, 2016)
Taxus leaves	Carbon dots	Hydrothermal treatment	1	(Liu *et al.*, 2020a)

The structural studies of GQDs were performed by TEM analysis. The TEM images along with particle size distribution of GQDs-500 and GQDs-900 are presented in Figure 6.4.

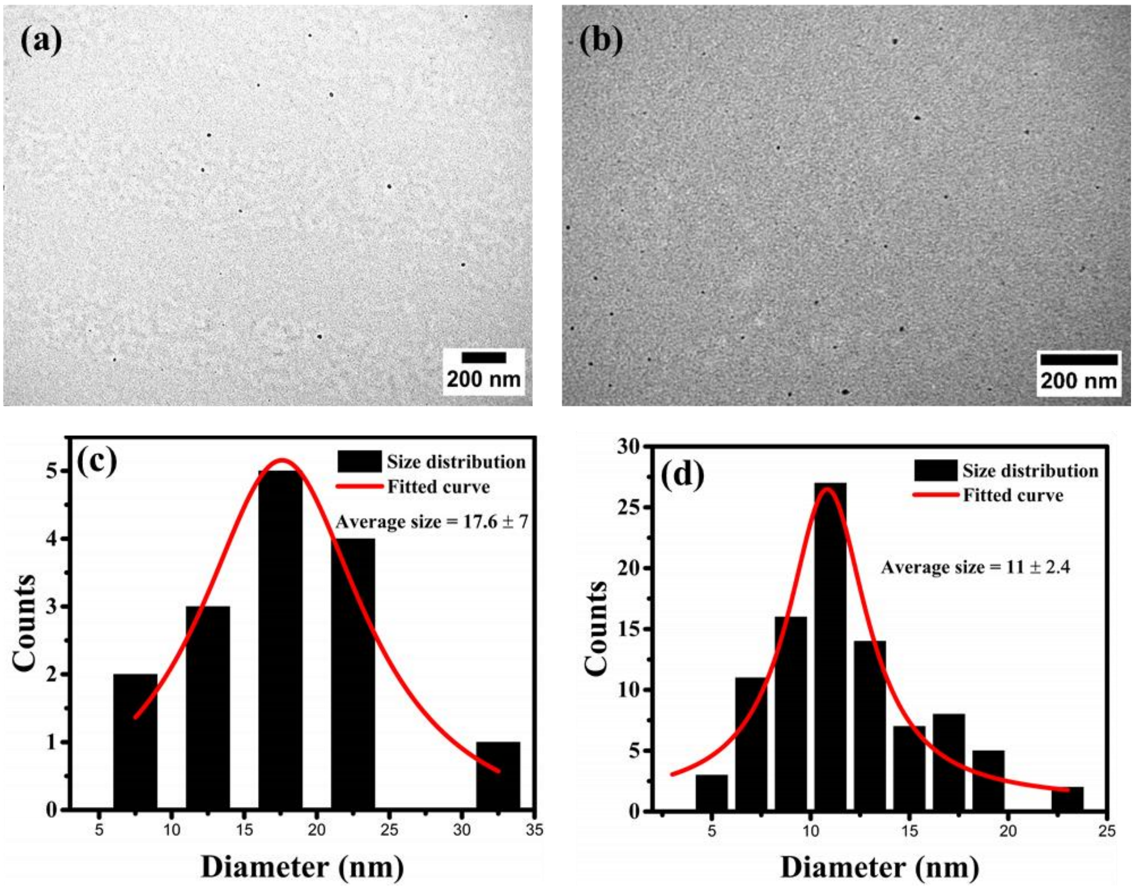

Figure 6.4. TEM images and respective particle size distribution of (a, c) GQDs-500 and (b, d) GQDs-900, calculated with ImageJ using several images.

The TEM results verify the synthesis of nano sized quantum dots by microwave treatment. The as-prepared quantum dots are well dispersed and possess almost spherical shape. The careful size measurements using software ‘ImageJ’ show that the GQDs-500 are in the size range of ~6 to ~34 nm. The average size was calculated to be ~17.6 nm. On the other hand, the GQDs-

900 exhibit a size range of 4 to 24 nm, with an average of 11 nm. The size measurements show that the overall size of GQDs-900 prepared at 900 W was smaller as compared to the size of GQDs-500 prepared at 500 W. This suggests that higher power will break the carbon skeleton more significantly and generate smaller particles. However, the GQDs-900 were not as spherical as their GQD-500 counterparts. That is perhaps due to significant deterioration of carbon domains at high power leading to irregular shaped articles.

6.2 Property and structural studies of modified GQDs.

The GQDs-500 and GQDs-900 were further modified by hydrothermal treatment and denoted as "GQDs-500-M" and "GQDs-900-M", where 'M' indicates the modified version. The optical properties of modified GQDs were also comprehensively studied by UV-Vis and PL spectroscopies. The UV-Vis spectra of GQDs-500-M and GQDs-900-M are displayed in Figure 6.5. The results indicate that UV absorption of GQDs-500-M is much stronger as compared to GQDs-900-M, consistent with the observations of their unmodified forms (Figure 6.2). The absorption peaks are observed at ~275 nm, which are attributed to π-π* transition in aromatics (Hasan *et al.*, 2018). It is worth noting that absorption spectra of modified GQDs show a blue shift as compared to their unmodified counterparts. This is possibly due to reduction in size after modification, as the smaller sized GQDs exhibit blue shift in their absorption (Lai *et al.*, 2020).

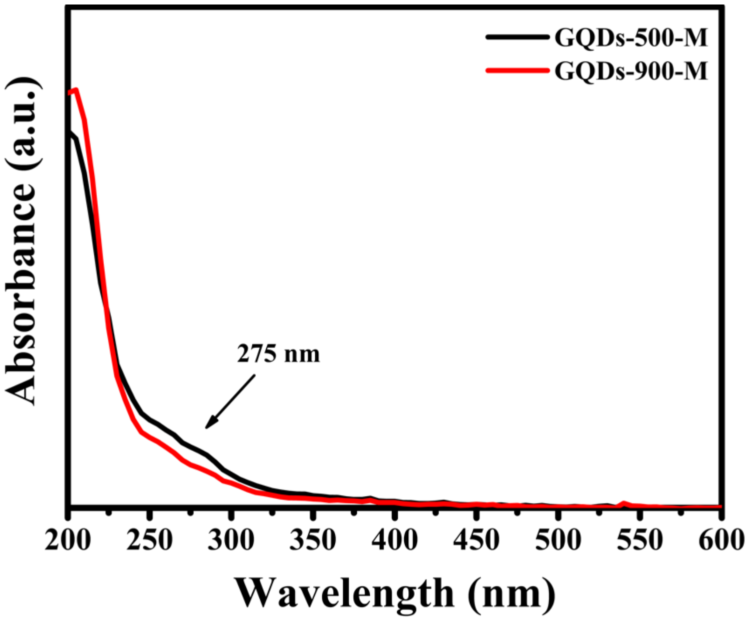

Figure 6.5 UV-Vis spectra of modified GQDs showing a strong absorption for GQDs-500-M as compared to GQDs-900-M.

The modified GQDs were further characterised by PL spectroscopy. Figure 6.6 shows the PL emission of modified GQDs at a range of excitation wavelengths. The as-prepared modified GQDs exhibit excitation dependent photo luminescence emission which is known to result from the quantum confinement effect due to particle size distribution, or different functional groups introducing various emissive states (Li *et al.*, 2012a; Ananthanarayanan *et al.*, 2014; Suryawanshi *et al.*, 2014). When excited by 340 nm laser, the GQDs-500-M show peak emission at a wavelength of 430 nm. The emission wavelength is higher than the excitation, which is known as Stokes shift. The GQDs-900-M also show a strong emission peak at 430 nm when excited by 330/340 nm. However, another small hump is also observed at about 520 nm, possibly due to some surface impurities or emissive traps. This abnormal behaviour of GQDs-900-M further suggest their distorted surface structure.

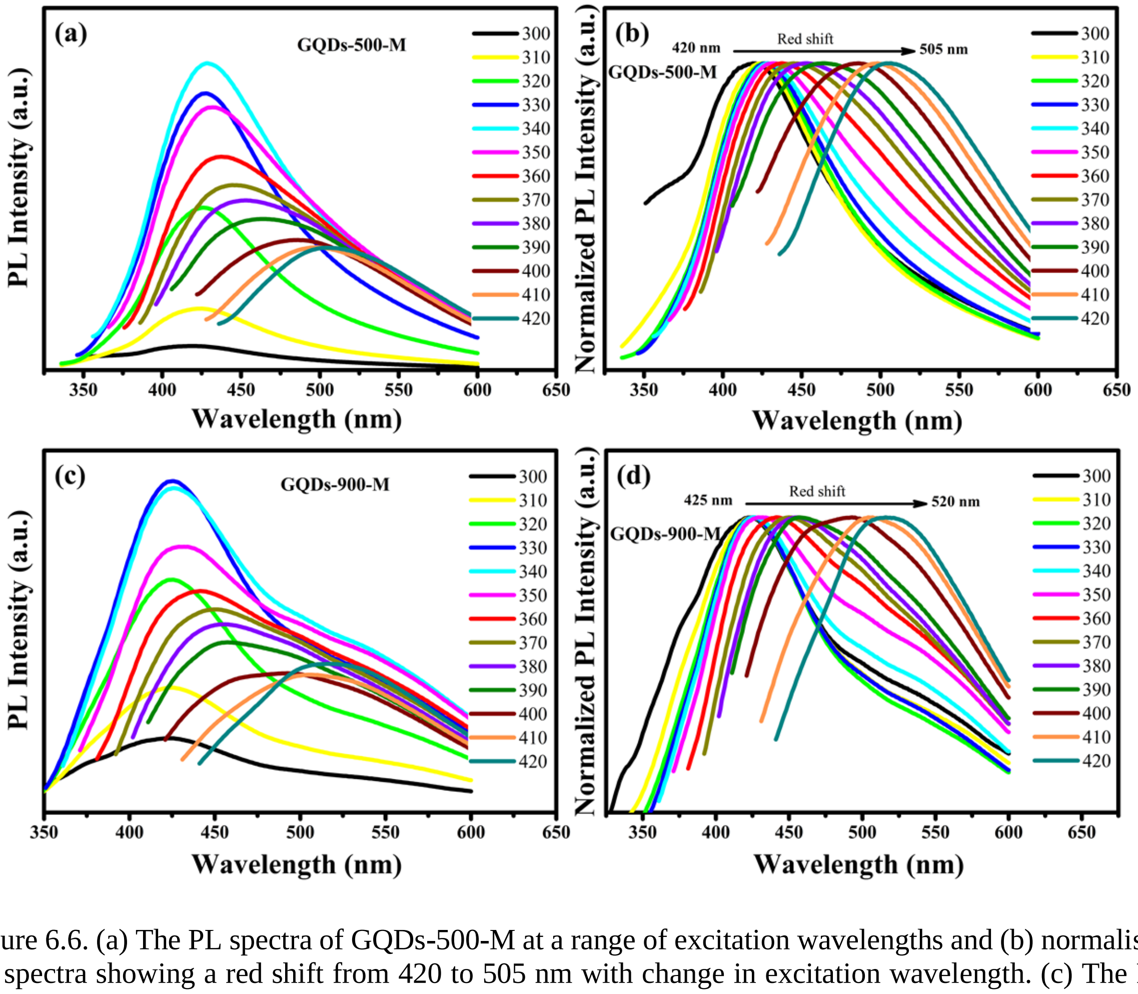

Figure 6.6. (a) The PL spectra of GQDs-500-M at a range of excitation wavelengths and (b) normalised PL spectra showing a red shift from 420 to 505 nm with change in excitation wavelength. (c) The PL spectra of GQDs-900-M at various excitation wavelengths and (d) normalised PL spectra displaying a red shift from 425 to 520 nm.

It is important to note that the emission peak position changes with change in excitation wavelength for both type of GQDs. When the excitation is changed from 300 to 400 nm in case of GQDs-500-M, the emission peak shifts from 420 to 505 nm, showing a red shift of 85 nm. While in case of GQDs-900-M, the emission peak shows a red shift of 95 nm. Thus, these GQDs show luminescence in a wide wavelength range. This property suggests the use of these GQDs in multicolour imaging applications.

The decreased PL intensity towards higher wavelength region for both type of GQDs is attributed to the decreased degree of quantum confinement in that region because low energy photons only excite large sized quantum dots (Wang *et al.*, 2016d). Thus, the higher wavelength excitations only generate emission in large sized GQDs. Since the bandgap of GQDs decreases with an increase in their size, low energy photon generates excitation in them, leading to a low intensity emission. Therefore, the intensity of emission declines as we go to the higher wavelength region. The band gap of both type of modified GQDs based on the absorption band was calculated to be 5.4 eV. It has been reported that n–π^* transition of carbonyl or carboxyl groups connected to carbon nanostructured materials generate PL emission around 430 nm when excited by 340 nm laser (Miao *et al.*, 2018). It is important to note that PL spectra of modified GQDs demonstrate a blue shift (>90 nm) as compared to their unmodified forms. The bandgap also shows a blue shift and increases from 5.12 to 5.4 eV. These findings suggest the reduction in size of GQDs after modification.

The structure and size distribution of modified GQDs were studied by TEM analysis. The low and high magnification TEM images of the GQDs-500-M are presented in Figure 6.7. The images show a drastic decrease in the size of modified GQDs as compared to their unmodified type. The high magnification TEM image (Figure 6.7 b) further shows that the particles are well dispersed and exist in a narrow size range. The size of these GQDs was calculated using ImageJ and the results are presented in Figure 6.7c. The results show that the size of GQDs-500-M fall in the range of 0.5 to 3.5 nm, with an average of 1.6 ± 0.55 nm. The results show a very narrow size distribution. The high resolution TEM image (Figure 6.7d) further reveals the crystalline structure of modified GQDs. The lattice spacing were calculated to be ~0.24 nm corresponding to ($11\bar{2}0$) plan of graphene (Wang *et al.*, 2016d)

It is well known that the photoluminescence properties have direct relationship with the size of GQDs due to quantum confinement effect (Sk *et al.*, 2014; Lai *et al.*, 2020{Zhu, 2017 #657)}. The band gap increases with a decrease in the size of the quantum dots and thus higher energy photons are required to generate excitation. Thus, GQDs with lower size are excited by lower wavelength photons and emit light in the blue region. The photoluminescence emission shifts towards blue with a decrease in the size of GQDs. The photoluminescence properties of GQDs-500-M verifies this here. The strongest emission of GQDs-500 with size range of 17 nm, was found at 520 nm, while the same quantum dots exhibit strongest emission at 420 nm after modification owing to the decrease in size down to 1.6 nm.

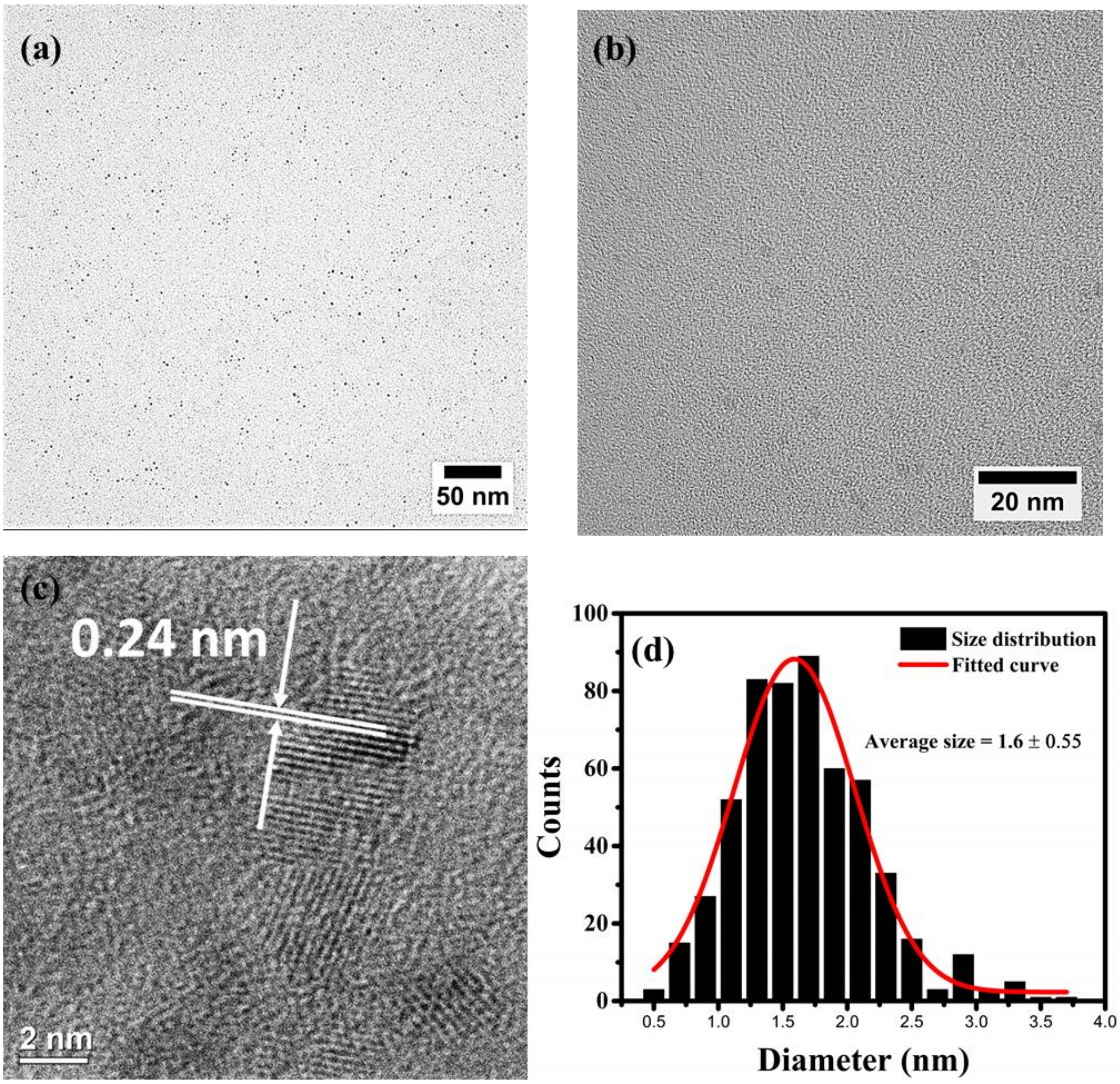

Figure 6.7. (a) Low magnification TEM image, (b) high magnification TEM image, (c) HRTEM image and (d) calculated size distribution of the GQDs-500-M.

The structural characterisation of GQDs was performed by Raman and FTIR analysis. Raman spectra (Figure 6.8) of GQDs-500-M and GQDs-900-M consist of two distinctive bands at about 1356 and 1569 cm^{-1}, known as disorder (D) band and crystalline (G) band, respectively. The D and G bands in the range of 1200-1800 cm^{-1} are indicative of a carbonaceous structure (Ferrari and Basko, 2013; Kim *et al.*, 2013).

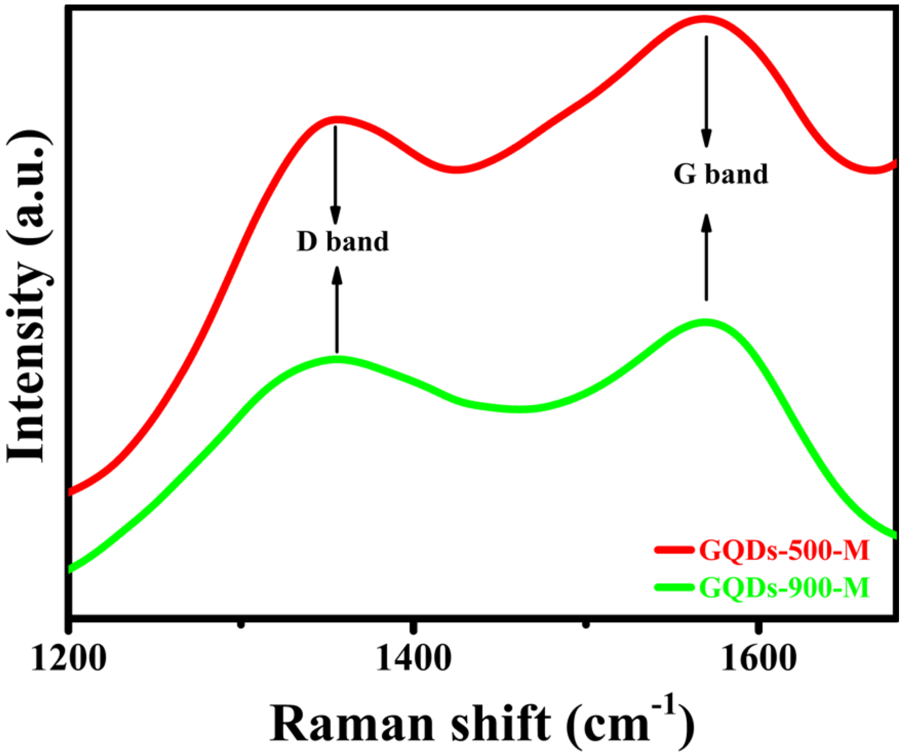

Figure 6.8. Raman spectra of GQDs-500-M and GQDs-900-M showing the bands in the range of 1200-1800 which are typically of carbonised materials.

The D band is related to the defect mediated zone-edge (near K-point) phonons that shows the defects, edges and disorder in the carbon lattice. The G band is associated with the in-plane vibration of sp^2 carbon atoms and usually indicates the crystallinity of the carbon (Tuinstra and Koenig, 1970). In graphene, the G band is related to E_{2g} phonons at Brillouin zone centre (Gupta *et al.*, 2006). The Intensity of G band provides useful information about the size of GQDs. Its intensity increases with increase in size of GQDs (Kim *et al.*, 2013). The intensity ratio of D band and G band (I_D/I_G) shows the density of disorder in the structure of carbon (Tuinstra and Koenig, 1970; Ferrari and Robertson, 2000). The I_D/I_G values of GQDs-500-M and GQDs-900-M are ~0.96 and ~0.98, which show their defective structure, possibly arising from the edge states at the periphery of GQDs (Kim *et al.*, 2013). These results are in good agreement with previously reported GQDs (Kim *et al.*, 2013; Yan *et al.*, 2018; Das *et al.*, 2020).

Figure 6.9 shows the FTIR spectra of GQDs-500-M and GQDs-900-M. The spectra of both type of GQDs shows a broad band at ~3300 cm^{-1} corresponding to the stretching vibrations of hydroxyl (O-H) groups. The peaks at ~1630 and ~1560 cm^{-1} are related to the stretching vibrations of C=O in carbonyl groups and stretching vibrations of C=C in aromatic groups. The multiple peaks at 1350-1500 cm^{-1} are attributed to the bending vibrations of C-C/C-H in alkanes. The bands at 1100-1250 cm^{-1} are due to stretching vibrations of C-O in ethers, esters, carboxylic acid and alcohols. A broad band at ~1000 cm^{-1} corresponds to the C-O stretching of ether group (Hu *et al.*, 2013a; He *et al.*, 2019). These results suggest large amount of oxygenated functional groups on the surface of both type of GQDs. These functional groups make them hydrophilic in nature and render them highly soluble in water.

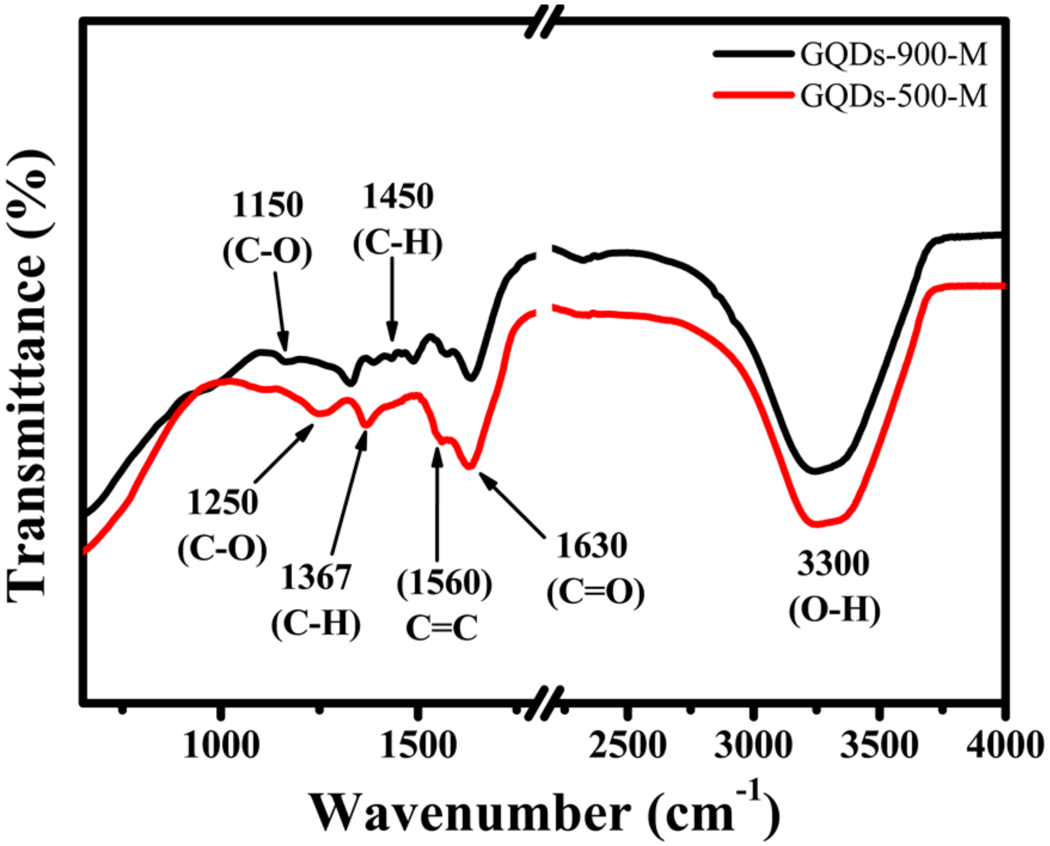

Figure 6.9. FTIR spectroscopy of GQDs-500-M and GQDs-900-M

The surface functionalization and elemental composition of the GQDs-500-M was further confirmed by X-ray photoelectron spectroscopy (XPS). The survey XPS spectrum shows three major peaks at 285.08, 400.08 and 532.08 eV, which are designated to C1s, N1s and O1s, respectively (Figure 6.10a). Another small peak at 347.08 eV associated with Ca 2p is also observed. The XPS elemental analysis reveals that the GQDs-500-M are mainly composed of C (55.15 at%), O (37.83 at%) and N (4.94 at%), with a limited amount of Ca from the feedstock.

The high resolution C1s spectrum (Figure 6.10b) can be deconvoluted into three peaks at ~284.9, ~286.2, and ~288.4 eV, corresponding to C-C/C=C, C-O-C and O-C=O groups, respectively (Ding *et al.*, 2015).

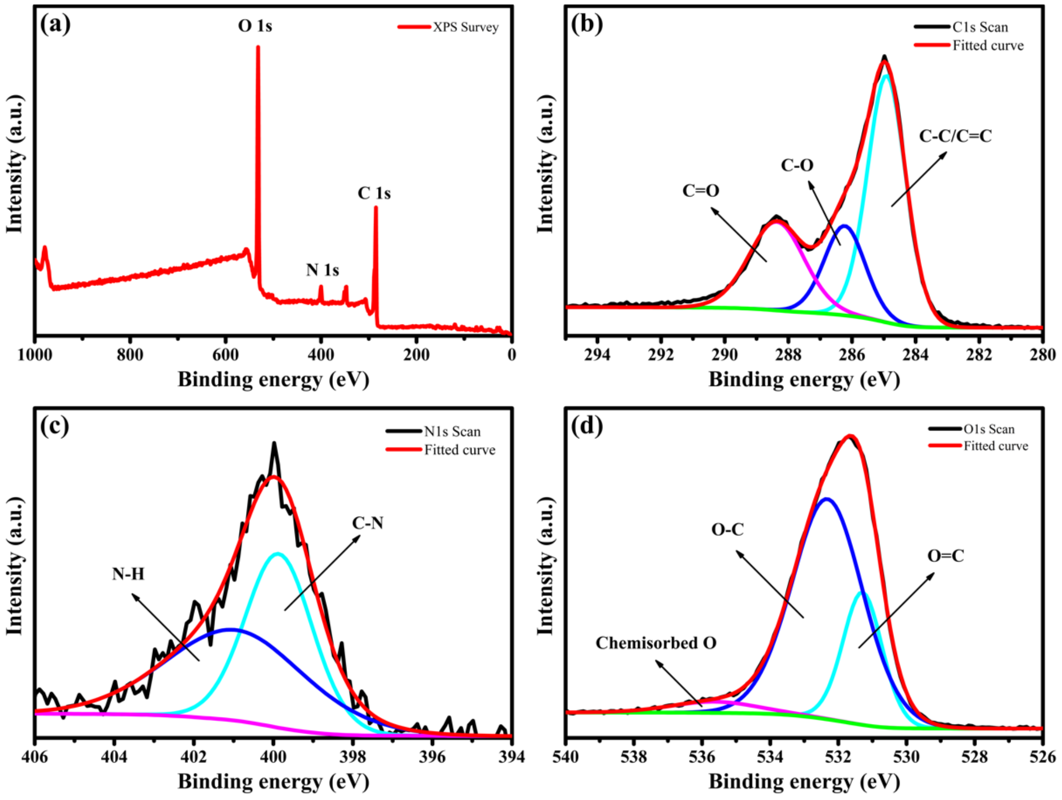

Figure 6.10. (a) XPS survey spectrum, (b) C1s, (c) N1s and (d) O1s high resolution spectra of GQDs-500-M, showing extensive number of oxygenated functionalities.

The N1s spectrum (Figure 6.10c) can be fitted into two broad bands at ~399.8 and ~400.9 eV, which can be attributed to the pyridinic (C-N-C) and pyrrolic (N-H) nitrogen species, respectively (Pels *et al.*, 1995b) The O1s spectrum (Figure 6.10d) consist of two major peaks at 531.3 and 532.3 eV, which can be ascribed to O=C and O-C, respectively (Sevilla and Fuertes, 2009a; Ding *et al.*, 2015). Another small peak at ~535.6 eV is related to chemisorbed oxygen or water. These results suggest the extensive presence of oxygenated functional groups in the matrix of modified GQDs, making them highly soluble in water with good stability. No detectable changes were observed in the GQDs after storing for two months.

6.3 Application as PL sensor

The as-synthesised GQDs exhibit strong photoluminescence and specific oxygenated surface functionalisation. The presence of these functional groups resulted in the hydrophilicity of the GQDs leading to good solubility in water (Hsu and Chang, 2012; Deka *et al.*, 2018; Wu *et al.*, 2018). Owing to the presence of these functional groups and strong emission, these GQDs were expected to be an ideal candidate for fluorescence sensing.

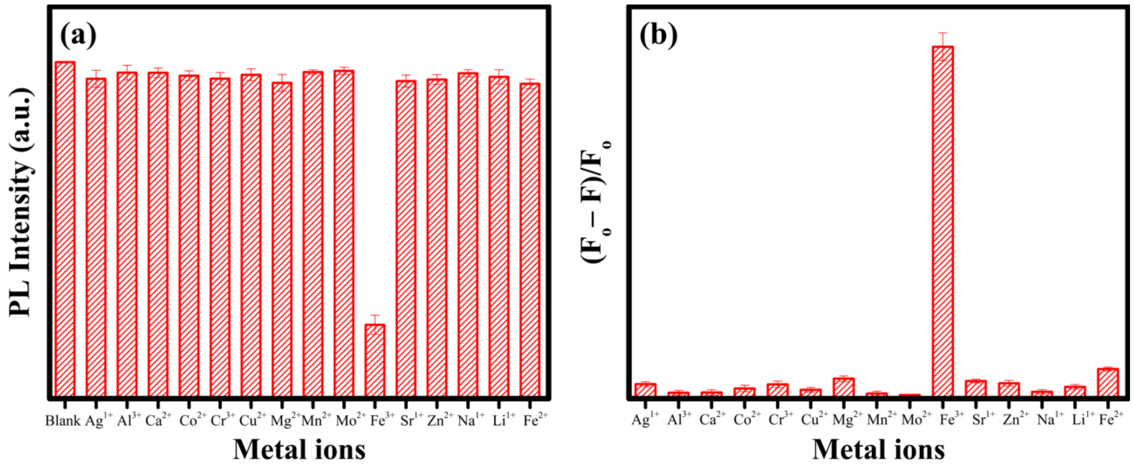

Figure 6.11. (a) Comparison of the photoluminescence (PL) intensities of GQDs-500-M in the presence of different metal ions (100 µM) at an excitation wavelength of 340 nm. (b) The comparison of the affinity of different metal ions towards GQDs-500-M (F_0 and F are the photoluminescence intensities of GQDs-500-M without and with 100 µM of different metal ions).

Among the various heavy metal ions, the detection and removal of ferric ions have always attracted extensive attention (Dutta Chowdhury and Doong, 2016; Das *et al.*, 2020; Lesani *et al.*, 2020). Generally, iron plays a key role in human life and its deficiency requires considerable attention among the global micronutrient deficiencies. Moreover, the iron percentage has to be monitored and balanced in biological and environmental systems (Sun and Lei, 2017). To achieve this, several researchers employed the quenching phenomenon of carbon quantum dots by the addition of Fe^{3+} (Ananthanarayanan *et al.*, 2014; Das *et al.*, 2020; Lesani *et al.*, 2020). The quenching percentage is related to the concentration of Fe^{3+}. In this study, the selective sensing of Fe^{3+} was performed by GQDs-500-M using 100 µM concentration of fourteen different metal ions: Ag^{1+}, Al^{3+}, Ca^{2+}, Co^{2+}, Cr^{3+}, Cu^{2+}, Mg^{2+}, Mn^{2+}, Mo^{2+}, Fe^{3+}, Sr^{1+}, Zn^{2+}, Zr^{1+}, Li^{1+}. The as-synthesised GQDs-500-M solution exhibited a strong photoluminescence at 422 nm when excited by a wavelength of 340 nm (Figure 6.6a). The photoluminescence intensities of GQDs-500-M were recorded with the addition of different metal ions. As shown in the Figure 6.11a, comparing with the control (blank) sample, the photoluminescence of GQDs was remarkably quenched only by the ferric ions among fourteen different metal ions. These results suggest the highly selective detection of Fe^{3+} by the as-prepared GQDs-500-M.

The mechanism of photoluminescence quenching is related to the strong affinity of Fe^{3+} ions towards the hydroxyl/carboxyl groups of GQDs-500-M, leading to a stable complex (Atchudan *et al.*, 2020). The photoluminescence quenching occurs when the excited electron in GQDs partially transfers to the d orbital of Fe^{3+} instead of undergoing radiative relaxation (Atchudan *et al.*, 2020). The affinity (coordination) of numerous metal ions toward GQDs-500-M was evaluated systematically under similar experimental conditions. Figure 6.11b shows that the ferric ions exhibit strongest affinity towards GQDs-500-M among fourteen different metal ions, suggesting its potential for selective sensing by GQDs-500-M. Thus, further study was carried out to investigate the effect of Fe^{3+} concentration on the fluorescence intensity. The photoluminescence spectra of GQDs-500-M with different concentration of Fe^{3+} is shown in Figure 6.12a. The spectra indicate that the photoluminescence intensity of GQDs-500-M is very sensitive to the concentration of Fe^{3+}. The photoluminescence intensity decreases with increase in the concentration of Fe^{3+}. Thus, the quenching efficiency of Fe^{3+} was determined by $(F_0 – F)/F_0$, where F_0 and F are the photoluminescence intensities of blank and with different concentrations of metal ions, respectively. A quick photoluminescence quenching with Fe^{3+} was observed, therefore the quenching test was performed at low concentration range from 1 to 50 µM of Fe^{3+}.

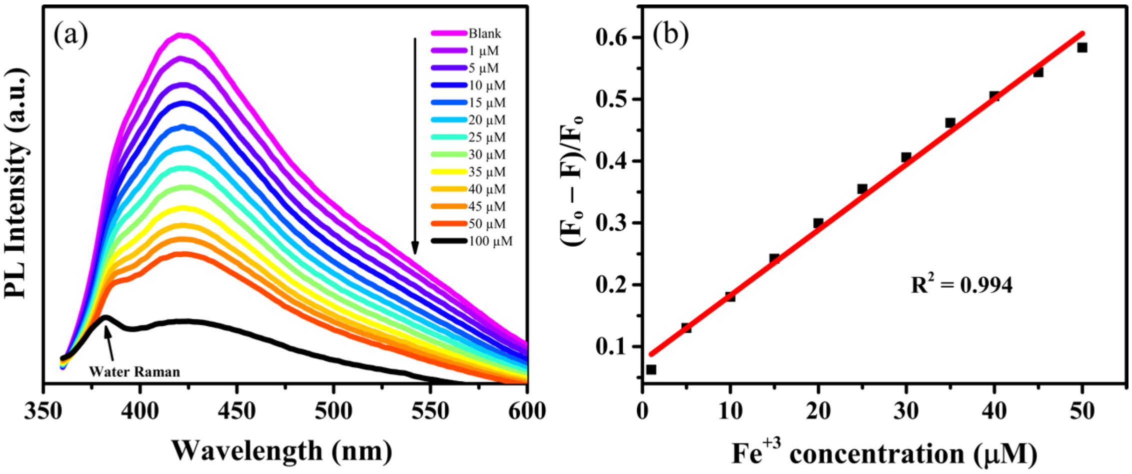

Figure 6.12. (a) The photoluminescence spectra of GQDs-500-M at different concentrations of Fe^{3+} and (b) corresponding linear plot (F_0 and F are the photoluminescence intensities of blank and with different concentrations of metal ions, respectively).

Meanwhile, a good linear plot is observed between the quenching efficiency and Fe^{3+} ions concentration (1 to 50 µM). As shown in Figure 6.12b, a linear regression value (R^2) of 0.994 was found which shows a good fitting and accurate detection of Fe^{3+} ion concentration. These results indicate that the as-prepared GQDs-500-M can be used as a selective and sensitive sensor for the detection of Fe^{3+} ions. The limit of detection (LOD) was found to 2.5 µM using the following equation:

$$\text{LOD} = 3.3\,\frac{\sigma}{S} \tag{6.2}$$

where, σ is the standard deviation of intercept and S is the slop of linear regression plot.

The detection limit of Fe^{3+} found in this study was much lower than the World Health Organisation (WHO) guideline limit of Fe^{3+} concentration (5.36 µM), suggesting that the as-prepared GQDs-500-M are promising in detecting trace amounts of Fe^{3+}. A comparison of the ferric ion detection by different carbon-based materials reported by various researchers is given in Table 6.3. The detection limit of 2.5 µM Fe^{3+} observed in this work is considerably lower than the values previously reported for detecting Fe^{3+}. Thus, it is believed the as-prepared GQDs-500-M are very promising for detecting the traces of Fe^{3+}.

Table 6.3. Comparison of the previously reported work on carbon-based materials with the present work for sensing of ferric ions.

Material	**Synthesis method**	**Linear range (µM)**	**LOD (µM)**	**Ref.**
GQDs	Electrochemical exfoliation	0-80	7.22	(Ananthanarayanan *et al.*, 2014)
CQDs	Thermal pyrolysis	0-300	13.68	(Xie *et al.*, 2017)
CQDs	Hydrothermal	0-20	3.7	(Wu *et al.*, 2017)
Carbon dots	Hydrothermal	0-500	7.4	(Wang *et al.*, 2017)
N doped carbon dots	Hydrothermal	0-50	10.98	(Khan *et al.*, 2017)
Carbon dots	Sonication	12.5-100	9.97	(Aslandaş *et al.*, 2015)
Carbon dots	Hydrothermal	0-500	28	(Li *et al.*, 2018)
Carbon dots	Thermal analysis	25-300	19	(Khan *et al.*, 2017)
Carbon dots	Microwave assisted	0-50	2.5	Present work

There is a great impact of environmental factors on the sensitivity and selectivity of sensor. For use in medical applications, due to presence of various interacting ions in the body, PBS (phosphate buffered saline) solution should be used to examine the sensitivity and selectivity of the sensor. Moreover, for examining the presence of heavy metal ions in real-world water samples, there will be influence of other salts and ions present in the water. Moreover, there will be variation in the value of pH as a result of other contaminants present in a water sample. Therefore, a best way to develop a sensor for practical applications is to use river water for sensitivity and selectivity tests. Due to limited timescale of PhD, in the present study, we have only focussed on the detection of Fe^{3+} under neutral conditions. For actual application, one will have to face challenges of variation in pH from sample to sample, so a sensor should be stable over a range of pH values; there might be influence of other heavy metals and ions present in the sample, which may have higher affinity toward GQDs than that of Fe^{3+}; various contaminants may quench the fluorescence of GQDs. All these factors would need to be countered in practical application of sensor. Therefore, for the development of actual sensor to be used in practical applications further study is required.

6.4 Summary

GQDs have been successfully synthesised through microwave treatment of biomass waste derived short range ordered carbon. The size of GQDs was in the range of 5 to 20 nm and exhibit excitation independent photoluminescence emission. This phenomenon is attributed to the intrinsic state emission of these GQDs. These GQD were further modified by simple hydrothermal treatment, leading to a substantial decrease in their size. The average size of modified GQDs-500-M was 1.6 ± 0.55 nm, with a very narrow size distribution. The decreased size resulted in increase in the bandgap and photoluminescence emission in the high energy region. The photoluminescence emission of GQDs-500-M exhibited a blue shift of about 100 nm as compared to their GQDs-500 unmodified counterparts. Moreover, these GQDs-500-M exhibit excitation-dependent emission which is attributed to the surface functionalisation and quantum confinement effect in these GQDs. In addition, GQDs-500-M were applied as photoluminescence sensor to detect the ferric ions. These GQDs were used a sensing probe to selectively detect Fe^{3+} ions with high sensitivity down to 2.5 μM. Based on these results, it is suggested that this kind of highly luminescent GQDs are expected to have promising application in developing other sensors due to their low cost, excellent solubility and low concentration sensing capabilities. The present study confirms the use of green, abundant and environmentally friendly biomass resource having little value to produce high valued nanoscale products.

Chapter 7 Intensified and sustainable production of graphene quantum dots directly from biomass waste

After acquiring highly pure GQDs and achieving high product yield, an intensified and sustainable approach was the final objective. In this chapter, scalable and sustainable synthesis of GQDs from biomass waste has been studied using two approaches. In first approach, the GQDs were prepared on gram scale using biomass derived biochar under mild acidic conditions. High quality GQDs with good crystallinity and uniform shape and size were obtained. The as-prepared GQDs exhibited narrow size distribution from 1.5 to 4.5 nm, with an average size of 3 ± 1.5 nm. The lattice parameter of GQDs was calculated to be 0.24 nm corresponding to the hexagonal $(11\bar{2}0)$ plane of graphene. Gram scale synthesis of biomass waste derived GQDs has not been reported previously elsewhere.

The second approach was employed to explore the sustainable synthesis of GQDs. The GQDs were produced directly from biomass in a single step via hydrothermal treatment without the use of any oxidising or reducing agent. Only water was used as hydroxyl scissors to cut the carbon domains into nano-sized fragments at high pressure. The hydrothermal carbonisation time and temperature played an important role in the carbonisation of the biochar precursor to produce GQDs. The GQDs produced at hydrothermal temperature of 250 °C for a duration of 12 h exhibited pronounced optical properties. TEM studies showed their uniform dispersion and consistent shape and size. Moreover, the GQDs demonstrated narrow size distribution of 1.5 –3.5 nm, with an average of ~2 ± 0.5 nm. These studies suggest the synthesis of high-valued GQDs on large scale is possible from value-less biomass waste.

7.1 Synthesis and characterisation of GQDs

The GQDs were synthesised by two step approach: firstly, biomass waste was converted into carbon rich biochar. Secondly, the biochar was cut down into small carbon domains under mild acidic conditions via a top-down approach. The process conditions were optimised to synthesise high quality GQDs. The resultant product yield of about 58% was obtained based on the weight of biochar precursor. The as-synthesised GQDs suspension was stable for several months without any perceptible changes, indicating the good stability of GQDs. The morphology and structure of GQDs were studied through TEM and HRTEM analysis.

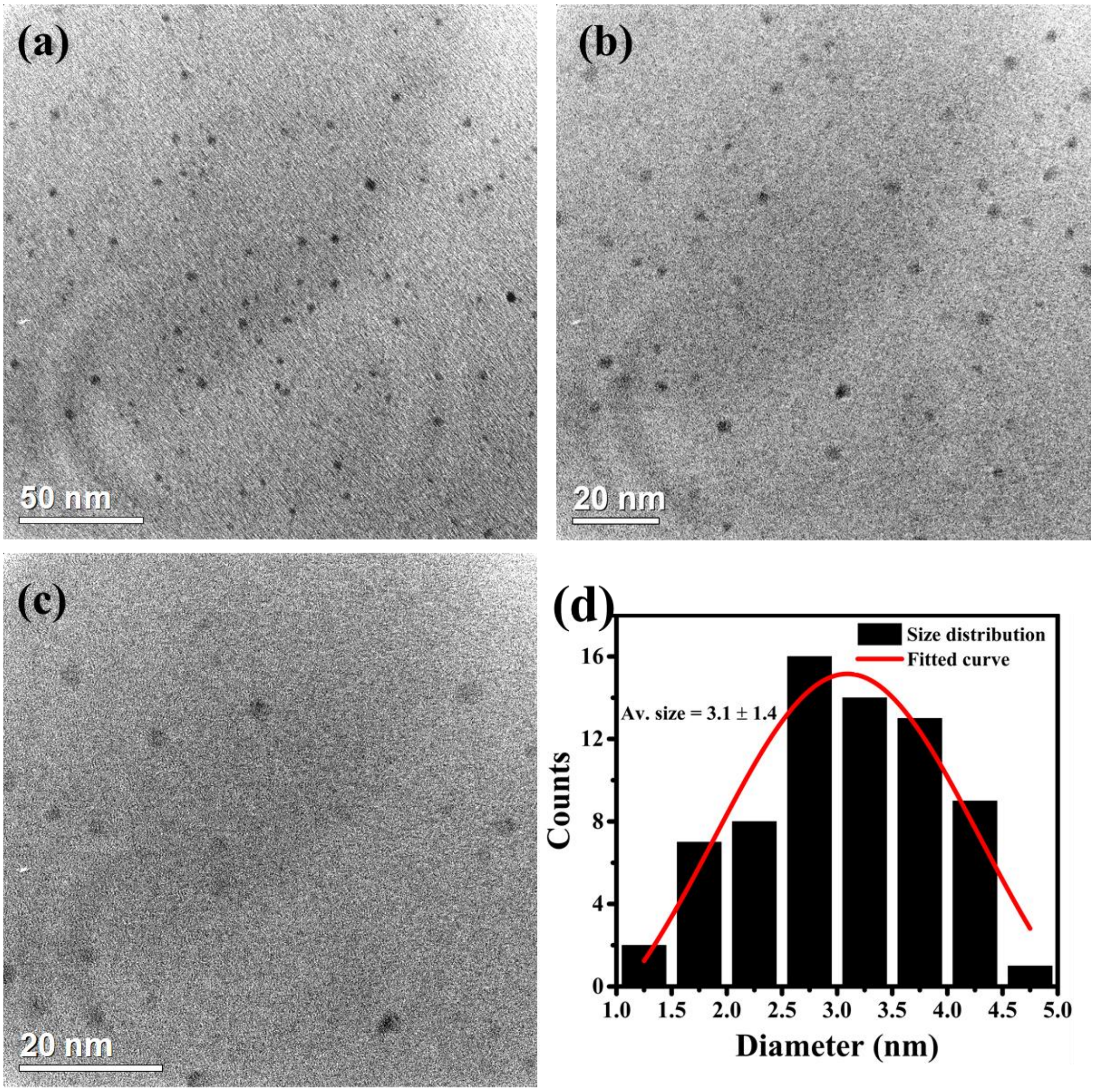

Figure 7.1. (a) The low magnification and (b, c) high magnification TEM images of GQDs showing uniform dispersion and shape. (d) Particle size distribution of GQDs displaying an average size of 3.1 ±1.4 nm.

The TEM images of GQDs presented in Figure 7.1 show their uniform dispersion. The absence of any agglomeration indicates the successful synthesis of high quality nanosized quantum dots. The high magnification TEM images (Figure 7.1b,c) further confirm the uniform shape and size distribution of as-synthesised GQDs. Careful size measurements were performed using ImageJ software and the results are summarised in a histogram in Figure 7.1d, indicating a very narrow size distribution with an average size of 3.1 ±1.4 nm. These results suggest the successful and uniform cutting of carbon domains into uniform sized GQDs in the process.

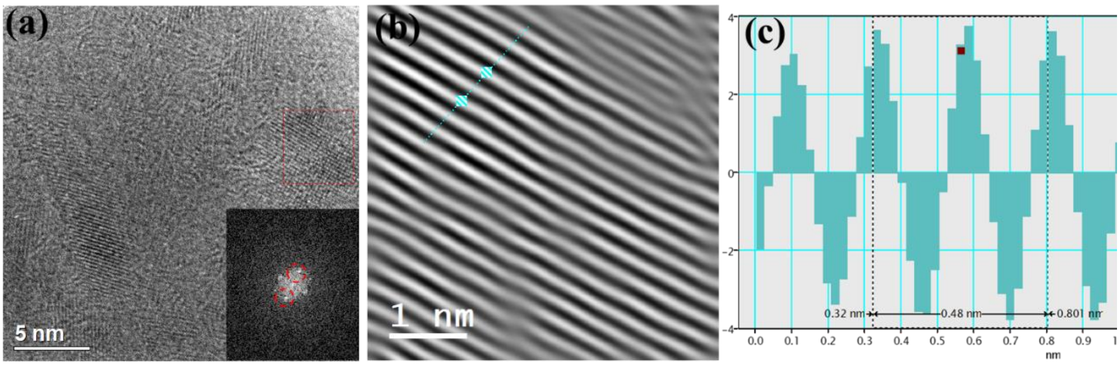

Figure 7.2. (a) High resolution TEM image of GQDs, inset is the FFT of the square marked in red, (b) Inverse FFT of the coordinates marked by circles in the inset in (a), displaying high resolution lattice fringes, and (c) the live profile of the line marked in (b), showing the distance between adjacent lattice fringes.

The more detailed atomic structure of GQDs was studied through HRTEM analysis. The HRTEM image in Figure 7.2a shows the obvious lattice fringes indicative of a highly crystalline structure of GQDs. The inset in Figure 7.2a shows the fast Fourier transform (FFT) image of the GQDs marked with a square. The FFT pattern shows six-spots of hexagonal pattern, indicating the graphene structure of as-prepared GQDs. The FFT pattern indicate the high crystallinity of the GQDs not observed in our previous studies. Figure 7.2b shows an inverse FFT of the coordinates marked with red circles in the inset in (a). It displays the obvious lattice fringes to calculate the distance between the adjacent atomic layers. Figure 7.2c is the live profile of the line marked in (b), showing the values of lattice parameters. The 2d distance was calculated to be 0.48 nm which gives a value of d = 0.24 nm. The interlayer spacing of 0.24 nm is related to the $(11\bar{2}0)$ plane of graphene, which agrees with the previous reports. All these results suggest that the obtained products are indeed GQDs with good crystallinity.

FTIR analysis was carried out to study the surface functionalisation of the biochar and as-prepared GQDs. Figure 7.3 shows the FTIR spectra of as-prepared biochar precursor and purified GQDs. The FTIR spectrum of biochar precursor is almost flat and does not show any significant surface functionalisation. On the other hand, a number of functional groups were added on the surface of GQDs during hydrothermal treatment. The FTIR spectrum of GQDs exhibit a broad band at ~3000-3500 cm^{-1}, which is attributed the stretching vibrations of hydroxyl (O-H) groups. The band at 1690 cm^{-1} is related to the C=O stretching in carbonyl groups. A doublet at ~1550 is related to the influence of carboxylate groups and nitro (N-O) compounds. The bands at 1389 and 1230 cm^{-1} are ascribed to the carboxy C-O deformation and epoxy C-O stretching vibrations, respectively. The bands at 920 cm^{-1} and 750 cm^{-1} are attributed to the out of plane bending vibration of C-O-C and C-H groups, respectively (Si and Samulski, 2008; Acik *et al.*, 2010; Hu *et al.*, 2013a).

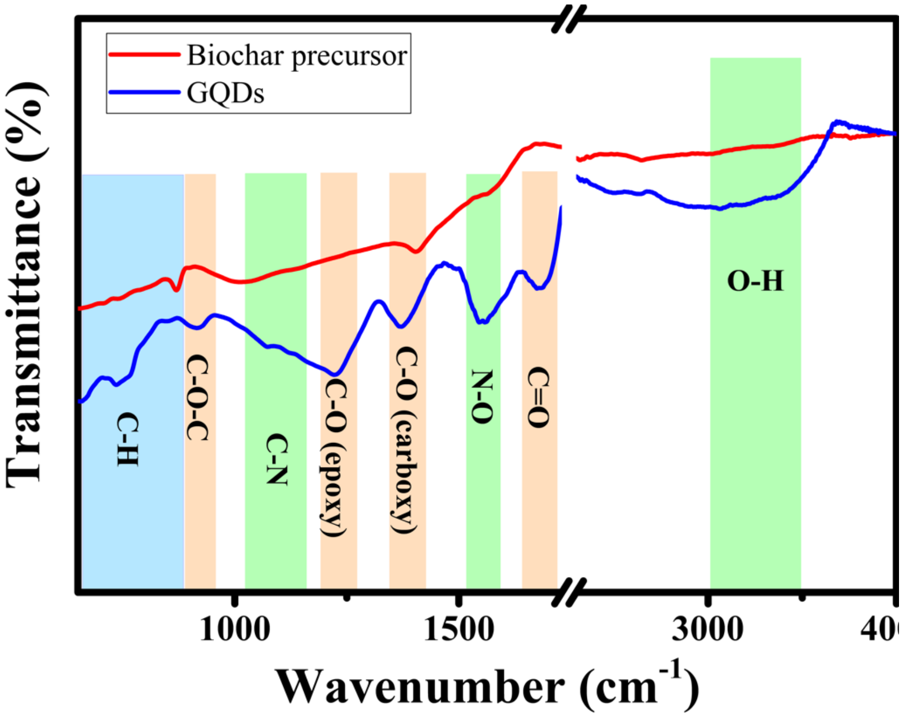

Figure 7.3. FTIR spectra of biochar precursor and purified GQDs, showing the introduction of the oxygenated and nitrous functional groups on the surface of GQDs.

In agreement with the previous reports (Pan *et al.*, 2010), the presence of epoxy groups indicate that these groups could act as chemically reactive sites for the cutting of underlying C-C bonds and then attachment at the edges of GQDs. The presence of a large amount of hydroxyl and carboxyl groups on the surface of GQDs convey hydrophilic properties and enrich the luminescence (Hsu and Chang, 2012). These oxygenated functional groups make GQDs dispersible in water and produce a stable suspension. Interestingly, the presence of C-N and NO- groups indicate the nitrogen-doping of GQDs with nitric acid during the synthesis process. Nitrogen doping is beneficial since it improves the luminescence properties of GQDs (Sun *et al.*, 2015). In addition, the presence of oxygenated and nitro functional groups on the surface of GQDs may act as a passivation layer and hinder their agglomeration (Tang *et al.*, 2012).

XPS analysis was performed to study the surface elemental composition of GQDs. Figure 7.4 shows the survey XPS spectrum and high resolution C1s, N1s and O1s spectra of as-synthesised GQDs. The survey XPS spectrum shows three main peaks at 284 eV, 400 eV and 532 eV corresponding to C1s, N1s and O1s, respectively. Another peak at about 347 eV is related to

Ca from the biomass precursor. The XPS analysis indicate that the GQDs are mainly composed of carbon (59.74%), nitrogen (0.53%) and oxygen (34.83%), with a limited amount of Ca from the biomass feedstock.

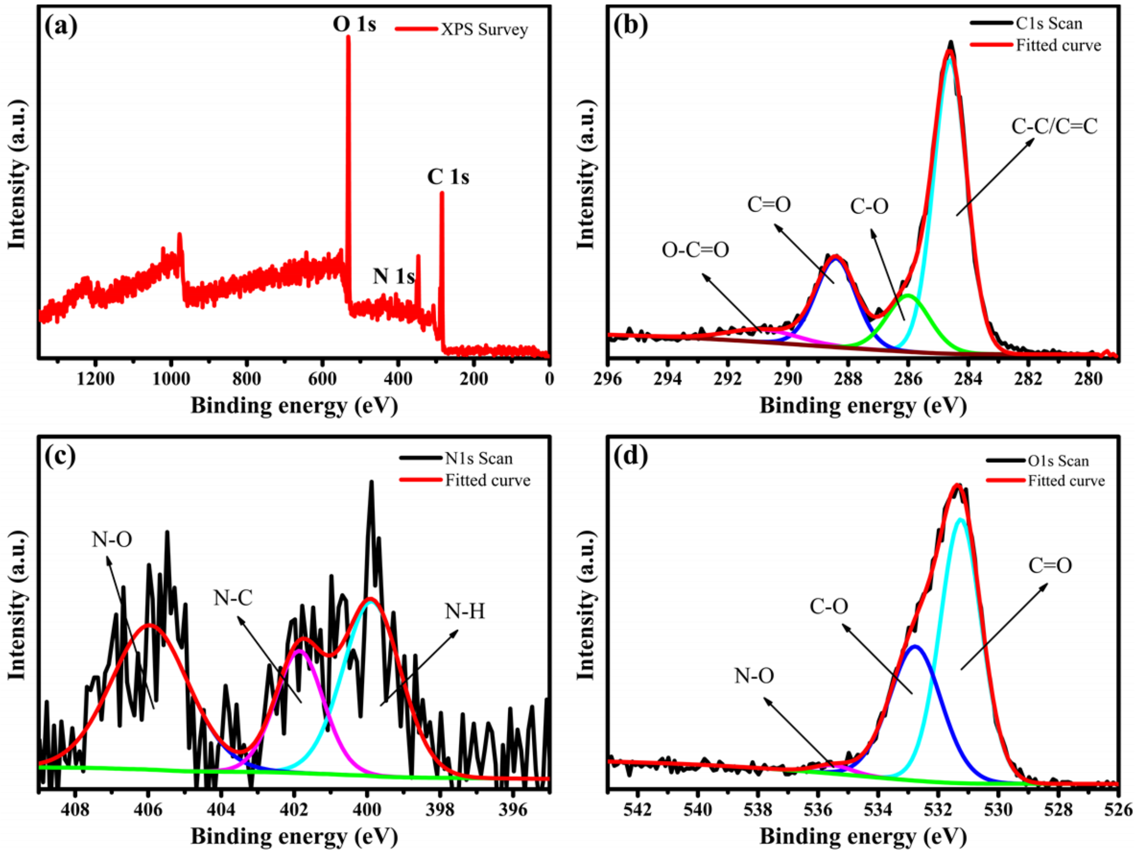

Figure 7.4. (a) XPS survey spectrum, (b) C1s, (c) N1s, and (d) O1s high resolution spectra of GQDs.

The high resolution C1s spectrum (Figure 7.4b) can be deconvoluted into four peaks, related to sp^2 carbon (C=C/C-C, 284.6 eV), sp^3 carbon (C-O/C-N, 286 eV), the carbonyl group (C=O, 288.4 eV) and the carboxyl group (COOH, 290.6 eV) (Ding *et al.*, 2015). The deconvolution of high resolution N1s spectrum shows three peaks, corresponding to amino nitrogen (399.9 eV), pyrrolic nitrogen (401.8 eV) and oxygenated nitrogen (405.9 eV). The O1s band in high resolution can be fitted to three peaks at 531.2, 532.8 and 533.9 eV, which can be attributed to C=O, C-O and O-C-O, respectively. The XPS analysis shows that the GQDs consist of three types of carbon: oxygenated carbon, nitrous carbon and graphitic carbon. The nitrous carbon originated from the nitric acid which introduced the nitrogen doping in GQDs with a small amount of nitration (Ding *et al.*, 2018). The presence of these functional groups on the surface of GQDs indicate that these oxygenated and nitro groups participated in the cleaving process of carbon domains and were left on the edges of GQDs. These results are in good agreement with that of FTIR which shows the presence of C=O, N-O and O-H groups in GQDs.

7.1.1 Optical properties study

The optical properties of the GQDs were studied through UV-visible and photoluminescence (PL) spectroscopies. The UV-vis spectrum of GQDs presented in Figure 7.5a indicates a strong absorption in the UV region. The spectrum shows a very pronounced band at about 270 nm and a shallow band at about 330 nm. The strong absorption band below 270 nm is attributed to the π-π* transition of aromatic carbon domains. The broader peak at ~330 nm in assigned to the n-π* transition between the oxygenated functional groups and sp^2 carbon domains (Ding *et al.*, 2018). The related photoluminescence excitation (PLE) spectra also show two peaks: one strong peak at ~308 nm and a shoulder peak at ~322 nm, which are related to the two absorption bands observed in the UV-vis spectrum. The corresponding PL spectra shows a strongest peak at ~385 nm when excited by 308 nm incident light. The emission wavelength is higher than the excitation, which is known as Stokes shift.

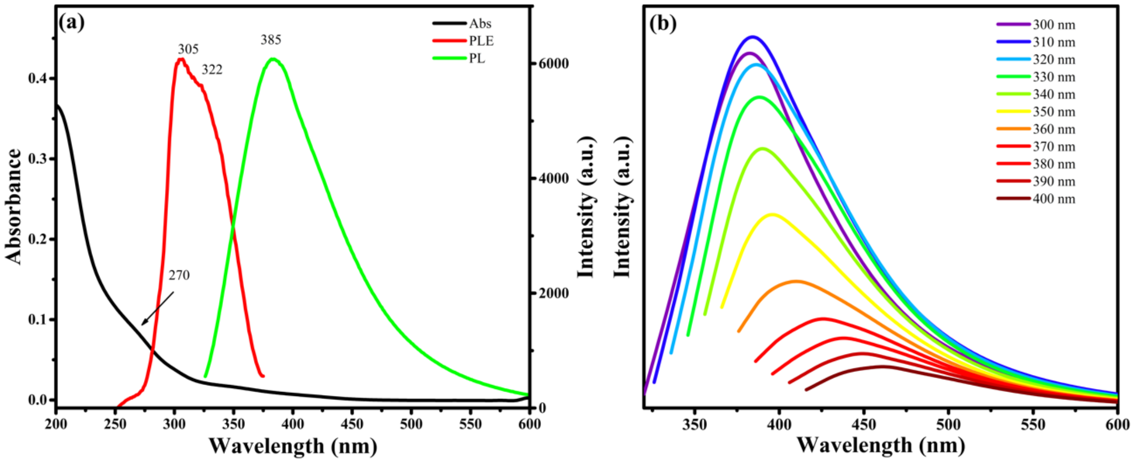

Figure 7.5. (a) UV-vis absorbance, PL and PLE spectra of GQDs. (b) PL spectra of GQDs excited by incident lights of various wavelengths from 300 to 400 nm with an increment of 10 nm.

The optical properties of GQDs were further explored through the study of their PL properties. Figure 7.5b shows the PL emission spectra of GQDs excited by a range of incident lights from 300 nm to 400 nm in wavelength with an increment of 10 nm. When excited by 300 nm incident light, the GQDs show an emission peak at 383 nm. The emission peak shows a gradual red-shift from 383 to 463 nm when the excitation wavelength is varied from 300 to 400 nm. The gradual red-shifting of PL emission shows the excitation dependent photoemission behavior of the GQDs. The emission wavelength depends on the size and surface functionalities of GQDs (Ye *et al.*, 2015). Thus, this excitation dependent behavior can be attributed to the incorporation of various functional groups of GQDs, introducing various emissive states (Li *et al.*, 2012a; Ananthanarayanan *et al.*, 2014; Suryawanshi *et al.*, 2014). The defects introduced by the oxygen or nitrogen functional groups act as capture centers for excitons and give rise to surface state related luminescence (Ding *et al.*, 2018). They can allow the tuning of the PL wavelength at different excitations, which is beneficial for specific applications, such as multicolor bioimaging. It is very interesting to note that our synthesis method could produce GQDs with the multi-color PL properties required for such applications. All these optical properties are correlate with the features of GQDs such as narrow size range, surface functionalisation and heteroatoms doping at the edges.

7.2 Sustainable synthesis of GQDs

After the successful production of GQDs at large scale, a more sustainable synthesis of GQDs was highly demanding. The GQDs were successfully produced directly from raw biomass waste via a simple hydrothermal approach without the use of any oxidising, reducing or passivating agent. Only water was used to hydrothermally cut the carbon domains into nano-sized fragments at high pressure. The hydrothermal carbonisation time and temperature plays an important role in the carbonisation of biochar precursor to produce GQDs. The low temperature and less time would not be sufficient for the cleavage of biochar into GQDs, while the high temperature and long carbonisation duration would destroy the surface and structure of GQDs, leading to less pronounced optical properties. Therefore, an optimum time and temperature is required to obtain high quality GQDs. The production of GQDs was systematically studied at a range of hydrothermal temperatures from 200 to 300 °C for various durations of 8, 12 and 24 h. The obtained products were named as GQDs-x or GQDs-x-y, where x indicates the hydrothermal temperature and y indicates the treatment time. For example, GQDs-200 indicates the series of GQDs synthesised at 200 °C, while GQDs-200-8 denotes the ones prepared at 200 °C for 8 h. The synthesised products were evaluated through the study of their optical properties.

The optical properties of the as-prepared GQDs were studied through the UV-visible and photoluminescence spectroscopies. The UV-vis absorbance spectra of GQDs synthesised at various time and temperatures are presented in Figure 7.6. All of the spectra showed very pronounced bands which indicate their strong absorption in the UV region. The UV-vis absorption spectra of GQDs synthesised at 200 °C for various durations are presented in Figure

7.6a. All three spectra exhibit two pronounced excitonic bands at 320 and 280 nm along with a shoulder at 250 nm. The strong absorption bands below 300 nm are associated with the π-π* transition of aromatic C=C domains (Pan *et al.*, 2010; Li *et al.*, 2012a). While the bands appearing at 320 nm are attributed to n-π* transition between oxygenated/nitrous functional groups (e.g. C=O, C-OH) (Qu *et al.*, 2014a; Wang *et al.*, 2014a; Ding *et al.*, 2018). Careful observation of the absorption spectra indicate that the bands become more pronounced with increase of reaction time from 8 to 24 h. The spectrum of GQDs-200-24 shows the suppression of the 320 nm band while enhancement in the 280 nm band. It indicates that the absorbance in GQDs-200-24 is mainly associated with π-π* transition of aromatic domains.

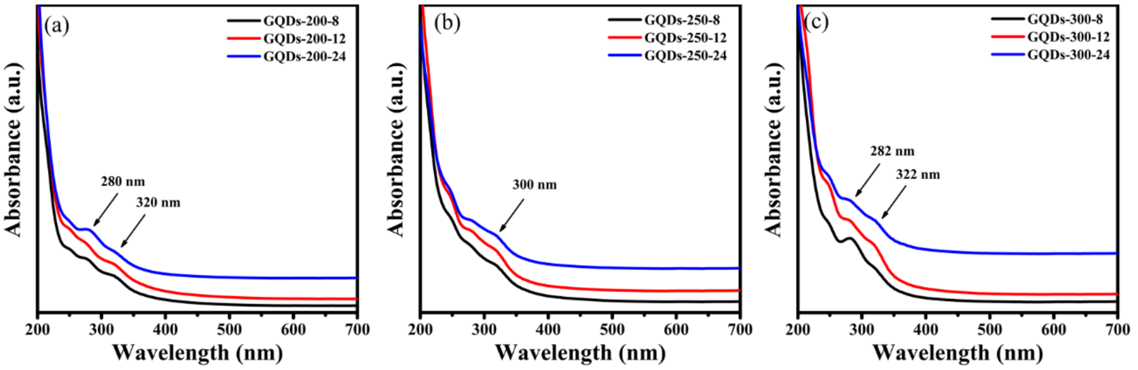

Figure 7.6. UV-visible absorbance spectra of GQDs (a) synthesised at 200 °C for a duration of 8-24 hours, (b) synthesised at 250 °C for a duration of 8-24 hours and (c) synthesised at 300 °C for a duration of 8-24 hours.

The UV-vis absorbance spectra of GQDs prepared at higher hydrothermal temperatures of 250 and 300 °C are presented in Figure 7.6b,c. The absorbance spectrum of GQDs-250-8 shows a pronounced band at 320 nm, while the bands below 300 nm are quite suppressed. The 320 nm band increase with increase in reaction time to 12h but again reduced upon the further increase of reaction time to 24 h. These observations suggest that the longer reaction time leads to the heterogeneous surface and structure of the GQDs. Therefore, the moderate reaction time of 12 h could be favourable for the enhanced absorption of these GQDs. As shown in Figure 7.6c, the UV-vis absorbance spectrum of GQDs-300-8 indicate a substantial increase in the 280 nm band, while the increase in hydrothermal duration shows growth in 320 nm band for GQDs-300-12. Like the GQDs prepared at 250 °C, the GQDs-300-24 also show a small decline in absorption bands which indicates the destruction of their surface and structure after long exposure to high pressure and temperature.

The optical properties of GQDs were further investigated through the study of their luminescence properties. The PL emission of GQDs depends on their size in accordance with the quantum confinement effect and on their surface functionalisation and defects (Ye *et al.*, 2015). The PL spectra of GQDs prepared at 200 °C for various durations are presented in Figure 7.7. The spectra exhibit PL emission at a range of incident lights from 300 to 400 nm excitation wavelength. The GQDs-200-8 show an emission peak at 386 nm when excited by 300 nm incident light. The PL emission intensity increases with increase in the excitation wavelength and shows a strongest emission peak at 405 nm when excited by 330 nm incident light. The emission peak displays a gradual redshift from 386 to 460 nm when the excitation wavelength is varied from 300 to 400 nm. This phenomenon shows the excitation dependent PL emission of the GQDs. This excitation dependent behavior can be attributed to the quantum confinement effect originating from different sized GQDs (Ye *et al.*, 2015; Yuan *et al.*, 2018), and/or incorporation of defect related emissive states such as oxygen/nitrogen functional groups (Maiti *et al.*, 2017; Miao *et al.*, 2018; Wu *et al.*, 2018).

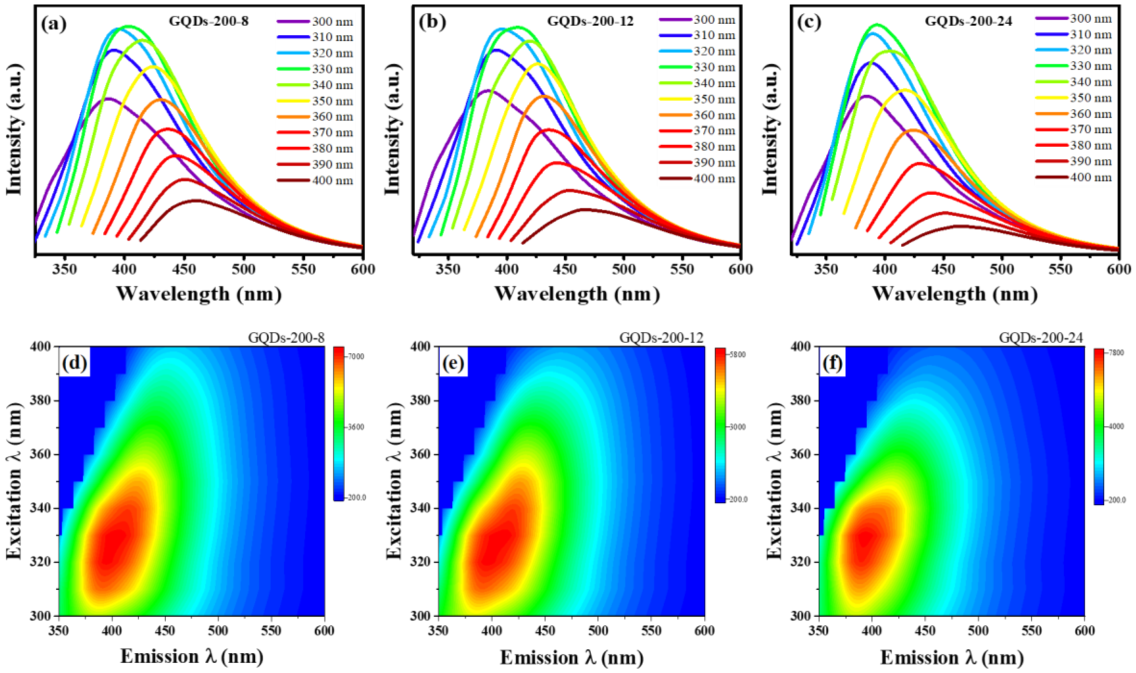

Figure 7.7. PL spectra of (a) GQDs-200-8, (b) GQDs-200-12, (c) GQDs-200-24 and (d-f) their corresponding contour maps.

The comparison of the PL spectra of three types of GQDs prepared at 200 °C demonstrate that the emission peak shows a blue shift with an increase in the reaction time. It can be observed in the Figure 7.7a-c that strongest emission peak shifts from 405 nm in GQDs-200-8 to 395 nm in GQDs-200-24 due to increase in reaction time from 8 to 24 h. This shifting of the emission peak toward higher energy region indicates the increase in their bandgap. The optical bandgap can be calculated from Eq. below:

$$E = hc/\lambda \tag{7.1}$$

where, E is Energy = bandgap, h is Plank's constant = 6.62×10^{-34} Js, c is velocity of light = 2.99×10^{8} ms^{-1} and λ is the wavelength of the emission peak.

The bandgaps calculated from Eq. 7.1 based on the strongest PL emission peak for GQDs-200-8, GQDs-200-12 and GQDs-200-24 are 3.06, 3.1 and 3.14, respectively. It is well known that the bandgap increases with decrease in the size of GQDs, leading to a blueshift in their PL emission (Peng *et al.*, 2012a; Sk *et al.*, 2014; Ye *et al.*, 2015). These results suggest that the GQDs prepared after 24 h of hydrothermal reaction have smaller size and exhibit larger bandgap.

Further investigations on the PL spectra of these GQDs were conducted with the help of contour maps presented in Figure 7.7e-f. The contour maps illustrate that the strong emission for GQDs-200-8 spans over a wide range, while this emission confines to a smaller region with increase in the hydrothermal duration to 24 h. The emission of GQDs-200-24 is confined to a very short wavelength range. These results can be confirmed from the size of the red regions of the contour maps related to the highest emission range. The red region of GQDs-200-8 and GQDs-200-12 are bigger in size and expand over a wide wavelength range, while the red region of GQDs-200-24 is very small. These results indicate the size distribution of these GQDs leading to a wide or narrow emission range. The wide emission range can be attributed to a large size distribution, while the confined emission can be attributed to a very narrow size distribution (Sk *et al.*, 2014; Lai *et al.*, 2020). Thus, it is suggested that the GQDs-200-24 exhibiting very strong and narrow emission consist of very narrow size distribution. These findings are sensible since longer hydrothermal duration would lead to the generation of small sized GQDs.

The optical properties of GQDs synthesised at higher hydrothermal temperatures of 250 and 300 °C were also studied using the contour map illustrations. The contour maps of GQDs-250 and GQDs-300 are given in Figure 7.8. The red region in the contour map is related to strongest PL emission region of the GQDs. The size and range of red region indicate the corresponding emission range which is associated with the quantum confinement effect originating from the bandgap of GQDs. Thus, the red region is directly related to the bandgap range for a specific group of GQDs. The bigger the size of red region, the larger the range of bandgap variation. A small size of red region indicates the narrow range of bandgap. As reported previously, the bandgap is directly associated with the size of GQDs (Sk *et al.*, 2014; Ye *et al.*, 2015). Hence, the narrow bandgap range shows the narrow size distribution of the GQDs. The carful observation of contour maps in Figure 7.8a-c shows that the red region of GQDs-250-8 is largest among all samples and its size decreases with increase in the reaction time to 12 h for GQDs-250-12, while its size minutely increases with increase in the reaction time to 24 h due to destruction of its surface. These observations suggest the narrow bandgap range of GQDs-250-12 among all, owing to the narrow size distribution. Moreover, the comparison of the PL intensity values of three types of GQDs demonstrate the highest value for GQDs-250-12. These results suggest that the GQDs-250-12 are the best among all with narrow bandgap, narrow size distribution and strong PL emission.

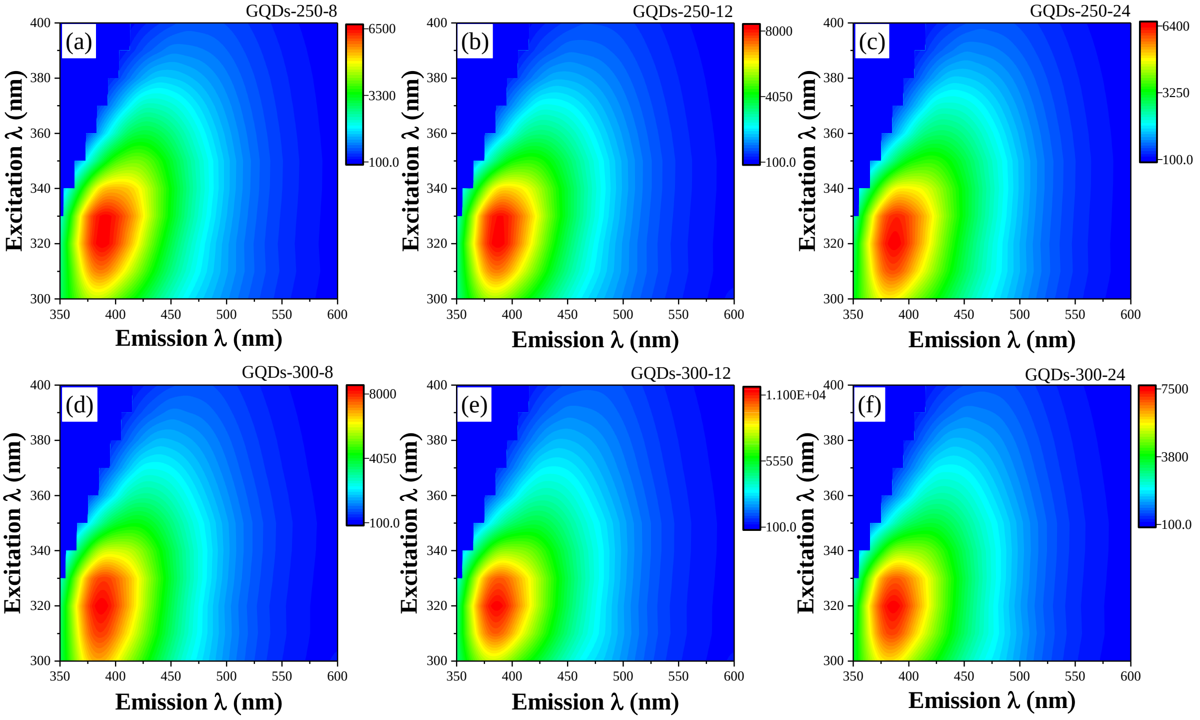

Figure 7.8. PL contour maps of the GQDs prepared at hydrothermal temperature of (a-c) 250 °C and (e-f) 300 °C for various duration of 8, 12 and 24 h.

The contour maps for GQDs-300 are presented in Figure 7.8e-f and reveal observations similar to their GQDs-250 counter parts. The red region of GQDs-300-12 is the smallest and shows highest PL intensity. The strong and narrow emission range indicate the narrow size distribution and high quality of GQDs-300-12. These results suggest that a hydrothermal reaction time of 12 h leads to substantial disintegration of carbon domains into uniform sized GQDs with narrow size distribution and extensive surface functionalisation. Upon the further increase of reaction time to 24 h, the PL properties of GQDs were suppressed possibly due to destruction of the surface morphology after long time exposure to high temperature and pressure. This is obvious from the PL intensity of GQDs. A comparison of the PL intensity of GQDs in Figure 7.8 shows that the intensity increases with an increase in the reaction time to 12 h and then further decreases with increase in the reaction time to 24 h. The PL intensity of GQDs obtained after 12 h reaction is the highest among all samples at any hydrothermal temperature. These observations indicate that the treatment time is the key factor to produce high quality GQDs. Thus, it is suggested that the 12 h reaction time is the most favorable for the synthesis of GQDs with narrow bandgap range, narrow size distribution and strong optical properties.

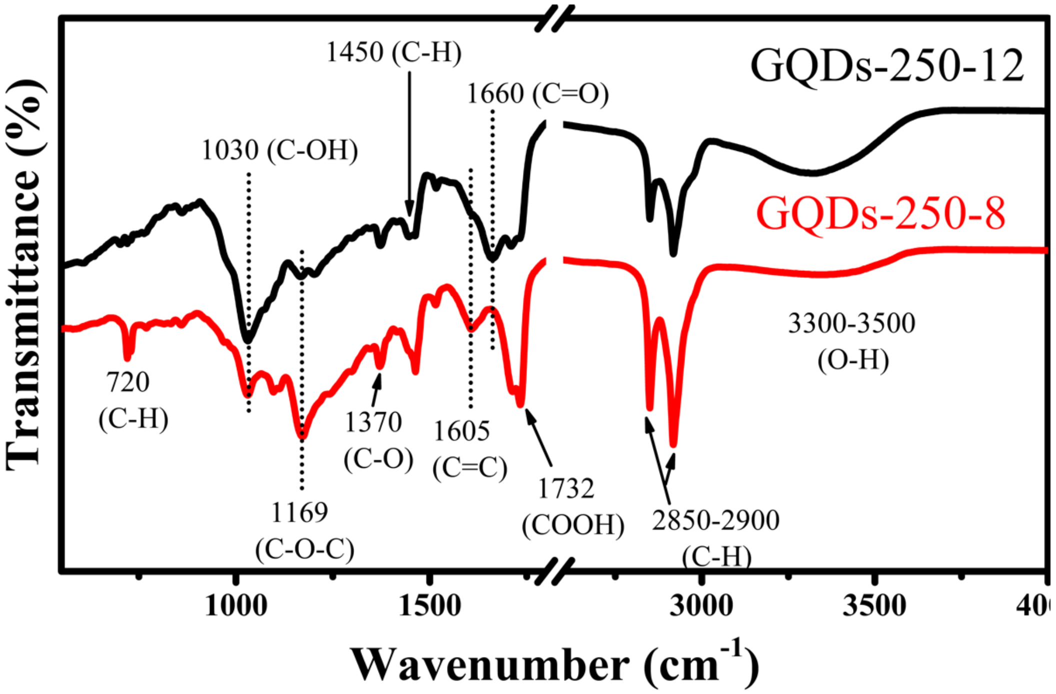

Figure 7.9. FTIR spectra of GQDs-250-08 and GQDs-250-12 showing extensive amount of oxygenated surface functional groups.

Infrared spectroscopy, being a versatile technique to identify the surface structure, was employed to study the surface functionalisation of as-prepared GQDs. Based on the optical properties study, two types of GQDs were selected for FTIR analysis, namely GQDs-250-08 and GQDs-250-12, due to a major difference in their optical properties. The FTIR spectra of both type of GQDs is given in Figure 7.9. The FTIR spectrum of GQDs-250-08 exhibits a broad band at ~3300-3500 cm^{-1} corresponding to the stretching vibrations of O-H groups. A doublet observed at ~2850-2900 cm^{-1} is attributed to the stretching of C-H groups in aldehydes. The peaks at ~1734 is related to the stretching vibrations of COOH groups (Tang *et al.*, 2016). The band at 1605 cm^{-1} belongs to the influence of C=C in aromatics. The peaks detected at ~1370 and ~1169 cm^{-1} are related to the stretching vibrations of carboxy and epoxy C-O-C groups, respectively (Li *et al.*, 2012a). The peak at ~1030 cm^{-1} is ascribed to the stretching of C-O-H groups (Acik *et al.*, 2010). The peaks below 900 cm^{-1} are associated with bending of C-H bonds in aromatics.

There is obvious difference in the FTIR spectra of GQDs-250-12. The first major change is the considerably pronounced O-H/N-H band at ~3300-3500 cm^{-1}, indicating a significant increase in the hydroxyl and amino groups on the surface. The second big change is the appearance of a new band at ~1660 cm^{-1} corresponding to the C=O bond which indicate the introduction of additional oxygenated functional groups. Third difference is the suppression of the C-O-C peak at 1169 cm^{-1}. Another difference is the increment in the strong epoxide C-OH peak at 1030 cm^{-1}. These findings indicate the decline in the C-O-C groups and increase in the C-OH and C=O groups with increase in the reaction. It has been reported previously that C-O-C epoxy groups take part in the rupture of C-C bonds of carbon domains and consequently transform into C-OH and C=O groups (Pan *et al.*, 2010; Li *et al.*, 2012a). Thus, it is suggested that GQDs-250-12 are produced by the epoxy (C-O-C) cutting of C-C bonds and transformation of C-O-C groups into C=O and C-OH groups, which results in the decreased size and increased number of functional groups attached on the surface. Moreover, these results are in agreement with the study of optical properties, where the PL properties of GQDs-250-12 are more pronounced than its counter parts owing to the decreased size and enhanced functional groups presence.

The surface elemental composition of GQDs-250-12 was further studied by XPS analysis. Figure 7.10 shows the XPS survey spectrum and high resolution C1s, N1s and O1s spectra of GQDs-250-12. The XPS survey spectrum demonstrates the presence of three major peaks corresponding to C1s (285 eV), N1s (400 eV) and O1s (532 eV). The XPS analysis designate that the GQDs are composed of carbon (68.74%), nitrogen (8.16%) and oxygen (23.11%). Interestingly, the presence of the N1s peak in the XPS spectrum indicate the incorporation of N doping in GQDs directly from the biomass precursor. The percentage of N doping (~8.2%) is consistent with previously reported GQDs (Hu *et al.*, 2013a; Sun *et al.*, 2015; Kang *et al.*, 2020). The incorporation of N atoms in carbon materials is typically associated with three types of configurations: pyridinic, pyrrolic and graphitic. Pyridinic N refers to the sp^2 hybridised N bonding with two C atoms. The presence of pyrrolic nitrogen indicate N bonding with C in five-atom ring structure. Graphitic nitrogen originates from the replacement of C atom in graphene lattice and results in the bonding with three neighboring C atoms (Kang *et al.*, 2020). To identify the C-N configuration in GQDs, N1s band was evaluated. The high resolution N1s spectrum (Figure 7.10c) can be divided into two peaks at 399.6 eV and 401.5 eV, corresponding to pyrrolic nitrogen and graphitic nitrogen, respectively (Qu *et al.*, 2014a; Kang *et al.*, 2020). Thus, the high resolution XPS results reveal the N doping in GQDs in the form of pyrrolic and graphitic carbon. This N doping in GQDs greatly improves the optical properties of GQDs (Sun *et al.*, 2015; Kang *et al.*, 2020).

The high resolution C1s spectrum (Figure 7.10b) can be fitted to three peaks, associated with sp^2 carbon (C=C/C-C, 284.5 eV), sp^3 carbon (C-O/C-N, 285.9 eV), and carbonyl groups (C=O, 287.9 eV) (Ding *et al.*, 2015). The O1s band in high resolution (Figure 7.10d) can be fitted to two peaks at 531.1 and 532.5 that can be attributed to C=O and C-O/O-C-O, respectively. The XPS analysis shows that the GQDs consist of three types of carbon: oxygenated carbon, nitrous carbon and graphitic carbon. The nitrogen doping and presence of extensive oxygen functional groups on the surface of GQDs result in the pronounced optical properties (Li *et al.*, 2011b; Sun *et al.*, 2015). Moreover, the absence of any impurity items indicates the high purity of GQDs. These results are in good agreement with that of FTIR which shows the presence of C=O, N-H and O-H groups in GQDs.

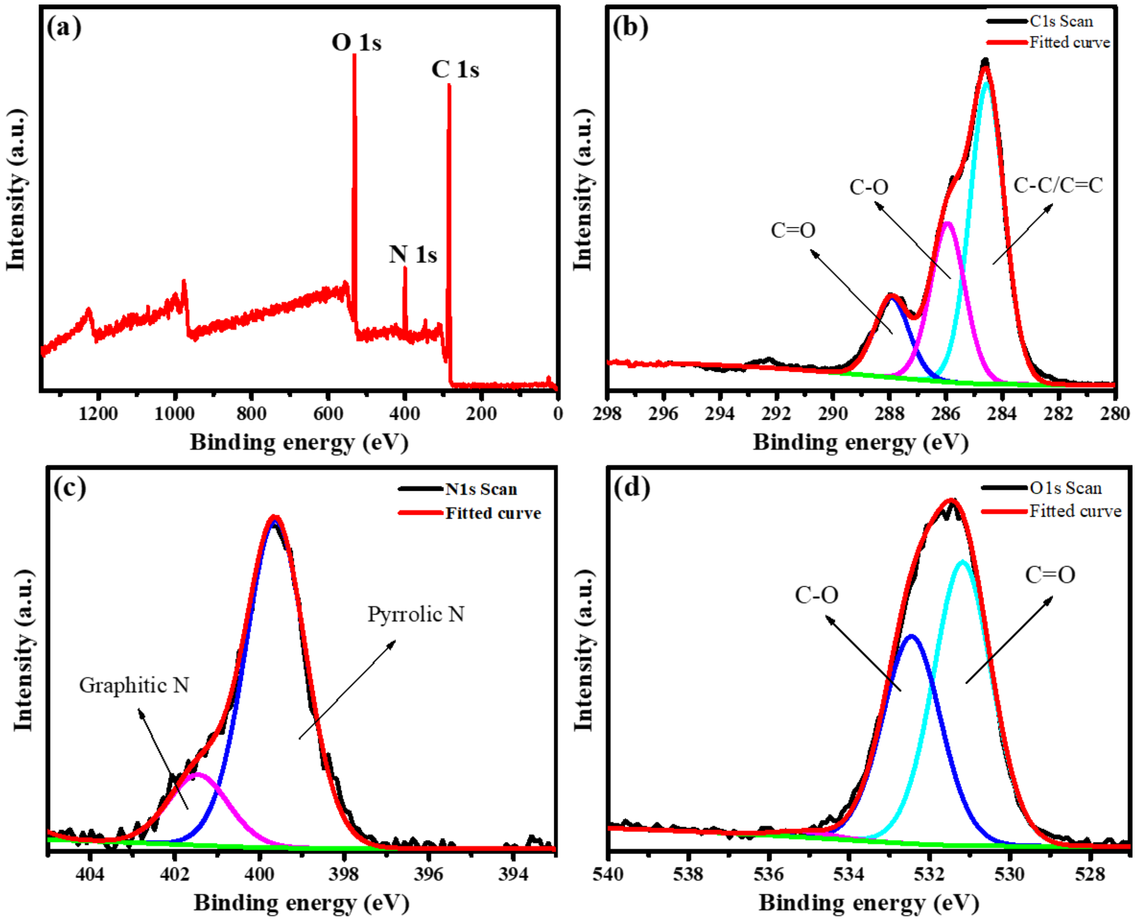

Figure 7.10. (a) XPS survey spectrum, (b) C1s, (c) N1s, and (d) O1s high resolution spectra of GQDs-250-12.

The morphology and size distribution of GQDs were studied through TEM analysis. Figure 7.11 shows the TEM images of GQDs-250-12, indicating their uniform dispersion. The even dispersion without any agglomeration signifies the successful synthesis of high quality nanosised quantum dots. The size of GQDs were measured to analyse size distribution of as-synthesised GQDs. The careful size measurements were performed using ImageJ software and the results are summarised in a histogram in Figure 7.11c. The results indicate a very narrow size distribution with an average size of ~2 ± 0.5 nm. These results suggest the successful and uniform disintegration of carbon rich biomass into uniform sized GQDs. These results are in good agreement with the study of their optical properties, where narrow PL emission range was observed for GQDs-250-12 which is attributed to the quantum confinement effect resulting from narrow size distribution.

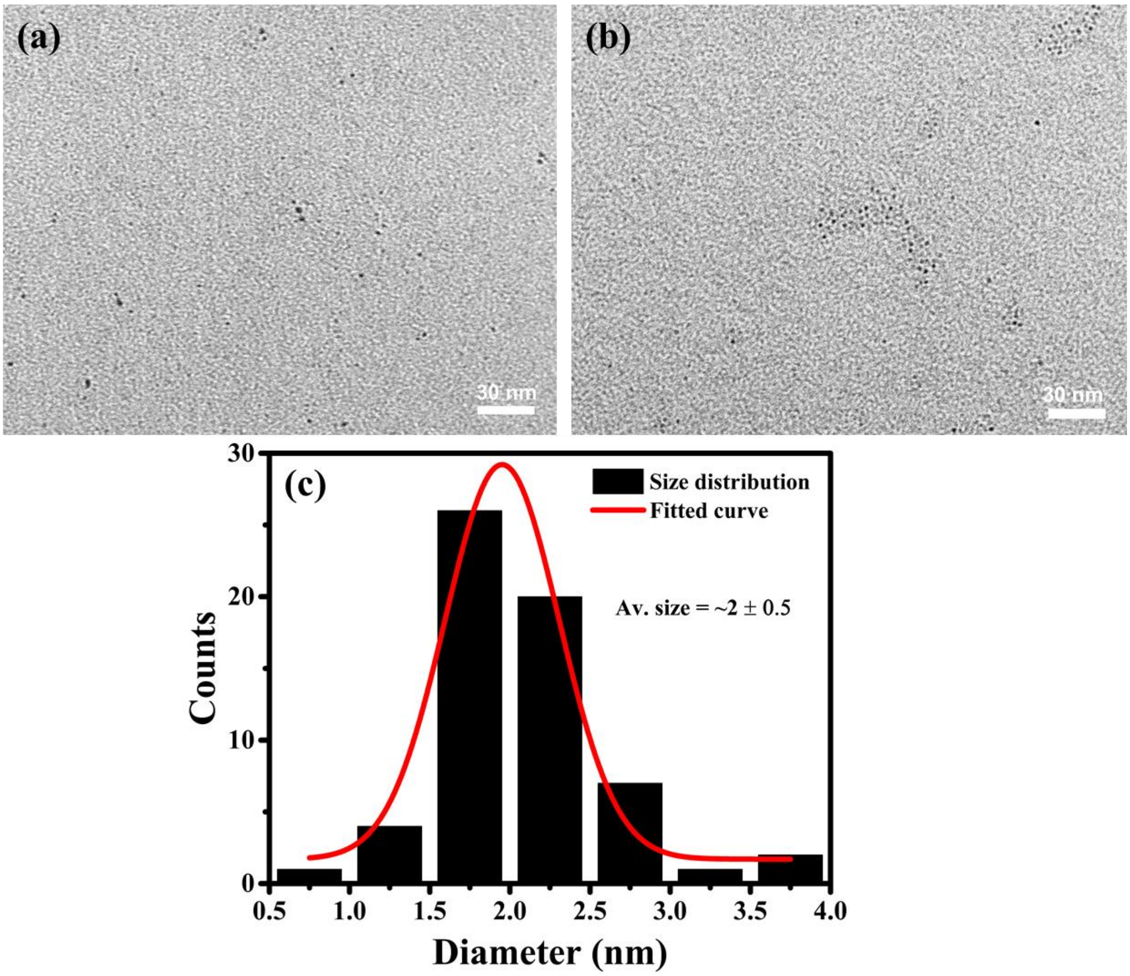

Figure 7.11. (a, b) TEM images of GQDs-250-12 showing relatively uniform size and dispersion, and (c) their corresponding size distribution histogram revealing an average size of ~2±0.5 nm.

7.3 Summary

In summary, high quality GQDs have been successfully synthesised on large scale using biomass waste via a green approach. Two approaches were employed to study and gram scale and green synthesis of GQDs. In first approach, the GQDs were prepared on a large scale under mild acidic conditions and demonstrated good crystallinity and uniform shape and size. As-prepared GQDs exhibited narrow size distribution with an average size of ~3 ± 1.5 nm. The lattice parameter of GQDs was calculated to be 0.24 nm corresponding to the $(11\bar{2}0)$ plane of graphene. In the second methodology, GQDs were produced directly from biomass in a single step via hydrothermal treatment using only water as hydroxyl scissors. The hydrothermal carbonisation time and temperature played an important role in the carbonisation of biochar precursor to produce GQDs. The GQDs synthesised at optimum conditions of 250 °C and 12 h displayed pronounced optical properties. The TEM study showed a uniform dispersion and consistent shape and the size of as-prepared GQDs. Moreover, the GQDs demonstrated narrow size distribution with an average of ~2 ± 0.5 nm. All the above results suggest that the high quality GQDs can be successfully produced at large scale using green precursors and green synthesis methodologies. These studies suggest the cost-effective and green synthesis of high valued GQDs on large scale is possible from biomass waste.

Chapter 8 Conclusions and future perspective

8.1 Conclusions

The aim of this study was to produce value-added products from value-less biomass waste, with a view to solve future energy needs and biowaste recycling problems. To this end, activated carbon (AC) and graphene quantum dots (GQDs) were successfully produced from biomass waste and their use in energy storage and sensor applications was evaluated. A series of AC samples were produced and their effect on the performance of vanadium redox flow batteries (VRBs) was examined. The lab synthesised ACs demonstrated superior performance to the commercially available graphite electrodes. Moreover, the sustainable synthesis of GQDs from biomass waste was studied systematically. A fundamental issue of the introduction of impurities in the product was addressed and highly pure GQDs were produced. The research proceeded with the aim of producing high yield of the products and up to 80% yield of the GQDs from the source was achieved. After achieving highly pure and high-yield GQDs, the large scale and green synthesis needs to be developed. This was achieved by hydrothermal carbonisation of biomass waste in a single step using water as scissors to cut the carbon domains into GQDs. As-prepared GQDs were employed for developing a highly selective and sensitive sensor for the detection of heavy metal ions in aqueous media. In all cases, a detailed characterisation and properties analyses were carried out for the carbon products developed.

The conversion of biomass into AC is of significant interest as it is simple yet efficient way to produce renewable and cost-effective carbon materials for a wide range of potential applications in energy storage, gas (methane, hydrogen, etc.) storage, air purification to gold purification and medicine to cosmetics. Owing to their intriguing properties and low cost, these biomass derived ACs stand out as a competitive candidate to replace the commercially available fossil-based carbon materials. In particular, these carbon materials have shown bright potential as an alternate electrode material in energy storage applications, such as vanadium redox flow battery (VRB). However, most of the studies reported until now mainly focused on the improvement of surface properties of electrode to upgrade the reaction kinetics. Unfortunately, less attention has been paid to explore the effect of electrode microstructure on the electrochemical performance of the battery. In this work, a systematic study was carried out to investigate the effect of electrode porous microstructure on the performance of the VRB. A range of ACs with varying levels of porosity were produced by impregnation of biochar with potassium hydroxide followed by activation at elevated temperature. The systematic study of porosity development and its influence on the performance of VRBs system was conducted. The specific surface area was systematically modified from ~10 m^2g^{-1} to 2085 m^2g^{-1} and microporosity up to 1930 m^2g^{-1} was achieved. The electrochemical performance of modified electrodes revealed that the high surface area porous carbon-based electrode exhibited higher electrocatalytic activity and reduced charge transfer resistance than the pristine bipolar graphite plate electrode. Static cell configuration of the VRB showed superior performance for the AC-modified electrodes at all current densities. The highly microporous electrode revealed dual benefits: firstly, it offered excess active sites to facilitate the reversible redox reactions; secondly, it improved the electrochemical performance due to improved charge transfer and high electrocatalytic activity. The perfect combination of low cost, effective structural design and high VRB performance suggest that this efficient electrode material may replace the conventional bipolar graphite electrodes in practical VRB applications.

During the past decade, a continuous research has been carried out to convert these carbon materials into superior luminescent nanomaterials. Among various fluorescent materials, GQDs have attracted extensive attention in a wide variety of applications owing to their excellent size-dependent optical properties. Despite several efforts, a thorough study on the suitable biomass precursor for the development of GQDs is still lacking. In this study, a systematic protocol was adapted to search out the suitable biomass-based precursor for the synthesis of high quality GQDs. A range of biochar samples with varying properties were prepared from biomass. A simple approach for the conversion of biochar into ultra-pure GQDs was established. A novel process combining carbonisation, oxidation and nitration with controlled hydrothermal fragmentation that removes the N-oxide groups in the formation of GQDs was developed. The removal of the neutralisation process by the introduction of hot water washing played a key role in the production of highly pure GQDs. The typical topographic morphology of GQDs indicated a size range of 2-20 nm with a thickness of 1 to 3 nm, corresponding to 3-9 layers of graphene. The surface area measurements further verified the TEM results confirming the presence of GQDs in bulk amount (100 mg). The band gaps of the GQDs were 2.95 and 2.67 eV, resulting in the controllable photoluminescence properties. This simple synthetic method has the advantages of low cost and sustainability and highlights the possibility of employing low-value biomass resources to produce high-value nanomaterials.

The potential of biomass conversion into GQDs to be further intensified was studied via a high yield synthesis of GQDs through microwave treatment of biomass derived short range ordered carbon. The GQDs were successfully synthesised with a high yield of over 80%, the highest value reported to date. The synthesised GQDs were highly hydrophilic and exhibited unique excitation independent photoluminescence emission attributed to intrinsic state emission. The size of GQDs was in the range of 5 to 20 nm depending on the microwave power. These GQD were further modified by simple hydrothermal treatment, leading to a substantial decrease in their size. The average size of modified GQDs was 1.6 ± 0.55 nm, with a very narrow size distribution. The modified GQDs were applied as photoluminescence sensor to detect ferric ions. These GQDs could selectively detect Fe^{3+} ions with high sensitivity down to 2.5 µM. Based on these results, it is suggested that this kind of highly luminescent GQDs could have promising application in the development of other sensors due to their low cost, excellent solubility and high sensing sensitivity. The utilisation of renewable resource along with simple microwave treatment paves the way to green, high yield and cost-effective synthesis of GQDs for sustainable applications.

Large scale and green synthesis of GQDs is an open challenge to realise the real-world applications. On this journey, several researchers have tried to develop large scale synthesis of GQDs from biomass, however, still the actual amount was in milligrams (Suryawanshi *et al.*, 2014; Wang *et al.*, 2016d). To tackle this challenge, two approaches were employed for the gram scale and green synthesis of GQDs. In the first approach, the GQDs were prepared on a large scale under mild acidic conditions and demonstrated good crystallinity and uniform shape and size. The as-prepared GQDs exhibited a narrow size distribution with an average size of ~3 ± 1.5 nm. The lattice parameter of GQDs was calculated to be 0.24 nm corresponding to the $(11\bar{2}0)$ plane of graphite. In the second methodology, GQDs were produced directly from biomass in a single step via hydrothermal treatment using only water as hydroxyl scissors. The hydrothermal carbonisation time and temperature played an important role in the carbonisation of the biochar precursor to produce GQDs. The GQDs synthesised at optimum conditions of 250 °C and 12 h displayed excellent optical properties. TEM showed a uniform dispersion and consistent shape and size of as-prepared GQDs. Moreover, the GQDs demonstrated a narrow size distribution with an average of ~2 ± 0.5 nm. All these results suggest that the production of high quality GQDs at large scale is possible using a waste precursor and green methodologies. These studies demonstrate the cost-effective and green synthesis of high valued products from little-value biomass waste.

8.2 Future work

The future of the research on GQDs knows no boundaries as it is a relatively new class of carbon material. However, there are some barriers for the development of these nanomaterials in numerous fields. The early research on bioimaging and biosensing applications of GQDs focussed on the fluorescence-based mechanism, however, development of near infrared photoluminescence emitting GQDs and magnetic resonance imaging will help in-vivo experiments. Therefore, advanced synthesis approaches are highly desirable for getting a precise control over property-application relationship. Nonetheless, often this aim has to be well-adjusted by the demands for low cost and large-scale productions. Moreover, the lack of precise characterisation approaches has created discrepancies in the understanding of its physicochemical and optical properties. The basic understanding of the optical, electronic, catalytic and electrochemical properties of the biomass derived GQDs is still very limited and sometimes even controversial due to their large heterogeneity of the precursor material. Careful consideration of chemical and electrochemical stability is required for the practical use of GQDs. But the studies in this respect are limited. Compared with the conventional fluorophores, relatively low quantum yield and broad emission band are the problems associated with the GQDs based fluorescent probes. The former issue can be resolved by reduction in the surface traps and by introduction of dopants, passivation layers, or chemical functionalities. The later one can be tackled by producing GQDs with narrow property distribution.

In this study advanced carbon-based nanomaterials have been successfully prepared from spent tea biomass waste. However, other type of biomass wastes should also be considered to acquire value-added nanomaterials. In addition, industrial scale production of biomass derived GQDs should be explored for the sustainable world. Moreover, investigation should be carried out to synthesise single crystal GQDs for competing with semiconductors. In this study, the synthesis of GQDs was mainly studied, future work should be carried out to evaluate the practical application of these GQDs. Further work can also be performed on the modification of the GQDs properties by doping, surface functionalisation and preparing composite materials for desired applications in bioimaging, sensors, energy and so on. Owing to an excellent range of optical properties of GQDs, their application in targeted drug delivery would be promising. Since GQDs exhibit properties superior to semiconductor quantum dots, they can be used as an alternate candidate to replace the toxic semiconductor dots in wide range of applications such as sensing, bioimaging, medicine, targeted drug delivery, and energy storage and conversion devices.

References

Abbas, A., Mariana, L.T. and Phan, A.N. (2018) 'Biomass-waste derived graphene quantum dots and their applications', *Carbon*, 140, pp. 77-99.

Abbas, A., Tabish, T.A., Bull, S.J., Lim, T.M. and Phan, A.N. (2020) 'High yield synthesis of graphene quantum dots from biomass waste as a highly selective probe for Fe^{3+} sensing', *Scientific Reports*, 10(1), p. 21262.

Acik, M., Lee, G., Mattevi, C., Chhowalla, M., Cho, K. and Chabal, Y. (2010) 'Unusual infrared-absorption mechanism in thermally reduced graphene oxide', *Nature materials*, 9(10), pp. 840-845.

Adinarayana, L., Chunduri, A., Kurdekar, A., Patnaik, S., Aditha, S., Prathibha, C. and Kamisetti, V. (2017) 'Single step synthesis of carbon quantum dots from coconut shell: evaluation for antioxidant efficacy and hemotoxicity', *J. Mater. Sci. Appl*, 3(6), pp. 83-93.

Aidas, K., Kongsted, J., Osted, A., Mikkelsen, K.V. and Christiansen, O. (2005) 'Coupled cluster calculation of the $n \rightarrow \pi^*$ electronic transition of acetone in aqueous solution', *The Journal of Physical Chemistry A*, 109(35), pp. 8001-8010.

Alam, H. and Ramakrishna, S. (2013) 'A review on the enhancement of figure of merit from bulk to nano-thermoelectric materials', *Nano Energy*, 2(2), pp. 190-212.

Alotto, P., Guarnieri, M. and Moro, F. (2014) 'Redox flow batteries for the storage of renewable energy: A review', *Renewable and Sustainable Energy Reviews*, 29, pp. 325-335.

Ananthanarayanan, A., Wang, X., Routh, P., Sana, B., Lim, S., Kim, D.H., Lim, K.H., Li, J. and Chen, P. (2014) 'Facile synthesis of graphene quantum dots from 3D graphene and their application for Fe3+ sensing', *Advanced Functional Materials*, 24(20), pp. 3021-3026.

Ananthanarayanan, A., Wang, Y., Routh, P., Sk, M.A., Than, A., Lin, M., Zhang, J., Chen, J., Sun, H. and Chen, P. (2015) 'Nitrogen and phosphorus co-doped graphene quantum dots: synthesis from adenosine triphosphate, optical properties, and cellular imaging', *Nanoscale*, 7(17), pp. 8159-8165.

Aslandaş, A.M., Balcı, N., Arık, M., Şakiroğlu, H., Onganer, Y. and Meral, K. (2015) 'Liquid nitrogen-assisted synthesis of fluorescent carbon dots from Blueberry and their performance in Fe3+ detection', *Applied Surface Science*, 356, pp. 747-752.

Atchudan, R., Edison, T.N.J.I., Perumal, S., Muthuchamy, N. and Lee, Y.R. (2020) 'Eco-friendly synthesis of tunable fluorescent carbon nanodots from Malus floribunda for sensors and multicolor bioimaging', *Journal of Photochemistry and Photobiology A: Chemistry*, 390, p. 112336.

Aziz, M.A., Hossain, S.I. and Shanmugam, S. (2020) 'Hierarchical oxygen rich-carbon nanorods: Efficient and durable electrode for all-vanadium redox flow batteries', *Journal of Power Sources*, 445, p. 227329.

Aziz, M.A., Oh, K. and Shanmugam, S. (2017) 'A sulfonated poly (arylene ether ketone)/polyoxometalate–graphene oxide composite: a highly ion selective membrane for all vanadium redox flow batteries', *Chemical Communications*, 53(5), pp. 917-920.

Bai, J.-M., Zhang, L., Liang, R.-P. and Qiu, J.-D. (2013) 'Graphene Quantum Dots Combined with Europium Ions as Photoluminescent Probes for Phosphate Sensing', *Chemistry – A European Journal*, 19(12), pp. 3822-3826.

Baker, S.N. and Baker, G.A. (2010) 'Luminescent carbon nanodots: emergent nanolights', *Angewandte Chemie International Edition*, 49(38), pp. 6726-6744.

Balcke, I., Kroepke, R. and Schulz, S. (2017) 'Cosmetic or dermatological preparation for application on wet skin'. Google Patents.

Baldinelli, A., Dou, X., Buchholz, D., Marinaro, M., Passerini, S. and Barelli, L. (2018) 'Addressing the energy sustainability of biowaste-derived hard carbon materials for battery electrodes', *Green chemistry*, 20(7), pp. 1527-1537.

Bardestani, R., Patience, G.S. and Kaliaguine, S. (2019) 'Experimental methods in chemical engineering: specific surface area and pore size distribution measurements—BET, BJH, and DFT', *The Canadian Journal of Chemical Engineering*, 97(11), pp. 2781-2791.

Bekyarova, E., Itkis, M.E., Ramesh, P., Berger, C., Sprinkle, M., de Heer, W.A. and Haddon, R.C. (2009) 'Chemical modification of epitaxial graphene: spontaneous grafting of aryl groups', *Journal of the American Chemical Society*, 131(4), pp. 1336-1337.

Bhattarai, A., Ghimire, P.C., Whitehead, A., Schweiss, R., Scherer, G.G., Wai, N. and Hng, H.H. (2018) 'Novel Approaches for Solving the Capacity Fade Problem during Operation of a Vanadium Redox Flow Battery', *Batteries*, 4(4).

Bhattarai, A., Wai, N., Schweiss, R., Whitehead, A., Scherer, G.G., Ghimire, P.C., Lim, T.M. and Hng, H.H. (2019) 'Vanadium redox flow battery with slotted porous electrodes and automatic rebalancing demonstrated on a 1 kW system level', *Applied Energy*, 236, pp. 437-443.

Biju, V. (2014) 'Chemical modifications and bioconjugate reactions of nanomaterials for sensing, imaging, drug delivery and therapy', *Chemical Society Reviews*, 43(3), pp. 744-764.

Bilbao, R., Millera, A. and Arauzo, J. (1989) 'Thermal decomposition of lignocellulosic materials: influence of the chemical composition', *Thermochimica acta*, 143, pp. 149-159.

Biswal, M., Banerjee, A., Deo, M. and Ogale, S. (2013) 'From dead leaves to high energy density supercapacitors', *Energy & Environmental Science*, 6(4), pp. 1249-1259.

Bouleghlimat, E., Davies, P.R., Davies, R.J., Howarth, R., Kulhavy, J. and Morgan, D.J. (2013) 'The effect of acid treatment on the surface chemistry and topography of graphite', *Carbon*, 61, pp. 124-133.

Bourlinos, A.B., Stassinopoulos, A., Anglos, D., Zboril, R., Karakassides, M. and Giannelis, E.P. (2008) 'Surface functionalized carbogenic quantum dots', *Small*, 4(4), pp. 455-458.

Brebu, M. and Vasile, C. (2010) 'Thermal degradation of lignin—a review', *Cellulose Chemistry & Technology*, 44(9), p. 353.

Bridgwater, A.V. (2012) 'Review of fast pyrolysis of biomass and product upgrading', *Biomass and bioenergy*, 38, pp. 68-94.

Brunauer, S., Emmett, P.H. and Teller, E. (1938) 'Adsorption of gases in multimolecular layers', *Journal of the American chemical society*, 60(2), pp. 309-319.

Buscema, M., Groenendijk, D.J., Steele, G.A., Van Der Zant, H.S. and Castellanos-Gomez, A. (2014) 'Photovoltaic effect in few-layer black phosphorus PN junctions defined by local electrostatic gating', *arXiv preprint arXiv:1407.2863*.

Butler, S.Z., Hollen, S.M., Cao, L., Cui, Y., Gupta, J.A., Gutiérrez, H.R., Heinz, T.F., Hong, S.S., Huang, J. and Ismach, A.F. (2013) 'Progress, challenges, and opportunities in two-dimensional materials beyond graphene', *ACS nano*, 7(4), pp. 2898-2926.

Buzaglo, M., Shtein, M. and Regev, O. (2015) 'Graphene quantum dots produced by microfluidization', *Chemistry of Materials*, 28(1), pp. 21-24.

Cappella, B. and Dietler, G. (1999) 'Force-distance curves by atomic force microscopy', *Surface Science Reports*, 34(1), pp. 1-104.

Castañeda, L.F., Walsh, F.C., Nava, J.L. and de León, C.P. (2017) 'Graphite felt as a versatile electrode material: Properties, reaction environment, performance and applications', *Electrochimica Acta*.

Chao, D., Zhu, C., Xia, X., Liu, J., Zhang, X., Wang, J., Liang, P., Lin, J., Zhang, H., Shen, Z.X. and Fan, H.J. (2015) 'Graphene quantum dots coated VO2 arrays for highly durable electrodes for Li and Na ion batteries', *Nano letters*, 15(1), pp. 565-573.

Chen, L., Guo, C.X., Zhang, Q., Lei, Y., Xie, J., Ee, S., Guai, G., Song, Q. and Li, C.M. (2013) 'Graphene quantum-dot-doped polypyrrole counter electrode for high-performance dye-sensitized solar cells', *ACS applied materials & interfaces*, 5(6), pp. 2047-2052.

Chen, Q., Hu, Y., Hu, C., Cheng, H., Zhang, Z., Shao, H. and Qu, L. (2014) 'Graphene quantum dots–three-dimensional graphene composites for high-performance supercapacitors', *Physical Chemistry Chemical Physics*, 16(36), pp. 19307-19313.

Cheng, H., Hu, C., Zhao, Y. and Qu, L. (2014) 'Graphene fiber: a new material platform for unique applications', *NPG Asia Materials*, 6(7), p. e113.

Chingombe, P., Saha, B. and Wakeman, R.J. (2005) 'Surface modification and characterisation of a coal-based activated carbon', *Carbon*, 43(15), pp. 3132-3143.

Choi, C., Kim, S., Kim, R., Choi, Y., Kim, S., Jung, H.-y., Yang, J.H. and Kim, H.-T. (2017) 'A review of vanadium electrolytes for vanadium redox flow batteries', *Renewable and Sustainable Energy Reviews*, 69, pp. 263-274.

Choi, C., Noh, H., Kim, S., Kim, R., Lee, J., Heo, J. and Kim, H.-T. (2019) 'Understanding the redox reaction mechanism of vanadium electrolytes in all-vanadium redox flow batteries', *Journal of Energy Storage*, 21, pp. 321-327.

Choi, S.-H. (2017) 'Unique properties of graphene quantum dots and their applications in photonic/electronic devices', *Journal of Physics D: Applied Physics*, 50(10), p. 103002.

Chu, P.K. and Li, L. (2006) 'Characterization of amorphous and nanocrystalline carbon films', *Materials Chemistry and Physics,* 96(2), pp. 253-277.

Chung, S., Revia, R.A. and Zhang, M. (2019) 'Graphene Quantum Dots and Their Applications in Bioimaging, Biosensing, and Therapy', *Advanced Materials*.

Corcuera, S. and Skyllas-Kazacos, M. (2012) 'State-of-charge monitoring and electrolyte rebalancing methods for the vanadium redox flow battery', *European Chemical Bulletin*, 1(12), pp. 511-519.

Cui, Y., Wang, H., Mao, N., Yu, W., Shi, J., Huang, M., Liu, W., Chen, S. and Wang, X. (2017) 'Tuning the morphology and structure of nanocarbons with activating agents for ultrafast ionic liquid-based supercapacitors', *Journal of Power Sources*, 361, pp. 182-194.

Dai, J. and Zeng, X.C. (2014) 'Bilayer phosphorene: effect of stacking order on bandgap and its potential applications in thin-film solar cells', *The journal of physical chemistry letters,* 5(7), pp. 1289-1293.

Dai, Y., Long, H., Wang, X., Wang, Y., Gu, Q., Jiang, W., Wang, Y., Li, C., Zeng, T.H., Sun, Y. and Zeng, J. (2014) 'Versatile Graphene Quantum Dots with Tunable Nitrogen Doping', *Particle & Particle Systems Characterization*, 31(5), pp. 597-604.

Das, R., Sugimoto, H., Fujii, M. and Giri, P.K. (2020) 'Quantitative Understanding of Charge Transfer Mediated Fe3+ Sensing and Fast Photoresponse by N-doped Graphene Quantum Dots Decorated on Plasmonic Au Nanoparticles', *ACS Applied Materials & Interfaces*.

De Boer, J., Linsen, B., Van der Plas, T. and Zondervan, G. (1965) 'Studies on pore systems in catalysts: VII. Description of the pore dimensions of carbon blacks by the t method', *Journal of Catalysis*, 4(6), pp. 649-653.

Deka, M.J., Dutta, A. and Chowdhury, D. (2018) 'Tuning the wettability and photoluminescence of graphene quantum dots via covalent modification', *New Journal of Chemistry*, 42(1), pp. 355-362.

Deng, J., Li, M. and Wang, Y. (2016) 'Biomass-derived carbon: Synthesis and applications in energy storage and conversion', *Green Chemistry*, 18(18), pp. 4824-4854.

Deng, Y., Luo, Z., Conrad, N.J., Liu, H., Gong, Y., Najmaei, S., Ajayan, P.M., Lou, J., Xu, X. and Ye, P.D. (2014) 'Black phosphorus–monolayer MoS2 van der Waals heterojunction p–n diode', *ACS nano*, 8(8), pp. 8292-8299.

Deng, Y., Zhao, D., Chen, X., Wang, F., Song, H. and Shen, D. (2013) 'Long lifetime pure organic phosphorescence based on water soluble carbon dots', *Chemical Communications*, 49(51), pp. 5751-5753.

Diao, S., Zhang, X., Shao, Z., Ding, K., Jie, J. and Zhang, X. (2017) '12.35% efficient graphene quantum dots/silicon heterojunction solar cells using graphene transparent electrode', *Nano Energy*, 31, pp. 359-366.

Ding, H., Yu, S.-B., Wei, J.-S. and Xiong, H.-M. (2015) 'Full-color light-emitting carbon dots with a surface-state-controlled luminescence mechanism', *ACS nano*, 10(1), pp. 484-491.

Ding, Z., Li, F., Wen, J., Wang, X. and Sun, R. (2018) 'Gram-scale synthesis of single-crystalline graphene quantum dots derived from lignin biomass', *Green chemistry*, 20(6), pp. 1383-1390.

Dong, Y., Li, G., Zhou, N., Wang, R., Chi, Y. and Chen, G. (2012a) 'Graphene Quantum Dot as a Green and Facile Sensor for Free Chlorine in Drinking Water', *Analytical Chemistry*, 84(19), pp. 8378-8382.

Dong, Y., Shao, J., Chen, C., Li, H., Wang, R., Chi, Y., Lin, X. and Chen, G. (2012b) 'Blue luminescent graphene quantum dots and graphene oxide prepared by tuning the carbonization degree of citric acid', *Carbon*, 50(12), pp. 4738-4743.

Duan, X., Sun, H., Ao, Z., Zhou, L., Wang, G. and Wang, S. (2016) 'Unveiling the active sites of graphene-catalyzed peroxymonosulfate activation', *Carbon*, 107, pp. 371-378.

Dutta Chowdhury, A. and Doong, R.-a. (2016) 'Highly sensitive and selective detection of nanomolar ferric ions using dopamine functionalized graphene quantum dots', *ACS applied materials & interfaces*, 8(32), pp. 21002-21010.

Dutta, M., Sarkar, S., Ghosh, T. and Basak, D. (2012) 'ZnO/graphene quantum dot solid-state solar cell', *The Journal of Physical Chemistry C*, 116(38), pp. 20127-20131.

Eda, G., Lin, Y.Y., Mattevi, C., Yamaguchi, H., Chen, H.A., Chen, I., Chen, C.W. and Chhowalla, M. (2010) 'Blue photoluminescence from chemically derived graphene oxide', *Advanced materials*, 22(4), pp. 505-509.

Fang, X., Li, M., Guo, K., Li, J., Pan, M., Bai, L., Luoshan, M. and Zhao, X. (2014) 'Graphene quantum dots optimization of dye-sensitized solar cells', *Electrochimica Acta*, 137, pp. 634-638.

Feng, L., Wu, Y.-X., Zhang, D.-L., Hu, X., Zhang, J., Wang, P., Song, Z.-L., Zhang, X.-B. and Tan, W. (2017) 'A Near Infrared Graphene Quantum Dots-Based Two-Photon Nanoprobe for Direct Bioimaging of Endogenous Ascorbic Acid in Living Cells', *Analytical Chemistry*.

Ferrari, A.C. and Basko, D.M. (2013) 'Raman spectroscopy as a versatile tool for studying the properties of graphene', *Nature Nanotechnology*, 8(4), pp. 235-246.

Ferrari, A.C., Meyer, J.C., Scardaci, V., Casiraghi, C., Lazzeri, M., Mauri, F., Piscanec, S., Jiang, D., Novoselov, K.S. and Roth, S. (2006) 'Raman spectrum of graphene and graphene layers', *Physical review letters*, 97(18), p. 187401.

Ferrari, A.C. and Robertson, J. (2000) 'Interpretation of Raman spectra of disordered and amorphous carbon', *Physical review B*, 61(20), p. 14095.

Franco, S., Mandla, V.R. and Ram Mohan Rao, K. (2017) 'Urbanization, energy consumption and emissions in the Indian context A review', *Renewable and Sustainable Energy Reviews*, 71, pp. 898-907.

Funke, A. and Ziegler, F. (2010) 'Hydrothermal carbonization of biomass: a summary and discussion of chemical mechanisms for process engineering', *Biofuels, Bioproducts and Biorefining*, 4(2), pp. 160-177.

Gani, A. and Naruse, I. (2007) 'Effect of cellulose and lignin content on pyrolysis and combustion characteristics for several types of biomass', *Renewable Energy*, 32(4), pp. 649-661.

Gao, P., Ding, K., Wang, Y., Ruan, K., Diao, S., Zhang, Q., Sun, B. and Jie, J. (2014) 'Crystalline Si/graphene quantum dots heterojunction solar cells', *The Journal of Physical Chemistry C*, 118(10), pp. 5164-5171.

Ge, J., Lan, M., Zhou, B., Liu, W., Guo, L., Wang, H., Jia, Q., Niu, G., Huang, X., Zhou, H., Meng, X., Wang, P., Lee, C.S., Zhang, W. and Han, X. (2014) 'A graphene quantum dot photodynamic therapy agent with high singlet oxygen generation', *Nature Communications*, 5.

Georgakilas, V., Perman, J.A., Tucek, J. and Zboril, R. (2015) 'Broad Family of Carbon Nanoallotropes: Classification, Chemistry, and Applications of Fullerenes, Carbon Dots, Nanotubes, Graphene, Nanodiamonds, and Combined Superstructures', *Chemical Reviews*, 115(11), pp. 4744-4822.

Georgakilas, V., Tiwari, J.N., Kemp, K.C., Perman, J.A., Bourlinos, A.B., Kim, K.S. and Zboril, R. (2016) 'Noncovalent Functionalization of Graphene and Graphene Oxide for Energy Materials, Biosensing, Catalytic, and Biomedical Applications', *Chemical Reviews*, 116(9), pp. 5464-5519.

Girit, Ç.Ö., Meyer, J.C., Erni, R., Rossell, M.D., Kisielowski, C., Yang, L., Park, C.-H., Crommie, M.F., Cohen, M.L., Louie, S.G. and Zettl, A. (2009) 'Graphene at the Edge: Stability and Dynamics', *Science*, 323(5922), pp. 1705-1708.

Goldemberg, J., Johansson, T.B., Reddy, A.K.N. and Williams, R.H. (1988) *Energy for a sustainable world*. New York: Wiley

Gullapalli, S. and Barron, A. (2010) 'Optical Characterization of Group 12-16 (II-VI) Semiconductor Nanoparticles by Fluorescence Spectroscopy', *Connexions*.

Guo, C.X., Yang, H.B., Sheng, Z.M., Lu, Z.S., Song, Q.L. and Li, C.M. (2010) 'Layered graphene/quantum dots for photovoltaic devices', *Angewandte Chemie International Edition*, 49(17), pp. 3014-3017.

Guo, S. and Dong, S. (2011) 'Graphene nanosheet: synthesis, molecular engineering, thin film, hybrids, and energy and analytical applications', *Chemical Society Reviews*, 40(5), pp. 2644-2672.

Guo, S., Dong, X., Wu, T. and Zhu, C. (2016) 'Influence of reaction conditions and feedstock on hydrochar properties', *Energy Conversion and Management*, 123, pp. 95-103.

Gupta, A., Chen, G., Joshi, P., Tadigadapa, S. and Eklund, P.C. (2006) 'Raman scattering from high-frequency phonons in supported n-graphene layer films', *Nano letters*, 6(12), pp. 2667-2673.

Gupta, V., Chaudhary, N., Srivastava, R., Sharma, G.D., Bhardwaj, R. and Chand, S. (2011) 'Luminscent graphene quantum dots for organic photovoltaic devices', *Journal of the American Chemical Society*, 133(26), pp. 9960-9963.

Halsey, G. (1948) 'Physical adsorption on non-uniform surfaces', *The Journal of chemical physics*, 16(10), pp. 931-937.

Hasan, M.T., Gonzalez-Rodriguez, R., Ryan, C., Faerber, N., Coffer, J.L. and Naumov, A.V. (2018) 'Photo-and Electroluminescence from Nitrogen-Doped and Nitrogen–Sulfur Codoped Graphene Quantum Dots', *Advanced Functional Materials*, 28(42), p. 1804337.

Hassan, M., Haque, E., Reddy, K.R., Minett, A.I., Chen, J. and Gomes, V.G. (2014) 'Edge-enriched graphene quantum dots for enhanced photo-luminescence and supercapacitance', *Nanoscale*, 6(20), pp. 11988-11994.

Hayat, K., Iqbal, H., Malik, U., Bilal, U. and Mushtaq, S. (2015) 'Tea and Its Consumption: Benefits and Risks', *Critical Reviews in Food Science and Nutrition*, 55(7), pp. 939-954.

He, C., Song, S., Liu, J., Maragou, V. and Tsiakaras, P. (2010) 'KOH-activated multi-walled carbon nanotubes as platinum supports for oxygen reduction reaction', *Journal of Power Sources*, 195(21), pp. 7409-7414.

He, G., Song, Y., Liu, K., Walter, A., Chen, S. and Chen, S. (2013) 'Oxygen reduction catalyzed by platinum nanoparticles supported on graphene quantum dots', *Acs Catalysis*, 3(5), pp. 831-838.

He, X., Zhang, S., Pan, H., Chen, J. and Xu, J. (2019) 'Horizontally Aggregation of Monolayer Reduced Graphene Oxide Under Deep UV Irradiation in Solution', *Nanoscale research letters*, 14(1), p. 117.

Hirose, T., Fujino, T., Fan, T., Endo, H., Okabe, T. and Yoshimura, M. (2002) 'Effect of carbonization temperature on the structural changes of woodceramics impregnated with liquefied wood', *Carbon*, 40(5), pp. 761-765.

Hoekman, S.K., Broch, A. and Robbins, C. (2011) 'Hydrothermal carbonization (HTC) of lignocellulosic biomass', *Energy & Fuels*, 25(4), pp. 1802-1810.

Hoffmann, R. (1968) 'Trimethylene and the addition of methylene to ethylene', *Journal of the American Chemical Society*, 90(6), pp. 1475-1485.

Hola, K., Zhang, Y., Wang, Y., Giannelis, E.P., Zboril, R. and Rogach, A.L. (2014) 'Carbon dots - Emerging light emitters for bioimaging, cancer therapy and optoelectronics', *Nano Today*, 9(5), pp. 590-603.

Hong, G., Diao, S., Antaris, A.L. and Dai, H. (2015) 'Carbon Nanomaterials for Biological Imaging and Nanomedicinal Therapy', *Chemical Reviews*, 115(19), pp. 10816-10906.

Hsu, P.-C. and Chang, H.-T. (2012) 'Synthesis of high-quality carbon nanodots from hydrophilic compounds: role of functional groups', *Chemical communications*, 48(33), pp. 3984-3986.

Hu, B., Wang, K., Wu, L., Yu, S.-H., Antonietti, M. and Titirici, M.-M. (2010) 'Engineering Carbon Materials from the Hydrothermal Carbonization Process of Biomass', *Advanced Materials*, 22(7), pp. 813-828.

Hu, C., Liu, Y., Yang, Y., Cui, J., Huang, Z., Wang, Y., Yang, L., Wang, H., Xiao, Y. and Rong, J. (2013a) 'One-step preparation of nitrogen-doped graphene quantum dots from oxidized debris of graphene oxide', *Journal of Materials Chemistry B*, 1(1), pp. 39-42.

Hu, C., Song, L., Zhang, Z., Chen, N., Feng, Z. and Qu, L. (2015) 'Tailored graphene systems for unconventional applications in energy conversion and storage devices', *Energy and Environmental Science*, 8(1), pp. 31-54.

Hu, S., Tian, R., Wu, L., Zhao, Q., Yang, J., Liu, J. and Cao, S. (2013b) 'Chemical regulation of carbon quantum dots from synthesis to photocatalytic activity', *Chemistry–An Asian Journal*, 8(5), pp. 1035-1041.

Hu, S.H., Chen, Y.W., Hung, W.T., Chen, I.W. and Chen, S.Y. (2012) 'Quantum-dot-tagged reduced graphene oxide nanocomposites for bright fluorescence bioimaging and photothermal therapy monitored in situ', *Advanced Materials*, 24(13), pp. 1748-1754.

Hu, Y., Zhao, Y., Lu, G., Chen, N., Zhang, Z., Li, H., Shao, H. and Qu, L. (2013c) 'Graphene quantum dots–carbon nanotube hybrid arrays for supercapacitors', *Nanotechnology*, 24(19), p. 195401.

Huang, H., Peng, L., Fang, W., Cai, S., Chu, X., Liu, Y., Gao, W., Xu, Z. and Gao, C. (2020) 'A polyimide-pyrolyzed carbon waste approach for the scalable and controlled electrochemical preparation of size-tunable graphene', *Nanoscale*, 12(22), pp. 11971-11978.

Iijima, S. (1991) 'Helical microtubules of graphitic carbon', *Nature*, 354(6348), pp. 56-58.

Iijima, S. and Ichihashi, T. (1993) 'Single-shell carbon nanotubes of 1-nm diameter', *Nature*, 363(6430), pp. 603-605.

Islam, M.S., Deng, Y., Tong, L., Roy, A.K., Faisal, S.N., Hassan, M., Minett, A.I. and Gomes, V.G. (2017) 'In-situ direct grafting of graphene quantum dots onto carbon fibre by low temperature chemical synthesis for high performance flexible fabric supercapacitor', *Materials Today Communications*, 10, pp. 112-119.

Jain, A., Balasubramanian, R. and Srinivasan, M.P. (2016) 'Hydrothermal conversion of biomass waste to activated carbon with high porosity: A review', *Chemical Engineering Journal*, 283, pp. 789-805.

Jänes, A., Kurig, H. and Lust, E. (2007) 'Characterisation of activated nanoporous carbon for supercapacitor electrode materials', *Carbon*, 45(6), pp. 1226-1233.

Jang, M.-H., Song, S.H., Ha, H.D., Seo, T.S., Jeon, S. and Cho, Y.-H. (2017) 'Origin of extraordinary luminescence shift in graphene quantum dots with varying excitation energy: An experimental evidence of localized sp2 carbon subdomain', *Carbon*, 118, pp. 524-530.

Jia, B., Gao, L. and Sun, J. (2007) 'Self-assembly of magnetite beads along multiwalled carbon nanotubes via a simple hydrothermal process', *Carbon*, 45(7), pp. 1476-1481.

Jia, X., Li, J. and Wang, E. (2012) 'One-pot green synthesis of optically pH-sensitive carbon dots with upconversion luminescence', *Nanoscale*, 4(18), pp. 5572-5575.

Jin, J., Fu, X., Liu, Q., Liu, Y., Wei, Z., Niu, K. and Zhang, J. (2013) 'Identifying the active site in nitrogen-doped graphene for the VO2+/VO2+ redox reaction', *Acs Nano*, 7(6), pp. 4764-4773.

Ju, J. and Chen, W. (2014) 'Synthesis of highly fluorescent nitrogen-doped graphene quantum dots for sensitive, label-free detection of Fe (III) in aqueous media', *Biosensors and Bioelectronics*, 58, pp. 219-225.

Kalgo, A.S. (2011) 'The development and optimisation of a fast pyrolysis process for bio-oil production'.

Kalita, H., Mohapatra, J., Pradhan, L., Mitra, A., Bahadur, D. and Aslam, M. (2016) 'Efficient synthesis of rice based graphene quantum dots and their fluorescent properties', *RSC Advances*, 6(28), pp. 23518-23524.

Kang, S., Jeong, Y.K., Ryu, J.H., Son, Y., Kim, W.R., Lee, B., Jung, K.H. and Kim, K.M. (2020) 'Pulsed laser ablation based synthetic route for nitrogen-doped graphene quantum dots using graphite flakes', *Applied Surface Science*, 506, p. 144998.

Kawano, T., Kubota, M., Onyango, M.S., Watanabe, F. and Matsuda, H. (2008) 'Preparation of activated carbon from petroleum coke by KOH chemical activation for adsorption heat pump', *Applied thermal engineering*, 28(8), pp. 865-871.

Kear, G., Shah, A.A. and Walsh, F.C. (2012) 'Development of the all-vanadium redox flow battery for energy storage: a review of technological, financial and policy aspects', *International Journal of Energy Research*, 36(11), pp. 1105-1120.

Khan, W.U., Wang, D., Zhang, W., Tang, Z., Ma, X., Ding, X., Du, S. and Wang, Y. (2017) 'High quantum yield green-emitting carbon dots for Fe (III) detection, biocompatible fluorescent ink and cellular imaging', *Scientific reports*, 7(1), pp. 1-9.

Khodadadei, F., Safarian, S. and Ghanbari, N. (2017) 'Methotrexate-loaded nitrogen-doped graphene quantum dots nanocarriers as an efficient anticancer drug delivery system', *Materials Science and Engineering: C*, 79, pp. 280-285.

Kim, J.K., Kim, S.J., Park, M.J., Bae, S., Cho, S.-P., Du, Q.G., Wang, D.H., Park, J.H. and Hong, B.H. (2015a) 'Surface-engineered graphene quantum dots incorporated into polymer layers for high performance organic photovoltaics', *Scientific reports*, 5.

Kim, K.J., Park, M.-S., Kim, Y.-J., Kim, J.H., Dou, S.X. and Skyllas-Kazacos, M. (2015b) 'A technology review of electrodes and reaction mechanisms in vanadium redox flow batteries', *Journal of materials chemistry a*, 3(33), pp. 16913-16933.

Kim, S. (2019) 'Vanadium Redox Flow Batteries: Electrochemical Engineering', in *Energy Storage Devices*. IntechOpen.

Kim, S., Hee Shin, D., Oh Kim, C., Seok Kang, S., Sin Joo, S., Choi, S.-H., Won Hwang, S. and Sone, C. (2013) 'Size-dependence of Raman scattering from graphene quantum dots: interplay between shape and thickness', *Applied Physics Letters*, 102(5), p. 053108.

Kim, S., Hwang, S.W., Kim, M.-K., Shin, D.Y., Shin, D.H., Kim, C.O., Yang, S.B., Park, J.H., Hwang, E. and Choi, S.-H. (2012) 'Anomalous behaviors of visible luminescence from graphene quantum dots: interplay between size and shape', *ACS nano*, 6(9), pp. 8203-8208.

Konstantatos, G., Badioli, M., Gaudreau, L., Osmond, J., Bernechea, M., De Arquer, F.P.G., Gatti, F. and Koppens, F.H.L. (2012) 'Hybrid grapheneĝquantum dot phototransistors with ultrahigh gain', *Nature Nanotechnology*, 7(6), pp. 363-368.

Kou, L., Huang, T., Zheng, B., Han, Y., Zhao, X., Gopalsamy, K., Sun, H. and Gao, C. (2014) 'Coaxial wet-spun yarn supercapacitors for high-energy density and safe wearable electronics', *Nature communications*, 5.

Kroto, H.W., Heath, J.R., O'Brien, S.C., Curl, R.F. and Smalley, R.E. (1985) 'C 60: buckminsterfullerene', *Nature*, 318(6042), pp. 162-163.

Kumar, G.S., Roy, R., Sen, D., Ghorai, U.K., Thapa, R., Mazumder, N., Saha, S. and Chattopadhyay, K.K. (2014) 'Amino-functionalized graphene quantum dots: origin of tunable heterogeneous photoluminescence', *Nanoscale*, 6(6), pp. 3384-3391.

Kumawat, M.K., Srivastava, R., Thakur, M. and Gurung, R.B. (2017) 'Graphene quantum dots from mangifera indica: Application in near-infrared bioimaging and intracellular nanothermometry', *ACS Sustainable Chemistry and Engineering*, 5(2), pp. 1382-1391.

Kwon, W., Kim, Y.-H., Kim, J.-H., Lee, T., Do, S., Park, Y., Jeong, M.S., Lee, T.-W. and Rhee, S.-W. (2016) 'High Color-Purity Green, Orange, and Red Light-Emitting Diodes Based on Chemically Functionalized Graphene Quantum Dots', *Scientific Reports*, 6, p. 24205.

Kwon, W., Kim, Y.-H., Lee, C.-L., Lee, M., Choi, H.C., Lee, T.-W. and Rhee, S.-W. (2014) 'Electroluminescence from graphene quantum dots prepared by amidative cutting of tattered graphite', *Nano letters*, 14(3), pp. 1306-1311.

Lai, C.-W., Hsiao, Y.-H., Peng, Y.-K. and Chou, P.-T. (2012) 'Facile synthesis of highly emissive carbon dots from pyrolysis of glycerol; gram scale production of carbon dots/mSiO 2 for cell imaging and drug release', *Journal of Materials Chemistry*, 22(29), pp. 14403-14409.

Lai, S., Jin, Y., Shi, L., Zhou, R., Zhou, Y. and An, D. (2020) 'Mechanisms behind excitation- and concentration-dependent multicolor photoluminescence in graphene quantum dots', *Nanoscale*, 12(2), pp. 591-601.

Lappetito, L. (2015) *Quantum Dots : a True "Particle in a Box" System*. Available at: http://physicsopenlab.org/2015/11/20/quantum-dots-a-true-particle-in-a-box-system/ and https://northbeggar.wordpress.com/2009/10/04/exciton/#respond (Accessed: January 05).

Lazim, Z.M., Mazuin, E., Hadibarata, T. and Yusop, Z. (2015) 'The removal of methylene blue and Remazol Brilliant Blue R dyes by using orange peel and spent tea leaves', *Journal Teknologi*, 74, pp. 129-135.

Lee, E., Ryu, J. and Jang, J. (2013a) 'Fabrication of graphene quantum dots via size-selective precipitation and their application in upconversion-based DSSCs', *Chemical Communications*, 49(85), pp. 9995-9997.

Lee, Y., Park, J., Ryu, C., Gang, K.S., Yang, W., Park, Y.-K., Jung, J. and Hyun, S. (2013b) 'Comparison of biochar properties from biomass residues produced by slow pyrolysis at 500 C', *Bioresource technology*, 148, pp. 196-201.

Lesani, P., Singh, G., Viray, C., Ramaswamy, Y., Zhu, D.M., Kingshott, P., Lu, Z. and Zreiqat, H. (2020) 'Two-Photon Dual-Emissive Carbon Dot-Based Probe: Deep Tissue Imaging and Ultrasensitive Sensing of Intracellular Ferric Ions', *ACS Applied Materials & Interfaces*.

Leung, P., Li, X., De León, C.P., Berlouis, L., Low, C.J. and Walsh, F.C. (2012) 'Progress in redox flow batteries, remaining challenges and their applications in energy storage', *Rsc Advances*, 2(27), pp. 10125-10156.

Leung, P., Shah, A.A., Sanz, L., Flox, C., Morante, J.R., Xu, Q., Mohamed, M.R., Ponce de León, C. and Walsh, F.C. (2017) 'Recent developments in organic redox flow batteries: A critical review', *Journal of Power Sources*, 360, pp. 243-283.

Li, B., Gu, M., Nie, Z., Shao, Y., Luo, Q., Wei, X., Li, X., Xiao, J., Wang, C. and Sprenkle, V. (2013a) 'Bismuth nanoparticle decorating graphite felt as a high-performance electrode for an all-vanadium redox flow battery', *Nano letters*, 13(3), pp. 1330-1335.

Li, H., He, X., Kang, Z., Huang, H., Liu, Y., Liu, J., Lian, S., Tsang, C.H.A., Yang, X. and Lee, S.T. (2010) 'Water-soluble fluorescent carbon quantum dots and photocatalyst design', *Angewandte Chemie*, 122(26), pp. 4532-4536.

Li, K., Zhao, X., Wei, G. and Su, Z. (2017) 'Recent Advance in the Cancer Bioimaging with Graphene Quantum Dots', *Current medicinal chemistry*.

Li, L., Wu, G., Yang, G., Peng, J., Zhao, J. and Zhu, J.-J. (2013b) 'Focusing on luminescent graphene quantum dots: current status and future perspectives', *Nanoscale*, 5(10), pp. 4015-4039.

Li, L.L., Ji, J., Fei, R., Wang, C.Z., Lu, Q., Zhang, J.R., Jiang, L.P. and Zhu, J.J. (2012a) 'A facile microwave avenue to electrochemiluminescent two-color graphene quantum dots', *Advanced Functional Materials*, 22(14), pp. 2971-2979.

Li, Q., Zhang, S., Dai, L. and Li, L.-s. (2012b) 'Nitrogen-doped colloidal graphene quantum dots and their size-dependent electrocatalytic activity for the oxygen reduction reaction', *Journal of the American Chemical Society*, 134(46), pp. 18932-18935.

Li, Q., Zhou, M., Yang, M., Yang, Q., Zhang, Z. and Shi, J. (2018) 'Induction of long-lived room temperature phosphorescence of carbon dots by water in hydrogen-bonded matrices', *Nature communications*, 9(1), pp. 1-8.

Li, X., Lau, S.P., Tang, L., Ji, R. and Yang, P. (2014) 'Sulphur doping: a facile approach to tune the electronic structure and optical properties of graphene quantum dots', *Nanoscale*, 6(10), pp. 5323-5328.

Li, Y., Hu, Y., Zhao, Y., Shi, G., Deng, L., Hou, Y. and Qu, L. (2011a) 'An electrochemical avenue to green-luminescent graphene quantum dots as potential electron-acceptors for photovoltaics', *Advanced Materials*, 23(6), pp. 776-780.

Li, Y., Zhao, Y., Cheng, H., Hu, Y., Shi, G., Dai, L. and Qu, L. (2011b) 'Nitrogen-doped graphene quantum dots with oxygen-rich functional groups', *Journal of the American Chemical Society*, 134(1), pp. 15-18.

Li, Y., Zhao, Y., Cheng, H., Hu, Y., Shi, G., Dai, L. and Qu, L. (2012c) 'Nitrogen-Doped Graphene Quantum Dots with Oxygen-Rich Functional Groups', *Journal of the American Chemical Society*, 134(1), pp. 15-18.

Liang, Z., Kang, M., Payne, G.F., Wang, X. and Sun, R. (2016) 'Probing Energy and Electron Transfer Mechanisms in Fluorescence Quenching of Biomass Carbon Quantum Dots', *ACS Applied Materials & Interfaces*, 8(27), pp. 17478-17488.

Libra, J.A., Ro, K.S., Kammann, C., Funke, A., Berge, N.D., Neubauer, Y., Titirici, M.-M., Fühner, C., Bens, O. and Kern, J. (2011) 'Hydrothermal carbonization of biomass residuals: a comparative review of the chemistry, processes and applications of wet and dry pyrolysis', *Biofuels*, 2(1), pp. 71-106.

Lijuan, K., Yongqiang, Y., Ruiyi, L. and Zaijun, L. (2016) 'Phenylalanine-functionalized graphene quantum dot-silicon nanoparticle composite as an anode material for lithium ion batteries with largely enhanced electrochemical performance', *Electrochimica Acta*, 198, pp. 144-155.

Lillo-Ródenas, M., Cazorla-Amorós, D. and Linares-Solano, A. (2003) 'Understanding chemical reactions between carbons and NaOH and KOH: an insight into the chemical activation mechanism', *Carbon*, 41(2), pp. 267-275.

Lim, C.S., Hola, K., Ambrosi, A., Zboril, R. and Pumera, M. (2015) 'Graphene and carbon quantum dots electrochemistry', *Electrochemistry Communications*, 52, pp. 75-79.

Lin, J., Chen, X. and Huang, P. (2016) 'Graphene-based nanomaterials for bioimaging', *Advanced Drug Delivery Reviews*, 105, pp. 242-254.

Lin, Y.-C., Cho, J., Tompsett, G.A., Westmoreland, P.R. and Huber, G.W. (2009) 'Kinetics and mechanism of cellulose pyrolysis', *The Journal of Physical Chemistry C*, 113(46), pp. 20097-20107.

Liu, J., Geng, Y., Li, D., Yao, H., Huo, Z., Li, Y., Zhang, K., Zhu, S., Wei, H., Xu, W., Jiang, J. and Yang, B. (2020a) 'Deep Red Emissive Carbonized Polymer Dots with Unprecedented Narrow Full Width at Half Maximum', *Advanced Materials*, 32(17), p. 1906641.

Liu, Q., Sun, J., Gao, K., Chen, N., Sun, X., Ti, D., Bai, C., Cui, R. and Qu, L. (2020b) 'Graphene quantum dots for energy storage and conversion: from fabrication to applications', *Materials Chemistry Frontiers*.

Liu, W., Li, C., Sun, X., Pan, W., Yu, G. and Wang, J. (2017) 'Highly crystalline carbon dots from fresh tomato: UV emission and quantum confinement', *Nanotechnology*, 28(48), p. 485705.

Liu, W., Yan, X., Chen, J., Feng, Y. and Xue, Q. (2013a) 'Novel and high-performance asymmetric micro-supercapacitors based on graphene quantum dots and polyaniline nanofibers', *Nanoscale*, 5(13), pp. 6053-6062.

Liu, W.W., Feng, Y.Q., Yan, X.B., Chen, J.T. and Xue, Q.J. (2013b) 'Superior Micro-Supercapacitors Based on Graphene Quantum Dots', *Advanced Functional Materials*, 23(33), pp. 4111-4122.

Long, R. (2013) 'Understanding the Electronic Structures of Graphene Quantum Dot Physisorption and Chemisorption onto the TiO2 (110) Surface: A First-Principles Calculation', *ChemPhysChem*, 14(3), pp. 579-582.

Lu, J., Yang, J.-x., Wang, J., Lim, A., Wang, S. and Loh, K.P. (2009) 'One-pot synthesis of fluorescent carbon nanoribbons, nanoparticles, and graphene by the exfoliation of graphite in ionic liquids', *ACS nano*, 3(8), pp. 2367-2375.

Lu, J., Yeo, P.S.E., Gan, C.K., Wu, P. and Loh, K.P. (2011) 'Transforming C60 molecules into graphene quantum dots', *Nature nanotechnology*, 6(4), pp. 247-252.

Lua, A.C., Yang, T. and Guo, J. (2004) 'Effects of pyrolysis conditions on the properties of activated carbons prepared from pistachio-nut shells', *Journal of Analytical and Applied Pyrolysis*, 72(2), pp. 279-287.

Luo, Z., Lu, Y., Somers, L.A. and Johnson, A.C. (2009) 'High yield preparation of macroscopic graphene oxide membranes', *Journal of the American Chemical Society*, 131(3), pp. 898-899.

Maharjan, M., Bhattarai, A., Ulaganathan, M., Wai, N., Oo, M.O., Wang, J.-Y. and Lim, T.M. (2017) 'High surface area bio-waste based carbon as a superior electrode for vanadium redox flow battery', *Journal of Power Sources*, 362, pp. 50-56.

Maharjan, M., Wai, N., Veksha, A., Giannis, A., Lim, T.M. and Lisak, G. (2019) 'Sal wood sawdust derived highly mesoporous carbon as prospective electrode material for vanadium redox flow batteries', *Journal of Electroanalytical Chemistry*, 834, pp. 94-100.

Mahesh, S., Lekshmi, C.L., Renuka, K.D. and Joseph, K. (2016) 'Simple and Cost-Effective Synthesis of Fluorescent Graphene Quantum Dots from Honey: Application as Stable Security Ink and White-Light Emission', *Particle & Particle Systems Characterization*, 33(2), pp. 70-74.

Maiti, S., Kundu, S., Roy, C.N., Das, T.K. and Saha, A. (2017) 'Synthesis of Excitation Independent Highly Luminescent Graphene Quantum Dots through Perchloric Acid Oxidation', *Langmuir*, 33(51), pp. 14634-14642.

Mao, S., Lu, G. and Chen, J. (2015) 'Three-dimensional graphene-based composites for energy applications', *Nanoscale*, 7(16), pp. 6924-6943.

Marinovic, A., Kiat, L.S., Dunn, S., Titirici, M.M. and Briscoe, J. (2017) 'Carbon-Nanodot Solar Cells from Renewable Precursors', *ChemSusChem*, 10(5), pp. 1004-1013.

McKendry, P. (2002) 'Energy production from biomass (part 1): overview of biomass', *Bioresource technology*, 83(1), pp. 37-46.

Miao, X., Qu, D., Yang, D., Nie, B., Zhao, Y., Fan, H. and Sun, Z. (2018) 'Synthesis of carbon dots with multiple color emission by controlled graphitization and surface functionalization', *Advanced Materials*, 30(1), p. 1704740.

Mihalache, I., Radoi, A., Mihaila, M., Munteanu, C., Marin, A., Danila, M., Kusko, M. and Kusko, C. (2015) 'Charge and energy transfer interplay in hybrid sensitized solar cells mediated by graphene quantum dots', *Electrochimica Acta*, 153, pp. 306-315.

Minke, C. and Turek, T. (2018) 'Materials, system designs and modelling approaches in techno-economic assessment of all-vanadium redox flow batteries – A review', *Journal of Power Sources*, 376, pp. 66-81.

Mohanty, N., Moore, D., Xu, Z., Sreeprasad, T.S., Nagaraja, A., Rodriguez, A.A. and Berry, V. (2012) 'Nanotomy-based production of transferable and dispersible graphene nanostructures of controlled shape and size', *Nature communications*, 3, p. 844.

Mondal, S., Rana, U. and Malik, S. (2015) 'Graphene quantum dot-doped polyaniline nanofiber as high performance supercapacitor electrode materials', *Chemical Communications*, 51(62), pp. 12365-12368.

Montoya, J.I., Chejne-Janna, F. and Garcia-Pérez, M. (2015) 'Fast pyrolysis of biomass: A review of relevant aspects.: Part I: Parametric study', *Dyna*, 82(192), pp. 239-248.

Motghare, K.A., Rathod, A.P., Wasewar, K.L. and Labhsetwar, N.K. (2016) 'Comparative study of different waste biomass for energy application', *Waste management*, 47, pp. 40-45.

Mueller, M.L., Yan, X., Dragnea, B. and Li, L.-s. (2010a) 'Slow hot-carrier relaxation in colloidal graphene quantum dots', *Nano letters*, 11(1), pp. 56-60.

Mueller, M.L., Yan, X., McGuire, J.A. and Li, L.-s. (2010b) 'Triplet states and electronic relaxation in photoexcited graphene quantum dots', *Nano letters*, 10(7), pp. 2679-2682.

Nakayama, Y., Soeda, F. and Ishitani, A. (1990) 'XPS study of the carbon fiber matrix interface', *Carbon*, 28(1), pp. 21-26.

Nassar, M.M. and MacKay, G. (2007) 'Mechanism of thermal decomposition of lignin', *Wood and Fiber Science*, 16(3), pp. 441-453.

Nelson, M. and Poulter, J. (2004) 'Impact of tea drinking on iron status in the UK: a review', *Journal of Human Nutrition and Dietetics*, 17(1), pp. 43-54.

Nirala, N.R., Khandelwal, G., Kumar, B., Vinita, Prakash, R. and Kumar, V. (2017) 'One step electro-oxidative preparation of graphene quantum dots from wood charcoal as a peroxidase mimetic', *Talanta*, 173, pp. 36-43.

Novoselov, K.S., Geim, A.K., Morozov, S.V., Jiang, D., Zhang, Y., Dubonos, S.V., Grigorieva, I.V. and Firsov, A.A. (2004) 'Electric Field Effect in Atomically Thin Carbon Films', *Science*, 306(5696), pp. 666-669.

Oh, Y., Yoo, J., Kim, Y., Yoon, J., Yoon, H., Kim, J.-H. and Park, S. (2014) 'Oxygen functional groups and electrochemical capacitive behavior of incompletely reduced graphene oxides as a thin-film electrode of supercapacitor', *Electrochimica Acta*, 116, pp. 118–128.

Omary, M.A. and Patterson, H.H. (1999) 'Luminescence, Theory* A2 - Lindon, John C', in *Encyclopedia of Spectroscopy and Spectrometry (Second Edition)*. Oxford: Academic Press, pp. 1372-1391.

Otowa, T., Tanibata, R. and Itoh, M. (1993) 'Production and adsorption characteristics of MAXSORB: High-surface-area active carbon', *Gas Separation & Purification*, 7(4), pp. 241-245.

Pan, D., Guo, L., Zhang, J., Xi, C., Xue, Q., Huang, H., Li, J., Zhang, Z., Yu, W. and Chen, Z. (2012) 'Cutting sp 2 clusters in graphene sheets into colloidal graphene quantum dots with strong green fluorescence', *Journal of Materials Chemistry*, 22(8), pp. 3314-3318.

Pan, D., Zhang, J., Li, Z. and Wu, M. (2010) 'Hydrothermal route for cutting graphene sheets into blue-luminescent graphene quantum dots', *Advanced materials*, 22(6), pp. 734-738.

Parasuraman, A., Lim, T.M., Menictas, C. and Skyllas-Kazacos, M. (2013) 'Review of material research and development for vanadium redox flow battery applications', *Electrochimica Acta*, 101, pp. 27-40.

Park, J., Moon, J., Kim, C., Kang, J.H., Lim, E., Park, J., Lee, K.J., Yu, S.-H., Seo, J.-H. and Lee, J. (2016) 'Graphene quantum dots: structural integrity and oxygen functional groups for high sulfur/sulfide utilization in lithium sulfur batteries', *NPG Asia Materials*, 8, p. e272.

Park, M., Ryu, J., Kim, Y. and Cho, J. (2014) 'Corn protein-derived nitrogen-doped carbon materials with oxygen-rich functional groups: a highly efficient electrocatalyst for all-vanadium redox flow batteries', *Energy & Environmental Science*, 7(11), pp. 3727-3735.

Park, N.-M., Choi, C.-J., Seong, T.-Y. and Park, S.-J. (2001) 'Quantum confinement in amorphous silicon quantum dots embedded in silicon nitride', *Physical Review Letters*, 86(7), p. 1355.

Pels, J., Kapteijn, F., Moulijn, J., Zhu, Q. and Thomas, K. (1995a) 'Evolution of nitrogen functionalities in carbonaceous materials during pyrolysis', *Carbon*, 33(11), pp. 1641-1653.

Pels, J.R., Kapteijn, F., Moulijn, J.A., Zhu, Q. and Thomas, K.M. (1995b) 'Evolution of nitrogen functionalities in carbonaceous materials during pyrolysis', *Carbon*, 33(11), pp. 1641-1653.

Peng, C., Yan, X.-b., Wang, R.-t., Lang, J.-w., Ou, Y.-j. and Xue, Q.-j. (2013) 'Promising activated carbons derived from waste tea-leaves and their application in high performance supercapacitors electrodes', *Electrochimica Acta*, 87, pp. 401-408.

Peng, H. and Travas-Sejdic, J. (2009) 'Simple Aqueous Solution Route to Luminescent Carbogenic Dots from Carbohydrates', *Chemistry of Materials*, 21(23), pp. 5563-5565.

Peng, J., Gao, W., Gupta, B.K., Liu, Z., Romero-Aburto, R., Ge, L., Song, L., Alemany, L.B., Zhan, X. and Gao, G. (2012a) 'Graphene quantum dots derived from carbon fibers', *Nano letters*, 12(2), pp. 844-849.

Peng, J., Gao, W., Gupta, B.K., Liu, Z., Romero-Aburto, R., Ge, L., Song, L., Alemany, L.B., Zhan, X., Gao, G., Vithayathil, S.A., Kaipparettu, B.A., Marti, A.A., Hayashi, T., Zhu, J.-J. and Ajayan, P.M. (2012b) 'Graphene Quantum Dots Derived from Carbon Fibers', *Nano Letters*, 12(2), pp. 844-849.

Ponce de León, C., Frías-Ferrer, A., González-García, J., Szánto, D.A. and Walsh, F.C. (2006) 'Redox flow cells for energy conversion', *Journal of Power Sources*, 160(1), pp. 716-732.

Ponomarenko, L.A., Schedin, F., Katsnelson, M.I., Yang, R., Hill, E.W., Novoselov, K.S. and Geim, A.K. (2008) 'Chaotic Dirac Billiard in Graphene Quantum Dots', *Science*, 320(5874), pp. 356-358.

Prasad, K.S., Pallela, R., Kim, D.M. and Shim, Y.B. (2013) 'Microwave-Assisted One-Pot Synthesis of Metal-Free Nitrogen and Phosphorus Dual-Doped Nanocarbon for Electrocatalysis and Cell Imaging', *Particle & Particle Systems Characterization*, 30(6), pp. 557-564.

Qian, Z., Shan, X., Chai, L., Ma, J., Chen, J. and Feng, H. (2014) 'Si-doped carbon quantum dots: a facile and general preparation strategy, bioimaging application, and multifunctional sensor', *ACS applied materials & interfaces*, 6(9), pp. 6797-6805.

Qu, D., Zheng, M., Du, P., Zhou, Y., Zhang, L., Li, D., Tan, H., Zhao, Z., Xie, Z. and Sun, Z. (2013) 'Highly luminescent S, N co-doped graphene quantum dots with broad visible absorption bands for visible light photocatalysts', *Nanoscale*, 5(24), pp. 12272-12277.

Qu, D., Zheng, M., Zhang, L., Zhao, H., Xie, Z., Jing, X., Haddad, R.E., Fan, H. and Sun, Z. (2014a) 'Formation mechanism and optimization of highly luminescent N-doped graphene quantum dots', *Scientific reports*, 4(1), pp. 1-11.

Qu, D., Zheng, M., Zhang, L., Zhao, H., Xie, Z., Jing, X., Haddad, R.E., Fan, H. and Sun, Z. (2014b) 'Formation mechanism and optimization of highly luminescent N-doped graphene quantum dots', *Scientific reports*, 4, p. 5294.

Rajender, G. and Giri, P.K. (2016) 'Formation mechanism of graphene quantum dots and their edge state conversion probed by photoluminescence and Raman spectroscopy', *Journal of Materials Chemistry C*, 4(46), pp. 10852-10865.

Ratner, B.D., Hoffman, A.S., Schoen, F.J. and Lemons, J.E. (2004) *Biomaterials science: an introduction to materials in medicine*. Academic press.

Raymundo-Pinero, E., Azaïs, P., Cacciaguerra, T., Cazorla-Amorós, D., Linares-Solano, A. and Béguin, F. (2005) 'KOH and NaOH activation mechanisms of multiwalled carbon nanotubes with different structural organisation', *Carbon*, 43(4), pp. 786-795.

Raymundo-Piñero, E., Azaïs, P., Cacciaguerra, T., Cazorla-Amorós, D., Linares-Solano, A. and Béguin, F. (2005) 'KOH and NaOH activation mechanisms of multiwalled carbon nanotubes with different structural organisation', *Carbon*, 43(4), pp. 786-795.

Ren, J., Zhang, Y., Bai, W., Chen, X., Zhang, Z., Fang, X., Weng, W., Wang, Y. and Peng, H. (2014) 'Elastic and wearable wire-shaped lithium-ion battery with high electrochemical performance', *Angewandte Chemie*, 126(30), pp. 7998-8003.

Ringer, M., Putsche, V. and Scahill, J. (2006) 'Large-scale pyrolysis oil', *Assessment*.

Ritter, K.A. and Lyding, J.W. (2009) 'The influence of edge structure on the electronic properties of graphene quantum dots and nanoribbons', *Nature materials*, 8(3), pp. 235-242.

Ronda, C., Bachmann, P.K., Hummel, H., Juestel, T. and Meriikhi, J. (2010) 'Luminescent Materials, Biological Applications', *Encyclopedia of Industrial Biotechnology*.

Ronda, C.R. (2007) *Luminescence: from theory to applications*. John Wiley & Sons.

Ronsse, F., Van Hecke, S., Dickinson, D. and Prins, W. (2013) 'Production and characterization of slow pyrolysis biochar: influence of feedstock type and pyrolysis conditions', *Gcb Bioenergy*, 5(2), pp. 104-115.

Roy, P., Periasamy, A.P., Chuang, C., Liou, Y.-R., Chen, Y.-F., Joly, J., Liang, C.-T. and Chang, H.-T. (2014) 'Plant leaf-derived graphene quantum dots and applications for white LEDs', *New Journal of Chemistry*, 38(10), pp. 4946-4951.

Roznyatovskaya, N., Noack, J., Fühl, M., Pinkwart, K. and Tübke, J. (2016) 'Towards an all-vanadium redox-flow battery electrolyte: electrooxidation of V(III) in V(IV)/V(III) redox couple', *Electrochimica Acta*, 211, pp. 926-932.

Roznyatovskaya, N., Noack, J., Pinkwart, K. and Tübke, J. (2020) 'Aspects of electron transfer processes in vanadium redox-flow batteries', *Current Opinion in Electrochemistry*, 19, pp. 42-48.

Rui, X., Parasuraman, A., Liu, W., Sim, D.H., Hng, H.H., Yan, Q., Lim, T.M. and Skyllas-Kazacos, M. (2013) 'Functionalized single-walled carbon nanotubes with enhanced electrocatalytic activity for Br-/Br3- redox reactions in vanadium bromide redox flow batteries', *Carbon*, 64, pp. 464-471.

Rui, X., Zhu, J., Sim, D., Xu, C., Zeng, Y., Hng, H.H., Lim, T.M. and Yan, Q. (2011) 'Reduced graphene oxide supported highly porous V 2 O 5 spheres as a high-power cathode material for lithium ion batteries', *Nanoscale*, 3(11), pp. 4752-4758.

Ruiyi, L., Yuanyuan, J., Xiaoyan, Z., Zaijun, L., Zhiguo, G., Guangli, W. and Junkang, L. (2015) 'Significantly enhanced electrochemical performance of lithium titanate anode for lithium ion battery by the hybrid of nitrogen and sulfur co-doped graphene quantum dots', *Electrochimica Acta*, 178, pp. 303-311.

Salvador, F., Sánchez-Montero, M.J. and Izquierdo, C. (2007) 'C/H2O reaction under supercritical conditions and their repercussions in the preparation of activated carbon', *The Journal of Physical Chemistry C*, 111(37), pp. 14011-14020.

Schmidt, L.D. and Dauenhauer, P.J. (2007) 'Chemical engineering: hybrid routes to biofuels', *Nature*, 447(7147), pp. 914-915.

Schwan, J., Ulrich, S., Batori, V., Ehrhardt, H. and Silva, S. (1996) 'Raman spectroscopy on amorphous carbon films', *Journal of Applied Physics*, 80(1), pp. 440-447.

Sekiya, R., Uemura, Y., Naito, H., Naka, K. and Haino, T. (2016) 'Chemical Functionalisation and Photoluminescence of Graphene Quantum Dots', *Chemistry-A European Journal*, 22(24), pp. 8198-8206.

Sevilla, M. and Fuertes, A.B. (2009a) 'Chemical and structural properties of carbonaceous products obtained by hydrothermal carbonization of saccharides', *Chemistry–A European Journal*, 15(16), pp. 4195-4203.

Sevilla, M. and Fuertes, A.B. (2009b) 'The production of carbon materials by hydrothermal carbonization of cellulose', *Carbon*, 47(9), pp. 2281-2289.

Shafizadeh, F. (1982) 'Introduction to pyrolysis of biomass', *Journal of Analytical and Applied Pyrolysis*, 3(4), pp. 283-305.

Shamsipur, M., Barati, A. and Karami, S. (2017) 'Long-wavelength, multicolor, and white-light emitting carbon-based dots: Achievements made, challenges remaining, and applications', *Carbon*, 124, pp. 429-472.

Shen, J., Zhu, Y., Chen, C., Yang, X. and Li, C. (2011) 'Facile preparation and upconversion luminescence of graphene quantum dots', *Chemical communications*, 47(9), pp. 2580-2582.

Shen, J., Zhu, Y., Yang, X. and Li, C. (2012a) 'Graphene quantum dots: emergent nanolights for bioimaging, sensors, catalysis and photovoltaic devices', *Chemical Communications*, 48(31), pp. 3686-3699.

Shen, J., Zhu, Y., Yang, X., Zong, J., Zhang, J. and Li, C. (2012b) 'One-pot hydrothermal synthesis of graphene quantum dots surface-passivated by polyethylene glycol and their photoelectric conversion under near-infrared light', *New Journal of Chemistry*, 36(1), pp. 97-101.

Shen, Y., Yu, S., Ge, S., Chen, X., Ge, X. and Chen, M. (2017) 'Hydrothermal carbonization of medical wastes and lignocellulosic biomass for solid fuel production from lab-scale to pilot-scale', *Energy*, 118, pp. 312-323.

Sheng, C. (2007) 'Char structure characterised by Raman spectroscopy and its correlations with combustion reactivity', *Fuel*, 86(15), pp. 2316-2324.

Si, Y. and Samulski, E.T. (2008) 'Synthesis of water soluble graphene', *Nano letters*, 8(6), pp. 1679-1682.

Sing, K.S. (1985) 'Reporting physisorption data for gas/solid systems with special reference to the determination of surface area and porosity (Recommendations 1984)', *Pure and applied chemistry*, 57(4), pp. 603-619.

Singh, G., Lakhi, K.S., Sil, S., Bhosale, S.V., Kim, I., Albahily, K. and Vinu, A. (2019a) 'Biomass derived porous carbon for CO2 capture', *Carbon*.

Singh, V., Kim, S., Kang, J. and Byon, H.R. (2019b) 'Aqueous organic redox flow batteries', *Nano Research*, pp. 1-14.

Sk, M.A., Ananthanarayanan, A., Huang, L., Lim, K.H. and Chen, P. (2014) 'Revealing the tunable photoluminescence properties of graphene quantum dots', *Journal of Materials Chemistry C*, 2(34), pp. 6954-6960.

Skyllas-Kazacos, M., Kasherman, D., Hong, D.R. and Kazacos, M. (1991) 'Characteristics and performance of 1 kW UNSW vanadium redox battery', *Journal of Power Sources*, 35(4), pp. 399-404.

Skyllas-Kazacos, M., Kazacos, G., Poon, G. and Verseema, H. (2010) 'Recent advances with UNSW vanadium-based redox flow batteries', *International Journal of Energy Research*, 34(2), pp. 182-189.

Song, S.H., Jang, M.H., Chung, J., Jin, S.H., Kim, B.H., Hur, S.H., Yoo, S., Cho, Y.H. and Jeon, S. (2014) 'Highly Efficient Light-Emitting Diode of Graphene Quantum Dots Fabricated from Graphite Intercalation Compounds', *Advanced Optical Materials*, 2(11), pp. 1016-1023.

Su, F., Tian, Z., Poh, C.K., Wang, Z., Lim, S.H., Liu, Z. and Lin, J. (2009) 'Pt nanoparticles supported on nitrogen-doped porous carbon nanospheres as an electrocatalyst for fuel cells', *Chemistry of Materials*, 22(3), pp. 832-839.

Su, Y.L., Yu, T.W., Chiang, W.H., Chiu, H.C., Chang, C.H., Chiang, C.S. and Hu, S.H. (2017) 'Hierarchically Targeted and Penetrated Delivery of Drugs to Tumors by Size-Changeable Graphene Quantum Dot Nanoaircrafts for Photolytic Therapy', *Advanced Functional Materials*.

Suh, W.H., Suslick, K.S., Stucky, G.D. and Suh, Y.-H. (2009) 'Nanotechnology, nanotoxicology, and neuroscience', *Progress in neurobiology*, 87(3), pp. 133-170.

Sun, B. and Skyllas-Kazacos, M. (1992) 'Chemical modification of graphite electrode materials for vanadium redox flow battery application—part II. Acid treatments', *Electrochimica Acta*, 37(13), pp. 2459-2465.

Sun, H., Gao, N., Dong, K., Ren, J. and Qu, X. (2014a) 'Graphene quantum dots-band-aids used for wound disinfection', *ACS Nano*, 8(6), pp. 6202-6210.

Sun, H., Wu, L., Gao, N., Ren, J. and Qu, X. (2013) 'Improvement of photoluminescence of graphene quantum dots with a biocompatible photochemical reduction pathway and its bioimaging application', *ACS applied materials & interfaces*, 5(3), pp. 1174-1179.

Sun, H., You, X., Deng, J., Chen, X., Yang, Z., Ren, J. and Peng, H. (2014b) 'Novel graphene/carbon nanotube composite fibers for efficient wire-shaped miniature energy devices', *Advanced Materials*, 26(18), pp. 2868-2873.

Sun, J., Yang, S., Wang, Z., Shen, H., Xu, T., Sun, L., Li, H., Chen, W., Jiang, X. and Ding, G. (2015) 'Ultra-High Quantum Yield of Graphene Quantum Dots: Aromatic-Nitrogen Doping and Photoluminescence Mechanism', *Particle & Particle Systems Characterization*, 32(4), pp. 434-440.

Sun, X. and Lei, Y. (2017) 'Fluorescent carbon dots and their sensing applications', *TrAC Trends in Analytical Chemistry*, 89, pp. 163-180.

Sun, Y., Wu, Q. and Shi, G. (2011) 'Graphene based new energy materials', *Energy and Environmental Science*, 4(4), pp. 1113-1132.

Suryawanshi, A., Biswal, M., Mhamane, D., Gokhale, R., Patil, S., Guin, D. and Ogale, S. (2014) 'Large scale synthesis of graphene quantum dots (GQDs) from waste biomass and their use as an efficient and selective photoluminescence on–off–on probe for Ag+ ions', *Nanoscale*, 6(20), pp. 11664-11670.

Tabish, T.A., Pranjol, M.Z.I., Hayat, H., Rahat, A.A., Abdullah, T.M., Whatmore, J.L. and Zhang, S. (2017) 'In vitro toxic effects of reduced graphene oxide nanosheets on lung cancer cells', *Nanotechnology*, 28(50), p. 504001.

Tang, D., Liu, J., Yan, X. and Kang, L. (2016) 'Graphene oxide derived graphene quantum dots with different photoluminescence properties and peroxidase-like catalytic activity', *RSC Advances*, 6(56), pp. 50609-50617.

Tang, L., Ji, R., Cao, X., Lin, J., Jiang, H., Li, X., Teng, K.S., Luk, C.M., Zeng, S. and Hao, J. (2012) 'Deep ultraviolet photoluminescence of water-soluble self-passivated graphene quantum dots', *ACS nano*, 6(6), pp. 5102-5110.

Tauc, J., Grigorovici, R. and Vancu, A. (1966) 'Optical properties and electronic structure of amorphous germanium', *physica status solidi (b)*, 15(2), pp. 627-637.

Tavakoli, M.M., Aashuri, H., Simchi, A., Kalytchuk, S. and Fan, Z. (2015) 'Quasi core/shell lead sulfide/graphene quantum dots for bulk heterojunction solar cells', *The Journal of Physical Chemistry C*, 119(33), pp. 18886-18895.

Tekin, K., Karagöz, S. and Bektaş, S. (2014) 'A review of hydrothermal biomass processing', *Renewable and sustainable Energy reviews*, 40, pp. 673-687.

Tetsuka, H., Asahi, R., Nagoya, A., Okamoto, K., Tajima, I., Ohta, R. and Okamoto, A. (2012) 'Optically tunable amino-functionalized graphene quantum dots', *Advanced Materials*, 24(39), pp. 5333-5338.

Themelis, N.J. and Arsova, L. (2015) 'Calculating Tons To Composting In The US', *Bio Cycle*, 56, p. 27.

Tilman, D., Hill, J. and Lehman, C. (2006) 'Carbon-negative biofuels from low-input high-diversity grassland biomass', *Science*, 314(5805), pp. 1598-1600.

Titirici, M.-M. and Antonietti, M. (2010) 'Chemistry and materials options of sustainable carbon materials made by hydrothermal carbonization', *Chemical Society Reviews*, 39(1), pp. 103-116.

Titirici, M.M., Thomas, A. and Antonietti, M. (2007) 'Replication and coating of silica templates by hydrothermal carbonization', *Advanced functional materials*, 17(6), pp. 1010-1018.

Toufiq Reza, M., Freitas, A., Yang, X., Hiibel, S., Lin, H. and Coronella, C.J. (2016) 'Hydrothermal carbonization (HTC) of cow manure: Carbon and nitrogen distributions in HTC products', *Environmental Progress & Sustainable Energy*, 35(4), pp. 1002-1011.

Tuinstra, F. and Koenig, J.L. (1970) 'Raman spectrum of graphite', *The Journal of Chemical Physics*, 53(3), pp. 1126-1130.

Ulaganathan, M., Aravindan, V., Yan, Q., Madhavi, S., Skyllas-Kazacos, M. and Lim, T.M. (2016) 'Recent advancements in all-vanadium redox flow batteries', *Advanced Materials Interfaces*, 3(1), p. 1500309.

Ulaganathan, M., Jain, A., Aravindan, V., Jayaraman, S., Ling, W.C., Lim, T.M., Srinivasan, M.P., Yan, Q. and Madhavi, S. (2015) 'Bio-mass derived mesoporous carbon as superior electrode in all vanadium redox flow battery with multicouple reactions', *Journal of Power Sources*, 274, pp. 846-850.

Van Tam, T., Kang, S.G., Kadumudi, F.B., Oh, E., Lee, S.G. and Choi, W.M. (2017) 'Synthesis of B-doped graphene quantum dots as metal-free electrocatalyst for oxygen reduction reaction', *Journal of Materials Chemistry A*.

Vázquez-Santos, M.B., Geissler, E., László, K., Rouzaud, J.-N., Martínez-Alonso, A. and Tascón, J.M.D. (2012) 'Comparative XRD, Raman, and TEM Study on Graphitization of PBO-Derived Carbon Fibers', *The Journal of Physical Chemistry C*, 116(1), pp. 257-268.

Walsh, F.C., Arenas, L.F., Ponce de León, C., Reade, G.W., Whyte, I. and Mellor, B.G. (2016) 'The continued development of reticulated vitreous carbon as a versatile electrode material: Structure, properties and applications', *Electrochimica Acta*, 215, pp. 566-591.

Wang, D.-W., Li, F., Zhao, J., Ren, W., Chen, Z.-G., Tan, J., Wu, Z.-S., Gentle, I., Lu, G.Q. and Cheng, H.-M. (2009) 'Fabrication of graphene/polyaniline composite paper via in situ anodic electropolymerization for high-performance flexible electrode', *ACS nano*, 3(7), pp. 1745-1752.

Wang, D., Kou, R., Choi, D., Yang, Z., Nie, Z., Li, J., Saraf, L.V., Hu, D., Zhang, J. and Graff, G.L. (2010) 'Ternary self-assembly of ordered metal oxide− graphene nanocomposites for electrochemical energy storage', *ACS nano*, 4(3), pp. 1587-1595.

Wang, D., Wang, L., Dong, X., Shi, Z. and Jin, J. (2012a) 'Chemically tailoring graphene oxides into fluorescent nanosheets for Fe3+ ion detection', *Carbon*, 50(6), pp. 2147-2154.

Wang, G., Guo, Q., Chen, D., Liu, Z., Zheng, X., Xu, A., Yang, S. and Ding, G. (2018a) 'Facile and highly effective synthesis of controllable lattice sulfur-doped graphene quantum dots via hydrothermal treatment of durian', *ACS applied materials & interfaces*.

Wang, J. and Kaskel, S. (2012) 'KOH activation of carbon-based materials for energy storage', *Journal of Materials Chemistry*, 22(45), pp. 23710-23725.

Wang, J., Zhang, X., Li, Z., Ma, Y. and Ma, L. (2020) 'Recent progress of biomass-derived carbon materials for supercapacitors', *Journal of Power Sources*, 451, p. 227794.

Wang, L., Chen, X., Lu, Y., Liu, C. and Yang, W. (2015a) 'Carbon quantum dots displaying dual-wavelength photoluminescence and electrochemiluminescence prepared by high-energy ball milling', *Carbon*, 94, pp. 472-478.

Wang, L., Li, W., Wu, B., Li, Z., Wang, S., Liu, Y., Pan, D. and Wu, M. (2016a) 'Facile synthesis of fluorescent graphene quantum dots from coffee grounds for bioimaging and sensing', *Chemical Engineering Journal*, 300, pp. 75-82.

Wang, L., Wang, Y., Xu, T., Liao, H., Yao, C., Liu, Y., Li, Z., Chen, Z., Pan, D. and Sun, L. (2014a) 'Gram-scale synthesis of single-crystalline graphene quantum dots with superior optical properties', *Nature communications*, 5(1), pp. 1-9.

Wang, L., Wang, Y., Xu, T., Liao, H., Yao, C., Liu, Y., Li, Z., Chen, Z., Pan, D. and Sun, L. (2014b) 'Gram-scale synthesis of single-crystalline graphene quantum dots with superior optical properties', *Nature communications*, 5.

Wang, L., Wu, B., Li, W., Wang, S., Li, Z., Li, M., Pan, D. and Wu, M. (2018b) 'Amphiphilic graphene quantum dots as self-targeted fluorescence probes for cell nucleus imaging', *Advanced Biosystems*, 2(8), p. 1700191.

Wang, M., Fang, Z., Zhang, K., Fang, J., Qin, F., Zhang, Z., Li, J., Liu, Y. and Lai, Y. (2016b) 'Synergistically enhanced activity of graphene quantum dots/graphene hydrogel composites: a novel all-carbon hybrid electrocatalyst for metal/air batteries', *Nanoscale*, 8(22), pp. 11398-11402.

Wang, R., Xia, G., Zhong, W., Chen, L., Chen, L., Wang, Y., Min, Y. and Li, K. (2019) 'Direct transformation of lignin into fluorescence-switchable graphene quantum dots and their application in ultrasensitive profiling of a physiological oxidant', *Green Chemistry*, 21(12), pp. 3343-3352.

Wang, S., Chen, Z.-G., Cole, I. and Li, Q. (2015b) 'Structural evolution of graphene quantum dots during thermal decomposition of citric acid and the corresponding photoluminescence', *Carbon*, 82, pp. 304-313.

Wang, S., Zhao, X., Cochell, T. and Manthiram, A. (2012b) 'Nitrogen-Doped Carbon Nanotube/Graphite Felts as Advanced Electrode Materials for Vanadium Redox Flow Batteries', *The Journal of Physical Chemistry Letters*, 3(16), pp. 2164-2167.

Wang, X., Sun, G., Li, N. and Chen, P. (2016c) 'Quantum dots derived from two-dimensional materials and their applications for catalysis and energy', *Chemical Society Reviews*, 45(8), pp. 2239-2262.

Wang, X., Sun, G., Routh, P., Kim, D.-H., Huang, W. and Chen, P. (2014c) 'Heteroatom-doped graphene materials: syntheses, properties and applications', *Chemical Society Reviews*, 43(20), pp. 7067-7098.

Wang, X., Sun, X., Lao, J., He, H., Cheng, T., Wang, M., Wang, S. and Huang, F. (2014d) 'Multifunctional graphene quantum dots for simultaneous targeted cellular imaging and drug delivery', *Colloids and Surfaces B: Biointerfaces*, 122, pp. 638-644.

Wang, Z., Long, P., Feng, Y., Qin, C. and Feng, W. (2017) 'Surface passivation of carbon dots with ethylene glycol and their high-sensitivity to Fe 3+', *RSC advances*, 7(5), pp. 2810-2816.

Wang, Z., Xia, J., Zhou, C., Via, B., Xia, Y., Zhang, F., Li, Y., Xia, L. and Tang, J. (2013) 'Synthesis of strongly green-photoluminescent graphene quantum dots for drug carrier', *Colloids and Surfaces B: Biointerfaces*, 112, pp. 192-196.

Wang, Z., Yu, J., Zhang, X., Li, N., Liu, B., Li, Y., Wang, Y., Wang, W., Li, Y. and Zhang, L. (2016d) 'Large-scale and controllable synthesis of graphene quantum dots from rice husk biomass: a comprehensive utilization strategy', *ACS applied materials & interfaces*, 8(2), pp. 1434-1439.

Wei, L., Sevilla, M., Fuertes, A.B., Mokaya, R. and Yushin, G. (2011) 'Hydrothermal Carbonization of Abundant Renewable Natural Organic Chemicals for High-Performance Supercapacitor Electrodes', *Advanced Energy Materials*, 1(3), pp. 356-361.

Williams, K.J., Nelson, C.A., Yan, X., Li, L.-S. and Zhu, X. (2013) 'Hot electron injection from graphene quantum dots to TiO2', *ACS nano*, 7(2), pp. 1388-1394.

Williams, P.T. and Besler, S. (1996) 'The influence of temperature and heating rate on the slow pyrolysis of biomass', *Renewable energy*, 7(3), pp. 233-250.

Williams, P.T. and Onwudili, J. (2006) 'Subcritical and supercritical water gasification of cellulose, starch, glucose, and biomass waste', *Energy & Fuels*, 20(3), pp. 1259-1265.

Wu, F., Gao, J., Zhai, X., Xie, M., Sun, Y., Kang, H., Tian, Q. and Qiu, H. (2019) 'Hierarchical porous carbon microrods derived from albizia flowers for high performance supercapacitors', *Carbon*, 147, pp. 242-251.

Wu, F., Su, H., Wang, K., Wong, W.-K. and Zhu, X. (2017) 'Facile synthesis of N-rich carbon quantum dots from porphyrins as efficient probes for bioimaging and biosensing in living cells', *International journal of nanomedicine*, 12, p. 7375.

Wu, X., Ma, L., Sun, S., Jiang, K., Zhang, L., Wang, Y., Zeng, H. and Lin, H. (2018) 'A versatile platform for the highly efficient preparation of graphene quantum dots: photoluminescence emission and hydrophilicity–hydrophobicity regulation and organelle imaging', *Nanoscale*, 10(3), pp. 1532-1539.

Wunsch, B., Stauber, T. and Guinea, F. (2008) 'Electron-electron interactions and charging effects in graphene quantum dots', *Physical Review B*, 77(3), p. 035316.

Xiao, B., Boudou, J.-P. and Thomas, K. (2005) 'Reactions of nitrogen and oxygen surface groups in nanoporous carbons under inert and reducing atmospheres', *Langmuir*, 21(8), pp. 3400-3409.

Xie, X. and Goodell, B. 1158 (2014) 'Thermal degradation and conversion of plant biomass into high value carbon products' *ACS Symposium Series* [Article]. pp. 147-158. Available at: https://www.scopus.com/inward/record.uri?eid=2-s2.0-84905400479&doi=10.1021%2fbk-2014-1158.ch008&partnerID=40&md5=b8149e15a0780b531d9eaea411c774af.

Xie, Z., Sun, X., Jiao, J. and Xin, X. (2017) 'Ionic liquid-functionalized carbon quantum dots as fluorescent probes for sensitive and selective detection of iron ion and ascorbic acid', *Colloids and Surfaces A: Physicochemical and Engineering Aspects*, 529, pp. 38-44.

Xu, C., Xu, B., Gu, Y., Xiong, Z., Sun, J. and Zhao, X.S. (2013) 'Graphene-based electrodes for electrochemical energy storage', *Energy and Environmental Science*, 6(6), pp. 1388-1414.

Yan, X., Cui, X., Li, B. and Li, L.-s. (2010a) 'Large, solution-processable graphene quantum dots as light absorbers for photovoltaics', *Nano letters*, 10(5), pp. 1869-1873.

Yan, X., Cui, X. and Li, L.-s. (2010b) 'Synthesis of large, stable colloidal graphene quantum dots with tunable size', *Journal of the American Chemical Society*, 132(17), pp. 5944-5945.

Yan, Y., Chen, J., Li, N., Tian, J., Li, K., Jiang, J., Liu, J., Tian, Q. and Chen, P. (2018) 'Systematic Bandgap Engineering of Graphene Quantum Dots and Applications for Photocatalytic Water Splitting and CO2 Reduction', *ACS nano*, 12(4), pp. 3523-3532.

Yang, K., Peng, J., Srinivasakannan, C., Zhang, L., Xia, H. and Duan, X. (2010) 'Preparation of high surface area activated carbon from coconut shells using microwave heating', *Bioresource technology*, 101(15), pp. 6163-6169.

Yang, P., Zhou, L., Zhang, S., Wan, N., Pan, W. and Shen, W. (2014a) 'Facile synthesis and photoluminescence mechanism of graphene quantum dots', *Journal of Applied Physics*, 116(24), p. 244306.

Yang, S., Li, W., Ye, C., Wang, G., Tian, H., Zhu, C., He, P., Ding, G., Xie, X. and Liu, Y. (2017a) 'C3N—A 2D Crystalline, Hole-Free, Tunable-Narrow-Bandgap Semiconductor with Ferromagnetic Properties', *Advanced Materials*, 29(16).

Yang, S., Sun, J., Li, X., Zhou, W., Wang, Z., He, P., Ding, G., Xie, X., Kang, Z. and Jiang, M. (2014b) 'Large-scale fabrication of heavy doped carbon quantum dots with tunable-photoluminescence and sensitive fluorescence detection', *Journal of Materials Chemistry A*, 2(23), pp. 8660-8667.

Yang, S., Yang, Y., He, P., Wang, G., Ding, G. and Xie, X. (2017b) 'Insights into the Oxidation Mechanism of sp2–sp3 Hybrid Carbon Materials: Preparation of a Water-Soluble 2D Porous Conductive Network and Detectable Molecule Separation', *Langmuir*, 33(4), pp. 913-919.

Yang, Y., Cui, J., Zheng, M., Hu, C., Tan, S., Xiao, Y., Yang, Q. and Liu, Y. (2012) 'One-step synthesis of amino-functionalized fluorescent carbon nanoparticles by hydrothermal carbonization of chitosan', *Chemical Communications*, 48(3), pp. 380-382.

Yang, Z., Sun, H., Chen, T., Qiu, L., Luo, Y. and Peng, H. (2013) 'Photovoltaic wire derived from a graphene composite fiber achieving an 8.45% energy conversion efficiency', *Angewandte Chemie*, 125(29), pp. 7693-7696.

Yang, Z., Zhang, J., Kintner-Meyer, M.C.W., Lu, X., Choi, D., Lemmon, J.P. and Liu, J. (2011) 'Electrochemical energy storage for green grid', *Chemical Reviews*, 111(5), pp. 3577-3613.

Yao, C., Zhang, H., Liu, T., Li, X. and Liu, Z. (2012) 'Carbon paper coated with supported tungsten trioxide as novel electrode for all-vanadium flow battery', *Journal of Power Sources*, 218, pp. 455-461.

Yao, X., Niu, X., Ma, K., Huang, P., Grothe, J., Kaskel, S. and Zhu, Y. (2017) 'Graphene Quantum Dots-Capped Magnetic Mesoporous Silica Nanoparticles as a Multifunctional Platform for Controlled Drug Delivery, Magnetic Hyperthermia, and Photothermal Therapy', *Small*, 13(2).

Yao, X. and Zhao, Y. (2017) 'Three-Dimensional Porous Graphene Networks and Hybrids for Lithium-Ion Batteries and Supercapacitors', *Chem*, 2(2), pp. 171-200.

Yashin, A.Y., Nemzer, B.V., Combet, E. and Yashin, Y.I. (2015) 'Determination of the chemical composition of tea by chromatographic methods: a review', *Journal of Food Research*, 4(3), pp. 56-87.

Ye, M., Dong, Z., Hu, C., Cheng, H., Shao, H., Chen, N. and Qu, L. (2014) 'Uniquely Arranged Graphene-on-Graphene Structure as a Binder-Free Anode for High-Performance Lithium-Ion Batteries', *Small*, 10(24), pp. 5035-5041.

Ye, R., Peng, Z., Metzger, A., Lin, J., Mann, J.A., Huang, K., Xiang, C., Fan, X., Samuel, E.L.G. and Alemany, L.B. (2015) 'Bandgap engineering of coal-derived graphene quantum dots', *ACS applied materials & interfaces*, 7(12), pp. 7041-7048.

Ye, R., Xiang, C., Lin, J., Peng, Z., Huang, K., Yan, Z., Cook, N.P., Samuel, E.L.G., Hwang, C.-C. and Ruan, G. (2013) 'Coal as an abundant source of graphene quantum dots', *Nature communications*, 4, p. 2943.

Yoffe, A.D. (1993) 'Low-dimensional systems: quantum size effects and electronic properties of semiconductor microcrystallites (zero-dimensional systems) and some quasi-two-dimensional systems', *Advances in Physics*, 42(2), pp. 173-262.

Yu, D., Goh, K., Wang, H., Wei, L., Jiang, W., Zhang, Q., Dai, L. and Chen, Y. (2014) 'Scalable synthesis of hierarchically structured carbon nanotube-graphene fibres for capacitive energy storage', *Nature nanotechnology*, 9(7), pp. 555-562.

Yu, J., Paterson, N., Blamey, J. and Millan, M. (2017) 'Cellulose, xylan and lignin interactions during pyrolysis of lignocellulosic biomass', *Fuel*, 191, pp. 140-149.

Yu, S.-H., Cui, X., Li, L.L., Li, K., Yu, B., Antonietti, M. and Cölfen, H. (2004) 'From starch to metal/carbon hybrid nanostructures: hydrothermal metal-catalyzed carbonization', *Advanced Materials*, 16(18), pp. 1636-1640.

Yuan, F., Yuan, T., Sui, L., Wang, Z., Xi, Z., Li, Y., Li, X., Fan, L., Chen, A. and Jin, M. (2018) 'Engineering triangular carbon quantum dots with unprecedented narrow bandwidth emission for multicolored LEDs', *Nature communications*, 9(1), p. 2249.

Zhang, F., Liu, F., Wang, C., Xin, X., Liu, J., Guo, S. and Zhang, J. (2016) 'Effect of Lateral Size of Graphene Quantum Dots on Their Properties and Application', *ACS Applied Materials & Interfaces*, 8(3), pp. 2104-2110.

Zhang, H. (2015) 'Ultrathin two-dimensional nanomaterials', *ACS nano*, 9(10), pp. 9451-9469.

Zhang, L., DeArmond, D., Alvarez, N.T., Malik, R., Oslin, N., McConnell, C., Adusei, P.K., Hsieh, Y.Y. and Shanov, V. (2017) 'Flexible Micro-Supercapacitor Based on Graphene with 3D Structure', *Small*.

Zhang, L., Zhang, Z.-Y., Liang, R.-P., Li, Y.-H. and Qiu, J.-D. (2014) 'Boron-doped graphene quantum dots for selective glucose sensing based on the “abnormal” aggregation-induced photoluminescence enhancement', *Analytical chemistry*, 86(9), pp. 4423-4430.

Zhang, M., Bai, L., Shang, W., Xie, W., Ma, H., Fu, Y., Fang, D., Sun, H., Fan, L. and Han, M. (2012a) 'Facile synthesis of water-soluble, highly fluorescent graphene quantum dots as a robust biological label for stem cells', *Journal of materials chemistry*, 22(15), pp. 7461-7467.

Zhang, T., Walawender, W.P., Fan, L., Fan, M., Daugaard, D. and Brown, R. (2004) 'Preparation of activated carbon from forest and agricultural residues through CO2 activation', *Chemical Engineering Journal*, 105(1-2), pp. 53-59.

Zhang, Z., Zhang, J., Chen, N. and Qu, L. (2012b) 'Graphene quantum dots: an emerging material for energy-related applications and beyond', *Energy & Environmental Science*, 5(10), pp. 8869-8890.

Zhao, J., Tang, L., Xiang, J., Ji, R., Hu, Y., Yuan, J., Zhao, J., Tai, Y. and Cai, Y. (2015a) 'Fabrication and properties of a high-performance chlorine doped graphene quantum dot based photovoltaic detector', *RSC Advances*, 5(37), pp. 29222-29229.

Zhao, S., Lan, M., Zhu, X., Xue, H., Ng, T.-W., Meng, X., Lee, C.-S., Wang, P. and Zhang, W. (2015b) 'Green synthesis of bifunctional fluorescent carbon dots from garlic for cellular imaging and free radical scavenging', *ACS applied materials & interfaces*, 7(31), pp. 17054-17060.

Zheng, A.-X., Cong, Z.-X., Wang, J.-R., Li, J., Yang, H.-H. and Chen, G.-N. (2013a) 'Highly-efficient peroxidase-like catalytic activity of graphene dots for biosensing', *Biosensors and Bioelectronics*, 49, pp. 519-524.

Zheng, X.T., Ananthanarayanan, A., Luo, K.Q. and Chen, P. (2015) 'Glowing graphene quantum dots and carbon dots: properties, syntheses, and biological applications', *Small*, 11(14), pp. 1620-1636.

Zheng, X.T., Than, A., Ananthanaraya, A., Kim, D.-H. and Chen, P. (2013b) 'Graphene quantum dots as universal fluorophores and their use in revealing regulated trafficking of insulin receptors in adipocytes', *Acs Nano*, 7(7), pp. 6278-6286.

Zhou, X., Zhang, Y., Wang, C., Wu, X., Yang, Y., Zheng, B., Wu, H., Guo, S. and Zhang, J. (2012) 'Photo-Fenton reaction of graphene oxide: a new strategy to prepare graphene quantum dots for DNA cleavage', *ACS nano*, 6(8), pp. 6592-6599.

Zhu, C., Chao, D., Sun, J., Bacho, I.M., Fan, Z., Ng, C.F., Xia, X., Huang, H., Zhang, H., Shen, Z.X., Ding, G. and Fan, H.J. (2015a) 'Enhanced Lithium Storage Performance of CuO Nanowires by Coating of Graphene Quantum Dots', *Advanced Materials Interfaces*, 2(2), p. 1400499.

Zhu, C., Yang, S., Wang, G., Mo, R., He, P., Sun, J., Di, Z., Kang, Z., Yuan, N. and Ding, J. (2015b) 'A new mild, clean and highly efficient method for the preparation of graphene quantum dots without by-products', *Journal of Materials Chemistry B*, 3(34), pp. 6871-6876.

Zhu, S., Zhang, J., Qiao, C., Tang, S., Li, Y., Yuan, W., Li, B., Tian, L., Liu, F. and Hu, R. (2011a) 'Strongly green-photoluminescent graphene quantum dots for bioimaging applications', *Chemical communications*, 47(24), pp. 6858-6860.

Zhu, S., Zhang, J., Tang, S., Qiao, C., Wang, L., Wang, H., Liu, X., Li, B., Li, Y. and Yu, W. (2012) 'Surface chemistry routes to modulate the photoluminescence of graphene quantum dots: From fluorescence mechanism to up-conversion bioimaging applications', *Advanced Functional Materials*, 22(22), pp. 4732-4740.

Zhu, Y., Murali, S., Stoller, M.D., Ganesh, K., Cai, W., Ferreira, P.J., Pirkle, A., Wallace, R.M., Cychosz, K.A. and Thommes, M. (2011b) 'Carbon-based supercapacitors produced by activation of graphene', *science*, 332(6037), pp. 1537-1541.

Zhu, Y., Murali, S., Stoller, M.D., Ganesh, K.J., Cai, W., Ferreira, P.J., Pirkle, A., Wallace, R.M., Cychosz, K.A. and Thommes, M. (2011c) 'Carbon-based supercapacitors produced by activation of graphene', *Science*, 332(6037), pp. 1537-1541.

Zhu, Z., Ma, J., Wang, Z., Mu, C., Fan, Z., Du, L., Bai, Y., Fan, L., Yan, H. and Phillips, D.L. (2014) 'Efficiency enhancement of perovskite solar cells through fast electron extraction: the role of graphene quantum dots', *Journal of the American Chemical Society*, 136(10), pp. 3760-3763.